The Pennsylvania State University

The Graduate School

Department of Materials Science and Engineering

BISMUTH PYROCHLORE-BASED THIN FILMS FOR DIELECTRIC ENERGY STORAGE

A Dissertation in

Materials Science and Engineering

by

Elizabeth K. Michael

Submitted in Partial Fulfillment
of the Requirements
for the Degree of

Doctor of Philosophy

August 2015

The dissertation of Elizabeth K. Michael was reviewed and approved* by the following:

Susan Trolier-McKinstry
Professor of Ceramic Science and Engineering
Dissertation Advisor
Chair of Committee

Thomas Jackson
Professor of Electrical and Engineering

Clive A. Randall
Professor of Materials Science and Engineering

Michael T. Lanagan
Professor of Engineering Science and Mechanics

Thomas R. Shrout
Professor of Materials Science and Engineering

Suzanne Mohney
Professor of Materials Science and Engineering
Head of the Department of Materials Science and Engineering

*Signatures are on file in the Graduate School

ABSTRACT

The drive towards the miniaturization of electronic devices has created a need for dielectric materials with large energy storage densities. These materials, which are used in capacitors, are a critical component in many electrical systems. Here, the development of dielectric energy storage materials for pulsed power applications, which require materials with the ability to accumulate a large amount of energy and then deliver it to the system rapidly, is explored.

The amount of electrostatic energy that can be stored by a material is a function of the induced polarization and the dielectric breakdown strength of the material. An ideal energy storage dielectric would possess a high relative permittivity, high dielectric breakdown strength, and low loss tangent under high applied electric fields. The bismuth pyrochlores are a compositionally tunable family of materials that meet these requirements.

Thin films of cubic pyrochlore bismuth zinc niobate, bismuth zinc tantalate, and bismuth zinc niobate tantalate, were fabricated using a novel solution chemistry based upon the Pechini method. This solution preparation is advantageous because it avoids the use of teratogenic solvents, such as 2-methoxyethanol. Crystalline films fabricated using this solution chemistry had very small grains that were approximately 27 nm in lateral size and 35 nm through the film thickness. Impedance measurements found that the resistivity of the grain boundaries was two orders of magnitude higher than the resistivity of the grain interior. The presence of many resistive grain boundaries impeded conduction through the films, resulting in high breakdown strengths for these materials.

In addition to high breakdown strengths, this family of materials exhibited moderate relative permittivities of between 55 ± 2 and 145 ± 5, for bismuth zinc tantalate and bismuth zinc niobate, respectively, and low loss tangents on the order of 0.0008 ± 0.0001. Increases in the

concentration of the tantalum end member increased the dielectric breakdown strength. For example, at 10 kHz, the room temperature breakdown strength of bismuth zinc niobate, $Bi_{1.5}Zn_{0.9}Nb_{1.5}O_{6.9}$, was 5.1 MV/cm, while the 10 kHz breakdown strength of bismuth zinc tantalate, $Bi_{1.5}Zn_{0.9}Ta_{1.5}O_{6.9}$, was 6.1 MV/cm. This combination of a high breakdown strength and a moderate permittivity led to a high discharged energy storage density for all film compositions. For example, at a measurement frequency of 10 kHz, bismuth zinc niobate exhibited a maximum recoverable energy storage density of 60.8 ± 2.0 J/cm^3, while bismuth zinc tantalate exhibited a recoverable energy storage density of 60.7 ± 2.0 J/cm^3. Intermediate compositions of bismuth zinc niobate tantalate were explored to maximize the energy storage density of the substitutional solid solution. At an optimized concentration of ten mole percent tantalum, the maximum recoverable 10 kHz energy storage density was ~66.9 ± 2.4 J/cm^3. These films of bismuth zinc niobate tantalate ($Bi_{1.5}Zn_{0.9}Nb_{1.35}Ta_{0.15}O_{6.9}$) sustained a maximum field of 5.5 MV/cm at 10 kHz, and demonstrated a relative permittivity of 122 ± 4. The films maintained a high energy storage density above 20 J/cm^3 though temperatures of 200°C.

The second major objective of this work was to integrate complex oxides processed at temperatures below 350°C onto flexible polyimide substrates for potential use in flexible energy storage applications. Nanocomposite films consisting of a nanocrystalline fluorite related to delta-bismuth oxide in an amorphous matrix were prepared by reducing the citric acid concentration of the precursor solution, relative to the crystalline films. These solutions were batched with the composition $Bi_{1.5}Zn_{0.9}Nb_{1.35}Ta_{0.15}O_{6.9}$. The nanocomposite had a relative permittivity of 50 ± 2 and dielectric losses on the order of 0.03 ± 0.01. For measurement frequencies of 1 kHz and 10 kHz, the nanocomposite demonstrated a breakdown strength of 3.8 MV/cm, and a room-temperature energy storage density of approximately 40.2 ± 1.7 J/cm^3. To determine the suitability of the nanocomposite films for use in flexible applications, free-standing flexible nanocomposite films underwent repetitive compressive and tensile bending around a

minimum bend diameter of 7 mm, which corresponded to a strain of 0.10%. After bending the films 30,000 times, the energy storage density of the films was unchanged, indicating that nanocomposite bismuth zinc niobate tantalate films may be suitable for flexible energy storage applications.

To demonstrate the broader applicability of the nanocomposite approach to developing energy storage dielectrics at low processing temperatures, films of nanocomposite lead titanate, $Pb_{1.1}TiO_{3.1}$, were deposited using an inverted mixing order solution preparation, and annealed at a maximum temperature of 400°C. X-ray diffraction indicated the presence of nanocrystalline ordering, and transmission electron microscopy confirmed the nucleation of isolated nanocrystals of lead oxide in an amorphous lead titanate matrix. The lead titanate nanocomposite demonstrated a relative permittivity of 33 ± 1 and a low loss tangent of 0.0008 ± 0.0001. The 10 kHz breakdown strength of the material was 5.0 MV/cm, resulting in an energy storage density of 28.4 ± 1.2 J/cm^3.

TABLE OF CONTENTS

LIST OF FIGURES

LIST OF TABLES

ACKNOWLEDGEMENTS

Putting together this acknowledgements section was the most stressful part of writing my thesis, as I was acutely worried that I would not be able to fully express my gratitude for all of the wonderfully helpful, encouraging, and inspiring people that contributed to my degree. This was also a very joyful process, in that I was able to reflect on all of the good people in my life, for whom I am extremely thankful.

First and foremost, I thank my advisor, Dr. Susan Trolier-McKinstry, for her tireless dedication to her students. I am constantly amazed not only by her eye for detail, but by how much personal attention she gives each of her students. I am indebted to her for bringing me into the group, for her high expectations, and for pushing me to work towards being a better scientist and engineer. Dr. McKinstry leads by example, demonstrating how to maintain professionalism in all circumstances, how to think creatively to design innovative approaches to tackle tricky lab problems, and to be critically thoughtful about the interpretation of data.

I would also like to thank the rest of the members of my committee- Dr. Clive Randall, Dr. Mike Lanagan, and Dr. Tom Shrout for their guidance throughout my degree. Additionally, the helpful discussions about my lab results and feedback about where to take my research with Dr. Tom Jackson shaped this project immeasurably. Thank you to all of the members of the STM research group, past and present, for bringing me up to speed when I joined the group and for sharing the joys and burdens of graduate school with me. A special thank you is reserved for Haoyu Li of the Jackson research group who graciously and patiently shared his knowledge, flexible testing system, and polyimide substrates.

Funding for this project came from a National Science Foundation Graduate Research Fellowship as well as the Dow Flexible Electronics project. The benefits of the Dow partnership have been many- from insight into the industrial research, development, and manufacturing

processes, to mentoring received from various project members (both from Dow and Penn State), culminating with a job offer that was gladly accepted.

Many thanks to all of the members of the Nanofab and MCL staff for their technical support, suggestions, and guidance throughout this project. I would like to thank Ke Wang for his help with transmission electron microscopy imaging and interpretation. I would also like to thank Steve Perini, Jeff Long, Andy Fitzgerald, Mike LaBella, and, of course, Beth Jones for training me in the Nanofab and MCL, helping me think through technical issues and experimental design, and for always maintaining a good sense of humor that made my time in lab a bit more fun.

Thank you to my family and friends for the endless support and love they shown me throughout the doctoral process, which I often equate to running a marathon. A special thank you is reserved for my parents and sister, each of whom played a very different, and critical, role to me finishing this degree. Although each of them wears a huge pair of "parent goggles" that causes them to think I am the next Nobel laureate, their contributions reach far beyond their enthusiastic encouragement and love. To my mum, for taking a special interest in what exactly it is that I do in lab, to my dad, for keeping me from taking myself and my work too seriously, and to Kelly, for her wisdom beyond her years, her sympathy with the stresses of grad school, and for not bragging too much that she started after, and then finished grad school, before me.

Finally, I would be completely remiss if I did not thank my fiancé (and very soon to be husband!) John Sapia. You have been my number one source of support, encouragement, inspiration, and love throughout this whole process, and I am not sure how this would have happened without you. I am very excited to start our next adventure together!

Chapter 1

Introduction

This chapter provides an introduction to the work presented in this thesis. In addition to discussing the rationale and applications of this research, a section is included to summarize the organization of the thesis.

1.1 Capacitors for Energy Storage Applications

Energy storage capacitors are a critical component in many electrical systems. Recent research has focused on the development of capacitors for pulsed power applications, which require materials with the ability to accumulate a large amount of energy and then deliver it to the system rapidly. In these applications, discharge occurs in less than one second, necessitating high frequencies on the order of several kilohertz [1, 2, 3, 4, 5, 6]. Pulsed power capacitors find uses in wide-ranging applications, from industrial lasers used for cutting and welding, to critical biomedical devices, such as heart defibrillators and x-ray equipment [7, 8]. For example, the miniaturization of pulsed power capacitors has allowed for the development of implantable defibrillators [8], which are surgically inserted in nearly 100,000 people annually in the United States [9]. These devices are approximately the size of a pocket watch [9], with the capacitor component of the pulse generator comprising the bulk of the device [8, 10]. Implantable heart defibrillators provide approximately 30 joules of energy to the human heart [11, 12]; improved energy storage densities of the capacitors in defibrillator pulse generators will allow for the further miniaturization of these devices, simplifying implantation procedures, reducing implant

morbidity, and minimizing recovery time after surgery [8, 13]. This defibrillator example requires the capacitor to remain charged to allow for immediate, high-frequency discharge upon detection of a heart event, although several power electronics applications, such as pulsed lasers, flash tubes, and military equipment, require constant cycling of the capacitors [14, 15]. Advances in renewable energy sources and hybrid/electric vehicles are also dependent on the development of capacitive materials with both high energy and high power storage densities [16, 17, 18].

For a system to simultaneously possess a high energy and high power storage density, batteries and capacitors are typically used in tandem [19, 20]. For example, hybrid/electric vehicles benefit from the use of battery and capacitor electrical systems, which ensure the power, lifetime, and reliability of the vehicle. As seen in the Ragone plot of Figure 1-1 [21], typical capacitors have a high power density and a relatively small energy storage density, while batteries are responsible for maintaining a high energy storage density for the system [5]. One approach to the optimization of energy storage devices used in electronic systems is to increase the energy storage density of dielectric capacitive materials.

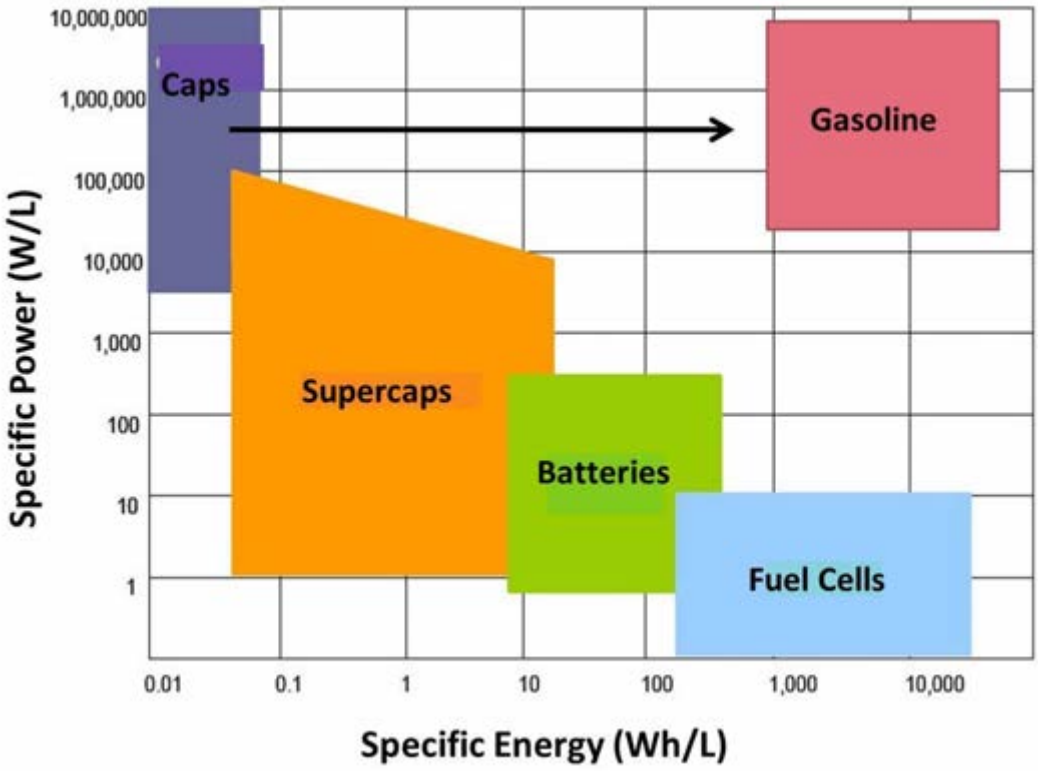

Figure 1-1. A Ragone plot illustrating the relative energy and power storage capability of several commercial energy storage technologies [21].

One of the objectives of this work was to develop lead-free dielectric thin film materials with high energy storage densities. In addition to demonstrating a high maximum discharged energy density, the films should possess a large energy storage density when the high field loss tangent is restricted to 2% [22], in order to minimize power dissipation through the material during cycling of the capacitors. This metric for high field loss tangents is in accordance with the Department of Energy's Freedom Car project to develop hybrid-electric vehicles and with the US Navy's goals to develop energy-efficient technologies for existing and future ships. Other applications have different requirements; for example, high temperature aerospace power electronics for the US Air Force mandate maximum loss tangents of 0.001 [23].

1.1.1 The Development of Dielectrics for Flexible Energy Storage Applications

In addition to developing high energy density materials for use in the existing technologies discussed above, it is also desirable to explore flexible applications. Flexible electronics have many potential uses, from consumer products, such as cell phones and portable keyboards, to biomedical devices, such as body-mounted sensors. In these instances, a high energy storage density component is required to ensure the lifetime and portability of the overall electronic device [24, 25, 26, 27, 28]. These energy storage materials need to be lightweight, possess a high energy density, and be compatible with flexible polymeric substrates. Furthermore, the dielectrics would be required to maintain excellent electrical performance with minimal structural degradation while undergoing various one-dimensional folds. A second possible application for flexible thin films is in wound capacitor technology. Wound capacitors are common in polymeric films [29] in which low permittivity values (usually $\varepsilon_r<10$) necessitate space-efficient construction of capacitors.

Many of the medium- to high-permittivity dielectric materials that are used in commercial thin film applications are crystallized at high temperatures (between 600°C and 800°C) [30, 31], limiting possible substrates to materials with high melting points. This is a consequence of the high crystallization temperatures required to produce moderate permittivity values. The development of materials and deposition techniques suitable for the growth of complex oxide thin films at and below 400°C on polymeric substrates, such as polyimide, is desirable for flexible electronics applications. Thus, the second objective of this work is to integrate complex oxides onto flexible polyimide substrates for potential use in flexible energy storage applications.

1.2 Thesis Organization

The overall goal of this work is to develop and characterize thin film materials suitable for use as energy storage dielectrics. As discussed above, this goal can be broadly divided into two major objectives. The first portion of this thesis describes the development of crystalline materials processed at temperatures of 600°C, while the second portion discusses the development of nanocomposite materials processed at temperatures compatible with polymeric substrates, enabling their use in flexible electronics.

To provide the context and necessary background for this thesis, chapter two discusses the properties that are important when engineering energy storage materials and summarizes the current state of the art energy storage dielectrics. Two of the materials examined extensively in this thesis, bismuth zinc niobate and bismuth zinc tantalate, are also discussed in chapter two. Chapter three details the experimental methods used throughout the work. Chapter four discusses the novel solution chemistry and thin film deposition process developed for the fabrication of bismuth pyrochlore thin films. More details about the conditions investigated for thin film densification can be found in Appendix A.

Chapter five begins the portion of the thesis pertaining to crystalline energy storage dielectrics processed at a maximum temperature of 600°C. This chapter discusses the dielectric properties and suitability of bismuth zinc niobate for energy storage applications. Chapter six expands the discussion of bismuth pyrochlores for dielectric energy storage by examining the behavior of bismuth zinc tantalate and bismuth zinc niobate tantalate, a solid solution formed from bismuth zinc niobate and bismuth zinc tantalate end members. The link between film microstructure and the resulting dielectric properties is probed via impedance spectroscopy.

Chapter seven pertains to low-temperature thin film deposition for flexible electronic devices. The development, characterization, and application-specific testing of nanocomposite

bismuth zinc niobate tantalate on flexible polyimide substrates is described in chapter seven. To explore the possibility of using a nanocomposite approach for low temperature processing of other complex oxide systems with a high energy storage density, nanocomposite lead titanate is investigated in chapter eight. Finally, chapter nine concludes the thesis and provides ideas for possible future work derived from this study.

1.3 References

1] P. Barber, S. Balasubramanian, Y. Anguchamy, S. Gong, A. Wibowo, H. Gao, H. J. Ploehn and H.-C. zur Loye, "Polymer composite and nanocomposite dielectric materials for pulse power energy storage," *Materials,* vol. 2, no. 4, pp. 1697-1733, 2009.

2] T. Filchev, F. Carastro, P. Wheeler and J. Clare, "High voltage high frequency power transformer for pulsed power application," in *14th International Power Electronics and Motion Control Conference*, pp. 165-170, 2010.

3] H. Bluhm, Pulsed Power Systems: Principles and Applications, Springer, 2006.

4] J. Sowash, "A heroic capacity," *American Ceramic Society Bulletin,* vol. 88, no. 4, pp. 19-25, 2009.

5] M. Winter and R. J. Brodd, "What are batteries, fuel cells, and supercapacitors?," *Chemical Reviews,* vol. 104, p. 4245−4269, 2004.

6] J. D. van Wyk, "Power electronics technology at the dawn of a new century- past achievements and future expectations," *Proceedings of the Power Electronics and Motion Control Conference,* vol. 1, pp. 9-20, 2000.

7] M. V. Fazio and H. C. Kirbie, "Ultracompact pulsed power," *Proceedings of the IEEE,* vol. 92, no. 7, pp. 1197-1204, 2004.

8] M. Glikson and P. A. Friedman, "The implantable cardioverter defibrillator," *The Lancet,* vol. 357, pp. 1107-1117, 2001.

9] American Heart Association, "American Heart Association," [Online]. Available: http://www.heart.org/HEARTORG/.

10] J. B. Ennis, F. W. MacDougall, R. A. Cooper, J. Bates and N. Ozkan, "Recent developments in pulse power applications," in *2nd International Symposium on Pulsed Power and*

Plasma Applications, Kyung-Nam, Korea, 2001.

11] D. Graham-Rowe, "Internal external defibrillator," MIT Technology Review, November 26, 2008, http://www.technologyreview.com/news/411249/internal-external-defibrillator/.

12] D. M. Zogbi, "Capacitors and the implantable defibrillator market," Passive Component Industry, October 30, 2001, http://www.passivecomponentmagazine.com/capacitors-and-the-implantable-defibrillator-market-oct-2001/.

13] F. W. MacDougall, J. B. Ennis, R. A. Cooper, J. Bates and K. Seal, "High energy density pulsed power capacitors," in *14th IEEE International Pulsed Power Conference Digest of Technical Papers*, pp. 513-517, 2003.

14] H. Tang and H. A. Sodano, "Ultra high energy density nanocomposite capacitors with fast discharge using $Ba_{0.2}Sr_{0.8}TiO_3$ nanowires," *Nano Letters,* vol. 13, pp. 1373-1379, 2013.

15] F. MacDougall, J. Ennis, X. H. Yang, K. Seal, S. Phatak, B. Spinks, N. Keller, C. Naruo and T. R. Jow, "Large high energy density pulse discharge capacitor characterization," in *IEEE International Pulsed Power Conference Proceedings*, Monterey, CA, pp. 1215-1218, 2005.

16] D. P. Shay, N. J. Podraza, N. J. Donnelly and C. A. Randall, "High energy density, high temperature capacitors utilizing Mn-doped $0.8CaTiO_3$–$0.2CaHfO_3$ ceramics," *Journal of the American Ceramic Society,* vol. 95, no. 4, p. 1348–1355, 2012.

17] K. Yao, S. Chen, M. Rahimabady, M. S. Mirshekarloo, S. Yu, F. E. H. Tay, T. Sritharan and L. Lu, "Nonlinear dielectric thin films for high-power electric storage with energy density comparable with electrochemical supercapacitors," *IEEE Transactions on Ultrasonics, Ferroelectrics, and Frequency Control,* vol. 58, no. 9, pp. 1968-1974, 2011.

18] W. J. Sarjeant, I. W. Clelland and R. S. Price, "Capacitive components for power electronics," *Proceedings of the IEEE,* vol. 89, no. 6, pp. 846-855, 2001.

19] S. Tong, B. Ma, M. Narayanan, S. Liu, R. Koritala, U. Balachandran and D. Shi, "Lead lanthanum zirconate titanate ceramic thin films for energy storage," *Applied Materials & Interfaces,* vol. 5, p. 1474−1480, 2013.

20] C. E. Holland, J. W. Weidner, R. A. Dougal and R. E. White, "Experimental characterization of hybrid power systems under pulse current loads," *Jounal of Power Sources,* vol. 109, no. 1, pp. 32-37, 2002.

21] J. Hruska, "Philadelphia unveils new hybrid subway trains that use Prius-like regenerative braking to feed energy back into the grid," *ExtremeTech,* April 16, 2014, http://www.extremetech.com/extreme/180636-philadelphia-unveils-new-hybrid-subway-system-that-uses-prius-like-regenerative-breaking-to-feed-energy-back-into-the-grid.

22] S. Islam, "Polymer nano-dielectrics for high density energy storage," Ph.D. Thesis, University of South Carolina, 2014.

[23] N. Venkat, T. D. Dang, Z. Bai, V. K. McNier, J. N. DeCerbo, B.-H. Tsao and J. T. Stricker, "High temperature polymer film dielectrics for aerospace power conditioning capacitor applications," *Materials Science and Engineering B,* vol. 168, pp. 16-21, 2010.

[24] V. L. Pushparaj, M. M. Shaijumon, A. Kumar, S. Murugesan, L. Ci, R. Vajtai, R. J. Linhardt, O. Nalamasu and P. M. Ajayan, "Flexible energy storage devices based on nanocomposite paper," *Proceedings of the National Academy of Sciences of the United States of America,* vol. 104, no. 34, p. 13574–13577, 2007.

[25] A. Kafy, K. K. Sadasivuni, H.-C. Kim, A. Akther and J. Kim, "Designing flexible energy and memory storage materials using cellulose modified graphene oxide nanocomposites," *Physical Chemistry Chemical Physics,* vol. 17, pp. 5923-5931, 2015.

[26] A. Yu, I. Roes, A. Davies and Z. Chen, "Ultrathin, transparent, and flexible graphene films for supercapacitor application," *Applied Physics Letters,* vol. 96, p. 253105, 2010.

[27] K. Jost, C. R. Perez, J. K. McDonough, V. Presser, M. Heon, G. Dion and Y. Gogotsi, "Carbon coated textiles for flexible energy storage," *Energy & Environmental Science,* vol. 4, no. 12, pp. 5060-5067, 2011.

[28] D. Wei, S. J. Wakeham, T. W. Ng, M. J. Thwaites, H. Brown and P. Beecher, "Transparent, flexible and solid-state supercapacitors based on room temperature ionic liquid gel," *Electrochemistry Communications,* vol. 11, no. 12, p. 2285–2287, 2009.

[29] S. O. Kasap, Principles of Electronic Materials and Devices, New York City: McGraw-Hill, 2005.

[30] R. L. Thayer, C. A. Randall and S. Trolier-McKinstry, "Medium permittivity bismuth zinc niobate thin film capacitors," *Journal of Applied Physics,* vol. 94, no. 3, pp. 1941-1947, 2003.

[31] J. Cheng, W. Zhu, N. Li, L. E. Cross and Z. Meng, "Characterization of the sol-gel derived PZT thick films on metal substrates," in *Recent Developments in Electronic Materials and Devices*, The American Ceramic Society, 2012, pp. 33-40.

Chapter 2

Literature Review

This chapter contains a review of some of the background pertinent to this investigation. Capacitive energy storage will be discussed, including the important materials properties that influence energy storage, the differences between the types of materials commonly used for energy storage, as well as an overview of the current state of the art energy storage materials. A discussion of bismuth zinc niobate and bismuth zinc tantalate, two of the bismuth pyrochlores explored in this work, will follow. Finally, a review of the physics involved in chemical solution deposition will be presented.

2.1 Dielectric Energy Storage

As discussed in Chapter 1, energy storage capacitors and dielectrics are a critical component in many electrical systems. The maximum energy density that can be stored by a material is a function of the induced polarization (relative permittivity) and breakdown strength of a material. The dielectric energy storage density is calculated using the following equation [1]:

$$J = \int_{P_0}^{P_{max}} EdP \approx \frac{\varepsilon_o \varepsilon_r E^2}{2}$$

in which J is the stored energy density, E is the applied electric field sustained by the material, P is the resulting polarization of the dielectric, P_o is the polarization at zero field, P_{max} is the maximum induced polarization, ε_o is the permittivity of free space, and ε_r is the relative

permittivity of the material. The integral in this equation represents the discharged energy storage density for all dielectric materials, while the approximation on the right-hand side of the equation is only strictly true for ideal, linear dielectric materials with a permittivity exceeding 30 (this permittivity restriction is due to the dependence of polarization on electric susceptibility; for large permittivities, the difference between permittivity and susceptibility is small) [2]. Although the integral should be used for energy storage calculations, the linear approximation captures the contributions of several important materials properties. Based upon an analysis of this equation, it can be seen that an ideal material for energy storage applications would possess a high relative permittivity, high breakdown strength, and a low loss tangent under high applied electric fields. In the case of a material with a hysteretic polarization response to field, the stored energy density is calculated using the decreasing field portion of the polarization-electric field loop.

2.1.1 Critical Materials Properties for Energy Storage

Realistically, it is difficult to simultaneously achieve a high relative permittivity, high breakdown strength, and a low loss tangent; a compromise between relative permittivity and breakdown strength is typically employed to attain high energy storage densities [2, 3, 4, 5, 6, 7]. Figure 2-1 shows the correlation between breakdown strength and relative permittivity for several materials reported to have a high energy storage density [1, 4, 5, 8, 9, 10, 11, 12, 13, 14, 15, 16, 17, 18, 19, 20, 21]. As seen in Figure 2-1, most energy storage materials do not possess both a high relative permittivity and high breakdown strength. Here, the properties that are essential to evaluating and engineering high energy storage density materials, particularly the relative permittivity and breakdown strength, are discussed.

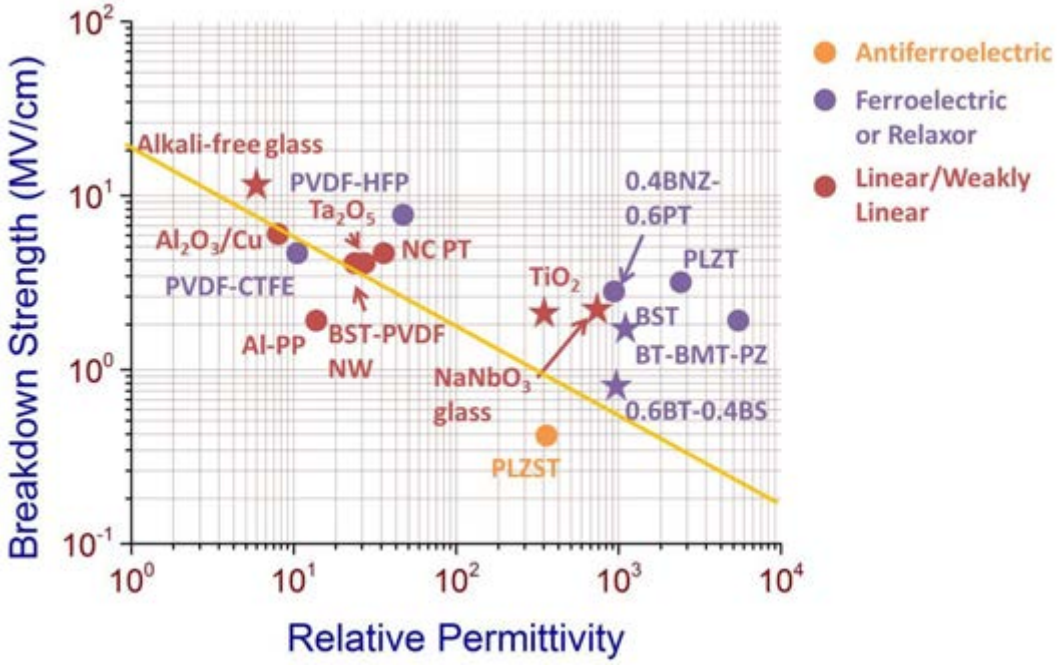

Figure 2-1. The maximum breakdown strength as a function of relative permittivity for materials reported to exhibit a high energy storage density [1, 4, 5, 8, 9, 10, 11, 12, 13, 14, 15, 16, 17, 18, 19, 20, 21]. The abbreviations are: PLZT, lead lanthanum zirconate titanate; PLZST, lanthanum-doped lead zirconate stannate titanate; PVDF, polyvinylidene fluoride; HFP, hexafluoropropene; CTFE, chlorotrifluoroethylene; PP, polypropylene; BST, barium strontium titanate; PZN-PMN-PT, lead zinc niobate-lead magnesium niobate-lead titanate; BT-BMT-PZ, barium titanate-bismuth magnesium titanate-lead zirconate; BNZ-PT, bismuth nickelate zirconate-lead titanate; Al-PP, aluminum-polypropylene nanocomposite.

2.1.1.1 Relative Permittivity

The relative permittivity of a material is defined as the polarizability of the material relative to the polarizability of a vacuum [22]. The degree of polarizability is an important factor when evaluating the energy storage capability of a material. Capacitors store energy in an electrostatic field. For a parallel plate structure, a potential difference is applied across the plates

(electrodes) of the capacitor, which sandwich a dielectric material. As the dielectric polarizes in response to the applied electric field, a second electric field will develop within the material that opposes the applied field. A positive charge will accumulate on one plate of the capacitor and a negative charge will accumulate on the other; similarly, charge densities will accumulate on both surfaces of the dielectric. This separation of charge is the mechanism by which energy is stored in a capacitor. The more polarizable the material is, the greater the magnitude of the charge that will be stored on the plates of the capacitor [23]. Thus, the permittivity is the macroscopic response capturing the polarization. It is related to the dielectric displacement and the electric field by the following equation [22]:

$$D = \varepsilon_o E + P \approx \varepsilon_o \varepsilon_r E$$

in which D is the dielectric displacement, P is the polarization, ε_o is the permittivity of free space ($8.85*10^{-12}$ F/m), ε_r is the relative permittivity, and E is the applied electric field. Polarization describes the response of bound charges in a material to the applied electric field, while the dielectric displacement accounts for both bound and free charges in the material [22].

There are four polarization mechanisms that contribute to the permittivity of a dielectric material [22]. The atomic, or electronic, polarizability is the distortion, or small displacement, of the electron cloud of the atom relative to the nucleus when an electric field is applied. The ionic polarizability involves a distortion in bond length between atoms of different charge when a field is applied; this causes a slight displacement in anion and cation sublattices. Dipolar polarizability is due to the alignment of permanent dipoles in an electric field so that they are oriented in the direction of the field. The fourth type of polarizability is space charge polarization, in which macroscopic migration of charges occurs until they are blocked by an insulating interface, such as a grain boundary. These mechanisms are shown schematically in Figure 2-2 [22].

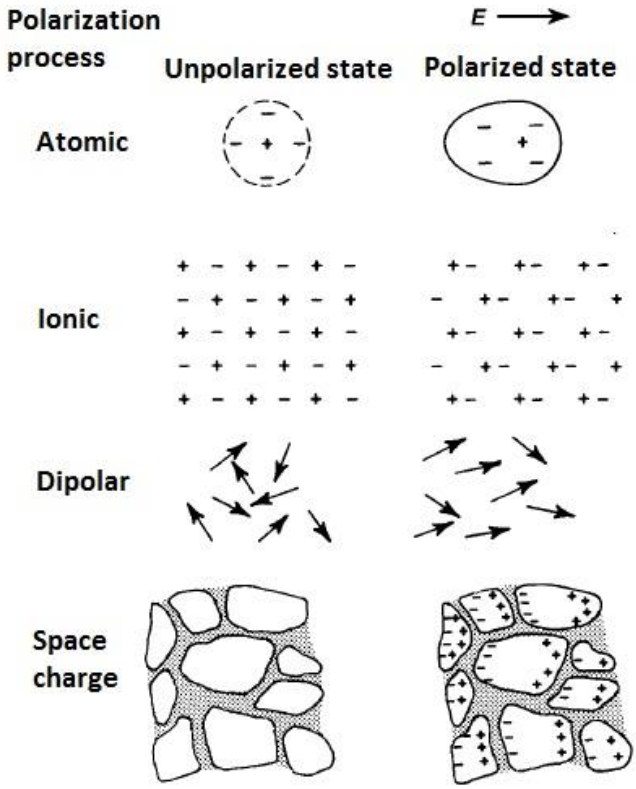

Figure 2-2. A schematic of the polarization mechanisms contributing to the relative permittivity of a dielectric material. From [22].

Not all polarization mechanisms may be active in a given material, but those that are present are additive [23], in accordance with the following equation:

$$\varepsilon_{total} = \varepsilon_{\infty} + \varepsilon_{electronic} + \varepsilon_{ionic} + \varepsilon_{dipolar} + \varepsilon_{space\ charge}$$

in which ε_{∞} is the permittivity in a vacuum, which has a value of one. Electronic polarization may contribute a permittivity of approximately 1.5 – 10, ionic polarization can contribute up to approximately 100, dipolar polarization can contribute up to 50,000, and space charge contributions can result in permittivities in excess of 100,000 [22, 23, 24]. For example, the only contribution to the permittivity of diamond is electronic polarization ($\varepsilon_r \sim 5$) [25], while a well-

made sample of barium titanate would have electronic, ionic, and dipolar contributions (room temperature ε_r ~2,000-4,500) [22]. Each mechanism has a frequency limit above which that contribution is no longer active; the loss of each contribution is associated with either a relaxation or a resonance [22, 23]. Space charge and dipolar relaxation processes are independent of temperature, while ionic and electronic polarization processes are associated with temperature-dependent resonances. Figure 2-3 depicts how each of these mechanisms contributes to the overall relative permittivity, and shows the frequency limit for each contribution [22].

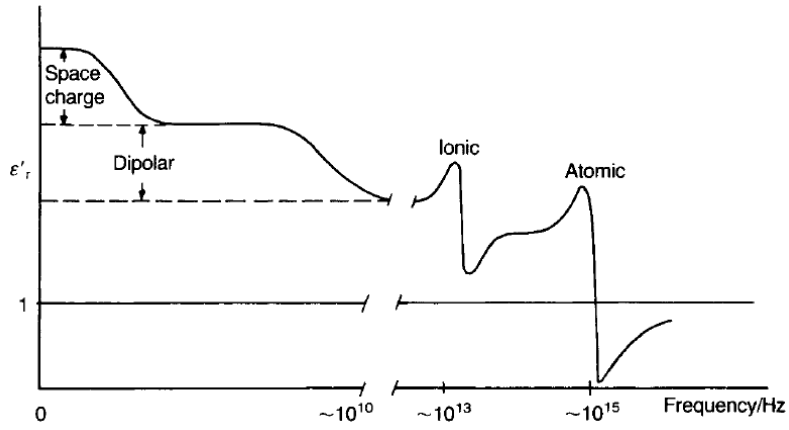

Figure 2-3. A schematic of the relative permittivity of a dielectric material as a function of frequency. From [22].

2.1.1.2 Loss Tangent

Permittivity is a complex quantity represented by the following equation [22, 23]:

$$\varepsilon^* = \varepsilon' - i\varepsilon''$$

where ε^* is the complex permittivity, ε' is the real part of the permittivity discussed in section 2.1.1.1, and ε'' is the imaginary component of the permittivity, which scales with the loss of the material. Each of the relaxation and resonance processes depicted in Figure 2-3 are associated

with a peak in the dielectric loss. The figure of merit used to quantify loss is *tanδ*, which is the ratio of the imaginary component of the permittivity to the real component of the permittivity [22]. Practically, the dielectric loss dissipates energy from the material in the form of heat [23]. There are two main extrinsic contributions to the measured dielectric loss for a centrosymmetric material [26, 27, 28]. In conductive loss, the flow of charge through the material causes energy to dissipate. The motion of charged defects in an alternating field also causes dissipation of heat and energy. In general, loss will increase with increasing temperature, due to enhanced conduction through the film.

Losses in a dielectric material are manifested by the area enclosed by a polarization-electric field loop [29], as shown in Figure 2-4. The minimization of loss is important in energy storage applications to minimize the dissipation of stored energy upon discharge. When calculating energy storage density for a material, it is critical that losses be *excluded* from the reported discharged energy density, as depicted in Figure 2-4(b).

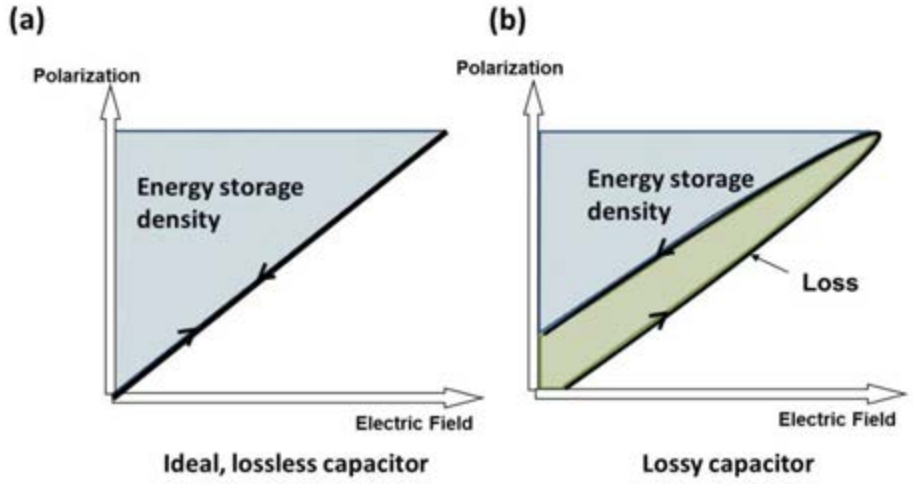

Figure 2-4. A schematic of an ideal, lossless capacitor (a) and a non-ideal, lossy capacitor (b). Loss reduces the discharged energy storage density of the material, and should not be included in energy storage calculations.

2.1.1.3 Dielectric Breakdown Strength

The dielectric breakdown strength is defined as the limiting electric field that can be applied before an irreversible change occurs to the insulative state of the dielectric [22]. Due to the squared dependence of energy storage density on breakdown strength, researchers are actively pursuing materials with a high maximum field, often at the expense of a high relative permittivity. It can be seen in the modified MacPhearson plot of Figure 2-1 that many materials with a high energy storage density fall above the historical "best-fit" line [7], primarily due to increases in the breakdown strengths associated with improved processing and/or reduction in dielectric thicknesses. Many of the extrinsic factors reducing the dielectric breakdown are directly related to processing of the material [22, 30]. For example, the thickness and geometry of the sample are important; as the sample volume that is probed increases, there is a higher likelihood that a critical flaw will be encountered, causing breakdown. Critical flaws, such as pores or inclusions, concentrate the local electric field. Surface roughness of the sample is also important, as asperities at interfaces will create concentrations in the local electric field. Furthermore, sample homogeneity, porosity, and electrode composition, which affect the Schottky barrier, may also influence the breakdown behavior of the sample. These extrinsic factors usually prevent experimentally accessing the intrinsic breakdown strength of a material, which is defined as breakdown caused by bond breaking in the material, usually due to an avalanche effect [22]. Avalanche breakdown is described as a series of events in which the injection of an electron into the material ionizes a species in the sample, creating another electron. The electron ejected during ionization will collide with, and ionize, more atoms in the material, creating an excess of electrons via an avalanche effect that will culminate in breakdown.

There are several additional dielectric breakdown mechanisms that may occur before the material reaches fields sufficient to initiate intrinsic failure [31, 32]. Electrochemical breakdown

involves the transport of ionic species. As an electric field is applied to the sample, charged ionic species (in oxide materials, these are often oxygen vacancies) will migrate through the sample. The buildup of charged ionic species at an electrode will initiate breakdown. Electromechanical breakdown occurs due to a coupling between the electric field and electrostriction (or piezoelectric strain, when present) in a material. Electrostriction can lead to high local stresses that may exceed the critical stress for a material, causing breakdown via mechanical failure. Electronic, or avalanche, breakdown occurs via the multiplication of conduction electrons in a sample as a field is applied. The excess of electrons created via this avalanche effect eventually culminate in sample breakdown. The final breakdown mechanism is thermal breakdown. This breakdown mechanism is driven by Joule heating, in which the applied electric field produces a current that will flow through the sample. Current flow will produce a finite amount of Joule heating, promoting more carriers and increasing the conductivity of the sample. Thermal runaway will cause dielectric breakdown.

Breakdown values follow a statistical distribution, and are usually reported in terms of Weibull statistics [33]. When reporting the breakdown strength of a material, it is important to not only report the Weibull modulus and the characteristic breakdown field, but also the measurement temperature, electrode and sample size, and the frequency at which the measurement was made. To date, there is no standardized set of measurement conditions used to define breakdown [22]; thus, it is important to report the conditions used during testing.

2.1.2 Materials for High Dielectric Energy Storage

Researchers are targeting a variety of materials classes to be used as energy storage dielectrics. Figure 2-5 (after Sherrit [34]) shows the polarization-electric field behavior of ideal (a) linear dielectric, (b) ferroelectric, (c) relaxor, and (d) antiferroelectric materials; the shaded area of the polarization-electric field hysteresis curve is the recoverable energy storage density. Each of these types of materials has distinct characteristics that influence their suitability for use as an energy storage dielectric.

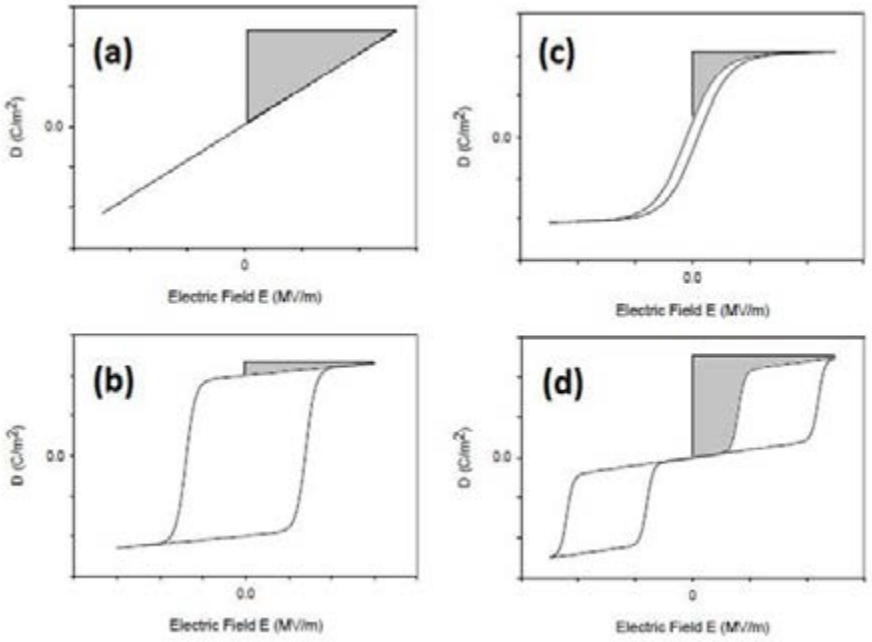

Figure 2-5. The energy storage density for several types of dielectric material: (a) linear, (b) ferroelectric, (c) relaxor, and (d) antiferroelectric. The shaded areas of the dielectric displacement (*D*)-electric field hysteresis curves are representative of the energy storage density (after Sherrit [34]).

Ferroelectric materials, such as lead zirconate titanate or barium titanate, are polar materials that can be reoriented, with an appropriate electric field, between equilibrium polarization states [22]. Ferroelectrics generally have high permittivities (often on the order of 1,000) due to the long-range ordering of the spontaneous polarization in the material, but the permittivity decreases significantly at high applied electric fields. Furthermore, the high remanent polarization values and hysteretic losses [35] contribute to higher energy losses. Many ferroelectric materials are further limited by their moderate breakdown strengths, which are often below 1 MV/cm [36]. Two ferroelectric materials that are attracting attention for their potential use in dielectric energy storage are PLZT, a lanthanum-doped lead zirconate titanate, and PVDF, polyvinylidene fluoride, a ferroelectric polymer that is often used as a co-polymer in composites or as a matrix material in nanocomposites. Hu et al. [37] demonstrated an energy density of ~30 J/cm^3 for PLZT films with a relative permittivity of 1400 and a breakdown strength of 2.3 MV/cm. Balachandran et al. [16] reported a best-case energy storage density of 85 J/cm^3 for PLZT films on nickel foils by demonstrating an electrode with a breakdown strength of 4.3 MV/cm. The Weibull plot for these films indicates a breakdown strength of 2.6 MV/cm, as shown in Figure 2-6 [16], giving a reproducible energy storage density on the order of that reported by Hu et al. [37] The loss tangent for these PLZT films was between 0.05 and 0.08 [16]. Reducing the hysteretic losses in the material and increasing the reproducible breakdown strength would improve the recoverable energy storage density of PLZT. PVDF and PVDF-containing composites exhibit large energy densities compared to other polymeric energy storage materials. For example, PVDF-CTFE (polyvinylidene fluoride-chlorotrifluoroethylene) has a permittivity of 13 and a breakdown strength of 6.2 MV/cm, resulting in an energy storage density of 25 J/cm^3 [38]. While PVDF-based materials show promise as energy storage dielectrics, the melting point of PVDF is 177°C, which limits the maximum operating temperature to 125°C [39]. Although

the use of copolymers increases the maximum operating temperature in many instances, PVDF-based materials are still limited by high hysteretic losses [40].

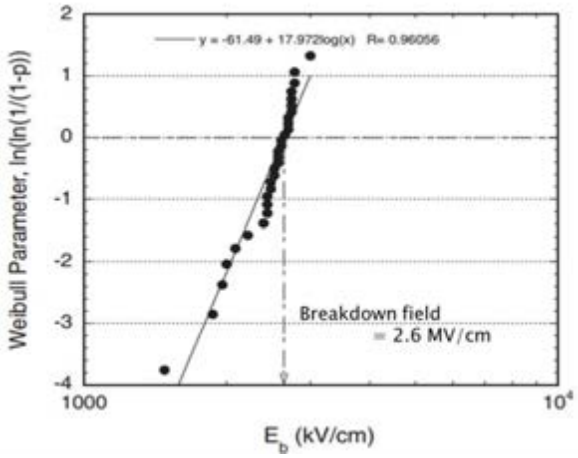

Figure 2-6. The Weibull plot for lanthanum-doped lead zirconate titanate [16]. The breakdown strength for this composition is approximately 2.6 MV/cm.

Relaxor ferroelectrics, whose long-range ordering is disrupted by the formation of polar clusters within a matrix, also offer relatively high permittivity values [41]. This class of material retains a field dependence to the permittivity, but they have much slimmer polarization-electric field hysteresis loops than most normal ferroelectrics, reducing the energy loss from the material. Solid solutions of barium titanate-bismuth scandate [17] and barium titanate-bismuth magnesium titanate [42] are relaxor materials that have been demonstrated to possess high energy storage densities. Barium titanate-bismuth magnesium titanate, for example, was demonstrated to have a relative permittivity in excess of 900 and dielectric losses of approximately 0.02. At an applied field of 1.9 MV/cm, these films exhibited an energy storage density of 37 J/cm^3. Thus, ferroelectric relaxors have the potential for high energy storage densities, provided that the breakdown strength of these materials is sufficiently high. However, relaxor ferroelectrics are still limited by their non-linear behavior and large high-field losses.

Antiferroelectric materials, such as lead zirconate, are distinguished by an antiparallel alignment of their spontaneous dipoles [43]. The application of a sufficiently strong electric field will produce a phase transformation to the ferroelectric state. The permittivity of the material will increase with the first-order phase transition that accompanies the transformation to ferroelectric behavior. Although these materials are promising due to a zero value for remanent polarization, the high field polarization dependence and losses associated with dipolar switching has limited their use as energy storage dielectrics [44, 45].

Linear and weakly nonlinear dielectrics, which are the focus of this study, are a topic of intense research effort due to the potential breakdown strength-permittivity compromise they offer. For example, Smith et al. [15] achieved an energy density in excess of 35 J/cm^3 using an alkali-free glass with a relative permittivity of 6 and a breakdown strength of 12 MV/cm. Linear dielectrics have no field dependence to their polarization, resulting in moderate permittivity values, usually less than 100 [36], across the entire field range. Although several weakly nonlinear dielectrics, including the materials studied in this work, exhibit some tunability, the field dependence is significantly reduced relative to ferroelectrics, relaxor ferroelectrics, and antiferroelectrics. Additionally, these materials exhibit relatively high breakdown strengths and low loss tangents (usually below 0.001). Ideal linear dielectrics allow for all the stored energy to be recovered upon discharge of the capacitor, although, in reality, linear dielectrics have some degree of high-field loss that reduces the discharged energy density. An increase in the breakdown strength of linear dielectrics and the reduction of high-field loss is critical to the improvement of this material class for their use in energy storage devices.

The frequency used to measure energy storage density values is often not reported; as many materials properties critical to evaluating a material for dielectric energy storage, such as breakdown strength, may be dependent on measurement frequency, comparing maximum discharged energy density can be difficult. Figure 2-7 shows a comparison of previous reports in

the literature for the maximum discharged energy density for several state of the art dielectrics. Data are plotted with energy storage density as a function of maximum processing temperature for several materials that are being actively explored for their potential use in energy storage applications [1, 4, 5, 9, 14, 15, 16, 17, 18, 19, 20, 37, 42, 46, 47, 48, 49]. Figure 2-7 includes lead-containing and lead-free oxide thin films, several high energy density polymers, nanocomposite materials, and glasses.

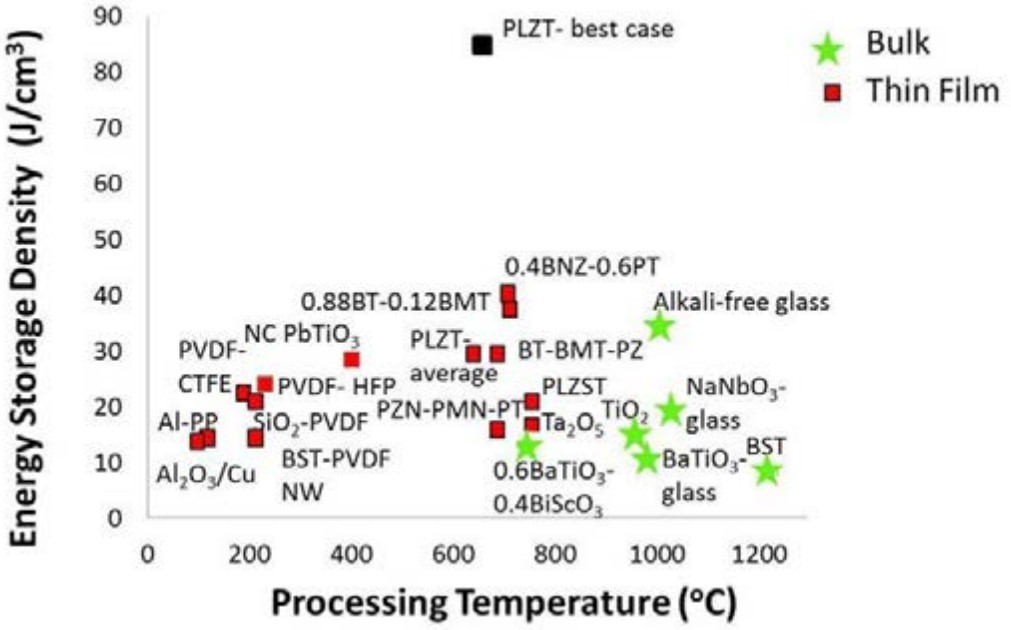

Figure 2-7. Energy storage density as a function of maximum processing temperature for several energy storage materials currently being investigated [1, 4, 5, 9, 14, 15, 16, 17, 18, 19, 20, 37, 42, 46, 47, 48, 49]. The abbreviations are: PLZT, lead lanthanum zirconate titanate; PLZST, lanthanum-doped lead zirconate stannate titanate; PVDF, polyvinylidene fluoride; HFP, hexafluoropropene; CTFE, chlorotrifluoroethylene; PP, polypropylene; BST, barium strontium titanate; PZN-PMN-PT, lead zinc niobate-lead magnesium niobate-lead titanate; BT-BMT-PZ, barium titanate-bismuth magnesium titanate-lead zirconate; BNZ-PT, bismuth nickelate zirconate-lead titanate; Al-PP, aluminum-polypropylene nanocomposite.

2.2 Bismuth Pyrochlores

Several bismuth-containing pyrochlores were explored throughout this thesis for use in energy storage applications. Two of the main materials systems, bismuth zinc niobate and bismuth zinc tantalate, are reviewed here. First, the cubic pyrochlore crystal structure is described.

2.2.1 Pyrochlore Crystal Structure

Cubic pyrochlore oxides have the general chemical formula $A_2B_2O_6O'$, which emphasizes the four crystallographically inequivalent atoms in the structure [50]. Ideal cubic pyrochlores have the space group *Fd3m*, and consist of two cation coordination polyhedra. The larger A-site cations are surrounded by eight anions to form a scalenohedra, or distorted cube. The scalenohedra consists of six oxygen (O) atoms that are equally spaced from the central cation, and two oxygen atoms (O') that have a shorter bond length with the central cation. The O' atoms are only bonded to the A-site cations [51]. The smaller B-site cations are octahedrally coordinated, and all six oxygen atoms are equidistant from the central cation. There are several descriptions that have been used to summarize the pyrochlore crystal structure. One of the most widely used descriptions depicts the structure as corner-linked BO_6 octahedra with A-site cations in the interstices. The crystal structure is shown in Figure 2-8 [52]. In this image, the BO_6 coordination polyhedra are shown; the A-site cation is represented by large, dark spheres, and the white spheres represent oxygen atoms.

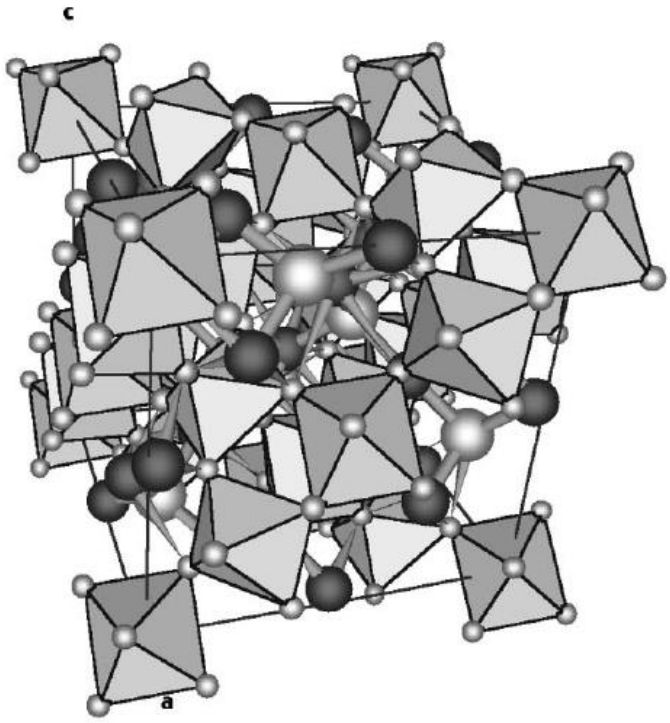

Figure 2-8. A schematic of the cubic pyrochlore crystal structure. The BO_6 coordination polyhedra are shown; the A-site cation is represented by large, dark spheres, and the white spheres represent oxygen atoms [52].

The bismuth pyrochlores investigated in this work are non-ideal cubic pyrochlores. In contrast to an ideal cubic pyrochlore structure, the A-site has been shown to possess a random occupancy by bismuth, zinc, and vacancies. Furthermore, the A-site cations in the $Bi_{1.5}Zn_{0.92}Nb_{1.5}O_{6.92}$ composition are randomly displaced by 0.39 Å from their ideal eightfold coordinated positions [53]. The displacement occurs along the six <112> directions perpendicular to the O'–A–O' links. In addition, the O' ions are randomly displaced by 0.46 Å along all twelve <110> directions for the $Bi_{1.5}Zn_{0.92}Nb_{1.5}O_{6.92}$ composition [53].

2.2.2 Cubic Pyrochlore Bismuth Zinc Niobate

Cubic pyrochlore bismuth zinc niobate ($Bi_{1.5}Zn_{1.0}Nb_{1.5}O_7$ and $Bi_{1.5}Zn_{0.5}Nb_{1.5}O_{6.5}$) is a weakly nonlinear dielectric [54] with a room temperature permittivity of 150-200 [54, 55, 56] and loss tangents on the order of 0.0005 to 0.005 [54, 56, 57, 59]. The temperature coefficient of capacitance for bismuth zinc niobate is approximately -400 ppm/°C [52]. Thayer [52] demonstrated that $Bi_{1.5}Zn_{0.5}Nb_{1.5}O_{6.5}$ thin films grown by chemical solution deposition possess a dielectric tunability of 26% at applied electric fields of 1.8 MV/cm at 77 K. A dielectric tunability of 45% for an applied electric field of 3 MV/cm was reported for the cubic pyrochlore composition $Bi_{1.5}Zn_{1.0}Nb_{1.5}O_7$ at 77 K [52]. It was hypothesized [52] that the large electric field quenches the contribution to the material's polarization stemming from random fields and interactions between disordered sites in the cubic pyrochlore crystal structure [53, 57]. The low-temperature dielectric relaxation of cubic pyrochlore bismuth zinc niobate reported by Cann et al. [58] and shown in Figure 2-9 [57] was also attributed to these random fields and interactions [53, 57]. Random electric fields introduce a statistical distribution into the local potential barrier heights for atoms moving between the available positions for a given site in the lattice [57]. The activation energy for moving between positions is no longer homogeneous, broadening the relaxation in the dielectric permittivity and loss, when compared to a single Debye relaxation. As discussed in section 2.2.1, bismuth zinc niobate is a disordered cubic pyrochlore in which the A-site possesses a random occupation of bismuth, zinc, and vacancies; each A-site cation occupies one of six closely spaced available positions, and each O' atom is displaced along 12 different directions [53]. The relaxation observed for bismuth zinc niobate may be due to the dynamic hopping between disordered A-site cations and O' anions among their closely spaced available positions [57]. Furthermore, the random occupancy of zinc atoms and vacancies on the bismuth site will produce additional random fields that may give rise to multiwell potentials with a wide

distribution of heights and transition rates. This rugged potential landscape can cause a broad dielectric relaxation.

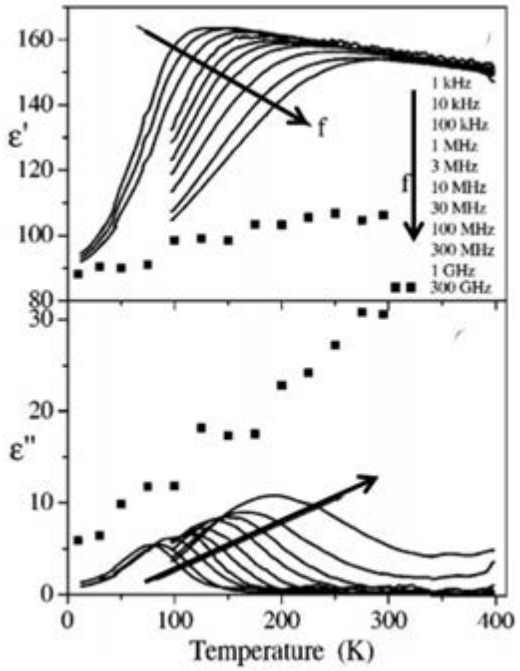

Figure 2-9. Permittivity and loss as a function of temperature for $Bi_{1.5}Zn_{1.0}Nb_{1.5}O_7$. Bismuth zinc niobate has a low-temperature dielectric relaxation [57].

The medium permittivity of $Bi_{1.5}Zn_{0.5}Nb_{1.5}O_{6.5}$ coupled with its low, negative temperature coefficient of capacitance [52] suggests that this material should have large energy storage densities across a range of temperatures despite the modest tunability in the material. Furthermore, Kamba et al. [57] demonstrated that the relative permittivity of bismuth zinc niobate above its dielectric relaxation temperature decreases very little across a measurement frequency range of 1 kHz to 1 GHz. The dielectric loss of these films has also been reported to remain constant above the dielectric relaxation temperature for a frequency range of 1 kHz to 1 GHz [57]. The reported temperature and frequency stabilities of capacitance and loss indicate that

bismuth zinc niobate may be suitable for energy storage devices that require high operating frequencies or temperatures, as in pulsed power applications. Breakdown strengths for bismuth zinc niobate have been reported to exceed 2.4 MV/cm [55].

In addition to the cubic pyrochlore crystal structure of bismuth zinc niobate, there is a closely related zirconolite structure adopted by materials with the composition $Bi_2Zn_{2/3}Nb_{4/3}O_7$. This composition has a lower relative permittivity around 80, and dielectric losses of approximately 0.005 [52]. Although zirconolite bismuth zinc niobate exhibits a lower tunability of approximately 20% at applied fields of 4.0 MV/cm for a measurement temperature of 77 K [52], it is anticipated that the lower polarizability of the material will not lead to energy storage densities of a magnitude comparable to those of the cubic pyrochlore. This composition was briefly investigated, and the results can be found in Appendix B.

2.2.3 Cubic Pyrochlore Bismuth Zinc Tantalate

Bismuth zinc tantalate, $Bi_{1.5}Zn_{1.0}Ta_{1.5}O_7$, is another bismuth-based cubic pyrochlore that was investigated in this work. Although this composition is much less well-studied than its niobate analogue, there are striking similarities in properties between the two materials, such as a moderate permittivity, low loss tangents, low temperature coefficients of capacitance, and a low temperature relaxation in the relative permittivity and loss. As seen in Figure 2-10, bismuth zinc tantalate has a relative permittivity of approximately 70 and dielectric losses of approximately 0.005 above its dielectric relaxation [58, 59, 60]. Thus, the permittivity of bismuth zinc tantalate is about half that of bismuth zinc niobate, while the losses for the two systems are comparable. The temperature coefficient of capacitance for bismuth zinc tantalate is approximately -170 ppm/°C [60, 61].

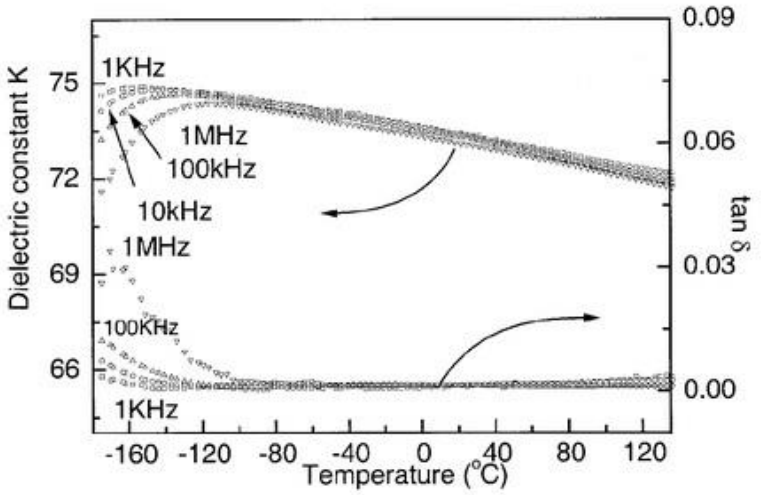

Figure 2-10. Permittivity and loss as a function of temperature for $Bi_{1.5}Zn_{1.0}Ta_{1.5}O_7$. The bismuth zinc tantalate ceramic has a low-temperature dielectric relaxation at approximately -140°C (from Youn, et al. [60]).

The dielectric breakdown strength for bismuth zinc tantalate has not been reported in the literature. It is known that one approach to enhancing the breakdown strength, and, hence, the energy storage capacity, of a dielectric is to increase the band gap of the material [62]. Tantalum oxide exhibits a band gap of approximately 4 eV [63], while niobium oxide has a band gap of approximately 3.4 eV [64]. Thus, it is anticipated that the lower polarizability (resulting in a lower relative permittivity) of the tantalate may be compensated by a higher breakdown strength, enabling improvements in the energy storage density of the deposited thin films.

2.3 Chemical Solution Deposition of Thin Films

Chemical solution deposition is a versatile method that can be used to fabricate a variety of thin film compositions. Several of the common solution chemistries are reviewed in Chapters 4 and 8, but the physics involved in spin casting are discussed here.

2.3.1 Film Formation via Spin Casting

The spin coating process can be divided into four stages: deposition, spin-up, spin-off, and evaporation, as shown in Figure 2-11 [65]. These stages are not typically distinct, as there is often overlap in the steps due to the short time scales of thin film fabrication [66]. During the deposition stage, an excess of solution is dispensed onto a spinning substrate. It is usually critical to ensure that the full substrate will be covered by the dispensed coating solution [66]. The solution will flow radially outward, driven by centrifugal forces, in the spin-up stage [67]. Excess solution will flow to the edges of the substrate during spin-off, leaving as droplets. As the film reduces in thickness, the rate of excess solution spin-off will decrease. This occurs because the thin layer of solution has a greater resistance to flow and also because the viscosity of the as-deposited material increases as volatile species are removed from the film during evaporation, the fourth stage of spin casting [67]. During spin-off, the film will develop a uniform thickness. Due to the balance that is established between centrifugal and viscous forces, the film thickness will remain uniform provided that the viscosity of the solution is uniform and not dependent on the shear. Prior to achieving this balance, centrifugal forces overwhelm gravity and other forces directed towards the center of the substrate, allowing the film to rapidly thin during spin-up.

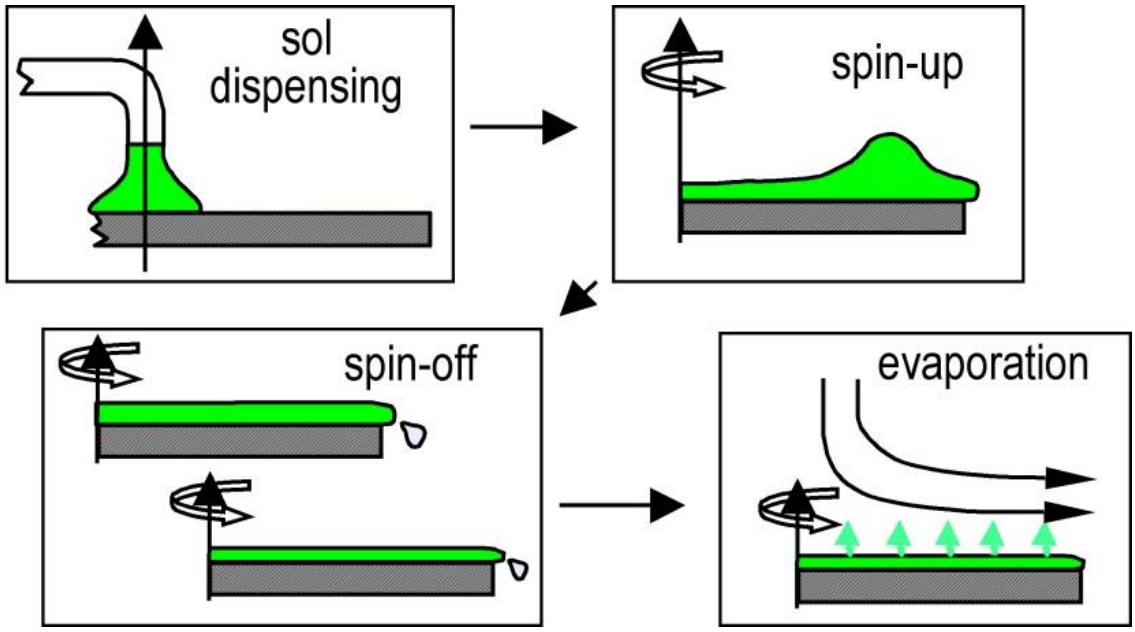

Figure 2-11. The four stages of spin casting: deposition, spin-up, spin-off, and evaporation [65]. These stages are rarely discrete, as there is typically overlap between the steps.

The spinning of the substrate creates a convective current in the atmosphere above the surface of the film that causes the rate of evaporation from the film to be uniform [67]. The spinning film will arrive at its final thickness by evaporation when the film becomes so thin and viscous that centrifugal, thinning forces cause radial flow to cease. The final thickness of the as-deposited film is dependent on the spin rate and the viscosity of the dispensed solution. Subsequent heating stages (drying and pyrolysis) and the accompanying densification mechanisms will be discussed in Chapter 4.

2.4 References

1] N. H. Fletcher, A. D. Hilton and B. W. Ricketts, "Optimization of energy storage density in ceramic capacitors," *Journal of Physics D: Applied Physics,* vol. 29, p. 253–258, 1996.

2] P. Barber, S. Balasubramanian, Y. Anguchamy, S. Gong, A. Wibowo, H. Gao, H. J. Ploehn and H.-C. zur Loye, "Polymer composite and nanocomposite dielectric materials for pulse power energy storage," *Materials,* vol. 2, no. 4, pp. 1697-1733, 2009.

3] Q. Wang and L. Zhu, "Polymer nanocomposites for electrical energy storage," *Journal of Polymer Science Part B: Polymer Physics,* vol. 49, pp. 1421-1429, 2011.

4] E. K. Michael and S. Trolier-McKinstry, "Amorphous-nanocrystalline lead titanate thin films for dielectric energy storage," *Journal of the Ceramic Society of Japan,* vol. 122, no. 4, p. 250-255, 2014.

5] L. A. Fredin, Z. Li, M. T. Lanagan, M. A. Ratner and T. J. Marks, "Substantial recoverable energy storage in percolative metallic aluminum-polypropylene nanocomposites," *Advanced Functional Materials,* vol. 23, no. 28, pp. 3560-3569, 2012.

6] V. Tomer, C. A. Randall, G. Polizos, J. Kostelnick and E. Manias, "High- and low-field dielectric characteristics of dielectrophoretically aligned ceramic/polymer nanocomposites," *Journal of Applied Physics,* vol. 103, p. 034115, 2008.

7] M. Klee, H. van Esch, W. Keur, B. Kumar, L. van Leukin-Peters, J. Liu, R. Mauczok, K. Neumann, K. Reimann, C. Renders, A. L. Roest, M. Tiggelman, M. de Wild, O. Wunnicke, and J. Zhao, "Ferroelectric thin-film capacitors and piezoelectric switches for mobile communication applications," *IEEE Transactions on Ultrasonics, Ferroelectrics, and Frequency Control,* vol. 56, no. 8, pp. 1505-1512, 2009.

8] H. Tang and H. A. Sodano, "Ultra high energy density nanocomposite capacitors with fast discharge using $Ba_{0.2}Sr_{0.8}TiO_3$ nanowires," *Nano Letters,* vol. 13, pp. 1373-1379, 2013.

9] X. Zhou, X. Zhao, Z. Suo, C. Zou, J. Runt, S. Liu, S. Zhang and Q. M. Zhang, "Electrical breakdown and ultrahigh electrical energy density in poly(vinylidene fluoride-hexafluoropropylene) copolymer," *Applied Physics Letters,* vol. 94, p. 162901, 2009.

10] Z. Xie, Z. Yue, G. Ruehl, B. Peng, J. Zhang, Q. Yu, X. Zhang and L. Li, "$Bi(Ni_{1/2}Zr_{1/2})O_3$-$PbTiO_3$ relaxor-ferroelectric films for piezoelectric energy harvesting and electrostatic storage," *Applied Physics Letters,* vol. 104, p. 243902, 2014.

11] T. Chen, J. Wang, X. Zhong, F. Wang, B. Li and Y. Zhou, "High energy density capacitors based on $0.88BaTiO_3$–$0.12Bi(Mg_{0.5,}Ti_{0.5})O_3/PbZrO_3$ multilayered thin films," *Ceramics International,* vol. 40, pp. 5327-5332, 2014.

12] J. Luo, J. Du, Q. Tang and C. Mao, "Lead sodium niobate glass-ceramic dielectrics and internal electrode structure for high energy storage density capacitors," *IEEE*

Transactions on Electron Devices, vol. 55, no. 12, pp. 3549-3554, 2008.

13] M. S. Mirshekarloo, K. Yao and T. Sritharan, "Large strain and high energy storage density in orthorhombic perovskite $(Pb_{0.97}La_{0.02})(Zr_{1-x-y}Sn_xTi_y)O_3$ antiferroelectric thin films," *Applied Physics Letters,* vol. 97, p. 142902, 2010.

14] A. V. Wagner, G. W. Johnson and T. J. W. Barbee, "High energy density capacitors fabricated by thin film technology," *Materials Research Society Symposium Proceedings,* vol. 574, pp. 219-224, 1999.

15] N. J. Smith, B. Rangarajan, M. T. Lanagan and C. G. Pantano, "Alkali-free glass as a high energy density dielectric material," *Materials Letters,* vol. 63, pp. 1245-1248, 2009.

16] U. Balachandran, M. Narayanan, S. Liu and B. Ma, "Development of film-on-foil ceramic dielectrics for embedded capacitors for power inverters in electric drive vehicles," *Japanese Journal of Applied Physics,* vol. 52, p. 05DA10, 2013.

17] H. Ogihara, C. A. Randall and S. Trolier-McKinstry, "High-energy density capacitors utilizing $0.7BaTiO_3$–$0.3BiScO_3$ ceramics," *Journal of the American Ceramic Society,* vol. 92, no. 8, pp. 1719-1724, 2009.

18] G. Sethi, M. Olszta, J. Li, J. Sloppy, M. W. Horn, E. C. Dickey and M. T. Lanagan, "Structure and dielectric properties of amorphous tantalum pentoxide thin film capacitors," *2007 Annual Report Conference on Electrical Insulation and Dielectric Phenomena,* pp. 815-818, 2007.

19] P. Khanchaitit, K. Han, M. R. Gadinski and Q. Wang, "Ferroelectric polymer networks with high energy density and improved discharged efficiency for dielectric energy storage," *Nature Communications,* vol. 4, p. 2845, 2013.

20] S. Chao and F. Dogan, "Processing and dielectric properties of TiO_2 thick films for high-energy density capacitor applications," *International Journal of Applied Ceramic Technology ,* vol. 8, no. 6, pp. 1363-1373, 2011.

21] E. K. Michael and S. Trolier-McKinstry, "Cubic pyrochlore bismuth zinc niobate thin films for high-temperature dielectric energy storage," *Journal of the American Ceramic Society,* vol. 98, no. 4, p. 1223-1229, 2015.

22] A. J. Moulson and J. M. Herbert, Electroceramics: Materials, Properties, Applications, West Sussex, England: John Wiley & Sons, Ltd, 2003.

23] S. O. Kasap, Principles of Electronic Materials and Devices, New York City: McGraw-Hill, 2005.

24] M. Lanagan, "Dielectric Properties and Metamaterials," in *US-Japan Winter School on New Functionality in Glass*, Kyoto, Japan, 2008.

C. Kittel, Introduction to Solid State Physics, Hoboken, NJ: John Wiley & Sons, Inc., 2005.

25]

A. Tagantsev, "Mechanisms of dielectric loss in microwave materials," *MRS Proceedings,* vol. 603, pp. 221-232, 1999.
26]

J. Krupka, J. Breeze, A. Centeno, N. Alford, T. Claussen and L. Jensen, "Measurements of permittivity, dielectric loss tangent, and resistivity of float-zone silicon at microwave frequencies," *IEEE Transactions on Microwave Theory and Techniques,* vol. 54, no. 11, pp. 3995-4001, 2006.
27]

G. L. Johnson, Solid State Tesla Coil, Manhattan, KS: Kansas State University, 2001, http://ece.k-state.edu/people/faculty/gjohnson/.
28]

J. F. Scott, "Ferroelectrics go bananas," *Journal of Physics: Condensed Matter,* vol. 20, p. 021001, 2008.
29]

M. M. Samantaray, A. Gurav, E. C. Dickey and C. A. Randall, "Electrode defects in multilayer capacitors part I: Modeling the effect of electrode roughness and porosity on electric field enhancement and leakage current," *Journal of American Ceramic Society,* vol. 95, no. 1, pp. 257-263, 2012.
30]

K. C. Kao, Dielectric Phenomena in Solids, San Diego: Elsevier Academic Press, 2004.
31]

J. J. O'Dwyer, Theory of Electrical Conduction and Breakdown in Solid Dielectrics, Oxford: Oxford University Press, 1973.
32]

M. Ohring, Materials Science of Thin Films, Hoboken, NJ: Academic Press, 1992.
33]

S. Sherrit, "Analytical model for the strain-field and polarization-field hysteresis curves for ferroic materials," in *Proceedings of SPIE 6526, Behavior and Mechanics of Multifunctional and Composite Materials 2007*, San Diego, CA, pp. 652608-1, 2007.
34]

O. Auciello, J. F. Scott and . R. Ramesh, "The physics of ferroelectric memories," *Physics Today,* vol. 51, no. 7, pp. 22-27, 1998.
35]

K. wa Gachigi, "Electrical energy storage in antiferroelectric—ferroelectric phase switching, chemically modified lead zirconate ceramics," Ph.D. Thesis, The Pennsylvania State University, PA, 1992.
36]

Z. Hu, B. Ma, S. Liu, M. Narayanan and U. Balachandran, "Relaxor behavior and energy storage performance of ferroelectric PLZT thin films with different Zr/Ti ratios," *Ceramics International,* vol. 40, pp. 557-562, 2014.
37]

X. Zhou, B. Chu, B. Neese, M. Lin and Q. M. Zhang, "Electrical energy density and discharge characteristics of a poly(vinylidene fluoride-chlorotrifluoroethylene) copolymer," *IEEE Transactions on Dielectrics and Electrical Insulation,* vol. 14, no. 5,
38]

pp. 1133-1138, 2007.

39] D. Tan and P. Irwin, "Polymer Based Nanodielectric Composites," in *Advances in Ceramics - Electric and Magnetic Ceramics, Bioceramics, Ceramics and Environment*, Rijeka, Croatia, InTech, 2011, pp. 115-132.

40] S. Wu, "High energy density, and low loss polymer dielectrics for energy storage capacitors and organic electronics," Ph.D Thesis, The Pennsylvania State University, 2014.

41] A. A. Bokov and Z. G. Ye, "Recent progress in relaxor ferroelectrics with perovskite structure," *Journal of Materials Science,* vol. 41, pp. 31-52, 2006.

42] D.-K. Kwon and M. H. Lee, "Temperature-stable high-energy-density capacitors using complex perovskite thin films," *IEEE Transactions on Ultrasonics, Ferroelectrics, and Frequency Control,* vol. 59, no. 9, pp. 1894-1899, 2012.

43] C. Kittel, "Theory of antiferroelectric crystals," *Physical Review,* vol. 82, no. 5, pp. 729-732, 1951.

44] D. P. Shay, "Development and characterization of high temperature, high energy density dielectric materials to establish routes towards power electronics capacitive devices," Ph. D. Thesis, The Pennsylvania State University, 2014.

45] M. E. Lines and A. M. Glass, Principles and Applications of Ferroelectrics and Related Materials, Oxford: Clarendon Press, 1977.

46] J. W. Claude, "Ferroelectric polymers for electrical energy storage," Ph.D Thesis, The Pennsylvania State University, 2008.

47] X. Su, B. C. Riggs, M. Tomozawa, J. K. Nelson and D. B. Chrisey, "Preparation of $BaTiO_3$/low melting glass core–shell nanoparticles for energy storage capacitor applications," *Journal of Materials Chemistry A,* vol. 2, pp. 18087-18096, 2014.

48] K. Yao, S. Chen, M. Rahimabady, M. S. Mirshekarloo, S. Yu, F. Eng Hock Tay, T. Sritharan and L. Lu, "Nonlinear dielectric thin films for high-power electric storage with energy density comparable with electrochemical supercapacitors," *IEEE Transactions on Ultrasonics, Ferroelectrics, and Frequency Control,* vol. 58, no. 9, pp. 1968-1974, 2011.

49] J. Sigman, G. L. Brennecka, P. G. Clem and B. A. Tuttle, "Fabrication of perovskite-based high-value integrated capacitors by chemical solution deposition," *Journal of the American Ceramic Society,* vol. 91, no. 6, pp. 1851-1857, 2008.

50] M. A. Subramanian, G. Aravamudan and G. V. Subba Rao, "Oxide pyrochlores- A review," *Progress in Solid State Chemistry,* vol. 15, no. 2, pp. 55-143, 1983.

51] A. R. West, Solid State Chemistry and its Applications, West Sussex: John Wiley & Sons, Ltd., 2014.

52] R. L. Thayer, C. A. Randall and S. Trolier-McKinstry, "Medium permittivity bismuth zinc niobate thin film capacitors," *Journal of Applied Physics,* vol. 94, no. 3, pp. 1941-1947, 2003.

53] I. Levin, T. G. Amos, J. C. Nino, T. A. Vanderah, C. A. Randall and M. T. Lanagan, "Structural study of an unusual cubic pyrochlore $Bi_{1.5}Zn_{0.92}Nb_{1.5}O_{6.92}$," *Journal of Solid State Chemistry,* vol. 168, no. 1, pp. 69-75, 2002.

54] W. Ren, S. Trolier-McKinstry, C. Randall and T. R. Shrout, "Bismuth zinc niobate pyrochlore dielectric thin films for capacitive applications," *Journal of Applied Physics,* vol. 89, no. 1, pp. 767-774, 2000.

55] J. Lu and S. Stemmer, "Low-loss, tunable bismuth zinc niobate films deposited by rf magnetron sputtering," *Applied Physics Letters,* vol. 83, no. 12, pp. 2411-2413, 2003.

56] X. Zhang, W. Ren, P. Shi, X. Wu, X. Chen and X. Yao, "Structures and dielectric properties of pyrochlore bismuth zinc niobate thin films with zinc compensation," *Journal of Alloys and Compounds,* vol. 553, pp. 8-13, 2013.

57] S. Kamba, V. Porokhonskyy, A. Pashkin, V. Bovtun, J. Petzelt, J. C. Nino, S. Trolier-McKinstry, M. T. Lanagan and C. A. Randall, "Anomalous broad dielectric relaxation in $Bi_{1.5}Zn_{1.0}Nb_{1.5}O_7$ pyrochlore," *Physical Review B,* vol. 66, p. 054106, 2002.

58] D. P. Cann, C. A. Randall and T. R. Shrout, "Investigation of the dielectric properties of bismuth pyrochlores," *Solid State Communications,* vol. 100, no. 7, pp. 529-534, 1996.

59] H.-J. Youn, C. Randall, A. Chen, T. Shrout and M. T. Lanagan, "Dielectric relaxation and microwave dielectric properties of Bi_2O_3–ZnO–Ta_2O_5 ceramics," *Journal of Materials Research,* vol. 17, no. 6, pp. 1502-1506, 2002.

60] H.-J. Youn, T. Sogabe, C. A. Randall, T. R. Shrout and M. T. Lanagan, "Phase relations and dielectric properties in the Bi_2O_3–ZnO–Ta_2O_5 system," *Journal of the American Ceramic Society,* vol. 84, no. 11, pp. 2557-2562, 2001.

61] C. C. Khaw, K. B. Tan and C. K. Lee, "High temperature dielectric properties of cubic bismuth zinc tantalate," *Ceramics International,* vol. 35, pp. 1473-1480, 2009.

62] A. Yoshikawa, H. Matsunami and Y. Nanishi, "Development and Applications of Wide Bandgap Semiconductors," in *Wide bandgap semiconductors: Fundamental properties and modern photonic and electronic devices*, Heidelberg, NY, Springer, 2007, pp. 1-23.

63] E. Franke, C. L. Trimble, M. J. DeVries, J. A. Woollam, M. Schubert and F. Frost, "Dielectric function of amorphous tantalum oxide from the far infrared to the deep ultraviolet spectral region measured by spectroscopic ellipsometry," *Journal of Applied Physics,* vol. 88, no. 9, pp. 5166-5174, 2000.

64] K. Yoshimura, T. Miki, S. Iwama and S. Tanemura, "Characterization of niobium oxide electrochromic thin films prepared by reactive d.c. magnetron sputtering," *Thin Solid*

Films, Vols. 281-282, pp. 235-238, 1996.

65] D. E. Bornside, C. W. Macosko and L. E. Scriven, "On the modeling of spin coating," *Journal of Imaging Technology,* vol. 13, no. 4, pp. 122-130, 1987.

66] D. P. Birnie III, "Spin Coating: Art and Science," in *Chemical Solution Deposition of Functional Oxide Thin Films*, New York, Springer, 2013, pp. 263-274.

67] C. J. Brinker and G. W. Scherer, Sol-gel Science: The Physics and Chemistry of Sol-gel Processing, Boston: Academic Press, 1990.

Chapter 3

Experimental Procedures

This chapter outlines the experimental procedures used throughout the work described in this thesis. An overview of film deposition procedures is given. Following processing details, the characterization techniques used on these films, which are broadly divided into structural and electrical characterization methods, are described.

3.1 Chemical Solution Deposition of Thin Films

Thin films of several crystalline bismuth pyrochlores, nanocomposite bismuth zinc niobate tantalate, and nanocomposite lead titanate were deposited and characterized. This section briefly reviews deposition processes, as more thorough discussions of solution chemistries and processing parameters can be found in Chapters 4 and 8.

3.1.1 The Deposition of Bismuth Pyrochlores

Crystalline bismuth pyrochlore and nanocomposite samples consisting of a nanocrystalline fluorite related to delta-bismuth oxide in an amorphous bismuth zinc niobate tantalate matrix were prepared. The solution chemistries for each material are similar; only the molar ratio of citric acid to organometallic precursor was varied. Here, the processing details of crystalline and nanocomposite films are given, including the methodology used to deposit nanocomposite films on flexible polyimide substrates.

3.1.1.1 The Preparation of Crystalline Bismuth Pyrochlore Thin Films

To prepare the solutions used to deposit bismuth pyrochlore films in this thesis, cation sources, whose chemical precursors and purities are listed in Table 3-1, were separately mixed in ethylene glycol for 30 minutes at 80°C to create homogeneous alcoholic solutions. Citric acid was added to each solution; following the addition of citric acid, all solution preparation was performed in air. The solutions were stirred on an 80°C hotplate for two hours to allow for chelation of the metal atoms. The molar ratio of citric acid to organometallic precursor was 3:1. Following chelation, the B-site cation solutions were combined and stirred for two hours at 80°C to promote intimate mixing. Finally, the A-site precursor solution was added to the B-site mixture; the solution was stirred at 80°C for one hour to allow the solution to homogenize. As an example, the solution preparation for bismuth zinc niobate is shown schematically in Figure 3-1. The typical molarity of the solutions used to deposit thin films in this work was 0.15 M, unless otherwise stated.

Table 3-1. Cation Sources for Chemical Solution Deposition Precursor Solutions

Required Cation	Cation Source	Purity
Bismuth	Bismuth nitrate pentahydrate	≥98%
Manganese	Manganese acetate tetrahydrate	≥99%
Niobium	Niobium ethoxide	99.95% trace metals basis
Silicon	Tetraethylorthosilicate	98%
Tantalum	Tantalum ethoxide	99.98% trace metals basis
Titanium	Titanium isopropoxide	97%
Zinc	Zinc acetate dihydrate	≥98%

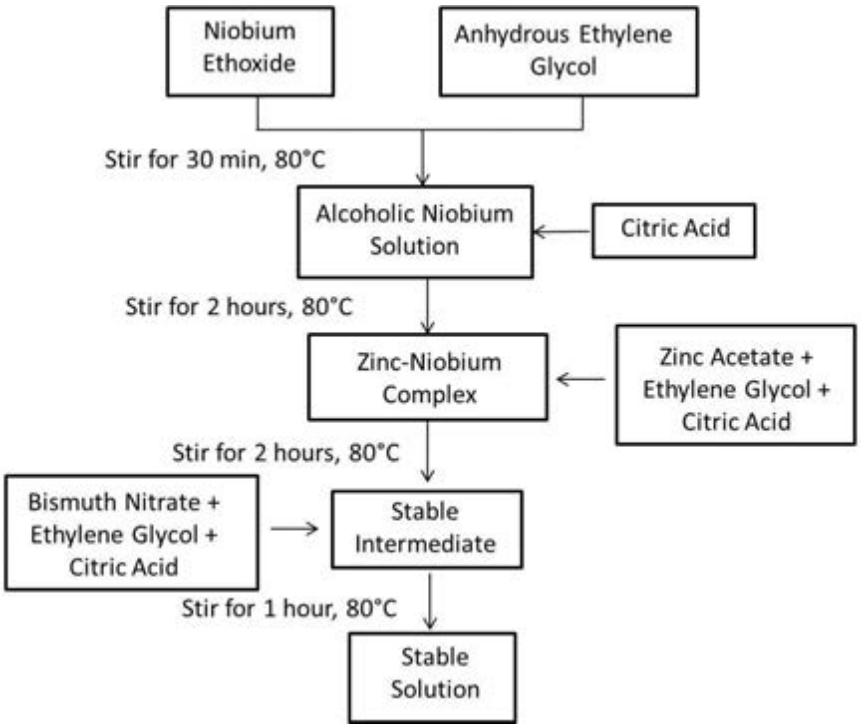

Figure 3-1. Flowchart for the preparation of the solution used to deposit bismuth zinc niobate thin films.

The solution was spin coated through a 5μm filter onto a platinized silicon wafer (Pt (100 nm)/Ti (20 nm)/SiO_2 (500 cm)/Si, NOVA Electronic Materials, Flower Mound, TX). The substrate was dried, pre-pyrolyzed, and pyrolyzed on hotplates to remove organic species and densify the film. The film was crystallized in a rapid thermal anneal system (RTP-600S, Modular Process Technology Corp., San Jose, CA) for two minutes at 600°C. This process of spin casting followed by four sequential heat treatments was repeated several times to build up film thickness.

3.1.1.2 The Preparation of Nanocomposite Bismuth Zinc Niobate Tantalate

Precursor solutions for the deposition of nanocomposite films of bismuth zinc niobate tantalate were prepared as described in section 3.1.1.1; for the preparation of nanocomposite films, the molar ratio of citric acid to organometallic precursor was reduced to 1:1. This lower ratio was critical to facilitate the reduction in the maximum temperature needed to remove carbon from the films, as discussed in Chapters 4 and 7.

To deposit the films on platinized silicon substrates, the 0.15 M solution was spin coated at 4000 rpm for 40 seconds. The substrate was dried on a hotplate at 250°C for three minutes and then pyrolyzed on a second hotplate at 350°C for ten minutes. This process was repeated several times to build up film thickness; the final film thickness was typically 110 nm after five layers were deposited.

To fabricate nanocomposite films on platinum-coated polyimide substrates, a chemical release layer was employed to remove the polyimide substrate from the rigid silicon carrier wafer. For these films, 100 nm of gold was sputtered (CMS-18 Sputter System, Kurt J. Lesker Company, Pittsburgh, PA) onto a silicon wafer. This wafer was coated with polyimide (PI-2611, HD MicroSystems, Parlin, NJ) via spin casting. The PI-2611 polyimide precursor was spin coated at 3000 rpm for 30 seconds. The substrate was soft-baked at 130°C for 90 seconds, and then cured in air at 300°C for eight hours. A single layer of polyimide was deposited, which yielded a thickness of approximately 5 μm. To serve as a bottom electrode for the nanocomposite film, 30 nm of titanium was sputtered onto the polyimide, followed by 100 nm of platinum. The sputtering conditions for depositing the bottom electrode are given in Table 3-2. A schematic of the final multilayer stack is shown in Figure 3-2.

Table 3-2. Sputtering Conditions for Depositing 30 nm Ti/100 nm Pt Bottom Electrodes

	30 nm Ti	100 nm Pt
Pressure (mTorr)	5.0	5.0
Substrate Temperature (°C)	25	25
Power (W)	200	200
Time (s)	300	417

Figure 3-2. A schematic of the multilayer stack used to fabricate nanocomposite bismuth zinc niobate tantalate thin films on flexible polyimide substrates.

Prior to film deposition, the substrate was thermally preconditioned. Although PI-2611 has a low moisture uptake relative to other polyimides [1], the substrate will absorb water from the atmosphere. To remove water from the polyimide prior to film deposition, the substrate was placed on a room-temperature hotplate and slowly heated to 120°C. The substrate was held at 120°C for thirty minutes. To precondition the polyimide, the wafer was subjected to a thermal cycle mimicking film deposition procedures prior to applying precursor solution; the substrate was placed on a 250°C hotplate for three minutes, followed by a 350°C hotplate for ten minutes.

To deposit the nanocomposite film, a 0.15 M solution was spin coated at 4000 rpm for 40 seconds. The multilayer stack was dried on a hotplate at 250°C for three minutes and then

pyrolyzed at 350°C for ten minutes. After reaching the desired film thickness, the polyimide substrate was released from the silicon carrier wafer. To release the polyimide, the gold was chemically etched using a commercially available potassium iodide/iodine etchant (Gold Etchant, Standard, Sigma-Aldrich). The etch rate of bulk gold in this etchant is 28 Å/s [2]; however, the films released at a much slower rate, presumably due to the need to transport etchant and dissolved byproducts via the exposed sides of the sample. Films were typically left in a room temperature etchant bath for 48 hours to release.

After release, films were flexed for tens of thousands of cycles using a system built by Haoyu Li of the Jackson research group. As shown in Figure 3-3, the system was constructed from an air slide table (SMC MXS16-30, Allied Electronics, Fort Worth, TX) connected to two needle valves (SPN400B, Parker Hannifin Corp., Cleveland, OH). To mount the samples on the system, the edges of the film were taped to the top of the air slide table adjacent to the gap created when the air slide is in the open position, as seen in Figure 3-3(b). The length of the gap, which was manually adjusted using a screw, was used to change the radius of curvature of the sample. The cycle speed was determined by manually adjusting the pressure of the needle valves attached to the air slide. The frequency and number of cycles was controlled by a LabView program (National Instruments, Austin, TX).

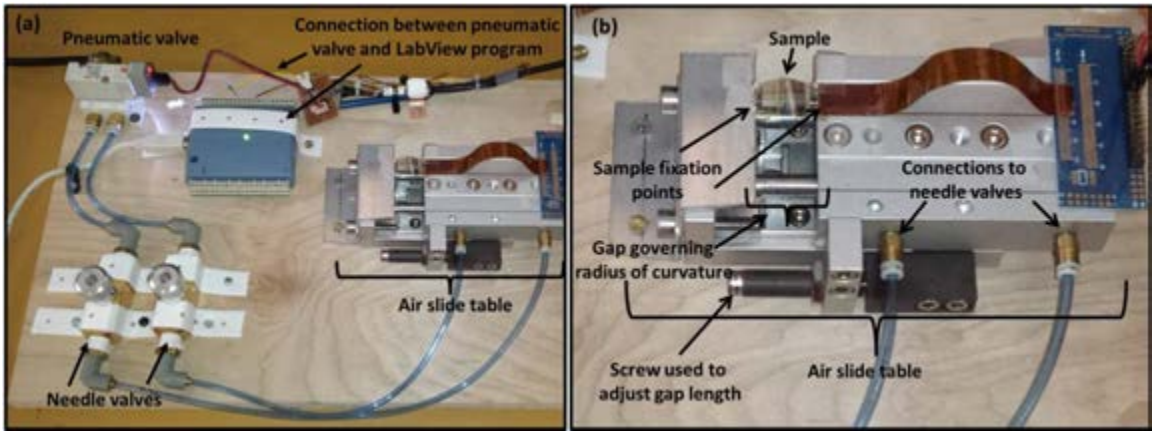

Figure 3-3. The (a) overall flexible testing system and (b) air slide table used for flexing released films (photo courtesy of Haoyu Li).

3.1.2 The Deposition of Nanocomposite Lead Titanate

To synthesize solutions for the deposition of nanocomposite lead titanate films, lead acetate trihydrate and titanium isoproxide were combined in acetic acid, and then stirred on an 85°C hotplate for approximately ten minutes to allow for chelation of the central metal atoms by acetyl ligands. Methanol was added to control the viscosity and stability of the solution [3], along with another aliquot of acetic acid. The solution was stirred for an additional ten minutes. Methanol and acetic acid were added to reach a final molarity of 0.4 M. The final solution contained a 3:2 molar ratio of acetic acid to methanol.

To deposit thin films, the precursor solution was diluted with acetic acid to 0.2 M immediately prior to spin coating at 3500 rpm for 30 seconds on a platinum-coated silicon wafer. The substrate was placed on a hotplate to dry at 175°C for one minute, followed by a one minute pyrolysis at 350°C to remove organics and promote densification in the film. The film was heat treated in a rapid thermal anneal system for two minutes. As discussed in Chapter 8, most films

were annealed at 400°C. The film thickness was typically between 300 and 400 nm after six layers were deposited. The processing route is shown schematically in Figure 3-4.

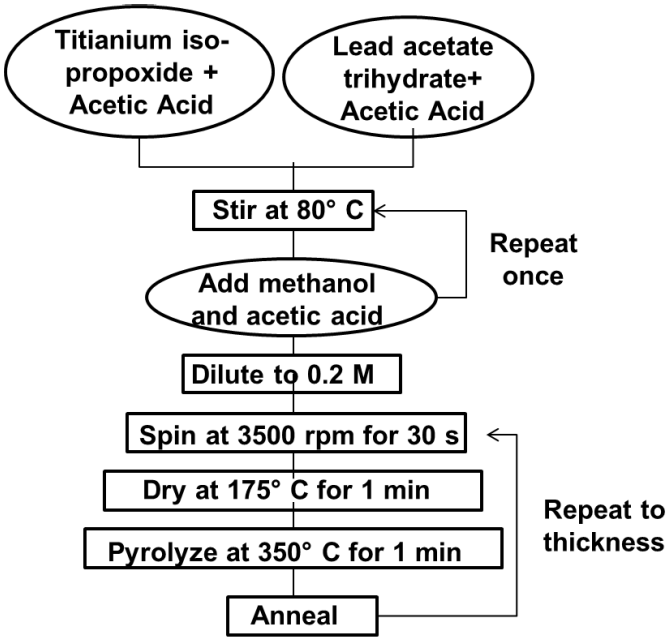

Figure 3-4. Flowchart for the processing of nanocomposite thin films of lead titanate. Solutions were prepared using an inverted mixing order solution preparation, spin cast onto a substrate, and thermally treated in three steps.

3.2 Structural Characterization Techniques

After deposition, several different techniques were used to probe the film structure and physical properties. Thermal gravimetric analysis was also used to investigate the weight loss behavior of the bismuth pyrochlore precursor solutions. These methods are detailed in this section.

3.2.1 Thermal Gravimetric Analysis and Mass Spectrometry

Optimal pyrolysis temperatures for the bismuth pyrochlore solution were determined using thermal gravimetric analysis (2050 TGA, TA Instruments, New Castle, DE) in air to simulate the film deposition atmosphere. In thermal gravimetric analysis, the mass of a sample is measured as a function of temperature; here, the ramp rate was 5°C/minute. Results are presented as weight percent of the sample as a function of temperature. Liquid solution samples were used.

For a 0.15 M sample of $Bi_{1.5}Zn_{0.9}Nb_{1.5}O_{6.9}$ solution containing a 3:1 molar ratio of citric acid to organometallic precursor, mass spectrometry was coupled to thermal gravimetric analysis. This work was performed by analysts at the Dow Chemical Company on a 199 μg liquid sample of the solution. For this experiment, the temperature regime over which the majority of the weight loss occurred was divided into two zones. The first temperature zone was from room temperature to 250°C to mirror the drying step of film deposition, and the second temperature zone was from 250°C to 400°C to mirror the pyrolysis steps. The solution was heated in air at a ramp rate of 50°C/minute, and the evolved gases from each temperature zone were identified using mass spectrometry.

3.2.2 X-Ray Diffraction

The phase content of the films were analyzed with an x-ray diffractometer (Empyrean, PANalytical, Almelo, The Netherlands) configured in focusing geometry using Cu Kα radiation. Patterns were collected over a 2θ range from 20° to 73°. The instrument step size was 0.02°, and the scan rate was 2° 2θ per minute. The diffraction patterns for films of bismuth pyrochlores were indexed to the bulk bismuth zinc niobate structure (PDF# 04-009-5437, 2002), while the nanocrystals of the nanocomposite were indexed to delta-bismuth oxide (PDF# 98-001-4679,

2014). The diffraction patterns for the lead titanate nanocomposite films were indexed to patterns of crystalline lead titanate (PDF# 00-006-0452, 1955) along with orthorhombic lead oxide (PDF# 00-035-1482, 1984). Patterns are presented on a logarithmic scale to accurately capture phase information, as weak secondary phase peaks are difficult to detect on a linear scale in the presence of high intensity peaks from the single crystal substrate and well-oriented electrodes.

3.2.3 Fourier-Transform Infrared Spectroscopy

Analysis of the organic content of the films was done using a Fourier transform infrared microscope (Bruker Hyperion 3000 Microscope, Bruker, Billerica, MA). The microscope was used in specular reflectance mode with a 15x objective for films with thicknesses greater than 100 nm; for films with a thickness of less than 100 nm, a grazing incidence objective was used. In both cases, an analysis area of 150 μm by 150 μm was used. A clean, bare platinized silicon substrate was used as a reference so that absorbance spectra could be calculated and analyzed. The doublet peak present at approximately 2350 cm^{-1} corresponds to atmospheric carbon dioxide. The characteristic absorption frequencies of organic functional groups attributable to the film were indexed to readily available tables, such as that in the work of Robert Silverstein [4].

3.2.4 Scanning Electron Microscopy

Film morphology was determined using scanning electron microscopy. A field emission scanning electron microscope (Leo 1530, LEO Electron Microscopy Ltd., Cambridge, England and Merlin, Carl Zeiss Microscopy LLC., Thornwood, NY) was used at an accelerating voltage of either 3.00 or 5.00 kV for secondary electron imaging. Samples were cleaved to allow cross-sectional images to be taken. Image J software was used to extract the average surface grain size

from highly contrasted micrographs using the average grain intercept method. In the average grain intercept method [5], a set of line segments was randomly drawn on a micrograph, and the number of times each line segment intercepts a grain boundary was tabulated. The average grain size was calculated by dividing the length of the line by the number of grain boundary intercepts. For statistical purposes, 200 intersections were used to ensure an accurate and representative value.

3.2.5 Transmission Electron Microscopy

The nanocrystals in the nanocomposite samples of bismuth zinc niobate tantalate and lead titanate were imaged using transmission electron microscopy. Sample preparation and imaging were done by Ke Wang, of the Materials Characterization Lab at Penn State University. Samples for transmission electron microscopy (JEM 2010, JEOL, Peabody, MA) were prepared by mechanical grinding to approximately 20 μm, followed by ion thinning (691 PIPS, Gatan, Inc., Pleasanton, CA) at an energy of 4 kV until the sample was electron transparent. An operating voltage of 200 kV was used for imaging.

3.2.6 UV-Vis Spectroscopy

The band gaps of $Bi_{1.5}Zn_{0.9}Nb_{(1.5-x)}Ta_{(x)}O_{6.9}$ films on magnesium oxide substrates were analyzed using UV-Vis spectroscopy (Lambda 950, Perkin-Elmer, Waltham, MA) in transmission mode over a wavelength range from 220 to 800 nm. The step size was 1 nm, and the transmission measurements were referenced to a clean, blank MgO single crystal. After data collection, Tauc plots were constructed to extract the band gap of the films. To create a Tauc plot [6], photon energy was plotted on the x-axis and the Tauc parameter was calculated and plotted

on the y-axis. For indirect transitions, the Tauc parameter is equal to the square root of the product of the photon energy and the absorption coefficient; for direction transitions, the Tauc parameter is the product of the photon energy and the absorption coefficient squared [6]. The resulting curve should remain close to the x-axis until the onset of absorption; as absorption begins, the trace will turn upwards and approximate a line. The linear portion of the curve is extrapolated to the x-axis; the intercept will approximate the material's band gap [6].

3.3 Electrical Characterization Techniques

This section describes the electrical characterization techniques used throughout this thesis. To begin the discussion, the details of electrode preparation are presented.

3.3.1 Lift-off Processing of Top Electrodes and Exposure of the Bottom Electrode

To measure the dielectric properties of the films, circular electrodes with diameters ranging from 100 μm to 3 mm were patterned on the film using a double layer lithography process. In this process, LOR 5A lift-off resist (MicroChem Corp., Newton, MA) was deposited on a sample at a spin rate of 4000 rpm for 45 seconds. The resist was cured at 180°C for two minutes. Shipley 1811 photoresist (MicroChem Corp., Newton, MA) was then deposited at 4000 rpm for 45 seconds and soft baked at 95°C for one minute. A mask aligner (MA/BA6, Karl Suss, Garching, Germany) was used to generate UV exposure from a mercury vapor lamp operating at eight mW/cm^2 for twelve seconds. The films were then developed using CD-26 (Shipley, Marlboro, MA) for one minute, rinsed in DI water, and dried with nitrogen. Prior to metallization, the pattern was verified using an optical microscope to ensure adequate exposure and proper development.

After patterning, the films were ashed in a plasma surface modification system (M4L RF Gas Plasma System, PVA TePla, Corona, CA) to remove any residual chemicals or adsorbed species from the surface of the film prior to metallization. Plasma was generated using flow rates of 50 sccm of helium and 200 sccm of oxygen; a 200 W plasma was sustained for two minutes to clean the film surface. A 500 Å thick layer of platinum was sputtered onto the film. After metallization, the sample was soaked in acetone to remove platinum from unpatterned areas. The film was rinsed in acetone and dried with nitrogen. To remove the lift off resist from the film, the sample was soaked in CD-26, rinsed with water, and dried. The bottom platinum electrode was exposed using a 30% aqueous hydrofluoric acid solution to remove the dielectric film. For the case of crystalline films, the film was annealed a final time at 600°C for two minutes in a rapid thermal annealing system to improve the film-top electrode interface. For nanocomposite samples, the films were annealed at 350°C for five minutes in a rapid thermal annealing system. Film thickness was measured using an α-step profilometer (Alpha-Step 500 Surface Profilometer, Tencor, Portsmouth, NH).

3.3.2 Dielectric Measurements

Dielectric measurements were performed on parallel-plate capacitor structures prepared as detailed in section 3.3.1. The capacitance and dielectric loss tangent of the films were measured with an LCR meter (Hewlett-Packard 4284A Precision, Agilent Technologies, Inc., Palo Alto, CA) at an AC oscillation voltage of 0.03 V over a frequency range from 100 Hz to 1 MHz prior to other electrical measurements. The relative permittivity, ε_r, of the films was calculated using the following equation [7]:

$$\varepsilon_r = \frac{Ct}{\varepsilon_o A}$$

in which C is the measured capacitance, t is the thickness of the dielectric layer, ε_o is the permittivity of free space, and A is the area of the top electrode. Temperature dependence of dielectric properties was measured using a Peltier heating stage (Temptronic, Mansfield, MA) on a Cascade probe station (Microtech, Beaverton, OR).

3.3.3 Polarization-Electric Field Measurements

Polarization-electric field behavior was measured using a multiferroic analyzer (Precision Multiferroic, Radiant Technologies, Inc., Albuquerque, NM). Measurements were typically performed at frequencies of 100 Hz, 1 kHz, and 10 kHz. As discussed throughout this thesis, some films did not undergo catastrophic electrical breakdown at these frequencies; for these films, polarization-electric field behavior was also measured at frequencies of 10 Hz to determine at which applied electric field catastrophic breakdown occurred.

The maximum energy storage density that can be stored by a material is a function of the relative permittivity and breakdown strength of a material. The energy storage density was calculated using the following equation [8]:

$$J = \int_{P_0}^{P_{max}} EdP$$

in which J is the stored energy density, E is the applied electric field sustained by the material, P is the resulting polarization of the dielectric, P_o is the polarization at zero field, and P_{max} is the maximum induced polarization. Polarization-electric field loops were used to quantify the energy storage density of the films. As shown schematically in Figure 3-5 [9], the discharged energy storage density is represented as the area between the positive y-axis and the maximum polarization value on the discharging field portion of the loop. Loss, which corresponds to the

area enclosed within the loop, was *never* included in the calculation of energy storage density, and the tunability of these materials was fully accounted for. The high field loss was calculated using the following equation [10]:

$$tan\delta = \frac{1}{2\pi}\frac{w_e}{J}$$

where $tan\delta$ is the loss tangent, J is the energy storage density, and w_e is the hysteresis, which was defined as the area enclosed by the positive field polarization-electric field loop. The power density was calculated as [11]:

$$P = \frac{\pi f J}{tan\delta}$$

in which P is the power density and f is the measurement frequency.

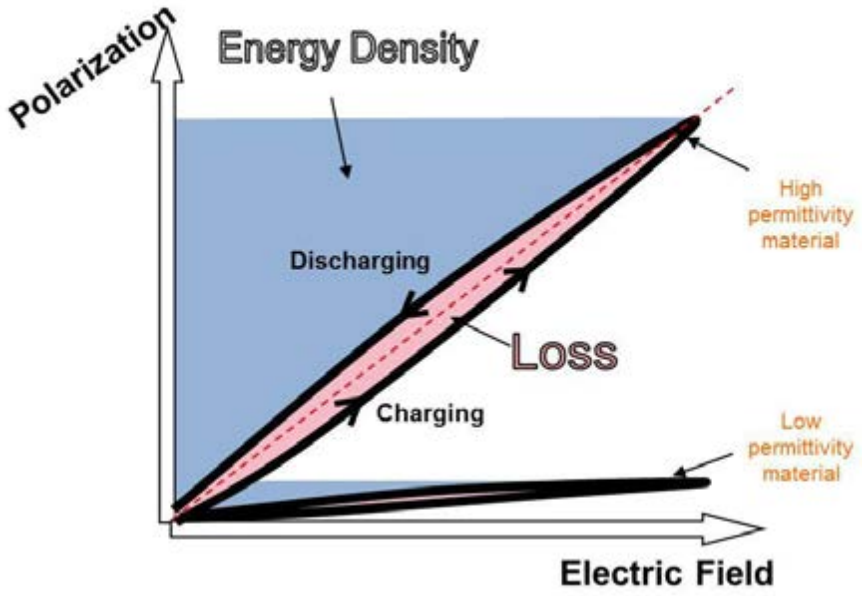

Figure 3-5. A schematic representation of the area of a polarization-electric field hysteresis loop used to quantify discharged energy storage density [9].

3.3.4 Current-Voltage Measurements

Leakage current measurements were made using a pA meter (Hewlett-Packard 4140B pA meter, Agilent Technologies, Inc.). Prior to any leakage current measurements, the time dependence of current under a constant voltage was measured to determine the steady state condition. Figure 3-6 shows current as a function of time for a thin film of bismuth zinc niobate under a constant bias of 20 V. It can be seen that after the application of voltage, current rapidly decreases with time until a steady state was reached. Based on Figure 3-6, the leakage current was measured 90 seconds after the voltage was changed to ensure that measurements were taken after the current reached steady state.

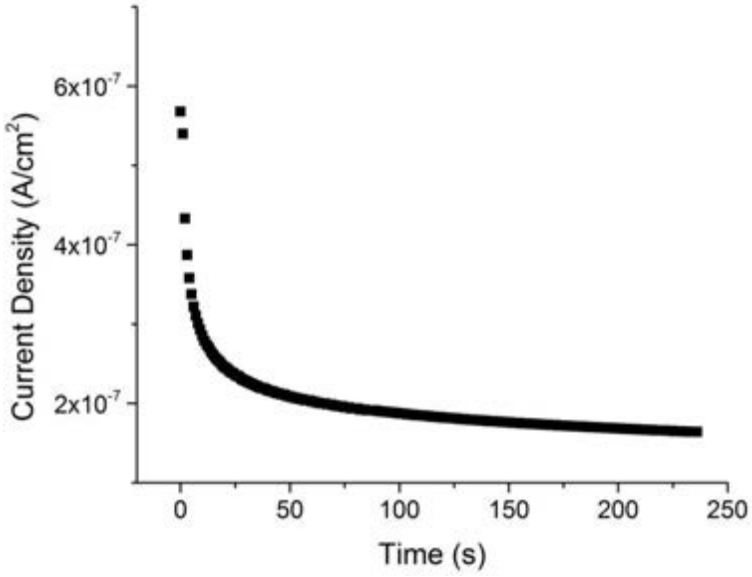

Figure 3-6. Current as a function of time for a 140 nm thick crystalline $Bi_{1.5}Zn_{0.9}Nb_{1.5}O_{6.9}$ thin film under a constant bias of 20 V.

3.3.5 Impedance Spectroscopy

Impedance measurements were performed using an impedance analyzer (ModuLab 2100A, Solartron Analytical, Hampshire, UK) connected to a probe station with a temperature-controllable stage under an oscillation voltage of 1 V. Measurements of capacitance as a function of voltage prior to impedance spectroscopy confirmed that this field was within the range of the linear response for the films. A frequency range of 0.001 Hz to 1 MHz was probed, and spectra were analyzed using Z-View software (Scribner Associates, Southern Pines, NC). Many of the impedance spectra collected had small features at high frequencies. To ensure that these features were captured in sufficient detail to create an accurate model, forty points per decade of data were collected over the frequency range between 100 Hz and 1 MHz (ten points per decade were collected for the remainder of the frequency range). The data were fit to equivalent circuits consisting of a capacitor and resistor in parallel for each semicircle in a spectrum.

3.4 References

1] HD MicroSystems, "PI-2600 series- low stress applications," September 2009. http://hdmicrosystems.com/HDMicroSystems/en_US/pdf/PI-2600_ProcessGuide.pdf.

2] Sigma-Aldrich, "Gold etchant, standard product specifications," 6 February 2015. http://www.sigmaaldrich.com/catalog/product/aldrich/651818?lang=en&region=US.

3] C. J. Brinker and G. W. Scherer, Sol-gel Science: the Physics and Chemistry of Sol-gel Processing, Boston: Academic Press, 1990.

4] R. M. Silverstein, F. X. Webster and D. Kiemle, Spectrometric Identification of Organic Compounds, Hoboken, NJ: John Wiley & Sons, Inc., 2005.

5] G. Vander Voort, "Precision and Reproducibility of Quantitative Measurements," in *Quantitative Microscopy and Image Analysis*, Materials Park, OH, ASM International, 1994, pp. 21-34.

J. Pankove, Optical Processes in Semiconductors, Mineola, NY: Courier Dover Publications,

6] 1971.

7] A. J. Moulson and J. M. Herbert, Electroceramics: Materials, Properties, Applications, West Sussex, England: John Wiley & Sons, Ltd, 2003.

8] N. H. Fletcher, A. D. Hilton and B. W. Ricketts, "Optimization of energy storage density in ceramic capacitors," *Journal of Physics D: Applied Physics,* vol. 29, p. 253–258, 1996.

9] D. P. Shay, "Development and characterization of high temperature, high energy density dielectric materials to establish routes towards power electronics capacitive devices," Ph.D Thesis, The Pennsylvania State University, 2014.

10] K. Uchino and S. Hirose, "Loss mechanisms in piezoelectrics: How to measure different losses separately," *IEEE Transactions of Ultrasonics, Ferroelectrics, and Frequency Control,* vol. 48, no. 1, pp. 307-231, 2008.

11] M. P. Manoharan, C. Zou, E. Furman, N. Zhang, D. I. Kushner, S. Zhang, T. Murata and M. T. Lanagan, "Flexible glass for high temperature energy storage capacitors," *Energy Technology,* vol. 1, pp. 313-318, 2013.

Chapter 4

Chemical Solution Deposition of Bismuth Pyrochlores

The development of a novel solution chemistry for the deposition of bismuth pyrochlore thin films and optimized processing procedures for films are presented in this chapter. The search for a new solution chemistry was motivated by the precursor toxicity and flammability of previously reported methods. The details of the synthetic approach developed in this work will be presented in this chapter. Finally, the link between film processing conditions and the resulting microstructure will be discussed.

4.1 Introduction: The Need for a New Solution Chemistry

Chemical solution deposition is a versatile method for the fabrication of thin films with a wide variety of chemistries and compositions on a range of substrates. In this thesis, chemical solution deposition was pursued as a means to deposit high quality thin films of various bismuth pyrochlore compositions, such as bismuth zinc niobate. Reported sol-gel solution preparations used for thin film deposition of bismuth zinc niobates follow the method outlined by Ren et al. and summarized in Figure 4-1 [1]. In this solution preparation route, zinc acetate dihydrate was combined with 2-methoxyethanol and vacuum distilled at 110°C to remove the waters of hydration. Thorough dehydration of the zinc acetate dihydrate was necessary to control the water content of the final solution and prevent selective hydrolysis of niobium. Following dehydration, niobium ethoxide was added to the zinc solution and refluxed under argon at 120°C for one hour.

Following the reflux, the zinc-niobium complex was vacuum distilled to remove byproducts and then cooled below 80°C. In a separate flask, bismuth acetate was mixed with pyridine and stirred for thirty minutes to dissolve the bismuth acetate, which is sparingly soluble in most common organic solvents [2, 3]. Acetic acid was added to the solution and stirred for one hour. This bismuth acetate solution was added to the cooled zinc-niobium precursor, and the mixture was refluxed at 120°C for thirty minutes to promote intimate mixing of the cations. Finally, the solution was vacuum distilled to remove reaction byproducts and diluted to a concentration of 0.3 M for film deposition.

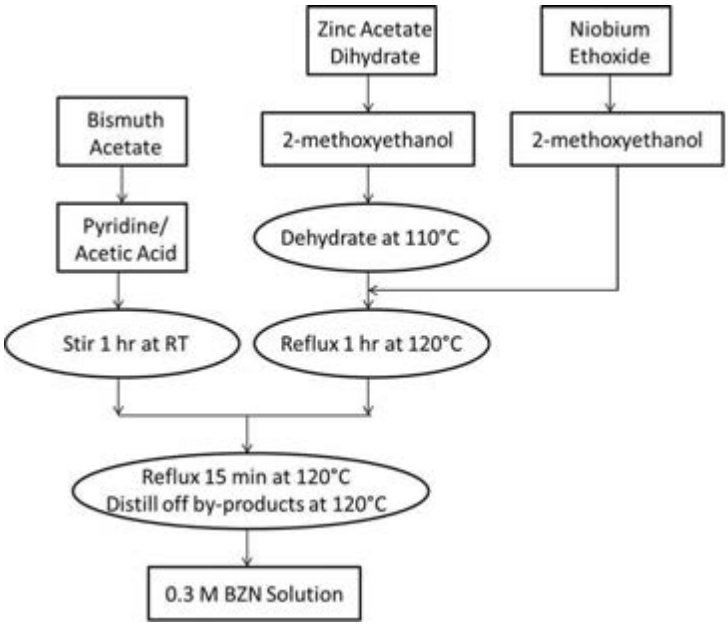

Figure 4-1. Flowchart for the sol-gel solution preparation of bismuth zinc niobate [1].

Due to good solubility and the low cost of many transition metal precursors, sol-gel processes based on 2-methoxyethanol are the most widely used of any of the chemical solution preparations for complex oxides [4, 5]. This solution preparation method can easily be adapted to accommodate a variety of compositions and allows excellent control of stoichiometry.

Furthermore, when properly prepared, the non-hydrolyzed solutions exhibit minimal ageing [4]. Unfortunately, the solution preparation requires many reaction steps and solution preparation times are lengthy. Furthermore, this solution preparation uses 2-methoxyethanol, a teratogen, and pyridine, which has a low flashpoint of 17°C [6], which present significant safety considerations and prohibit their use in some manufacturing facilities.

4.2 The Development of a Novel Solution Chemistry for Bismuth Pyrochlores

To circumvent the use of these chemicals, a novel solution preparation was developed in this work based on the Pechini process [7], which produces homogeneous, well-dispersed solutions with minimal cation segregation [8]. The Pechini method has been used to prepare a variety of thin film materials, including $(Bi_{1-x}Nb_x)FeO_3$ [9], $Pb(Mg_{1/3}Nb_{2/3})O_3$ [10], and $KNbO_3$ [11]. Multicomponent oxide materials prepared via a Pechini process exhibit exceptional homogeneity when compared to multicomponent oxides prepared using a sol-gel synthesis [12]. The sol-gel solution preparation discussed in Section 4.1 can suffer from chemical and phase inhomogeneity due to differences in the hydrolysis and condensation reaction kinetics for each individual cation [13]. The Pechini process, on the other hand, involves the formation of metal complexes and dehydration reactions that drive esterification. The metal complexes are immobilized in a rigid polyester network which reduces the ability of the cations to segregate, ensuring excellent compositional homogeneity [13, 14].

In the Pechini method, metal cationic species are chelated by an α-hydroxycarboxylic acid to form a polybasic acid chelate complex, as shown in Figure 4-2. Metal cations can be supplied by either metal salts or organometallic precursors [10], depending on precursor availability and cost. Citric acid is most commonly used as a chelating group [10], although ethylenediaminetetraacetic acid is also frequently used due to its superior chelating properties.

[15] Most metal citrate complexes are fairly stable due to strong coordination of the metal cation by carboxyl and hydroxyl groups [10, 12, 16].

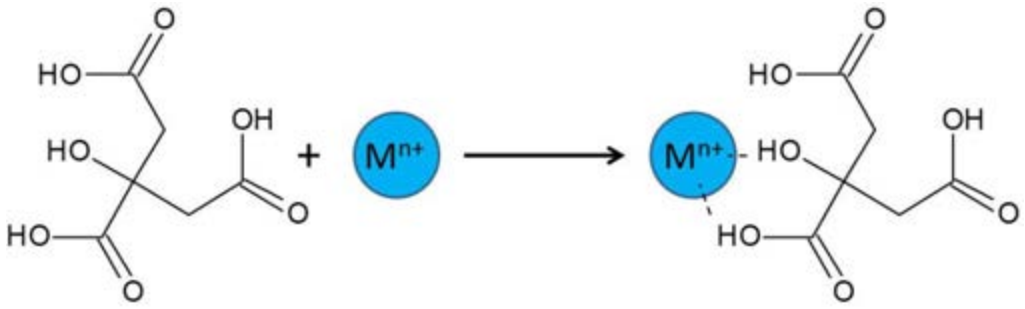

Figure 4-2. The chelation of a metal cation by citric acid to form a polybasic acid chelate complex.

In the presence of a polyhydroxyl alcohol, such as ethylene glycol, the polybasic acid chelates undergo polyesterification, forming a polymer network with a uniform distribution of cations. [10] As shown in Figure 4-3, condensation reactions occur during polyesterification, producing water. The water is formed from a hydroxide ion from the carboxylic acid and a proton from the alcohol; these functional groups are circled in Figure 4-3 [17]. These condensation and polymerization reactions are promoted by heat [12]. As the polymerization reaction proceeds, the viscosity of the solution increases [18, 19]; however, the viscosity of the resulting solution can be adjusted with water [20].

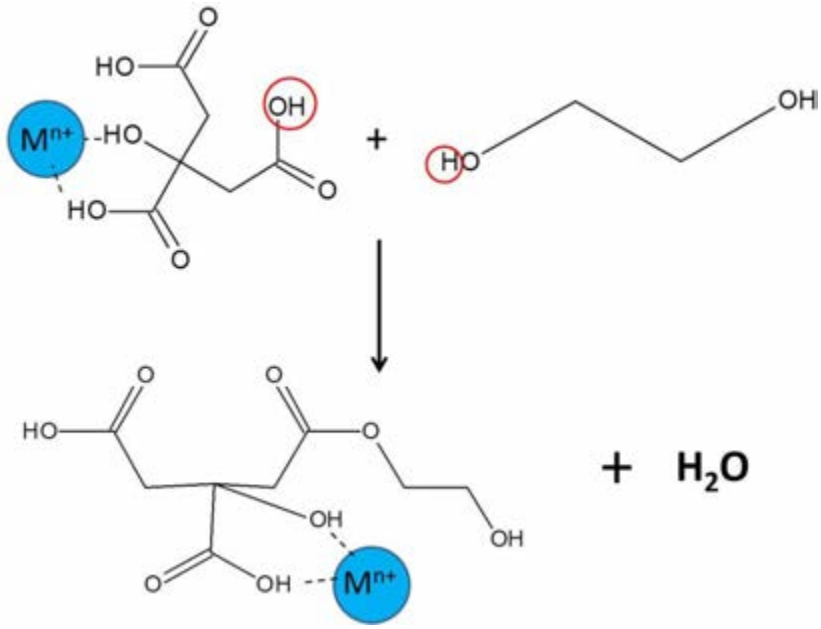

Figure 4-3. The polyesterification of ethylene glycol and the polybasic acid chelate complex formed during the Pechini reaction mechanism. The ions that condense to form water are circled.

To prepare the solutions used to deposit bismuth zinc niobate films in this thesis, bismuth nitrate pentahydrate, zinc acetate dihydrate, and niobium ethoxide were separately mixed in ethylene glycol for 30 minutes at 80°C to create homogeneous alcoholic solutions. All chemicals were measured in a nitrogen atmosphere, sealed into an Erlenmeyer flask using Parafilm, and stirred outside of the glovebox. All subsequent solution preparation was performed in an ambient atmosphere. When films were prepared that contained tantalum, the cation source used was tantalum ethoxide, and it was added directly to the flask containing the niobium ethoxide and ethylene glycol. The maximum achievable molarity of the final solutions was limited by the solubility of the zinc acetate dihydrate in ethylene glycol; heating the solution promoted complete dissolution of the cationic precursors in ethylene glycol [11, 15], allowing the stabilization of 0.15 M solutions. Citric acid was added to each solution, which was then stirred on an 80°C

hotplate for two hours to allow for chelation of the metal atoms. Following chelation, the zinc and niobium solutions were combined and stirred for two hours at 80°C to promote intimate mixing. Finally, the bismuth precursor was added to the zinc-niobium intermediate; the mixture was stirred at 80°C for one hour to allow the solution to homogenize. It is essential that the solution temperature is maintained between 80°C and 110°C throughout the synthesis, as this is the temperature regime at which ethylene glycol and citric acid esterify without forming a viscous polymer resin [15, 21]. The solution preparation is shown schematically in Figure 4-4. This preparation exhibits exceptional versatility in terms of solution composition, stoichiometry, and molarity. Table 4-1 lists the various compositions and structures of bismuth-containing thin films that were explored using this chemistry; the reagents that served as a source for cations not discussed previously are also listed. The typical molarity of the solutions used to deposit thin films in this work was 0.15 M, unless otherwise noted.

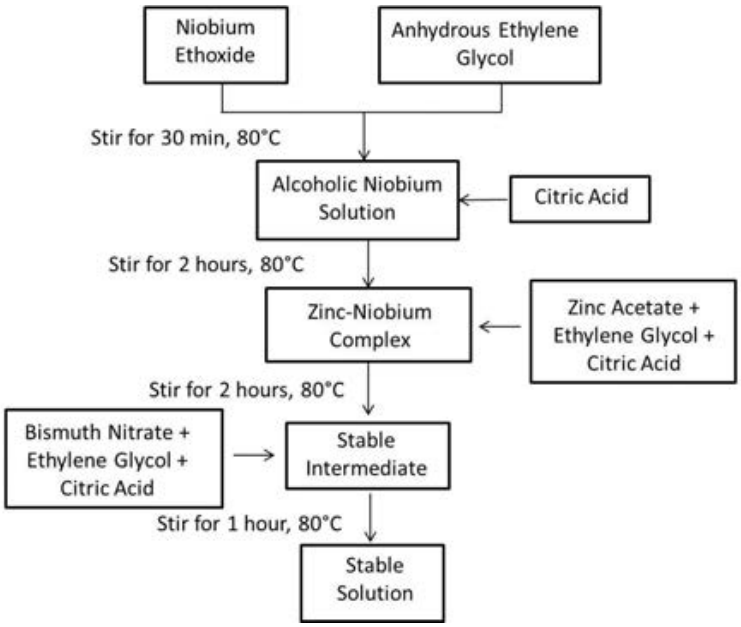

Figure 4-4. Flowchart for the preparation of the solution used to deposit bismuth zinc niobate thin films.

Table 4-1. Thin Film Compositions, Cation Sources, and Crystal Structures of Films Prepared using a Pechini-Based Solution Chemistry

Solution Composition	Cation Sources	Crystal Structure
$Bi_{1.5}Zn_{0.5}Nb_{1.5}O_{6.5}$	--	Cubic pyrochlore
$Bi_{1.35}Zn_{0.5}Nb_{1.5}O_{6.35}$	--	Cubic pyrochlore
$Bi_{1.5}Zn_{0.9}Nb_{1.5}O_{6.9}$	--	Cubic pyrochlore
$Bi_{1.5}Zn_{0.9}Ta_xNb_{(1.5-x)}O_{6.9}$, $0 \leq x \leq 1.5$	--	Cubic pyrochlore
$Bi_{1.5}Zn_{0.9}Ta_{0.15}Nb_{1.335}Mn_{0.015}O_{6.9}$	Manganese acetate tetrahydrate	Cubic pyrochlore
$Bi_{1.5}Zn_{(0.9-x)}Ti_xTa_{0.15}Nb_{1.5}O_{6.9}$, x = 0.009, 0.018	Titanium isopropoxide	Cubic pyrochlore
$Bi_{1.5}Zn_{0.9}Ta_{0.15}Nb_{1.32}Si_{0.03}O_{6.9}$	Tetraethylorthosilicate	Cubic pyrochlore
$Bi_{1.5}Zn_{0.9}Ta_{1.47}Si_{0.03}O_{6.9}$	Tetraethylorthosilicate	Cubic pyrochlore
$Bi_2Zn_{2/3}Nb_{4/3}O_7$		Zirconolite

In these films, it is critical to control the ratio of the chelating complex to cationic species [15], thereby modulating the extent of metal chelation in the solution. If this ratio is not sufficiently high, precipitation of the solution will occur; conversely if this ratio is too high, then complete removal of organics from the film can be difficult. It has been reported that higher temperatures and longer processing times are required to combust the polymer network of the solution relative to alcohol-based sol-gel solutions [15, 22, 23, 24]. In the bismuth zinc niobate system, niobium ethoxide is especially moisture sensitive, and bismuth nitrate pentahydrate cannot be dehydrated; a sufficient molar ratio of citric acid must be used in order to stabilize niobium ethoxide against hydrolysis by the hydrated metal salts. Most Pechini chemistries involving a readily hydrolysable precursor, such as niobium and tantalum, use a citric acid to organometallic molar ratio of at least 3:1 [11, 15]. In this study, a 3:1 molar ratio of citric acid to metal cations was used for crystalline films, while a 1:1 molar ratio was used for nanocomposite films (discussed in Chapter 7) to facilitate the removal of organic species at temperatures of 350°C.

The ratio of ethylene glycol to citric acid controls the degree of esterification in the solution [15]. As the concentration of citric acid increases, the reaction depicted in Figure 4-3 moves towards completion, creating a more extensive polymer network and increasing the viscosity of the solution, often by several orders of magnitude [21, 25, 26]. As the solution viscosity increases, foaming of the films may occur during thermal decomposition of the polymer following film deposition [21]. The original Pechini patent employs a molar ratio of ethylene glycol to citric acid of 4:1 [7]; more recent reports have used ratios of 5:1 and higher to deposit films [25, 26, 27]. Here, the molar ratio of ethylene glycol to citric acid was maintained at 6:1. When smaller ratios were used, the solution viscosity increased and it was difficult to filter the solution prior to deposition on the substrate.

Solutions prepared using this process were stable towards hydrolysis and exhibited no precipitation for up to a year, regardless of whether a 3:1 or 1:1 molar ratio of citric acid to organometallic was used. As the solutions aged, their viscosity increased, which is likely a consequence of continued polyesterification between the citric acid and ethylene glycol. Films deposited using the aged solutions had less controlled levels of porosity, so fresh solutions were typically made after three months to ensure good density in the final films.

4.3 Chemical Solution Deposition of Thin Films

The development of parameters for depositing reasonably dense films of bismuth zinc niobate is presented in this section. The initial processing parameters used to deposit these films resulted in porous films with significantly reduced permittivity values. To improve the properties and microstructure of the films, routes to densification were pursued. A 0.15 M solution of bismuth zinc niobate ($Bi_{1.5}Zn_{0.9}Nb_{1.5}O_{6.9}$) with a 3:1 molar ratio of citric acid to organometallic

precursor was used for the optimization of processing parameters. The results of this optimization were extrapolated to other solutions.

4.3.1 Initial Film Processing Parameters and Indications of a Non-Ideal Microstructure

Thin films of bismuth zinc niobate were spin coated at 5,000 rpm for 30 seconds on a platinum-coated silicon wafer. The substrate was dried on a hotplate at 250°C for three minutes to facilitate the removal of water and organic species with a relatively lower boiling point, and then pyrolyzed for three minutes at 400°C to remove the final organic species from the film. The film was crystallized in a rapid thermal anneal system (RTP-600S, Modular Process Technology Corp., San Jose, CA) for two minutes at 600°C. This process of spin casting followed by three sequential heat treatments was repeated several times to build up film thickness.

The polarization-electric field behavior at 1 kHz is shown in Figure 4-5. The hysteresis loop indicates that the $Bi_{1.5}Zn_{0.9}Nb_{1.5}O_{6.9}$ is a slightly nonlinear, low loss dielectric. The film exhibited a 1 kHz AC breakdown strength of 4 MV/cm, which is higher than what is typically seen in the literature, but the relative permittivity of the film was approximately 98 (loss tangents were 0.003). This permittivity was significantly lower than anticipated; the expected permittivity values are between 150 and 200 [28, 29]. Scanning electron microscopy revealed that these suppressed permittivity values were due to incomplete densification of the films; the microstructure of these porous films is shown in Figure 4-6. Porosity is a common problem in films deposited from solutions with high molecular weight precursors [5, 30, 31], such as the polymeric network found in solutions based on the Pechini method. It was hypothesized that improvements in the microstructure of the film would result in improved permittivity values for the material.

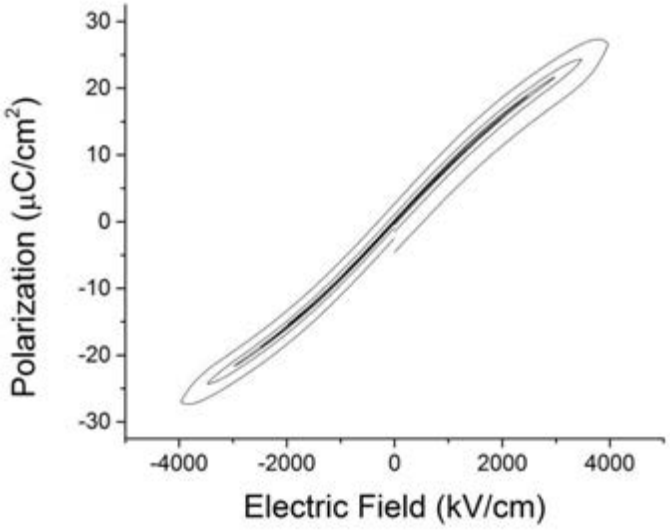

Figure 4-5. The polarization-electric field behavior for an incompletely densified $Bi_{1.5}Zn_{0.9}Nb_{1.5}O_{6.9}$ thin film. The film was 250 nm thick and was deposited in four layers.

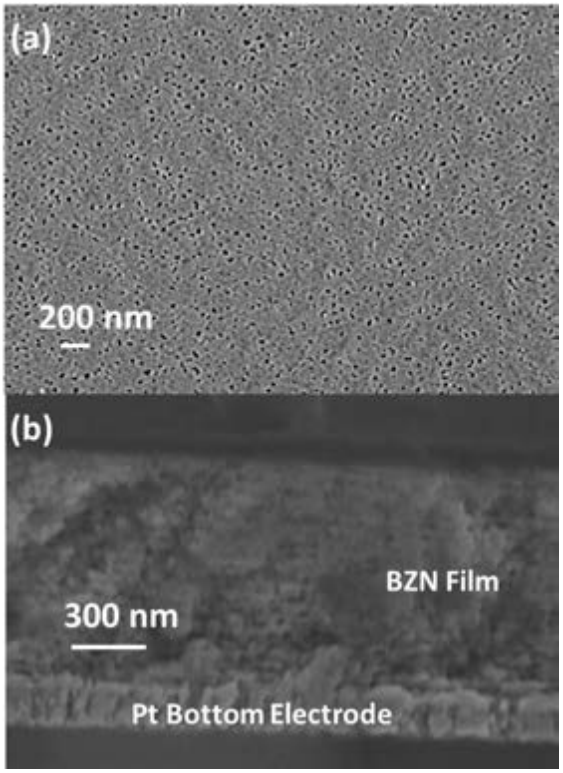

Figure 4-6. (a) SEM image of the incompletely densified $Bi_{1.5}Zn_{0.9}Nb_{1.5}O_{6.9}$ film surface. (b) SEM image of the $Bi_{1.5}Zn_{0.9}Nb_{1.5}O_{6.9}$ film cross-section.

4.3.2 Densification of Bismuth Zinc Niobate Thin Films

To improve the properties and microstructure of the bismuth zinc niobate films, the film processing parameters were optimized. As previously stated, a 0.15 M solution of bismuth zinc niobate ($Bi_{1.5}Zn_{0.9}Nb_{1.5}O_{6.9}$) with a 3:1 molar ratio of citric acid to organometallic precursor was used for the optimization of processing parameters.

4.3.2.1 Thin Film Densification Mechanisms

The development of pores in chemical solution deposited films with high molecular weight precursor solutions is a challenge that inhibits the growth of fully dense films [30]. During heat treatments of the film, the organic groups in the deposited solution are volatized. During the viscous sintering process that accompanies film pyrolysis, these gaseous species may coalesce [5]. As these pockets of gas escape from the collapsing structure, they leave pores or channels through the film. In a solution with large organic clusters, this is especially problematic, as the organics typically require both higher volatization temperatures and are sterically bulky, leaving behind a larger open volume upon evaporation [5, 30, 31]. These regions of open volume must be collapsed prior to crystallization to achieve dense films.

There are four densification mechanisms for sol-gel deposited thin films [32]: (1) capillary forces, (2) condensation reactions, (3) structural relaxation, and (4) viscous sintering. Thin film densification occurs rapidly relative to the densification of bulk materials, so these mechanisms may occur simultaneously [33]. In general, capillary forces accompany the evaporation of solvent from the as-deposited film (drying step) [32]; the pressures created by the evaporation of the solvent from the film drive the collapse of the amorphous, as-deposited network [24]. Condensation reactions, which form metal-oxygen-metal connecting bonds via the

expulsion of water, typically begin to occur during the drying stage [34]. Although condensation reactions densify the film, they eventually compete with evaporation, stiffening the film and decreasing its ability to collapse [5]. The levels of porosity that develop at this stage are established by a competition between the rate of evaporation and the rate of condensation, which can be controlled by the partial pressure of the solvent in the atmosphere and the pH of the precursor solution, respectively [5]. Ideally, the condensation rate should be low enough such that the species in solution are able to efficiently pack together on the substrate and collapse by high capillary pressure after deposition, rather than allowing the precursor species to rapidly form metal-oxygen-metal bonds that resist densification. The final densification mechanisms, structural relaxation (skeletal densification) and viscous sintering, occur at higher temperatures that are characteristic of pyrolysis steps and are driven by a reduction in interfacial energy [35]. In these mechanisms, the as-deposited material rearranges to eliminate porosity and reduce the solid-vapor interfacial area [5]. Viscous sintering involves the breaking and reforming of bonds during viscous flow, whereas structural relaxation is a diffusive process that does not involve bond breaking [32].

4.3.2.2 The Pursuit of Dense Thin Films

Figure 4-7(a) shows the thermal gravimetric analysis of a 0.15 M $Bi_{1.5}Zn_{0.9}Nb_{1.5}O_{6.9}$ solution with a molar ratio of citric acid to organometallic precursor of 3:1; for thermal gravimetric analysis, a sample of the solution in its as-prepared form was used (the solution was not dried prior to analysis). It can be seen that approximately half of the weight loss was complete when the solution reached 250°C, and that by 400°C, approximately 11% weight loss remained. Mass spectroscopy of the gases volatized during the 250°C drying step shows that the evolved species were carbon dioxide, formaldehyde, acetaldehyde, ethylene oxide, ethylene

glycol, and 2-hydroxyethyl acetate. Mass spectroscopy of the gases volatized during the 400°C pyrolysis step shows that the evolved species were carbon dioxide, ethylene glycol, acetaldehyde, 2-hydroxyethyl acetate, 1,2-dioxane, and 3-methylideneoxolane-2,5-dione. Some of these evolved gases are byproducts of citric acid decomposition, which occurs at 175°C [36], and some are directly attributable to bond breaking of the polyester network comprising the solution. Many of these gases are sterically bulky and weight loss of the solution is significant [37], with 82% of the solution's mass being lost over a temperature range from 20°C to 400°C. Large solution weight loss and bulky volatized organic groups are factors that have the potential to act as a barrier to complete film densification. As a comparison and to illustrate the importance of the citric acid concentration on film processing conditions, Figure 4-7(b) shows the thermal gravimetric analysis of a 0.15 M $Bi_{1.5}Zn_{0.9}Nb_{1.5}O_{6.9}$ solution with a molar ratio of citric acid to organometallic precursor of 1:1. It can be seen that approximately 75% of the weight loss occurs when the solution reaches 175°C, and that the weight loss occurring after 350°C was approximately six percent.

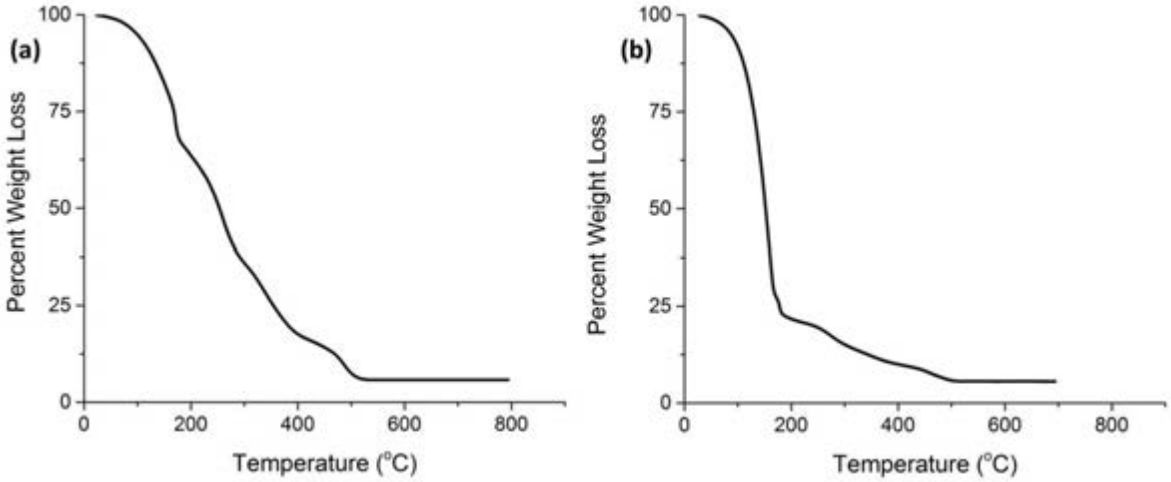

Figure 4-7. Thermal gravimetric analysis of 0.15 M $Bi_{1.5}Zn_{0.9}Nb_{1.5}O_{6.9}$ solutions with a (a) 3:1 and (b) 1:1 molar ratio of citric acid to organometallic precursor.

To improve the density of the films, it was important to determine at which point in the thermal cycle the pores formed. To assess whether porosity developed during the rapid crystallization step due to elimination of residual organics during the rapid thermal annealing step, an infrared spectrum was taken of a film after pyrolysis, but prior to crystallization. Figure 4-8 shows no peaks that correspond to the vibrations of organic functional groups, which confirms that most of the organic species are removed from the film prior to crystallization. The detection limit for routine infrared spectroscopy is on the order of 0.1 wt% [38], which corresponds to less than one volume percent porosity. This is smaller than the observed levels of porosity in the films. Thus, it is possible that residual organic species remaining in the film after the 400°C pyrolysis treatment contributed to pore formation, but they were not the sole cause. Therefore, it was concluded that the majority of the pores formed during the drying or pyrolysis steps.

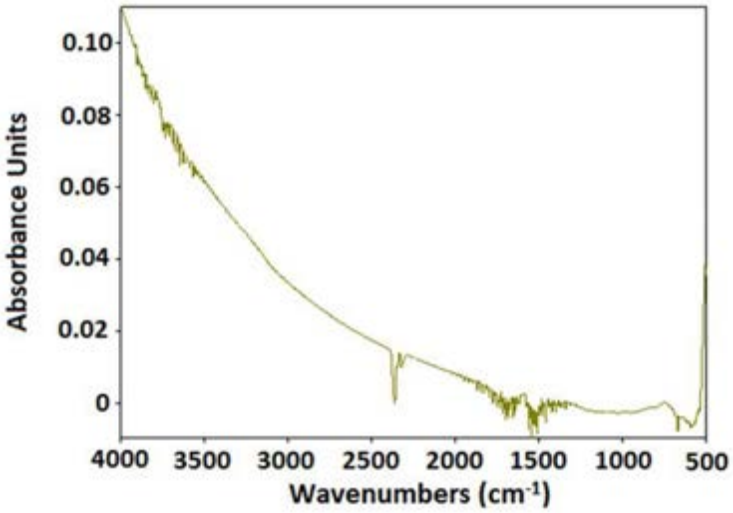

Figure 4-8. Infrared spectrum of the bismuth zinc niobate thin films after pyrolysis. The film was dried on a hotplate at 250°C for three minutes then pyrolyzed for three minutes at 400°C.

To test this hypothesis, SEM images were taken of films after the 250°C drying step and also after the 400°C pyrolysis step. The SEM image of the film after drying shows a dense film that is free of pores, indicating that the evaporation rates during drying were likely sufficiently high to overcome the rigidifying effects of condensation. Figure 4-9 shows the SEM image of the film after the pyrolysis treatment; extensive porosity is evident throughout the film, indicating that the pyrolysis step needed to be optimized to yield dense films.

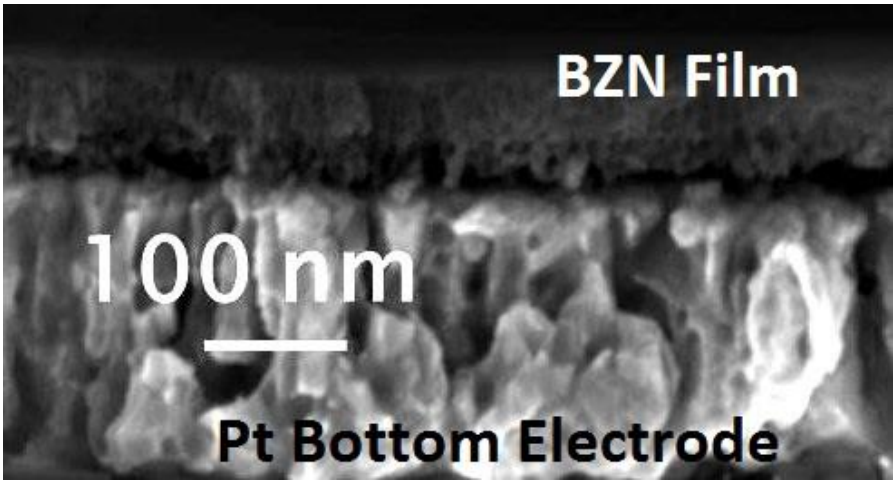

Figure 4-9. SEM image of the bismuth zinc niobate thin film after drying on a hotplate at 250°C for three minutes and pyrolyzing for three minutes at 400°C.

As shown in Figure 4-7, the mass loss that occurred between 250°C and 400°C was substantial, with approximately thirty two percent of the solution mass being lost in this temperature window. This weight loss is attributable to the decomposition and volatilization of organic species during film pyrolysis. When the film was transferred from the 250°C hotplate to the 400°C hotplate, a significant volume of gas was rapidly removed from the film, leaving large amounts of open volume. As non-bridging hydroxyl and alkyl functional groups are removed from a solution, the viscosity of the as-deposited material will increase [32, 34]. The film, which

now consists of cross-linked metal-oxygen-metal bonds, loses much of its plasticity and forms a rigid, porous body that is resistant to viscous flow and resulting densification [34]. The structure may be too rigid to fully collapse the pores despite subsequent heat treatments. During densification experiments, extensive porosity persisted after a twenty minute pyrolysis step at 400°C.

The pyrolysis temperatures were chosen to be 350°C and 400°C to facilitate complete removal of organics and densification prior to crystallization. It is likely that the use of two pyrolysis steps slows the pyrolysis process, allowing the removal of organic species, followed by the rearrangement of molecular groups into a dense film. Figure 4-10(a) shows an infrared spectrum of a film after the 250°C drying step, but prior to the 350°C pre-pyrolysis step. The spectrum shows peaks that correspond to a variety of organic functional groups and are consistent with the mass spectroscopy results and structure shown in Figure 4-3. Due to the variety of functional groups present in the film with characteristic absorptions in the same wavenumber region [39] and the overlapping peaks in the spectrum, it was not possible to assign a precise identity to each peak (such as distinguishing between an ether and an ester C-O stretch). However, the peaks in Figure 4-10(a) can be broadly divided into seven groupings of peaks and a functional group and type of vibration can be determined for the peak clusters; these assignments are given in Table 4-2. Figure 4-10(b) shows an infrared spectrum of the film after the 350°C pre-pyrolysis step but prior to the 400°C pyrolysis step. Figure 4-10(b) shows no peaks that correspond to the vibrations of organic functional groups. As discussed previously, the routine detection limit for infrared spectroscopy is approximately 0.1 wt%; thus, it is possible that residual organic species remain in the film after the 350°C pre-pyrolysis treatment. When the film was transferred to the 400°C hotplate, densification continued to occur, likely via a viscous flow mechanism, as further structural rearrangements occurred at higher temperatures [24].

Using profilometry, it was determined that the thickness of a single layer prior to the 400°C heat treatment was 60 ± 3 nm, while the thickness after the 400°C pyrolysis step was 45 ± 3 nm. It appears that the 350°C pre-pyrolysis step is critical to the deposition of dense films; when the 350°C pyrolysis step was omitted, extensive porosity developed in the film. A table containing more of the pyrolysis conditions that were explored can be found in Appendix A.

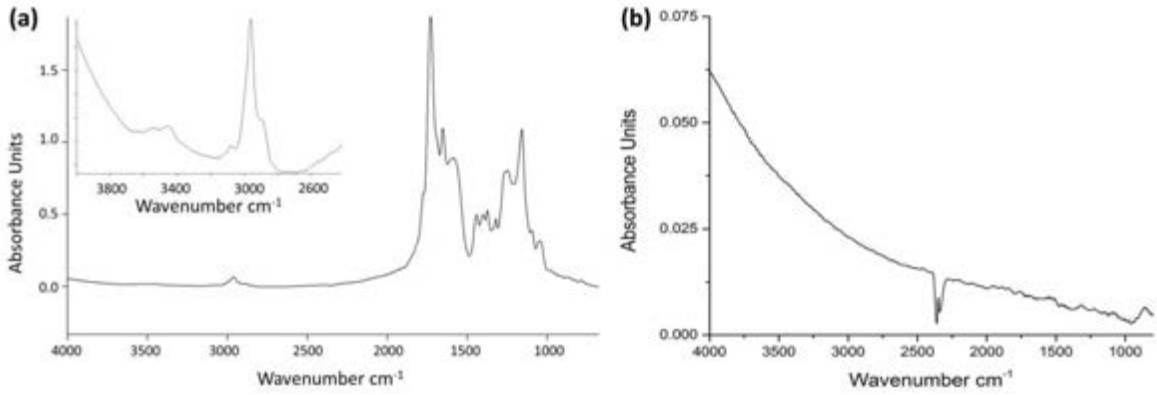

Figure 4-10. (a) Infrared spectrum of the film after drying at 250°C for three minutes. (b) Infrared spectrum of the film after a 250°C drying step for three minutes and a pre-pyrolysis step of ten minutes at 350°C.

Table 4-2. IR Peak Assignments for a $Bi_{1.5}Zn_{0.9}Nb_{1.5}O_{6.9}$ Film after a 250°C Drying Step

Peak Positions (Wavenumbers, cm^{-1})	Functional Group
3542, 3460	O-H Alcohol Stretch
3080, 2961, 2890	C-H Alkane Stretch, =C-H Alkene Stretch
1729	C=O Aldehyde, C=O Ester Stretch
1653, 1590	C=C Alkene Stretch
1442, 1403, 1374	C-H Alkane Bend
1247, 1159	C-O Ester Stretch, C-O Ether Stretch
1097, 1046	C-O Ester Stretch, C-O Ether Stretch, C-O Alcohol Stretch

4.3.3 Optimized Film Processing Parameters

To deposit reasonably dense films, the 0.15 M solution of $Bi_{1.5}Zn_{0.9}Nb_{1.5}O_{6.9}$ was spin coated through a 5 μm filter at 6000 rpm for 45 seconds on a platinum-coated silicon wafer. The substrate was dried on a hotplate at 250°C for three minutes, pre-pyrolyzed on a second hotplate at 350°C for ten minutes, then pyrolyzed for ten minutes at 400°C to remove organic species and densify the film. The film was crystallized in a rapid thermal anneal system for two minutes at 600°C. This process of spin casting followed by four sequential heat treatments was repeated several times to build up film thickness. The film thickness was typically 160 nm after four layers were deposited.

4.4 Thin Film Microstructure of Bismuth Zinc Niobate Thin Films

Figure 4-11(a) shows an SEM image of the surface of a bismuth zinc niobate film deposited using the procedure described in section 4.3.3. The grain size of the films was calculated using the average grain intercept method. The film had small grains that were approximately 27 nm in lateral size and 35 nm through the thickness of the film. The link between the small grain size and the dielectric properties of the films will be discussed in Chapter 6. Figure 4-11(b) shows a reasonably dense cross-section of the film on a platinum bottom electrode. A modest amount of porosity exists between layers of the final film; two examples of this porosity are highlighted with arrows in Figure 4-11(b). The interface between the platinum substrate and the bismuth zinc niobate film is smooth, which minimizes electric field amplifications that are typical of non-uniform interfaces. [40]

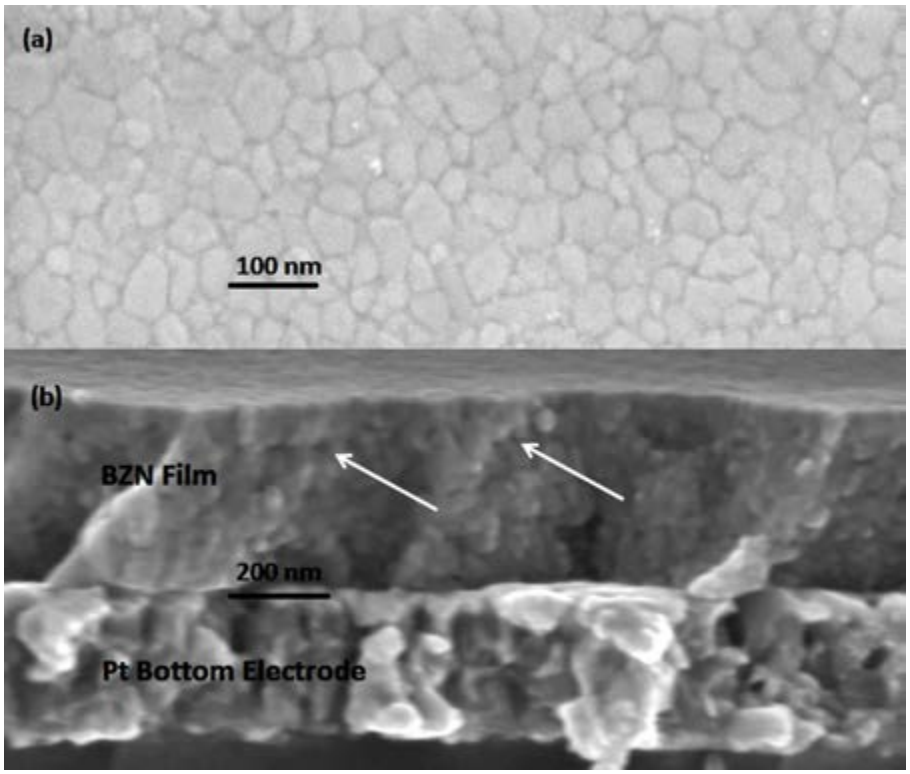

Figure 4-11. (a) SEM image of the mostly dense $Bi_{1.5}Zn_{0.9}Nb_{1.5}O_{6.9}$ film surface used in this study. (b) SEM image of the $Bi_{1.5}Zn_{0.9}Nb_{1.5}O_{6.9}$ film cross-section. Two examples of the modest porosity that exists between layers of the final film are highlighted with arrows.

4.5 References

1] W. Ren, S. Trolier-McKinstry, C. Randall and T. R. Shrout, "Bismuth zinc niobate pyrochlore dielectric thin films for capacitive applications," *Journal of Applied Physics,* vol. 89, no. 1, pp. 767-774, 2000.

2] M. Toyoda, Y. Hamaji, K. Tomono and D. A. Payne, "Synthesis and characterization of $Bi_4Ti_3O_{12}$ thin films by sol-gel processing," *Japanese Journal of Applied Physics,* vol. 32, pp. 4158-4162, 1993.

3] T. J. Boyle, "Sol-gel type synthesis of $Bi_2(Sr,Ta_2)O_9$ using an acetate based system," US Patent 5468679, 4 November 1997.

R. Schwartz, "Chemical solution deposition of perovskite thin films," *Chemistry of*

4] *Materials,* vol. 9, pp. 2325-2340, 1997.

5] C. J. Brinker and G. W. Scherer, Sol-gel Science: the Physics and Chemistry of Sol-gel Processing, Boston: Academic Press, 1990.

6] S. Aldrich, "Sigma Aldrich Co. LLC," [Online]. Available: http://www.sigmaaldrich.com/united-states.html.

7] M. P. Pechini, "Method of preparing lead and alkaline earth titanates and niobates and coating method using the same to form a capacitor," US Patent 3330697A, 11 July 1967.

8] P. Vaqueiro and M. A. Lopez-Quintela, "Influence of complexing agents and pH on yttrium-iron garnet synthesized by the sol-gel method," *Chemistry of Materials,* vol. 9, pp. 2836-2841, 1997.

9] A. Z. Simoes, L. S. Cavalcante, F. Moura, N. C. Batista, E. Longo and J. A. Varela, "Structure, microstructure, ferroelectric/electromechanical properties and retention characteristics of $[Bi_{1-x}Nb_x]FeO_3$ thin films," *Applied Physics A: Materials Science and Processing,* vol. 109, pp. 703-714, 2012.

10] P. D. Spagnol, J. A. Varela, M. A. Bertochi, B. D. Stojanovic and S. M. Tebcherani, "Effect of precursor solution on the formation of perovskite phase of $Pb(Mg_{1/3}Nb_{2/3})O_3$ thin films," *Thin Solid Films,* vol. 410, pp. 177-182, 2002.

11] A. Z. Simoes, A. Ries, C. S. Riccardi, A. H. Gonzalez, M. A. Zaghete, B. D. Stojanovic, M. Cilense and J. A. Varela, "Potassium niobate thin films prepared through polymeric precursor method," *Materials Letters,* vol. 58, pp. 2537-2540, 2004.

12] K. Nishio and T. Tsuchiya, "Sol-gel processing of thin films with metal salts," in *Handbook of Sol-Gel Science and Technology*, Norwell, Massachusetts, Kluwer Academic Publishers, 2005, pp. 59-76.

13] M. Kakihana and M. Yoshimura, "Synthesis and characteristics of complex multicomponent oxides prepared by polymer complex method," *Bulletin of the Chemical Society of Japan,* vol. 72, pp. 1427-1443, 1999.

14] N. G. Eror and H. U. Anderson, "Polymeric precursor synthesis of ceramic materials," in *MRS Proceedings*, vol. 73, p. 571-577, 1986.

15] M. Galceran, M. C. Pujol, M. Aguilo and F. Diaz, "Sol-gel modified Pechini method for obtaining nanocrystalline $KRE(WO_4)_2$ (RE = Gd and Yb)," *Journal of Sol-Gel Science and Technology,* vol. 42, pp. 79-88, 2007.

16] M. Liu and D. Wang, "Preparation of $La_{1-z}Sr_zCo_{1-y}Fe_yO_{3-x}$ thin films, membranes, and coating on dense and porous substrates," *Journal of Materials Research,* vol. 10, pp. 3210-3221, 1995.

H. U. Anderson, M. J. Pennell and J. P. Guha, "Polymeric synthesis of lead magnesium

17] niobate powders," *Advanced Ceramics,* vol. 21, pp. 91-98, 1987.

18] M. Arima, M. Kakihana, Y. Nakamura, M. Yashima and M. Yoshimura, "Polymerized complex route to barium titanate powders using barium-titanium mixed-metal citric acid complex," *Journal of the American Ceramic Society,* vol. 79, pp. 2847-2856, 1996.

19] M. Kakihana, T. Okubo, M. Arima, O. Uchiyama, M. Yashima, M. Yoshimura and Y. Nakamura, "Polymerized complex synthesis of perovskite lead titanate at reduced temperatures: Possible formation of heterometallic (Pb, Ti)-citric acid complex," *Chemistry of Materials,* vol. 9, pp. 451-456, 1997.

20] A. Z. Simoes, F. G. Garcia and C. S. Riccardi, "Piezoresponse behavior of niobium doped bismuth ferrite thin films grown by chemical method," *Journal of Alloys and Compounds,* vol. 493, no. 1-2, pp. 158-162, 2010.

21] V. Petrykin and M. Kakihana, "Chemistry and Applications of Polymeric Gel Precursors," in *Handbook of Sol-Gel Science and Technology: Sol-Gel Processing*, Norwell, MA, Kluwer Academic Publishers, 2005, pp. 77-104.

22] R. Sukumar, W. Sigmund and F. Aldinger, "Nanostructured yttria powders via gel combustion," *Journal of Materials Research,* vol. 14, no. 4, pp. 1524-1531, 1999.

23] D. A. Neumayer, P. R. Duncombe, R. B. Laibowitz and A. Grill, "Chemical solution deposition of $BaSrTiO_3$ films," *Integrated Ferroelectrics,* vol. 18, no. 1-4, pp. 297-309, 1997.

24] R. W. Schwartz and M. Narayanan, "Thermodynamics and Heating Processes," in *Chemical Solution Deposition of Functional Oxide Thin Films*, Wien, Springer, 2013, pp. 343-382.

25] L.-W. Tai and P. A. Lessing, "Modified resin-intermediate processing of perovskite powders: Part I. Optimization of polymeric precursors," *Journal of Materials Research,* vol. 7, no. 2, pp. 502-510, 1992.

26] L.-W. Tai and P. A. Lessing, "Modified resin-intermediate processing of perovskite powders: Part II. Processing for fine, nonagglomerated Sr-doped lanthanum chromite powders," *Journal of Materials Research,* vol. 7, no. 2, pp. 511-519, 1992.

27] A. V. Rosario and E. C. Pereira, "Optimisation of the electrochromic properties of Nb_2O_5 thin films produced by sol–gel route using factorial design," *Solar Energy Materials and Solar Cells,* vol. 71, no. 1, pp. 41-50, 2002.

28] J. Lu and S. Stemmer, "Low-loss, tunable bismuth zinc niobate films deposited by rf magnetron sputtering," *Applied Physics Letters,* vol. 83, no. 12, pp. 2411-2413, 2003.

29] R. L. Thayer, C. A. Randall and S. Trolier-McKinstry, "Medium permittivity bismuth zinc niobate thin film capacitors," *Journal of Applied Physics,* vol. 94, no. 3, pp. 1941-1947, 2003.

[30] M. A. Khan, R. Kurchania, S. Corkovic, Q. Zhang and S. J. Milne, "Compaction of lead zirconate titanate sol-gel coatings," *Materials Letters,* vol. 60, no. 12, pp. 1463-1465, 2006.

[31] A. Chowdhury, M. A. Khan, C. James and S. J. Milne, "Densification and enhanced polarisation in lead zirconate titanate sol–gel thin films," *Materials Chemistry and Physics,* vol. 113, no. 1, pp. 135-139, 2009.

[32] G. W. Scherer, C. J. Brinker and E. P. Roth, "Sol -> Gel -> Glass: III. Viscous sintering," *Journal of Non-Crystalline Solids,* vol. 72, no. 2-3, pp. 369-389, 1985.

[33] R. W. Schwartz and M. Narayanan, "Chemical Solution Deposition — Basic Principles," in *Solution Processing of Inorganic Materials*, Hoboken, NJ, John Wiley & Sons, Inc, 2009, pp. 33-76.

[34] G. W. Scherer, "Sintering of sol-gel films," *Journal of Sol-Gel Science and Technology,* vol. 8, pp. 353-363, 1997.

[35] Y. Frenkel, "Viscous flow of crystalline bodies under action of surface tension," *Journal of Physics (Moscow),* vol. 9, no. 5, pp. 385-391, 1945.

[36] M. M. Barbooti and D. A. Al-Sammerrai, "Thermal decomposition of citric acid," *Thermochimica Acta,* vol. 98, pp. 119-126, 1986.

[37] R. W. Schwartz, T. Schneller and R. Waser, "Chemical solution deposition of electronic oxide films," *Comptes Rendus Chimie,* vol. 7, no. 5, pp. 433-461, 2004.

[38] The Pennsylvania State University - Materials Research Institute, "Materials Research Institute Materials Characterization Lab," [Online]. Available: http://www.mri.psu.edu/facilities/mcl/capabilities/characterization-techniques/ft-ir.asp. [Accessed 25 February 2015].

[39] R. M. Silverstein, F. X. Webster and D. Kiemle, Spectrometric Identification of Organic Compounds, Hoboken, NJ: John Wiley & Sons, Inc., 2005.

[40] M. M. Samantaray, A. Gurav, E. C. Dickey and C. A. Randall, "Electrode defects in multilayer capacitors part I: Modeling the effect of electrode roughness and porosity on electric field enhancement and leakage current," *Journal of American Ceramic Society,* vol. 95, no. 1, pp. 257-263, 2012.

Chapter 5

Cubic Pyrochlore Bismuth Zinc Niobate for High-Temperature Dielectric Energy Storage

In this chapter, cubic pyrochlore bismuth zinc niobate thin films prepared using the solution chemistry and processing parameters discussed in Chapter 4 are examined. The low-field properties of these films will be presented, followed by a review of the DC properties, including tunability and leakage current. Finally, the high-field AC and energy storage properties will be discussed.

5.1 Phase Identification and Microstructure of Bismuth Zinc Niobate

Crystalline $Bi_{1.5}Zn_{0.9}Nb_{1.5}O_{6.9}$ films were prepared using the method described in Chapter 4 and analyzed using x-ray diffraction to verify the phase content of the films. The XRD pattern obtained for these films is shown in Figure 5-1(a); the pattern of a bare platinized silicon substrate is shown in Figure 5-1(b). The diffraction peaks are consistent with the cubic pyrochlore structure of bismuth zinc niobate (PDF # 04-009-5437, 2002). There are no peaks that correspond to the formation of a secondary phase or to reaction intermediates, such as ZnO, Bi_2O_3, or Nb_2O_5. This is consistent with the findings of Thayer et al. [1] that $Bi_{1.5}Zn_{0.5}Nb_{1.5}O_{6.5}$ is the stable phase through film firing temperatures of 650°C. At firing temperatures in excess of 700°C, they found that $Bi_{1.5}Zn_{0.5}Nb_{1.5}O_{6.5}$ decomposed into a mixture of cubic pyrochlore and $BiNbO_4$ phases.

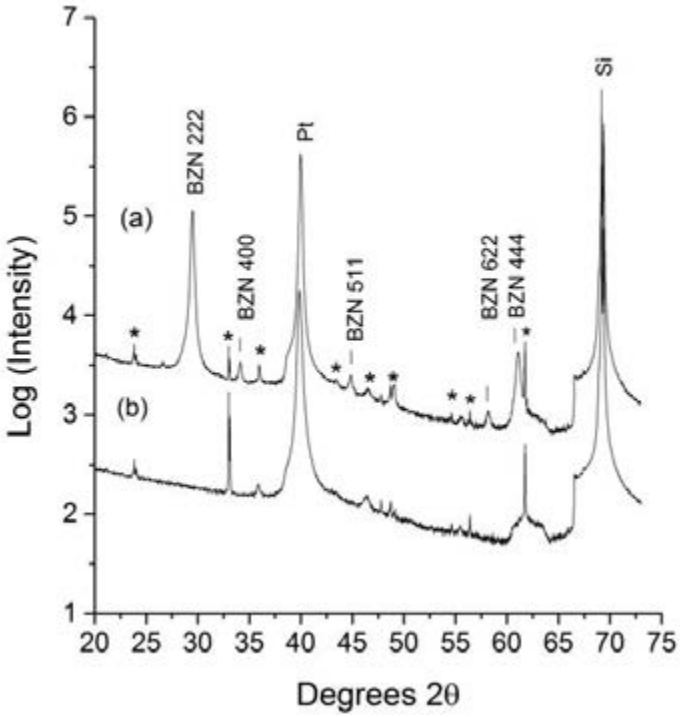

Figure 5-1. (a) The x-ray diffraction pattern of cubic pyrochlore $Bi_{1.5}Zn_{0.9}Nb_{1.5}O_{6.9}$ on a platinized silicon substrate. Peaks marked with an asterisk (*) are due to the substrate or are diffraction from X-ray wavelengths other than Cu Kα. (b) The x-ray diffraction pattern of a bare platinized silicon substrate.

Figure 5-2(a) shows an SEM image of the bismuth zinc niobate film surface, and Figure 5-2(b) shows a cross-section of the film on a platinum bottom electrode. Although the film exhibited reasonable density, a modest amount of porosity exists between layers of the final film. The film had small grains that were approximately 27 nm in lateral size and 35 nm through the thickness of the film. The interface between the platinum substrate and the bismuth zinc niobate film is smooth, which minimizes electric field amplifications that are typical of non-uniform interfaces. [2]

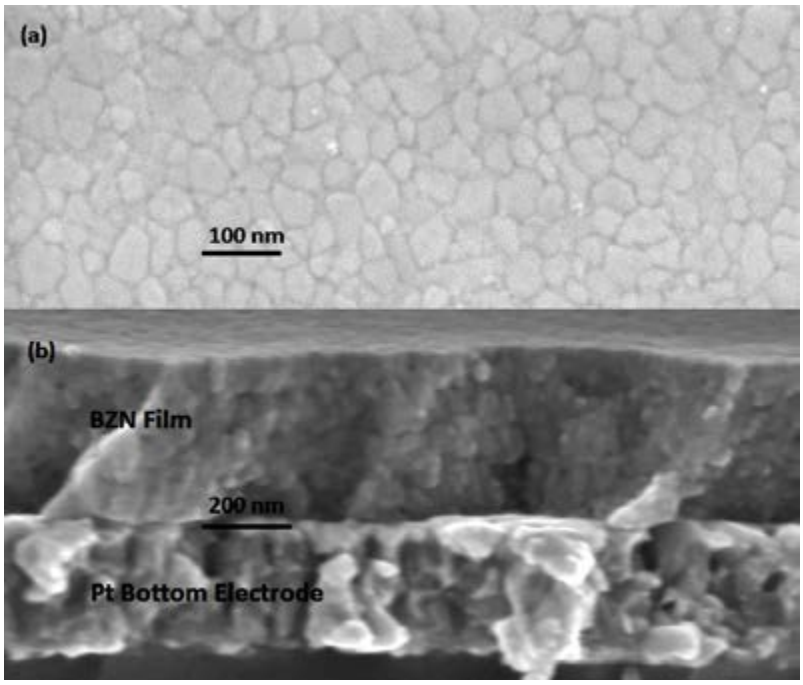

Figure 5-2. (a) SEM image of the mostly dense $Bi_{1.5}Zn_{0.9}Nb_{1.5}O_{6.9}$ film surface used in this study. (b) SEM image of the $Bi_{1.5}Zn_{0.9}Nb_{1.5}O_{6.9}$ film cross-section.

5.2 Low Field Properties of Bismuth Zinc Niobate

The permittivity and loss as a function of frequency for films of $Bi_{1.5}Zn_{0.9}Nb_{1.5}O_{6.9}$ was measured to facilitate a comparison with the values found in the literature. It has been demonstrated that the cubic pyrochlore bismuth zinc niobate is a weakly nonlinear dielectric [3] with a room temperature permittivity of 150-200 [3, 4, 5] and loss tangents on the order of 0.0005 to 0.005 [1, 3, 4, 6]. Figure 5-3 shows the permittivity and loss as a function of frequency for the films in this work. As can be seen from the figure, the relative permittivity of the films was 145 and the loss tangent was 0.00065. This permittivity value is slightly lower than other reports in the literature, which may be due to the small amount of porosity between the layers of the dielectric. The low loss tangent is comparable to those exhibited by sputtered $Bi_{1.5}Zn_{0.9}Nb_{1.5}O_{6.9}$

films, and approximately an order of magnitude lower than most films fabricated by chemical solution deposition [1, 3, 4, 6].

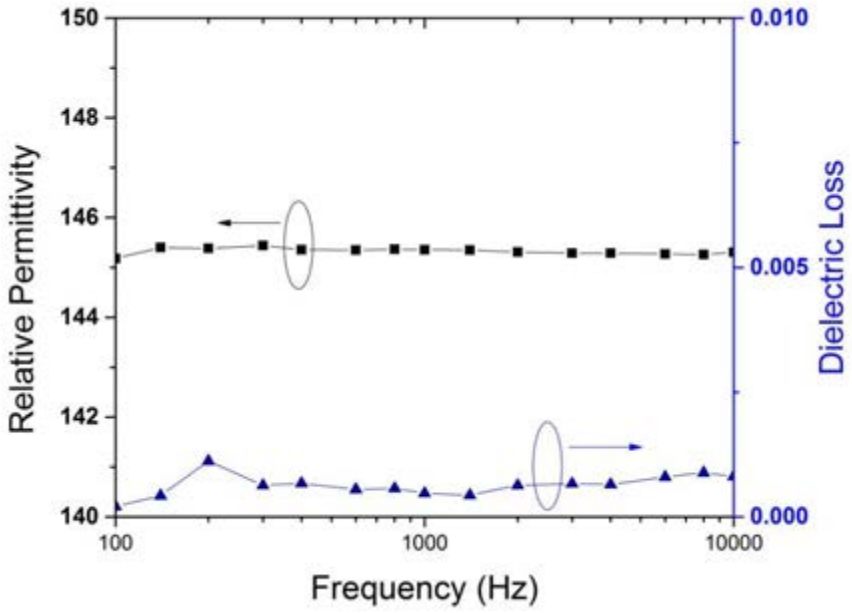

Figure 5-3. The relative permittivity and loss as a function of frequency for thin films of $Bi_{1.5}Zn_{0.9}Nb_{1.5}O_{6.9}$.

Figure 5-4 shows the polarization versus electric field behavior for cubic pyrochlore bismuth zinc niobate measured using an AC electric field of 2.5 MV/cm at a measurement frequency of 1 kHz. The hysteresis loop shows $Bi_{1.5}Zn_{0.9}Nb_{1.5}O_{6.9}$ to be a slightly nonlinear, low loss dielectric. The plot also confirms the relative permittivity value of 145±5 measured using an LCR meter.

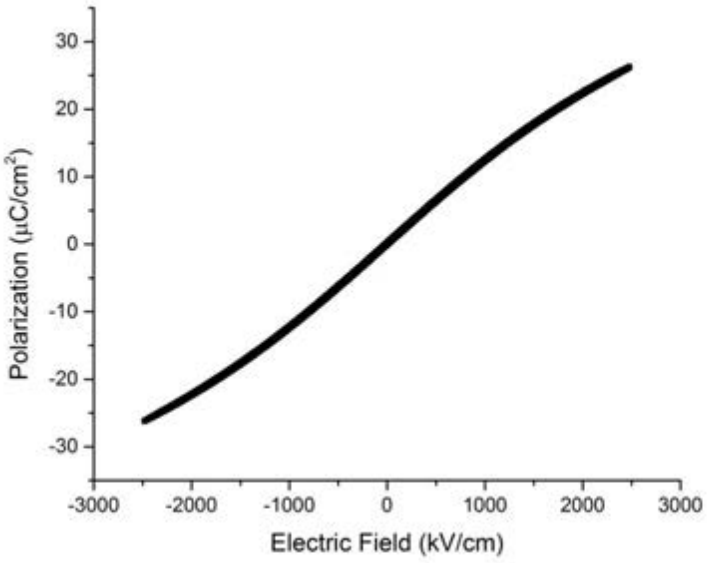

Figure 5-4. Polarization-electric field behavior for cubic pyrochlore $Bi_{1.5}Zn_{0.9}Nb_{1.5}O_{6.9}$, a slightly nonlinear, low loss dielectric.

5.3 DC Properties of Bismuth Zinc Niobate

The DC properties, including the tunability, leakage current, and high voltage I-V characteristics, of bismuth zinc niobate thin films are presented.

5.3.1 Tunability

The dielectric tunability of a material is defined as the percent change in the relative permittivity under DC bias. The tunability is calculated from the difference in the permittivity maximum (usually the material in an unbiased state) and the permittivity at a specified DC bias field [7]:

$$\text{Tunability (\%)} = \frac{\varepsilon_{r,max} - \varepsilon_{r,min}}{\varepsilon_{r,max}} \text{ x } 100\%$$

in which $\varepsilon_{r,\,max}$ and $\varepsilon_{r,\,min}$ are the maximum and minimum relative permittivity values for the film. For the bismuth zinc niobate materials system, Thayer [1] demonstrated that $Bi_{1.5}Zn_{0.5}Nb_{1.5}O_{6.5}$ thin films grown by chemical solution deposition possess a dielectric tunability of 26% at applied electric fields of 1.8 MV/cm at 77 K. A dielectric tunability of 45% for an applied electric field of 3 MV/cm was reported for the cubic pyrochlore composition $Bi_{1.5}Zn_{1.0}Nb_{1.5}O_7$ at 77 K [1]. It was hypothesized [1] that the large electric fields used to measure tunability quenches the contribution to the material's polarization stemming from random fields and interactions between disordered sites in the cubic pyrochlore crystal structure [8].

As shown in Figure 5-5, the $Bi_{1.5}Zn_{0.9}Nb_{1.5}O_{6.9}$ films examined here exhibited a room temperature tunability of 42% at DC fields of 2.5 MV/cm and an AC oscillation voltage of 0.03 V.

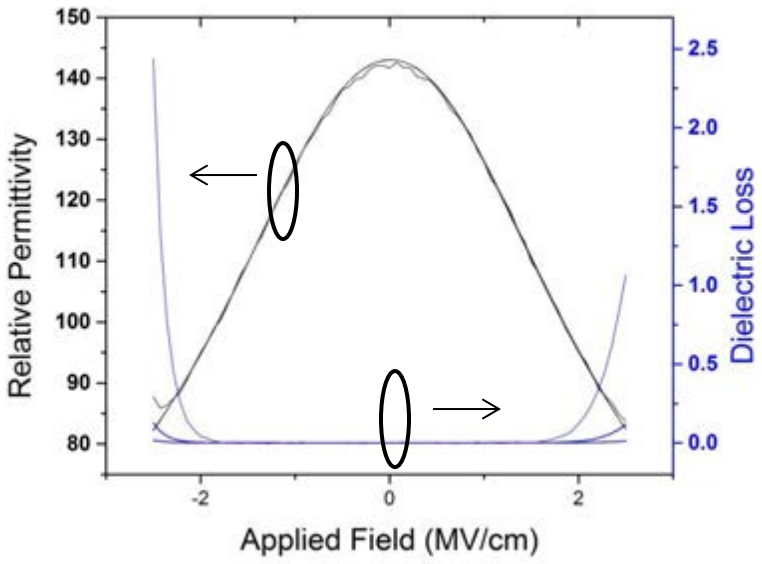

Figure 5-5. Permittivity and loss as a function of DC electric field for $Bi_{1.5}Zn_{0.9}Nb_{1.5}O_{6.9}$, used to calculate tunability.

5.3.2 Leakage Current of Bismuth Zinc Niobate

Figure 5-6 shows the leakage current density as a function of DC electric field for cubic pyrochlore bismuth zinc niobate thin films. The DC breakdown strength in these films, defined as the field at which the films reached catastrophic electrical breakdown, depended on the sample area. For electrodes with a diameter of 200 μm, indicated in Figure 5-6 by open squares, the DC breakdown strength of the material was between 3 and 4 MV/cm. When the diameter of the electrodes was increased to 2 mm, indicated by filled squares in Figure 5-6, the DC breakdown strength of the material was between 2 and 3 MV/cm. This difference in the DC breakdown strength is due to the decreased probability of encountering a critical flaw when probing a smaller volume of a material. These critical defects reduce the maximum electric field that can be placed across the material before it undergoes catastrophic electrical breakdown. The DC breakdown strength is defined by some authors as the electric field at which the current surpasses 0.1 $\mu A/cm^2$ [9]; the field at which the leakage current surpasses 0.1 $\mu A/cm^2$ for these films of bismuth zinc niobate is 1.5 MV/cm. The energy storage density at this field level is 13.5 ± 0.5 J/cm^3; the energy storage density under AC electric field is discussed in section 5.4.2.

The leakage current for this material is low, on the order of 10^{-10} A/cm^2, up to fields of approximately 1 MV/cm. The magnitude of the leakage current is slightly lower than in other reports, while the DC breakdown strength of these films exceeds those reported in the literature [10].

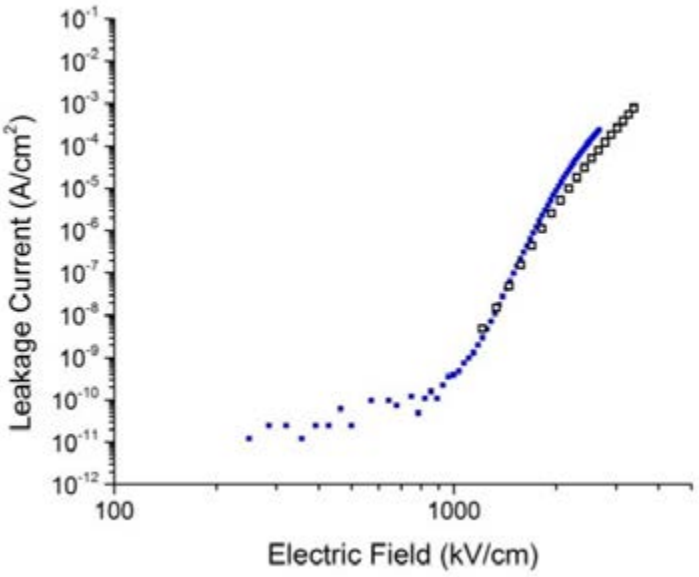

Figure 5-6. Leakage current density as a function of the DC electric field for $Bi_{1.5}Zn_{0.9}Nb_{1.5}O_{6.9}$. When the diameter of the electrodes were 200 μm (open squares), the films had a DC breakdown strength between 3 and 4 MV/cm; when the diameter of the top electrode was increased to 2 mm (closed squares), the DC breakdown strength was between 2 and 3 MV/cm.

5.3.3 High Voltage I-V Characteristics for Automotive Applications

The power inverters and DC-links in batteries of hybrid/electric vehicles require capacitive materials that can sustain 400 to 600 V without breakdown [10, 11, 12]. A thin film of cubic pyrochlore bismuth zinc niobate with a thickness of 1.6 μm was deposited on platinized silicon for high voltage tests. Figure 5-7 shows the current-voltage characteristics of the thick film of cubic pyrochlore bismuth zinc niobate. As can be seen in the figure, the film could withstand a voltage of 600 V without the occurrence of catastrophic breakdown, making cubic pyrochlore bismuth zinc niobate a candidate for power inverter and battery applications in hybrid/electric vehicles. The magnitude of the leakage current for thicker films of bismuth zinc

niobate is higher than that of thin films of bismuth zinc niobate. This is likely due to the increased probability of encountering a large critical flaw resulting from the deposition of films with many layers. These defects will also reduce the maximum electric field that can be placed across the material before it undergoes catastrophic electrical breakdown. Additional work to improve the materials processing to further increase the breakdown strength for large area electrodes should be conducted.

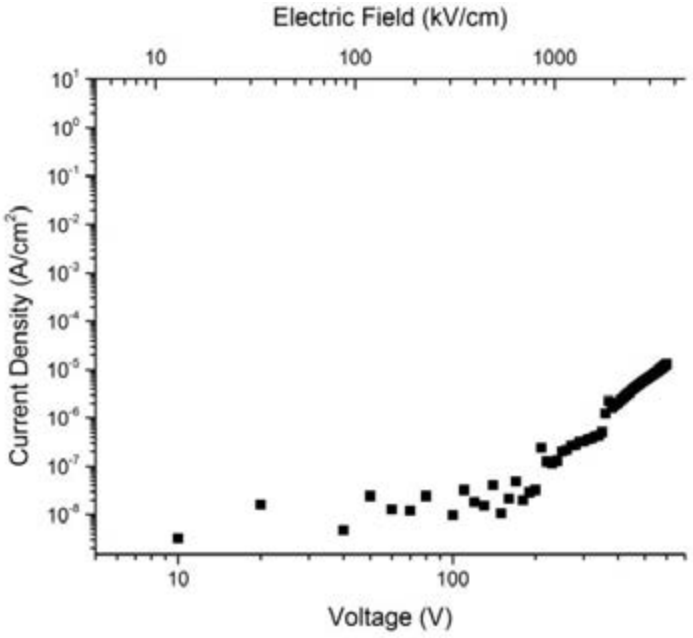

Figure 5-7. The current-voltage characteristics for a 1.6 μm film of cubic pyrochlore bismuth zinc niobate. These comparatively thicker films sustain 600 V without catastrophic breakdown.

5.4 High Field AC Properties of Bismuth Zinc Niobate

These thin films of bismuth zinc niobate withstand high AC electric fields. Here, the Weibull analysis for the films is presented, along with the energy and power storage characteristics.

5.4.1 AC Breakdown Measurements and Weibull Statistics

Figure 5-8 shows polarization-electric field hysteresis loops at different frequencies for the highest fields sustained by the bismuth zinc niobate films. The area used to calculate energy storage density (discussed in Section 5.4.2) is shaded. The width of the hysteresis loops increased as the material was swept to higher electric fields, which is indicative of an increase in the dielectric loss of the film. When the electric field was removed from the film, the material recovered, indicating that the increase in loss at high applied electric fields was due to an increase in conduction rather than a permanent damage mechanism.

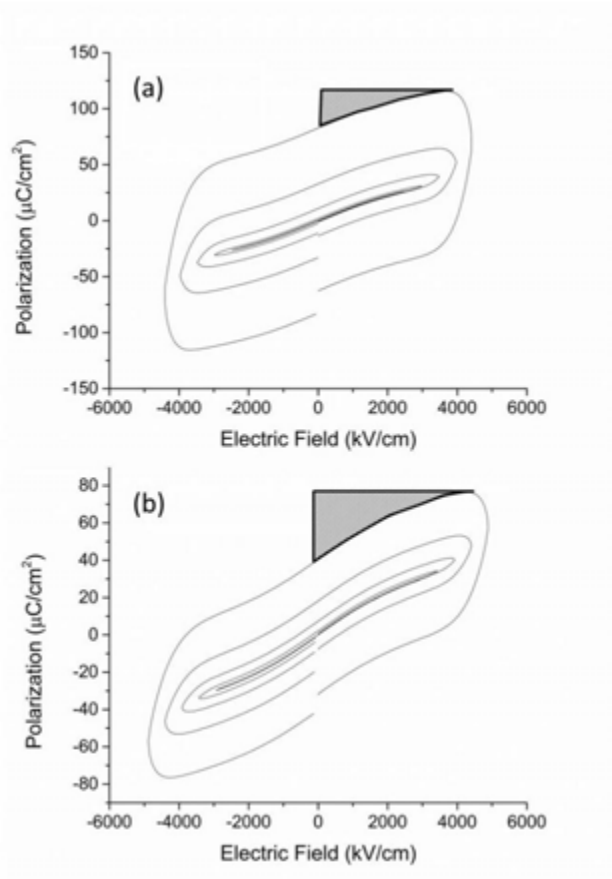

Figure 5-8. The polarization-electric field behavior for bismuth zinc niobate films. The highest field sustained by the material is dependent on the measurement frequency: (a) 4.7 MV/cm at 1 kHz, (b) 5.1 MV/cm at 10 kHz. The shaded area was used to calculate the energy storage density.

Weibull plots, shown in Figure 5-9, were constructed to determine the catastrophic electrical breakdown strength and maximum AC fields sustained by these films. The values of the Weibull parameters are given in Table 5-1. The Weibull parameter for each condition was calculated using a total of fifteen electrodes with a 200 μm diameter. When the diameter of the electrodes was increased to 1 mm, the Weibull parameters were the same within the error bars. As evidenced by the large Weibull parameters, these breakdown strengths, and the resulting energy storage values, exhibited little variation from electrode to electrode. Furthermore, there was little variation from sample to sample. At a measurement frequency of 1 kHz, the material sustained a maximum electric field of 4.7 MV/cm, and for measurement frequencies of 100 Hz and 10 kHz, the films sustained fields of 5.0 MV/cm and 5.1 MV/cm, respectively. At 10 Hz, the films underwent catastrophic electrical breakdown at applied fields of 5.2 MV/cm. This breakdown strength exceeds those reported in the literature for $Bi_{1.5}Zn_{0.9}Nb_{1.5}O_{6.9}$.

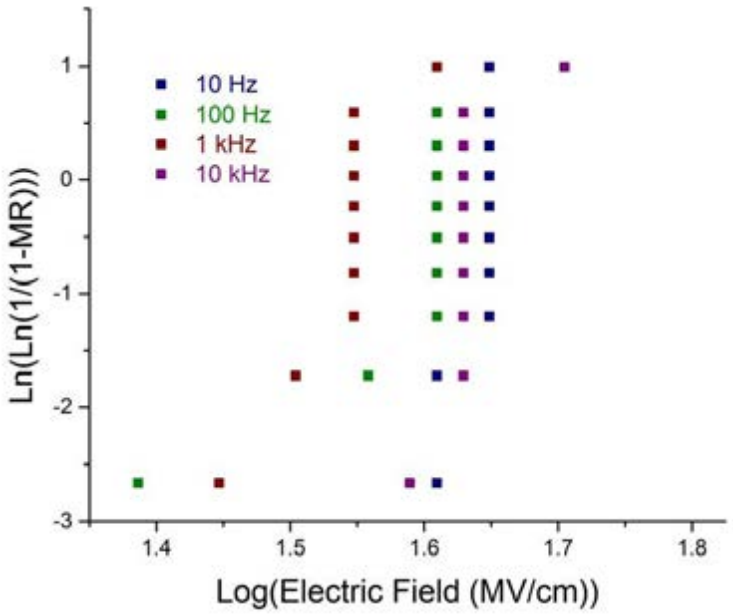

Figure 5-9. The Weibull plots for the maximum AC electric fields (100 Hz, 1 kHz, and 10 kHz) sustained by bismuth zinc niobate, as well as the catastrophic electric breakdown (10 Hz).

Table 5-1. Weibull Parameters for the Breakdown Strength and Maximum Fields Sustained by $Bi_{1.5}Zn_{0.9}Nb_{1.5}O_{6.9}$

	10 Hz	100 Hz	1 kHz	10 kHz
Breakdown Strength/Maximum Field (MV/cm)	5.2 ± 0.1	5.0 ± 0.1	4.7 ± 0.1	5.1 ± 0.1
Weibull Parameter	53.2 ± 2.4	12.0 ± 1.1	23.8 ± 1.7	27.9 ± 1.9

5.4.2 Energy and Power Storage Characteristics of Bismuth Zinc Niobate

The high breakdown strength and low losses in the material contributed to a high energy storage density despite the moderate permittivity of the films. Figure 5-10(a) shows the maximum discharged energy storage density achieved for the bismuth zinc niobate films as a function of temperature and measurement frequency. These calculations reflect discharged energy densities, in which the losses of the material (the area enclosed within the hysteresis loop) are not included in the reported energy density. Likewise, the modest tunability in the permittivity is fully accounted for. The maximum energy storage densities achieved at each of the three measurement frequencies is comparable, making bismuth zinc niobate a suitable candidate for integration into energy storage devices for a variety of applications. At 100 Hz, the maximum energy storage density for bismuth zinc niobate was 46.7 J/cm^3. At 1 kHz, the maximum energy storage density was 48.9 J/cm^3, and at 10 kHz, the maximum energy storage density was 60.8 J/cm^3. The energy storage density as a function of temperature for several other materials is shown in Figure 5-10(a) for comparison [13, 14, 15].

Some applications, including several of the pulsed power applications mentioned in Chapter 1, require that the loss of the material remain low [16]. In the case of these bismuth zinc niobate films, the maximum energy storage density for the system was limited by the loss tangent of the film, rather than the breakdown strength of the material. Figure 5-10(b) shows the energy storage density of the bismuth zinc niobate films when the high field loss tangent was restricted to

a maximum value of 0.02 (loss does not exceed 2%). Although the energy storage densities under restricted loss conditions were reduced, the energy storage values were still high for all measurement frequencies.

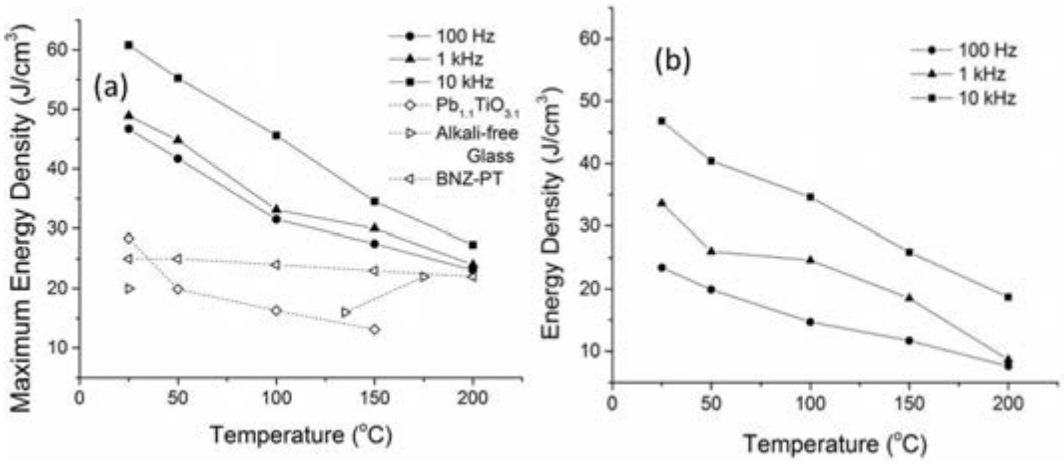

Figure 5-10. (a) The maximum energy storage density of bismuth zinc niobate and several other high energy storage density materials as a function of temperature [13, 14, 15]. (b) The energy storage density of bismuth zinc niobate when loss values are required to remain below 2%.

Furthermore, the energy storage density remained high as the temperature was increased; for all three measurement frequencies, the maximum energy storage density exceeded 20 J/cm^3 at 200°C. This is slightly higher than the maximum energy storage density reported for any material at 200°C [14]. The decrease in energy density of the bismuth zinc niobate capacitors at increased temperatures is due to a decrease in the breakdown strength of the material at elevated temperatures. As the temperature increased, the conductivity of the film increased. At 200°C, the breakdown strength of the material at 100 Hz was 3.5 MV/cm, while the breakdown strength at 1 kHz was 3.2 MV/cm and 10 kHz was 3.3 MV/cm. Figure 5-11 shows the 200°C polarization-electric field hysteresis loop for bismuth zinc niobate at a measurement frequency of

10 kHz; the maximum energy storage density was 27.3 J/cm^3. At 1 kHz, the energy storage density was 24.0 J/cm^3 and at 100 Hz, the energy storage density was 23.1 J/cm^3.

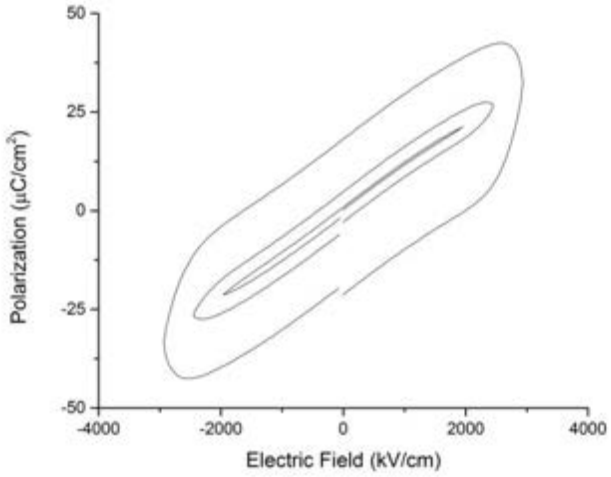

Figure 5-11. The 10 kHz polarization-electric field hysteresis loops for bismuth zinc niobate at 200°C. The maximum energy storage density was 27.3 J/cm^3.

Power density was calculated using the following equation [14]:

$$P = \frac{\pi f J}{tan\delta}$$

in which P is the power density, f is the measurement frequency, $tan\delta$ is the high-field loss tangent of the film, and J is energy storage density. The calculated power densities for the films at measurement frequencies of 1 kHz and 10 kHz are listed in Table 5-2 as a function of temperature.

Table 5-2. Power Storage Density of $Bi_{1.5}Zn_{0.9}Nb_{1.5}O_{6.9}$ as a Function of Temperature

Temperature (°C)	Power Storage Density at 10 kHz (MW/cm^3)	Power Storage Density at 1 kHz (MW/cm^3)
25	700	20
50	650	20
100	630	8.0
150	98	34
200	66	1.5

The moderate relative permittivity of these films, as well as their low dielectric loss values and high breakdown strengths, resulted in a high energy storage density. Further improvements in the energy storage density of cubic pyrochlore bismuth zinc niobate could be realized through the complete elimination of porosity between the deposited layers of the film. Additionally, enhancements in the breakdown strength of these films may improve the energy storage density of the bismuth-based cubic pyrochlore films.

5.5 Conclusions

Capacitive materials with both high energy and high power storage densities are required for power electronics. Linear dielectrics are advantageous for energy storage applications because they offer a compromise between breakdown strength and relative permittivity, in addition to exhibiting low loss tangents. Here, thin films of cubic pyrochlore bismuth zinc niobate, a weakly nonlinear dielectric, were investigated for their use in energy storage device applications. The films exhibited a medium relative permittivity of 145. At frequencies of 1 kHz, the films exhibited a low loss tangent of 0.00065, and a maximum field of approximately 4.7 MV/cm. At 100 Hz and 10 kHz, the dielectric loss of the films increased to 0.0065, although the maximum field sustained by the films increased to 5.0 MV/cm and 5.1 MV/cm. The films maintained a high energy storage density across a range of frequencies and temperatures. At a

measurement frequency of 10 kHz, the maximum energy storage density was ~60.8 J/cm^3 while at a measurement frequency of 100 Hz, the maximum energy density was ~46.7 J/cm^3. As temperature was increased to 200°C, the maximum energy storage density remained high. At measurement frequencies of 10 kHz, the maximum energy density was ~27.3 J/cm^3, while at 100 Hz, the maximum energy storage density was ~23.1 J/cm^3. Cubic pyrochlore bismuth zinc niobate possessed a DC breakdown strength of between 3 and 4 MV/cm and a low leakage current of approximately 10^{-10} A/cm^2 up to fields of 1 MV/cm.

5.6 References

1] R. L. Thayer, C. A. Randall and S. Trolier-McKinstry, "Medium permittivity bismuth zinc niobate thin film capacitors," *Journal of Applied Physics,* vol. 94, no. 3, pp. 1941-1947, 2003.

2] M. M. Samantaray, A. Gurav, E. C. Dickey and C. A. Randall, "Electrode defects in multilayer capacitors part I: Modeling the effect of electrode roughness and porosity on electric field enhancement and leakage current," *Journal of American Ceramic Society,* vol. 95, no. 1, pp. 257-263, 2012.

3] W. Ren, S. Trolier-McKinstry, C. Randall and T. R. Shrout, "Bismuth zinc niobate pyrochlore dielectric thin films for capacitive applications," *Journal of Applied Physics,* vol. 89, no. 1, pp. 767-774, 2000.

4] J. Lu and S. Stemmer, "Low-loss, tunable bismuth zinc niobate films deposited by rf magnetron sputtering," *Applied Physics Letters,* vol. 83, no. 12, pp. 2411-2413, 2003.

5] X. Zhang, W. Ren, P. Shi, X. Wu, X. Chen and X. Yao, "Structures and dielectric properties of pyrochlore bismuth zinc niobate thin films with zinc compensation," *Journal of Alloys and Compounds,* vol. 553, pp. 8-13, 2013.

6] J. Park, J. Lu, S. Stemmer and R. A. York, "Microwave dielectric properties of tunable capacitors employing bismuth zinc niobate thin films," *Journal of Applied Physics,* vol. 97, p. 084110, 2005.

7] R. A. York, "Tunable Dielectrics for RF Circuits," in *Multifunctional Adaptive Microwave Circuits and Systems*, Scitech Publishing, 2009.

I. Levin, T. G. Amos, J. C. Nino, T. A. Vanderah, C. A. Randall and M. T. Lanagan, "Structural study of an unusual cubic pyrochlore $Bi_{1.5}Zn_{0.92}Nb_{1.5}O_{6.92}$," *Journal of Solid*

8] *State Chemistry,* vol. 168, no. 1, pp. 69-75, 2002.

9] H. Bartzsch, D. Gloβ, P. Frach, M. Gittner, E. Schultheiβ, W. Brode, and J. Hartung, "Electrical insulation properties of sputter-deposited SiO_2, Si_3N_4, and Al_2O_3 films at room temperature and 400°C," *Physica Status Solidi A,* vol. 206, no. 3, pp. 514-519, 2009.

10] R. Thayer, "Bismuth zinc niobate films for dielectric applications," M.S. Thesis, The Pennsylvania State University, 2002.

11] M. März, A. Schletz, B. Eckardt, S. Egelkraut and H. Rauh, "Power Electronics System Integration for Electric and Hybrid Vehicles," *2010 6th International Conference on Integrated Power Electronics Systems (CIPS)* , p. 1-10, 2010.

12] E. Karden, S. Ploumen, B. Fricke, T. Miller and K. Snyder, "Energy storage devices for future hybrid electric vehicles," *Journal of Power Sources,* vol. 168, pp. 2-11, 2007.

13] E. K. Michael and S. Trolier-McKinstry, "Amorphous-nanocrystalline lead titanate thin films for dielectric energy storage," *Journal of the Ceramic Society of Japan,* vol. 122, no. 4, p. 250-255, 2014.

14] M. P. Manoharan, C. Zou, E. Furman, N. Zhang, D. I. Kushner, S. Zhang, T. Murata and M. T. Lanagan, "Flexible glass for high temperature energy storage capacitors," *Energy Technology,* vol. 1, pp. 313-318, 2013.

15] Z. Xie, Z. Yue, G. Ruehl, B. Peng, J. Zhang, Q. Yu, X. Zhang and L. Li, "$Bi(Ni_{1/2}Zr_{1/2})O_3$-$PbTiO_3$ relaxor-ferroelectric films for piezoelectric energy harvesting and electrostatic storage," *Applied Physics Letters,* vol. 104, p. 243902, 2014.

16] S. Islam, "Polymer nano-dielectrics for high density energy storage," Ph.D. Thesis, University of South Carolina, 2014.

17] N. H. Fletcher, A. D. Hilton and B. W. Ricketts, "Optimization of energy storage density in ceramic capacitors," *Journal of Physics D: Applied Physics,* vol. 29, p. 253–258, 1996.

18] N. J. Smith, B. Rangarajan, M. T. Lanagan and C. G. Pantano, "Alkali-free glass as a high energy density dielectric material," *Materials Letters,* vol. 63, pp. 1245-1248, 2009.

19] U. Balachandran, M. Narayanan, S. Liu and B. Ma, "Development of film-on-foil ceramic dielectrics for embedded capacitors for power inverters in electric drive vehicles," *Japanese Journal of Applied Physics,* vol. 52, p. 05DA10, 2013.

20] G. Sethi, M. Olszta, J. Li, J. Sloppy, M. W. Horn, E. C. Dickey and M. T. Lanagan, "Structure and dielectric properties of amorphous tantalum pentoxide thin film capacitors," *2007 Annual Report Conference on Electrical Insulation and Dielectric Phenomena,* pp. 815-818, 2007.

21] X. Zhou, X. Zhao, Z. Suo, C. Zou, J. Runt, S. Liu, S. Zhang and Q. M. Zhang, "Electrical breakdown and ultrahigh electrical energy density in poly(vinylidene fluoride-

hexafluoropropylene) copolymer," *Applied Physics Letters,* vol. 94, p. 162901, 2009.

22] M. S. Mirshekarloo, K. Yao and T. Sritharan, "Large strain and high energy storage density in orthorhombic perovskite $(Pb_{0.97}La_{0.02})(Zr_{1-x-y}Sn_xTi_y)O_3$ antiferroelectric thin films," *Applied Physics Letters,* vol. 97, p. 142902, 2010.

23] H. Ogihara, C. A. Randall and S. Trolier-McKinstry, "High-energy density capacitors utilizing $0.7BaTiO_3$–$0.3BiScO_3$ ceramics," *Journal of the American Ceramic Society,* vol. 92, no. 8, pp. 1719-1724, 2009.

24] A. V. Wagner, G. W. Johnson and T. W. Barbee, "High energy density capacitors fabricated by thin film technology," *MRS Proceedings,* vol. 574, p. 219,1999.

25] P. Khanchaitit, K. Han, M. R. Gadinski and Q. Wang, "Ferroelectric polymer networks with high energy density and improved discharged efficiency for dielectric energy storage," *Nature Communications,* vol. 4, p. 2845, 2013.

26] L. A. Fredin, Z. Li, M. T. Lanagan, M. A. Ratner and T. J. Marks, "Substantial recoverable energy storage in percolative metallic aluminum-polypropylene nanocomposites," *Advanced Functional Materials,* vol. 23, no. 28, pp. 3560-3569, 2012.

27] S. Chao and F. Dogan, "Processing and dielectric properties of TiO_2 thick films for high-energy density capacitor applications," *International Journal of Applied Ceramic Technology ,* vol. 8, no. 6, pp. 1363-1373, 2011.

28] J. W. Claude, "Ferroelectric polymers for electrical energy storage," Ph.D Thesis, The Pennsylvania State University, 2008.

Chapter 6

Compositional Tuning of Bismuth Pyrochlores for Dielectric Energy Storage

The bismuth pyrochlores are a compositionally tunable family of materials that possess high breakdown strengths and moderate permittivities, in addition to exhibiting low loss tangents, making them candidates for dielectric energy storage [1]. It was demonstrated in Chapter 5 that bismuth zinc niobate thin films prepared using a Pechini-based solution chemistry possess a 10 kHz energy storage density of approximately 60 J/cm^3. Further improvement in the energy storage density of $Bi_{1.5}Zn_{0.9}Nb_{1.5}O_{6.9}$ would be expected if the breakdown strength of the material could be increased. In this chapter, the compositional tunability of $Bi_{1.5}Zn_{0.9}Nb_{(1.5-x)}Ta_{(x)}O_{6.9}$ thin films was evaluated, particularly with respect to permittivity and breakdown strength, properties that are critical for their use in dielectric energy storage applications.

6.1 Investigation of $Bi_{1.5}Zn_{0.9}Nb_{(1.5-x)}Ta_{(x)}O_{6.9}$ as a Solid Solution

To enhance the breakdown strength of bismuth zinc niobate, it is useful to increase the band gap of the material [2]. Tantalum oxide exhibits a band gap of approximately 4 eV [3], while niobium oxide has a band gap of approximately 3.4 eV [4]. Above its dielectric relaxation, bismuth zinc tantalate has a relative permittivity of approximately 70 and dielectric losses of approximately 0.005 [5, 6, 7]. Thus, the reported permittivity value of bismuth zinc tantalate is about half that of bismuth zinc niobate, while the losses for the two systems are comparable. It is anticipated that the lower polarizability of the tantalate may be compensated by a higher

breakdown strength, enabling improvements in the energy storage density of the deposited thin film. In this section, the formation of the $Bi_{1.5}Zn_{0.9}Nb_{(1.5-x)}Ta_{(x)}O_{6.9}$ solid solution are discussed, along with the dielectric properties of the bismuth zinc tantalate end member.

6.1.1 Phase Identification and Band Gap Analysis

Crystalline $Bi_{1.5}Zn_{0.9}Nb_{(1.5-x)}Ta_{(x)}O_{6.9}$ films were prepared using the method described in Chapter 4. The diffraction patterns of $Bi_{1.5}Zn_{0.9}Nb_{1.5}O_{6.9}$ (BZN), $Bi_{1.5}Zn_{0.9}Nb_{1.425}Ta_{0.075}O_{6.9}$ (BZNT-5), $Bi_{1.5}Zn_{0.9}Nb_{1.35}Ta_{0.15}O_{6.9}$ (BZNT-10), $Bi_{1.5}Zn_{0.9}Nb_{1.275}Ta_{0.225}O_{6.9}$ (BZNT-15), and $Bi_{1.5}Zn_{0.9}Ta_{1.5}O_{6.9}$ (BZT) are shown in Figure 6-1. The diffraction patterns indicate that the films have a cubic pyrochlore structure (PDF # 04-009-5437, 2002); there are no peaks that correspond to the formation of a secondary phase. Bismuth zinc niobate and bismuth zinc tantalate should produce a substitutional solid solution, in accordance with the Hume-Rothery rules [8]. Tantalum and niobium both have an ionic radius of 64 pm [9], an electronegativity of 1.5 and 1.6 [10], respectively, and an oxidation state of +5. In this case, given the similarity between the tantalate and niobate end members, it was not possible to use lattice parameters to assess Vegard's law [11, 12, 13]. High resolution transmission electron microscopy could be used in the future to assess whether there is any preferential ordering of niobium and tantalum.

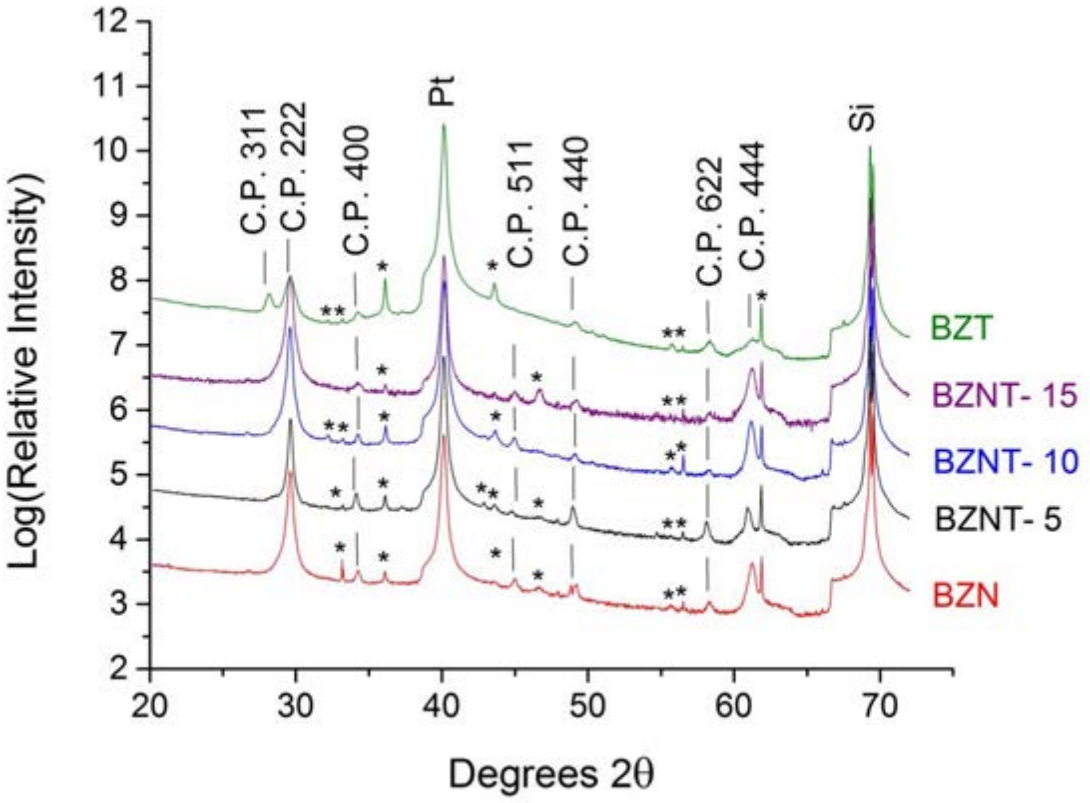

Figure 6-1. X-ray diffraction patterns of $Bi_{1.5}Zn_{0.9}Nb_{1.5}O_{6.9}$ (BZN), $Bi_{1.5}Zn_{0.9}Nb_{1.425}Ta_{0.075}O_{6.9}$ (BZNT-5), $Bi_{1.5}Zn_{0.9}Nb_{1.35}Ta_{0.15}O_{6.9}$ (BZNT-10), $Bi_{1.5}Zn_{0.9}Nb_{1.275}Ta_{0.225}O_{6.9}$ (BZNT-15), and $Bi_{1.5}Zn_{0.9}Ta_{1.5}O_{6.9}$ (BZT) films on platinum-coated silicon. Peaks labelled with the abbreviation *C.P.* correspond to the cubic pyrochlore structure, while peaks labelled with an asterisk (*) are due to the substrate or to diffraction from wavelengths other than Cu Kα.

Figure 6-2 shows the direct band gap Tauc plot [14] of $Bi_{1.5}Zn_{0.9}Nb_{1.5}O_{6.9}$ (dashed line), $Bi_{1.5}Zn_{0.9}Ta_{1.5}O_{6.9}$ (dotted line), and $Bi_{1.5}Zn_{0.9}Nb_{1.35}Ta_{0.15}O_{6.9}$ (solid line) films deposited on magnesium oxide substrates. To ensure that small errors (in the background subtraction or absorbance) due to small differences in film thickness do not perturb the analysis, the maximum absorbance numbers were normalized to the same value. Therefore, the observed shift in absorbance onset was due to a change in band gap. As seen in Figure 6-2, the band gap of

bismuth zinc niobate was 3.72 ± 0.06 eV, while that of bismuth zinc tantalate was 3.88 ± 0.04 eV. The band gap for the solid solution sample shown fell between the magnitudes of the band gaps of the end members. All three compositions exhibited direct band gaps, which is consistent with the type of transition reported for other bismuth-based pyrochlores [15, 16]. The observed shift in band gap was reproducible across the surface of the film, and across multiple films of these compositions.

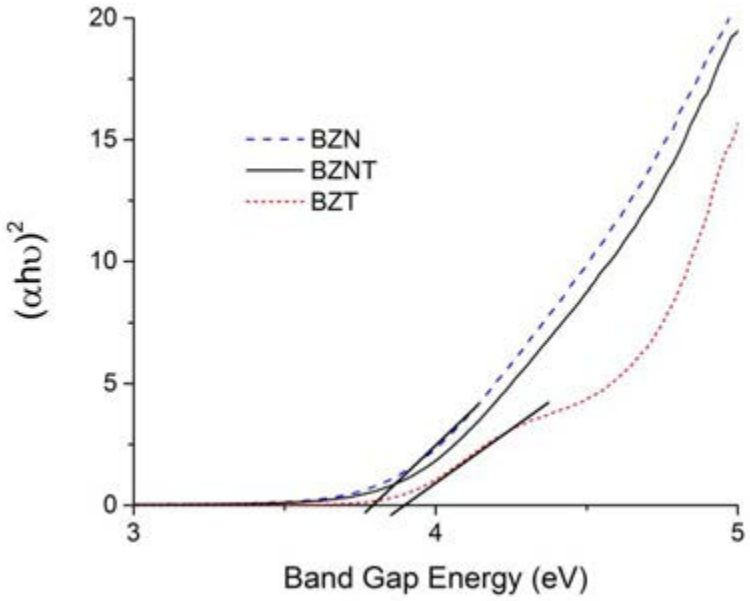

Figure 6-2. The normalized Tauc plots of $Bi_{1.5}Zn_{0.9}Nb_{1.5}O_{6.9}$ (dashed line), $Bi_{1.5}Zn_{0.9}Ta_{1.5}O_{6.9}$ (dotted line), and $Bi_{1.5}Zn_{0.9}Nb_{1.35}Ta_{0.15}O_{6.9}$ (solid line) on a magnesium oxide substrate. The shift in the onset of absorbance indicates that modification with tantalum increased the band gap of the material. The linear fits used to determine the band gap are superimposed over the Tauc plots. The abbreviations on the y-axis are: α, absorption coefficient; h, Planck's constant; v, frequency.

6.1.2 Dielectric Properties of the Bismuth Zinc Tantalate End Member

The low-field properties of bismuth zinc tantalate films are presented, followed by a review of the tunability. Finally, the high-field AC and energy storage properties are discussed to determine whether the increase in band gap due to substitution of the niobium end member for tantalum correlates to an increase in the breakdown strength of the material.

6.1.2.1 Low Field Dielectric Properties of Bismuth Zinc Tantalate

Films of $Bi_{1.5}Zn_{0.9}Ta_{1.5}O_{6.9}$ were deposited on platinized silicon substrates as described in Chapter 4. To facilitate a comparison with the values reported in the literature, the relative permittivity and loss tangent as a function of frequency was measured. It has been demonstrated that bismuth zinc tantalate has a room-temperature permittivity of approximately 70 and dielectric losses of approximately 0.005 [5, 6, 7]. As seen in Figure 6-3, these films of bismuth zinc tantalate exhibited a room-temperature relative permittivity of 55±2 and a loss tangent of 0.0004±0.0001. The measured permittivity value is lower than previously reported values for bulk ceramics, which may be due to small amounts of porosity that exist between the layers of the film. Using a logarithmic dielectric mixing rule, it was determined that the film possessed approximately four to six volume percent porosity to yield this suppressed permittivity value. The loss tangent is approximately an order of magnitude lower than previous reports in the literature [5, 6, 7].

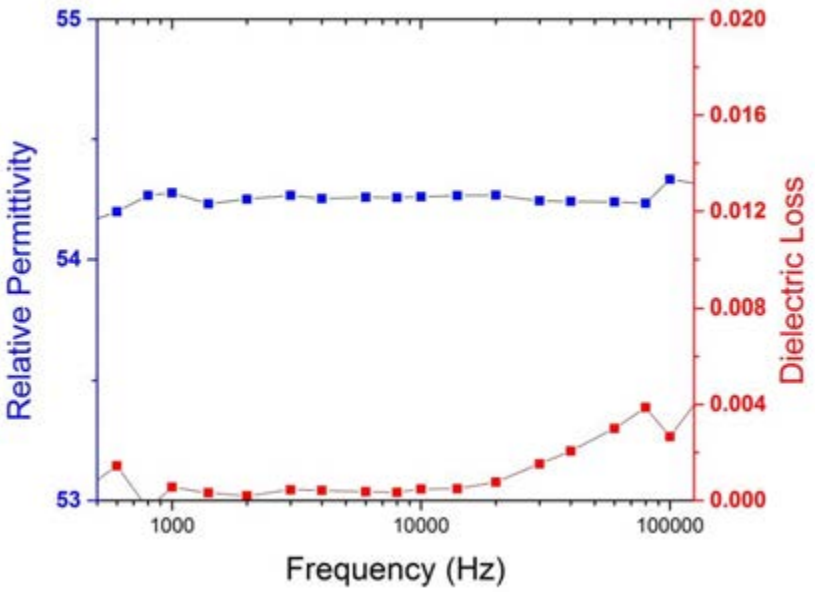

Figure 6-3. The relative permittivity and dielectric loss of thin films of $Bi_{1.5}Zn_{0.9}Ta_{1.5}O_{6.9}$ as a function of frequency.

Figure 6-4 shows the polarization-electric field behavior for the bismuth zinc tantalate films at a measurement frequency of 10 kHz and an AC field of 3 MV/cm. In addition to confirming the permittivity and loss measured using an LCR meter, the hysteresis loop shows that bismuth zinc tantalate is a very weakly nonlinear, low loss dielectric.

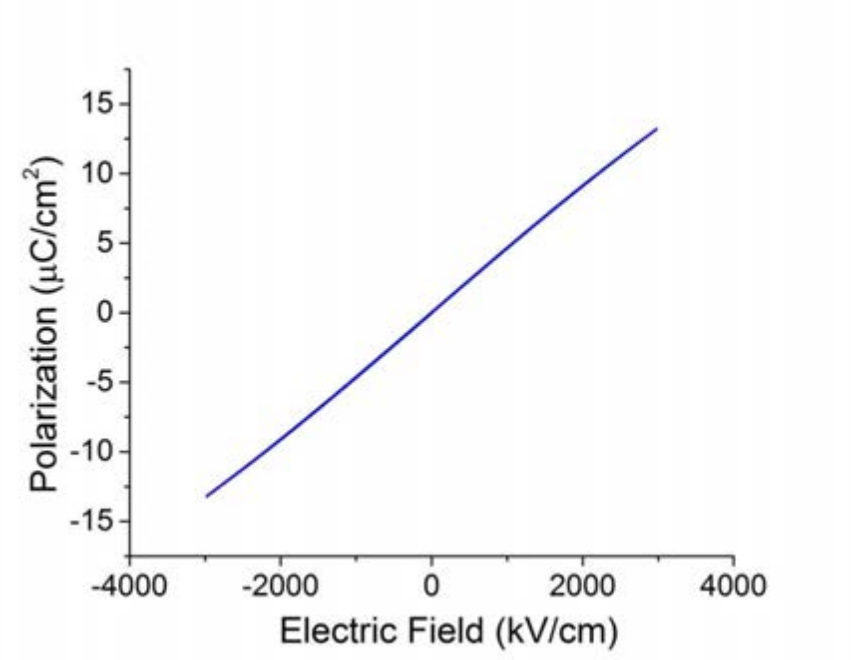

Figure 6-4. The 10 kHz polarization-electric field behavior for bismuth zinc tantalate, $Bi_{1.5}Zn_{0.9}Ta_{1.5}O_{6.9}$; the films are low loss, weakly nonlinear dielectrics.

6.1.2.2 Tunability of Bismuth Zinc Tantalate

The tunability of bismuth zinc tantalate (indicated by squares) and bismuth zinc niobate (indicated by triangles) films under identical field conditions are shown in Figure 6-5. The tunability of the bismuth zinc tantalate film was approximately an order of magnitude lower than that of bismuth zinc niobate. At DC fields of 1.5 MV/cm and an AC oscillation voltage of 0.03 V, bismuth zinc tantalate exhibited a tunability of 4.5%; under identical field and measurement conditions, bismuth zinc niobate exhibited a tunability of 24%. As will be discussed in the next section, the reduction in the tunability of the tantalate composition helped to offset the reduced permittivity values when calculating the energy storage density of the films.

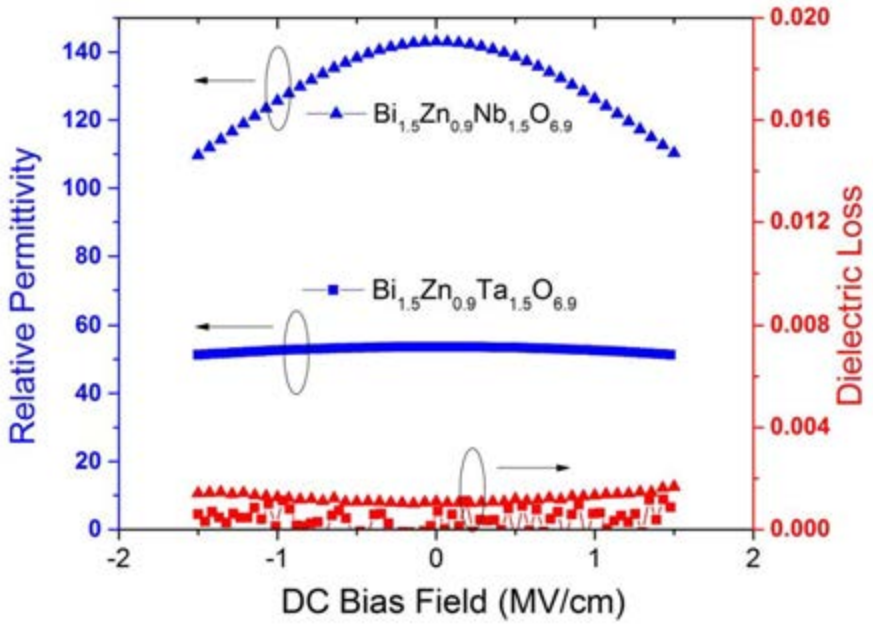

Figure 6-5. The permittivity and loss as a function of DC bias for films of bismuth zinc tantalate (squares) and bismuth zinc niobate (triangles).

6.1.2.3 High Field AC Properties of Bismuth Zinc Tantalate

As anticipated, the breakdown strength of the tantalate films was higher than that of the bismuth zinc niobate films, and the high field loss tangent remained low. Weibull plots were used to determine the breakdown strength of these films. The values of the Weibull parameters are given in Table 6-1. The Weibull parameter for each condition was calculated using a total of ten electrodes. The large Weibull parameter values indicate that the breakdown strengths exhibited little variation from electrode to electrode. As shown in Figure 6-6(a) and listed in Table 6-1, the 1 kHz breakdown strength of this film was 5.5 MV/cm. At 10 kHz, the breakdown strength was 6.1 MV/cm, as seen in Figure 6-6(b). The combination of an improved breakdown strength and lower high field loss correlates well with an increase in the band gap of the material.

Table 6-1. Weibull Parameters for the Breakdown Strength of $Bi_{1.5}Zn_{0.9}Ta_{1.5}O_{6.9}$

	1 kHz	10 kHz
Breakdown Strength (MV/cm)	5.5 ± 0.1	6.1 ± 0.1
Weibull Parameter	34.0 ± 2.4	95.1 ± 6.0

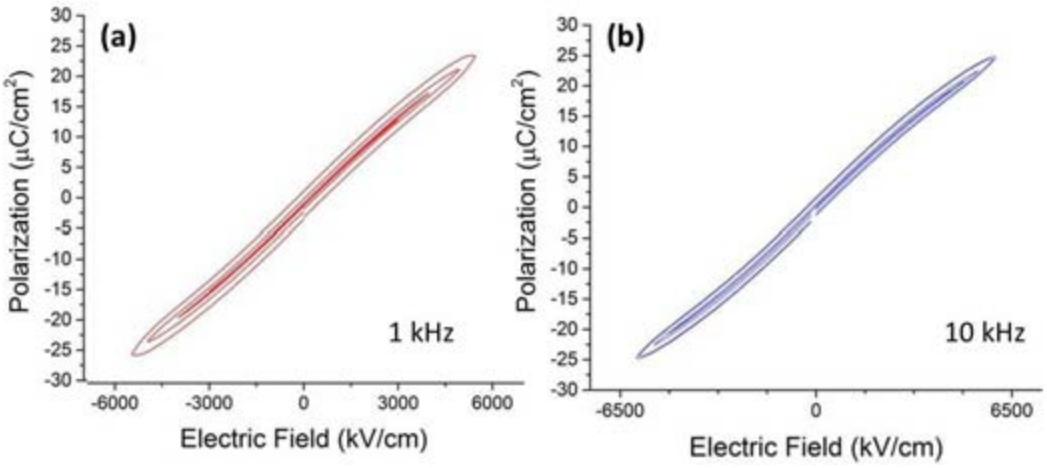

Figure 6-6. The polarization-electric field behavior at (a) 1 kHz and (b) 10 kHz for films of $Bi_{1.5}Zn_{0.9}Ta_{1.5}O_{6.9}$.

The maximum discharged energy storage density for the bismuth zinc tantalate films was 60.7±2.0 J/cm^3 at 10 kHz, which is comparable with the maximum discharged energy storage density of the bismuth zinc niobate films in Chapter 5 [17]. In this case, any improvement in the energy storage density of the tantalate composition due to the enhancement in breakdown strength, reduced tunability, and lower high field loss was offset by the reduction in relative permittivity of the bismuth zinc tantalate. However, some applications require that the loss of the material remain below 2% [18]; for many materials targeting these applications, the maximum energy storage density is limited by the loss of the film, rather than the breakdown strength. It

was found that bismuth zinc tantalate exhibited extremely low high field losses across a range of temperatures and frequencies. As seen in Figure 6-7, for most temperatures and frequencies, the films could be subjected to their maximum field prior to breakdown without the loss tangent exceeding 2%, resulting in extremely high efficiencies for the material.

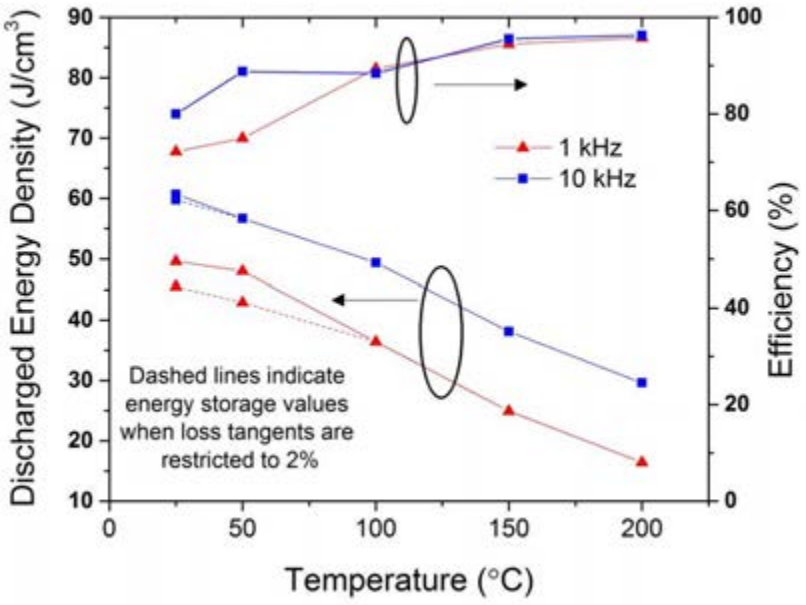

Figure 6-7. The energy storage density and discharge efficiency of $Bi_{1.5}Zn_{0.9}Ta_{1.5}O_{6.9}$. Energy storage density data points connected by solid lines represent the maximum energy storage density of the material, while data points connected by a dashed line represent the energy storage density of $Bi_{1.5}Zn_{0.9}Ta_{1.5}O_{6.9}$ when loss values are required to remain below 2%. For many temperatures and frequencies, these two values are identical.

6.2 Optimization of Energy Storage via Tantalum Modification

To determine if any intermediate tantalum concentrations enhance the energy storage density of the films, the tantalum concentration was varied from zero to fifteen percent. An

overview of the results for each of the compositions are given, followed by a more complete characterization of the optimized composition, $Bi_{1.5}Zn_{0.9}Nb_{1.35}Ta_{0.15}O_{6.9}$.

6.2.1 A Comparison of Bismuth Zinc Niobate Tantalate Compositions

The energy storage density as a function of tantalum concentration was investigated, and the results are summarized in Table 6-2. As the concentration of tantalum increased, the permittivity of the films decreased and the maximum field sustained by the films increased. A concentration of 10% tantalum was determined to be optimal, as the energy storage density was maximized at this tantalum concentration.

Table 6-2. Energy Storage Density of $Bi_{1.5}Zn_{0.9}Nb_{(1.5-x)}Ta_{(x)}O_{6.9}$ as a Function of Tantalum Concentration

	BZN	BZN with 5% Ta	BZN with 10% Ta	BZN with 15% Ta	BZT
Permittivity	145 ± 5	130 ± 5	122 ± 4	108 ± 4	55 ± 2
1 kHz Maximum Field (MV/cm)	4.7	4.9	5.0	5.1	5.5
10 kHz Maximum Field (MV/cm)	5.1	5.4	5.5	5.7	6.1
1 kHz Energy Storage (J/cm^3)	47.1 ± 1.7	46.7 ± 1.6	54.1 ± 1.9	49.6 ± 1.8	49.6 ± 1.7
10 kHz Energy Storage (J/cm^3)	60.8 ± 2.0	61.7 ± 2.2	66.9 ± 2.4	65.0 ± 2.3	60.7 ± 2.0

6.2.2 Dielectric Properties of Optimized Bismuth Zinc Niobate Tantalate

Bismuth zinc niobate tantalate with ten mole percent tantalum was found to have optimized energy storage properties. A more complete characterization of the optimized composition, $Bi_{1.5}Zn_{0.9}Nb_{1.35}Ta_{0.15}O_{6.9}$, is given here.

6.2.2.1 Low Field Dielectric Properties of $Bi_{1.5}Zn_{0.9}Nb_{1.35}Ta_{0.15}O_{6.9}$

The relative permittivity of the optimized film composition is 122 ± 4 and the loss tangent is 0.0008 ± 0.0001. The permittivity of the tantalum-modified film is lower than that of bismuth zinc niobate films prepared in the same manner (~145), while the loss tangents are of the same order of magnitude. The permittivity values of the tantalum-modified films are somewhat lower than predicted values, which may be due, in part, to modest amounts of porosity in the deposited films. Using a linear average between the niobate and tantalate thin film end members, a permittivity of 131 is predicted; film porosity levels, extracted via dielectric mixing rules, predict that an additional two volume percent porosity in the films is required to reduce the permittivity to 122. Figure 6-8 shows the relative permittivity as a function of measurement temperature for the $Bi_{1.5}Zn_{0.9}Nb_{1.35}Ta_{0.15}O_{6.9}$ films. The temperature coefficient of capacitance (TCC) was calculated from this data using the following equation:

$$TCC = \frac{1}{C}\frac{\partial C}{\partial T}$$

where C is the capacitance and T is the temperature. The measured temperature coefficient of capacitance for bismuth zinc niobate tantalate films was -317 ppm/°C. This is reasonable, as the reported temperature coefficient of capacitance for bismuth zinc niobate is approximately -400ppm/°C [19].

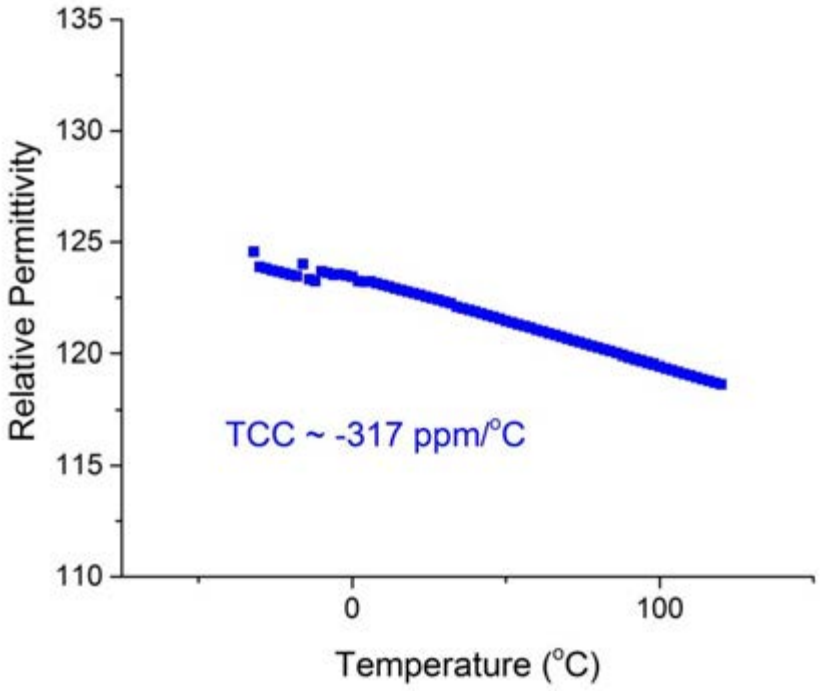

Figure 6-8. Relative permittivity of $Bi_{1.5}Zn_{0.9}Nb_{1.35}Ta_{0.15}O_{6.9}$ as a function of temperature, which was used to calculate the temperature coefficient of capacitance.

6.2.2.2 DC Properties of $Bi_{1.5}Zn_{0.9}Nb_{1.35}Ta_{0.15}O_{6.9}$

Figure 6-9 shows the leakage current density as a function of DC electric field for cubic pyrochlore bismuth zinc niobate tantalate thin films. The leakage current for this material is low, on the order of 10^{-10} A/cm^2 up to fields of 1 MV/cm. The DC breakdown strength in these films, defined as the field at which the material experienced catastrophic electrical breakdown, exhibited a dependence on the area of the sample. For electrodes with a diameter of 200 μm, indicated in Figure 6-9 by open squares, the DC breakdown strength of the material was 3.4 MV/cm. When the diameter of the electrodes was increased to 2 mm, indicated by filled squares in Figure 6-9, the DC breakdown strength of the material was reduced to 2.4 MV/cm. The change in breakdown strength is due to the decreased probability of encountering a critical flaw

when probing a smaller area of a material. These critical defects reduce the maximum electric field that can be placed across the material before it undergoes catastrophic electrical breakdown. The field at which the leakage current for these films of bismuth zinc niobate tantalate surpasses 0.1 μA/cm^2 [20] is 1.5 MV/cm. The energy storage density at this field level is 11.4 ± 0.4 J/cm^3.

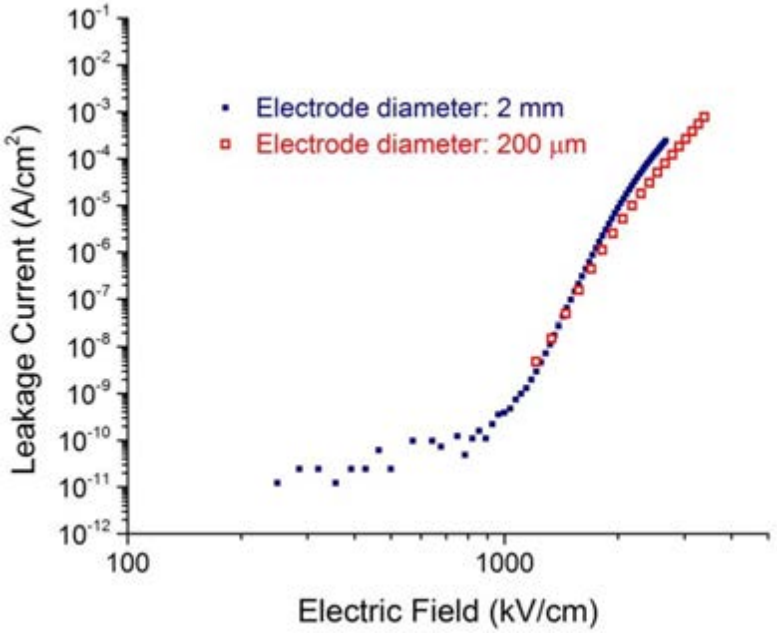

Figure 6-9. The leakage current as a function of DC field for thin films of $Bi_{1.5}Zn_{0.9}Nb_{1.35}Ta_{0.15}O_{6.9}$. When the diameter of the electrodes were 200 μm (open squares), the films had a DC breakdown strength of 3.4 MV/cm; when the diameter of the top electrode was 2 mm (closed squares), the DC breakdown strength was 2.4 MV/cm.

6.2.2.3 High Field AC Properties of $Bi_{1.5}Zn_{0.9}Nb_{1.35}Ta_{0.15}O_{6.9}$

As an example of tantalum modification leading to an enhancement in the energy storage density, Figure 6-10 shows the high-field polarization versus electric field behavior for bismuth zinc niobate with 10% tantalum at a measurement frequency of (a) 1 kHz and (b) 10 kHz; the area used to calculate the energy storage density is shaded. For the optimized composition,

$Bi_{1.5}Zn_{0.9}Nb_{1.35}Ta_{0.15}O_{6.9}$, and a measurement frequency of 10 kHz, the material sustained an electric field of 5.5 MV/cm. At a lower measurement frequency of 1 kHz, the films sustained fields of 5.0 MV/cm. The films reached catastrophic electrical breakdown at applied fields of 5.5 MV/cm at 10 Hz. This breakdown strength exceeds that of the $Bi_{1.5}Zn_{0.9}Nb_{1.5}O_{6.9}$ films in Chapter 5 by approximately 0.3±0.1 MV/cm [17].

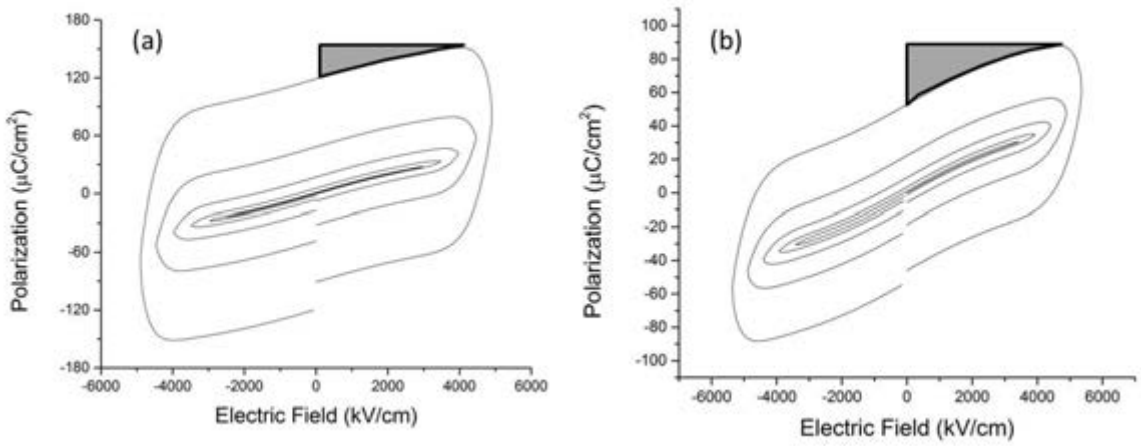

Figure 6-10. The polarization-electric field behavior for films of $Bi_{1.5}Zn_{0.9}Nb_{1.35}Ta_{0.15}O_{6.9}$ at (a) 1 kHz and (b) 10 kHz. The shaded area was used to calculate the energy storage density.

The high breakdown strength of tantalum-modified bismuth zinc niobate contributed to a high energy storage density. Figure 6-11 shows the maximum storage density achieved for the bismuth zinc niobate tantalate films as a function of temperature and measurement frequency; these data points are connected by a solid line. These large energy storage densities indicate that bismuth zinc niobate tantalate may be suitable for dielectric energy storage, particularly in pulsed power applications. The maximum energy storage density was ~66.9±2.4 J/cm^3 for measurement frequencies of 10 kHz, while for a measurement frequency of 1 kHz, the maximum recoverable energy density was ~54.1±1.9 J/cm^3. The dashed lines in Figure 6-11 show the energy storage

density of the bismuth zinc niobate tantalate films recalculated with the maximum fields reduced to keep the high field loss tangent below 0.02. Although the energy storage densities under these loss conditions are reduced, the energy storage values are still high for all measurement frequencies.

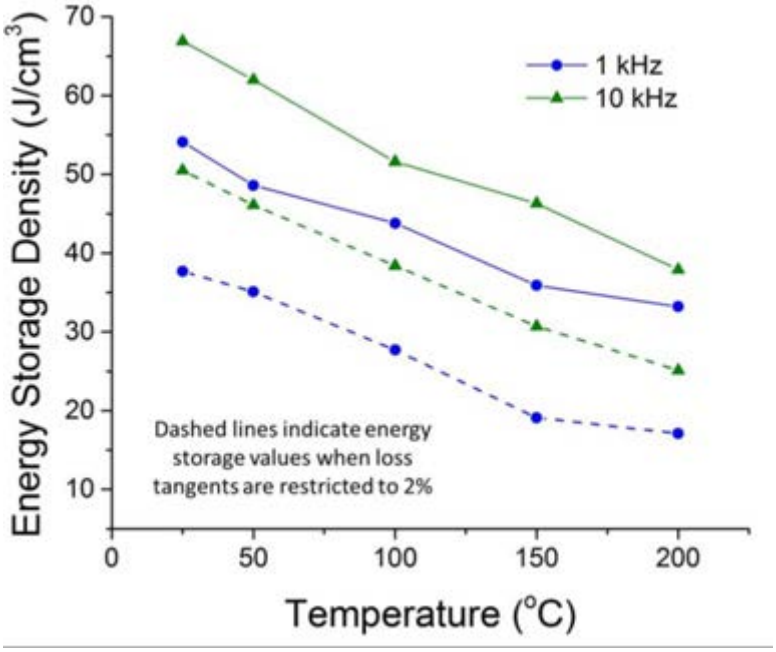

Figure 6-11. The energy storage density of $Bi_{1.5}Zn_{0.9}Nb_{1.35}Ta_{0.15}O_{6.9}$. Data points connected by solid lines represent the maximum energy storage density of the material, while data points connected by a dashed line show the energy storage density of $Bi_{1.5}Zn_{0.9}Nb_{1.35}Ta_{0.15}O_{6.9}$ when loss values are required to remain below 2%.

As the temperature was increased, the maximum discharged energy storage density of the films remained high, and exceeded 20 J/cm^3 at 200°C. This is comparable to the maximum energy storage density reported for BZN films and borosilicate glass at 200°C [17]. The reduction in the energy density of bismuth zinc niobate tantalate at elevated temperatures was due to a decrease in the breakdown strength, as well as an increase in the loss tangent, of the material

at higher temperatures. As an example, at 200°C and a measurement frequency of 10 kHz, the breakdown field of the material was reduced to 4.0 MV/cm.

The maximum delivered power density for a linear dielectric is related to the energy storage density using the following equation:

$$P = \frac{\pi f J}{tan\delta}$$

in which P is the maximum power density, f is the measurement frequency, and $tan\delta$ is the loss tangent for the electric field at which J, the energy storage density, is calculated. The power densities for bismuth zinc niobate tantalate are listed in Table 6-3.

Table 6-3. Power Storage Density of $Bi_{1.5}Zn_{0.9}Nb_{1.35}Ta_{0.15}O_{6.9}$

Temperature (°C)	Power Storage Density at 10 kHz (MW/cm^3)	Power Storage Density at 1 kHz (MW/cm^3)
25	850 ± 35	45 ± 2
50	720 ± 30	40 ± 2
100	710 ± 30	25 ± 1
150	700 ± 30	8 ± 0.5
200	530 ± 20	3 ± 0.5

Despite the decrease in the relative permittivity of bismuth zinc niobate upon modification with tantalum, the energy storage density of the material was improved due to the increase in the breakdown strength achieved by compositionally tuning the band gap. High energy storage density values are maintained at elevated temperatures up to 200°C.

6.2.2.4 Linking the Microstructure and Dielectric Properties of $Bi_{1.5}Zn_{0.9}Nb_{1.35}Ta_{0.15}O_{6.9}$

The high breakdown strengths for these films were attributable, at least in part, to a fine-grained microstructure. As seen in Figure 6-12(a) and described in Chapter 4, the films exhibited small grains that were approximately 27 nm in lateral size and 35 nm through the film thickness. In dielectric energy storage applications, smaller grains may be advantageous. Grain boundaries in oxide thin films are often resistive [21, 22, 23]; thus, the presence of many grain boundaries likely impedes conduction through the film, increasing breakdown strength. Impedance spectroscopy measurements revealed that the grain boundaries in these bismuth pyrochlore films had a much higher resistivity than the interior of the grains. Figure 6-12(b) shows the impedance spectra of a $Bi_{1.5}Zn_{0.9}Nb_{1.35}Ta_{0.15}O_{6.9}$ film measured from 180°C to 200°C. The spectra show two overlapping semicircles indicative of grain and grain boundary resistances [24, 25]. The modeled resistivity values for the grain boundary and grain interior are given in Table 6-4. The corresponding conductivities exhibited Arrhenius behavior, as shown in Figure 6-12(c), allowing for the activation energies to be calculated. The activation energy for the interior of the grain was 0.20 ± 0.002 eV, while the activation energy for grain boundary conduction was 1.12 ± 0.003 eV. The resistivity values for the grain boundary are two orders of magnitude higher than the resistivity values for the grain interior, confirming that resistive grain boundaries likely impede conduction through the film, contributing to the high breakdown strengths observed here.

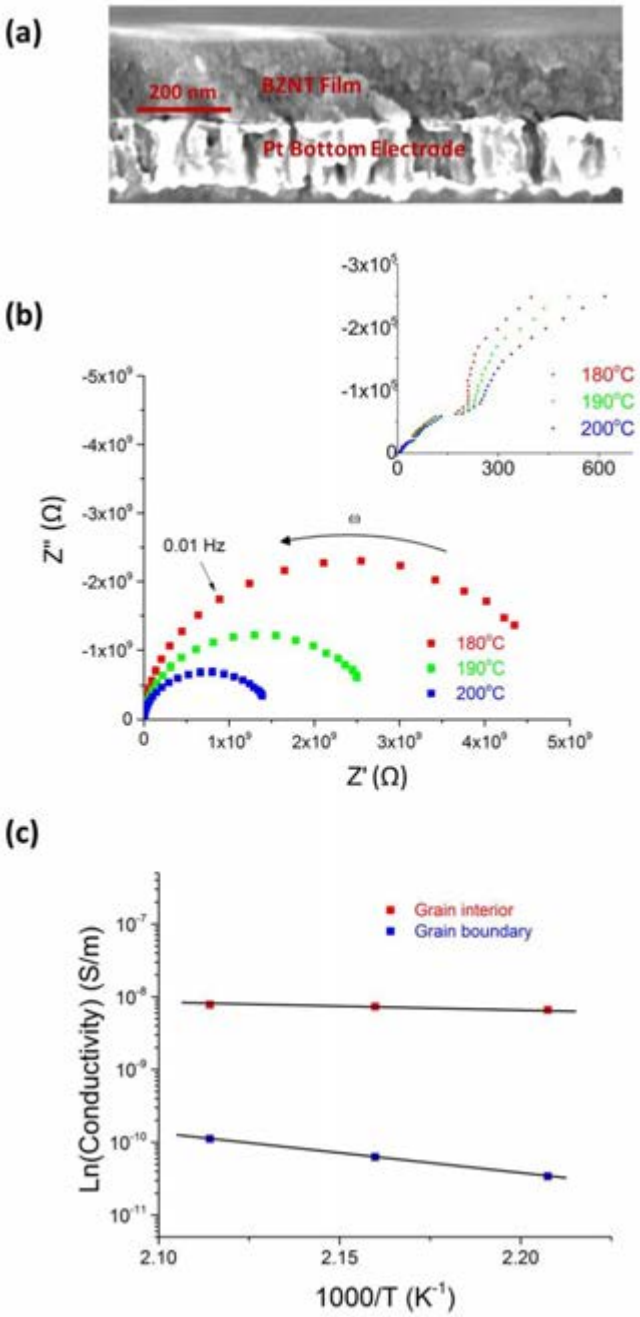

Figure 6-12. (a) SEM cross section of the $Bi_{1.5}Zn_{0.9}Nb_{1.35}Ta_{0.15}O_{6.9}$ film used for impedance spectroscopy. (b)The impedance spectra of the $Bi_{1.5}Zn_{0.9}Nb_{1.35}Ta_{0.15}O_{6.9}$ film measured from 180°C to 200°C. (c) The Arrhenius plot for the $Bi_{1.5}Zn_{0.9}Nb_{1.35}Ta_{0.15}O_{6.9}$ film used to extract activation energies for conduction.

Table 6-4. Resistivity Values of $Bi_{1.5}Zn_{0.9}Nb_{1.35}Ta_{0.15}O_{6.9}$ Films

Temperature (°C)	Resistivity of the Grain Boundaries (Ω*m)	Resistivity of the Grain Interior (Ω*m)
180	$2.90*10^{10} \pm 1.6*10^{8}$	$1.83*10^{8} \pm 6.9*10^{6}$
190	$1.56*10^{10} \pm 9.3*10^{7}$	$1.63*10^{8} \pm 1.7*10^{7}$
200	$8.67*10^{9} \pm 5.2*10^{7}$	$1.40*10^{8} \pm 2.6*10^{7}$

To confirm that the microstructure had a critical role in influencing the high resistivity of the films, films with a quasi-columnar microstructure were deposited on platinized silicon substrates. The columnar microstructure was intended to reduce the number of grain boundaries that would be encountered by charge moving through the thickness of the film. It was hypothesized that such a microstructure would decrease the overall resistivity of the material by reducing the number of high-resistivity grain boundaries, decreasing the breakdown strength of the film. To change the grain structure, very thin layers of material were deposited during each step to inhibit the formation of the block-like grains exhibited by other films. To deposit thin layers, a solution was prepared, as described in Chapter 4, with a molarity of 0.075 M (the films in this work were typically prepared from solutions with a molarity of 0.15 M). To produce a film with a sufficient thickness, eight layers were deposited to yield a final film thickness of 95 nm. The microstructure of the films prepared using the solution with a concentration of 0.075 M is shown in Figure 6-13. These micrographs indicate that the films are quite dense, with a mostly columnar microstructure; however, the presence of grain boundaries parallel to the film-electrode interface can be seen. Due to the resolution limitations of the scanning electron microscope used in this study, transmission electron microscopy should be used to quantify the density of grain boundaries that may impede conduction through the film.

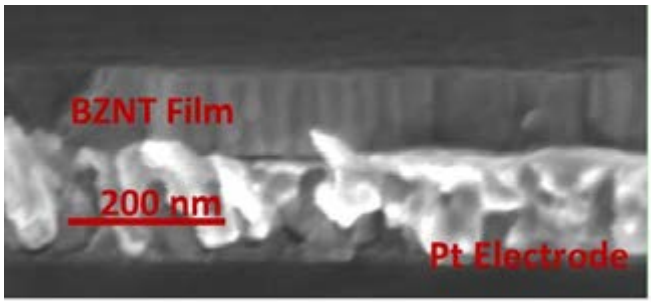

Figure 6-13. The microstructure of $Bi_{1.5}Zn_{0.9}Nb_{1.35}Ta_{0.15}O_{6.9}$ films deposited using a solution with a concentration of 0.075M. These films exhibited a dense quasi-columnar microstructure.

Impedance spectroscopy of this film, shown in Figure 6-14(a), indicated that there is a significant decrease in the resistivity of the film that is attributed to grain boundary contributions, as evidenced by the smaller low frequency semicircle. The high frequency semicircle, shown in the inset of Figure 6-14(a), which captures the grain interior contributions, remains unchanged despite alterations to the microstructure. Table 6-5 summarizes the modeled resistivity values as a function of temperature for the grain boundaries of this film. It can be seen that the resistivity of the grain boundaries at each temperature is somewhat lower than those of the fine-grained microstructure. The corresponding conductivities exhibited Arrhenius behavior, as shown in Figure 6-14(b), allowing for the activation energies to be calculated. The activation energy for the interior of the grain was 0.19 ± 0.02 eV, while the activation energy for grain boundary conduction was 1.40 ± 0.07 eV.

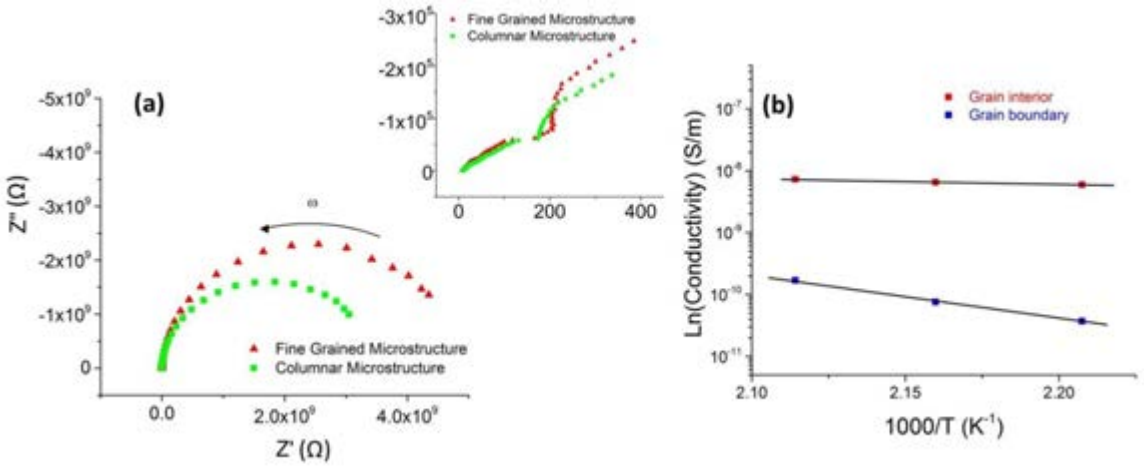

Figure 6-14. (a)The impedance spectra of $Bi_{1.5}Zn_{0.9}Nb_{1.35}Ta_{0.15}O_{6.9}$ films with a columnar (green squares) and fine-grained (red triangles) microstructures measured at 180°C. (b) The Arrhenius plot for the columnar $Bi_{1.5}Zn_{0.9}Nb_{1.35}Ta_{0.15}O_{6.9}$ film used to extract activation energies for conduction.

Table 6-5. Resistivity Values of Columnar $Bi_{1.5}Zn_{0.9}Nb_{1.35}Ta_{0.15}O_{6.9}$ Films

Temperature (°C)	Resistivity of the Grain Boundaries (Ω*m)
180	$2.70*10^{10} \pm 1.2*10^{8}$
190	$1.32*10^{10} \pm 7.1*10^{7}$
200	$5.91*10^{9} \pm 2.9*10^{7}$

To correlate the decrease in resistivity with the dielectric properties of the $Bi_{1.5}Zn_{0.9}Nb_{1.35}Ta_{0.15}O_{6.9}$ film with a columnar microstructure, capacitance and loss as a function of frequency and polarization-electric field behavior was measured. Figure 6-15(a) shows the permittivity and loss as a function of frequency for the films. The permittivity for the film was approximately 131 ± 4, which is consistent with the predicted permittivity value, and the dielectric loss was approximately 0.0005 ± 0.0001. These improved permittivity values are due

to the improvement in the density of the columnar films as well as the absence of low permittivity grain boundaries in the material. The polarization-electric field behavior shown in Figure 6-15(b) and (c) confirm that the reduction of the grain boundary contribution to the resistivity of the film decreased the breakdown strength of the films. At 1 kHz (part b), the breakdown strength of the film was 4.1 MV/cm, while the 10 kHz breakdown (part c) was 4.6 MV/cm. Therefore, it was concluded that the presence of grain boundaries parallel to the film electrodes impedes conduction through the material, enhancing the breakdown strength and the maximum energy storage density of the films. The maximum room-temperature energy storage density of the columnar films was 44.9 ± 1.3 J/cm^3 at 1 kHz and 55.7 ± 1.7 J/cm^3 at 10 kHz, while the discharged energy storage density under 2% loss restrictions was 35.8 ± 1.0 J/cm^3 at 1 kHz and 46.2 ± 1.3 J/cm^3 at 10 kHz.

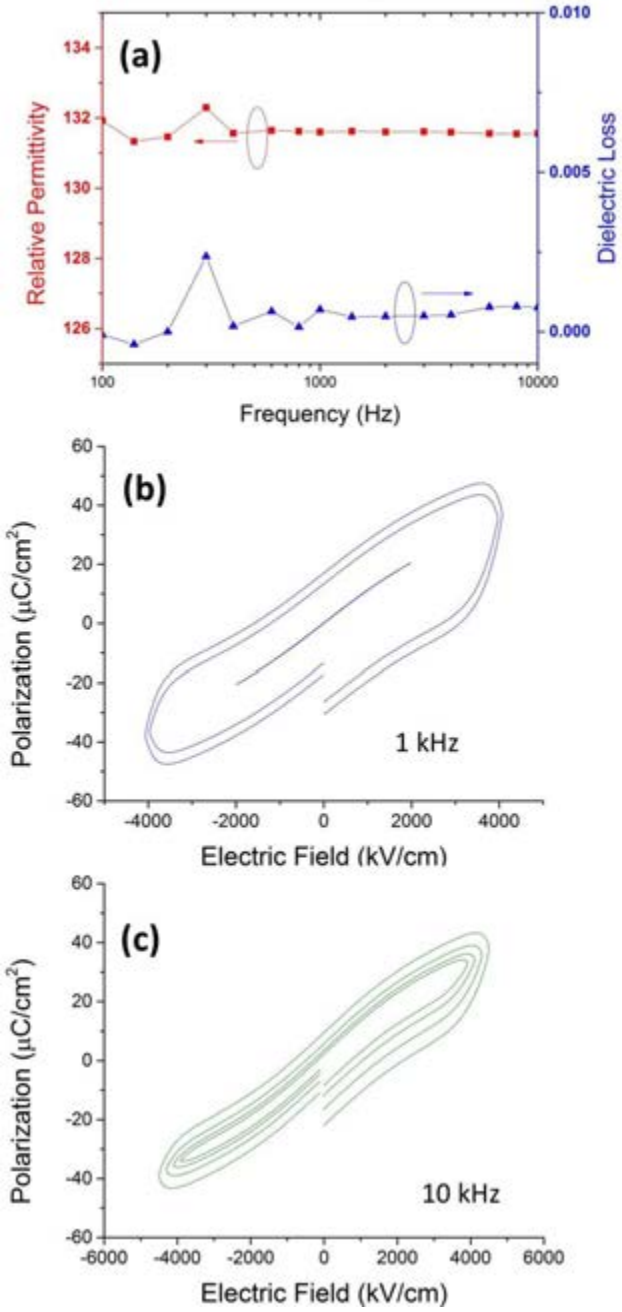

Figure 6-15. (a) The permittivity and loss as a function of frequency for films of $Bi_{1.5}Zn_{0.9}Nb_{1.35}Ta_{0.15}O_{6.9}$ with a columnar microstructure. The more columnar microstructure reduced the breakdown strength of the films, as seen in the polarization-electric field behavior at (b) 1 kHz and (c) 10 kHz.

6.3 Doping Bismuth Zinc Niobate Tantalate

Increases in the energy storage density of the optimized bismuth zinc niobate tantalate films could be achieved through the minimization of the high field loss tangent. Several approaches were explored to decrease the high field loss exhibited by the films, with limited success. In an attempt to decrease the high field loss, films of bismuth zinc niobate tantalate were acceptor doped with manganese on the niobium site or donor doped with titanium on the zinc site. In addition, films were doped with silicon to determine if it was possible to further increase the breakdown strength by improving the insulation resistance of the grain boundaries. The results of each of these doping experiments are discussed in this section.

6.3.1 Acceptor Doping with Manganese on the Niobium Site

As demonstrated in section 6.2.2.4, the grain boundaries in these films of bismuth zinc niobate tantalate were quite resistive. It has been demonstrated that oxide dielectrics often possess oxidized, resistive grain boundaries; the minimization of oxygen vacancies in the material produces these higher resistivity values [21, 22, 23]. If it can be assumed that oxygen vacancies are not the dominant defect present in these films, it is possible that metal vacancies dominate conduction [26]. Bismuth, and particularly zinc, are volatile elements, making it plausible that either bismuth or zinc vacancies exist in the material [27, 28, 29]. As shown in the following defect equation for the formation of an electronically compensated zinc vacancy, metal vacancies are compensated by holes:

$$Zn_{Zn}^{x} \rightarrow V_{Zn}'' + 2h^{\cdot} + Zn \uparrow$$

It may be possible to minimize the number of holes available for conduction through the film by introducing acceptor sites into the material. To test this hypothesis, bismuth zinc niobate tantalate films were doped with manganese on the niobium site (Mn'''_{Nb}).

The films of $Bi_{1.5}Zn_{0.9}Nb_{1.335}Mn_{0.015}Ta_{0.15}O_{6.9}$ exhibited a permittivity of approximately 134±4 and low dielectric losses, as shown in Figure 6-16(a). As seen in Figure 6-16(b) and (c), the breakdown strength for these films was reduced to values below those of the undoped films. At 1 kHz, the films exhibited a breakdown strength of 2.7 MV/cm, and at 10 kHz, the films exhibited a breakdown strength of 3.0 MV/cm.

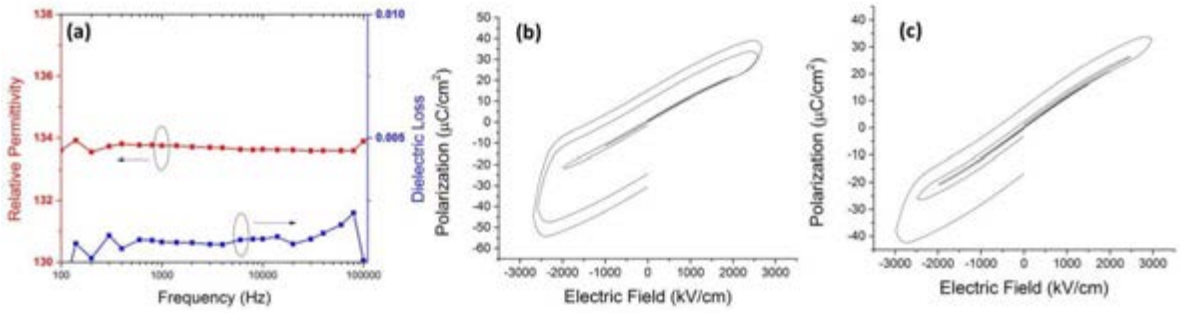

Figure 6-16. The (a) relative permittivity, (b) 1 kHz polarization-electric field behavior, and (c) 10 kHz polarization-electric field behavior for films of $Bi_{1.5}Zn_{0.9}Nb_{1.335}Mn_{0.015}Ta_{0.15}O_{6.9}$.

6.3.2 Donor Doping with Titanium on the Zinc Site

Donor doping was also attempted to minimize high field loss in the film. If metal vacancies are not the dominant defect in a metal oxide dielectric, it is possible that oxygen vacancies dominate conduction [26]. The following defect equation for the formation of an oxygen vacancy demonstrates that these vacancies can be electronically compensated by electrons:

$$O_O^x \rightarrow \frac{1}{2}O_2 + V_O^{\cdot\cdot} + 2e'$$

If the material is compensated electronically, it may be possible to minimize conduction through the film by introducing donors into the material.

Films of bismuth zinc niobate tantalate were doped with 1% and 2% titanium on the zinc site ($Ti_{Zn}^{\cdot\cdot}$). Both films yielded similar results; the results for 2% titanium doped films, $Bi_{1.5}Zn_{0.882}Ti_{0.18}Nb_{1.5}Ta_{0.15}O_{6.9}$, will be presented here. The films of $Bi_{1.5}Zn_{0.882}Ti_{0.018}Nb_{1.5}Ta_{0.15}O_{6.9}$ exhibited a permittivity of approximately 117±4 and low dielectric losses, as shown in Figure 6-17(a). Figure 6-17(b) and (c) show that the breakdown strength for these films was reduced to values below those of the undoped films. At 1 kHz, the films exhibited a breakdown strength of 4.1 MV/cm, and at 10 kHz, the films exhibited a breakdown strength of 4.5 MV/cm.

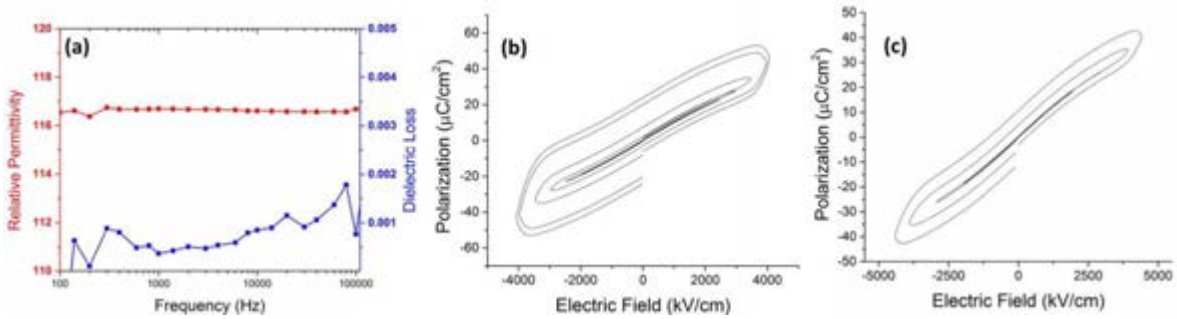

Figure 6-17. The (a) relative permittivity, (b) 1 kHz polarization-electric field behavior, and (c) 10 kHz polarization-electric field behavior for films of $Bi_{1.5}Zn_{0.882}Ti_{0.18}Nb_{1.5}Ta_{0.15}O_{6.9}$.

Impedance spectroscopy of these films and the acceptor doped films discussed in section 6.3.1 showed no change in the resistivity of the high-frequency semicircle that captures the grain interior contribution to the conductivity. Thus, it is likely that the dopants in these films segregated to the grain boundaries. Titanium dioxide has a band gap of 3.2 eV [30], while manganese dioxide has a band gap of 1.3 eV [31]; it is possible that these low band gap dopants

increased conduction through the grain boundaries of the film, resulting in the reduced breakdown strengths measured here. In the future, doping experiments, such as varying the dopant concentration, should be further explored.

6.3.3 Grain Boundary Doping with Silicon

In an attempt to engineer the segregation of dopants to the grain boundaries of the material, films of bismuth zinc niobate tantalate were doped with silicon. Silicon dioxide has a band gap of 8.7 eV [32], and would not be expected to substitute well into the pyrochlore structure. Thus, the goal was to have the silicon segregate to the grain boundaries to improve the breakdown strength of the films. Impedance spectroscopy indicated that the resistivity of the $Bi_{1.5}Zn_{0.9}Nb_{1.32}Si_{0.03}Ta_{0.15}O_{6.9}$ films increased somewhat, which correlated with an increase in the breakdown strength of the films, as seen in Figure 6-18(b) and (c). At 1 kHz, the breakdown strength of the films was 5.2 MV/cm (0.2 MV/cm higher than the undoped composition), and at 10 kHz, the breakdown strength of the films was 5.6 MV/cm (0.1 MV/cm higher than the undoped composition). Due to the low polarizability of the silicon, the permittivity of the films was reduced to 114 ± 4 and the loss tangents were unaffected, as seen in Figure 6-18(a). The 1 kHz energy storage density of the film was 56.0 ± 2.0 J/cm^3 and a 10 kHz energy density was 67.9 ± 3.5 J/cm^3. These values do not present an improvement in the energy storage density for the material, as they are within the error bars for the energy storage density of the undoped bismuth zinc niobate tantalate films.

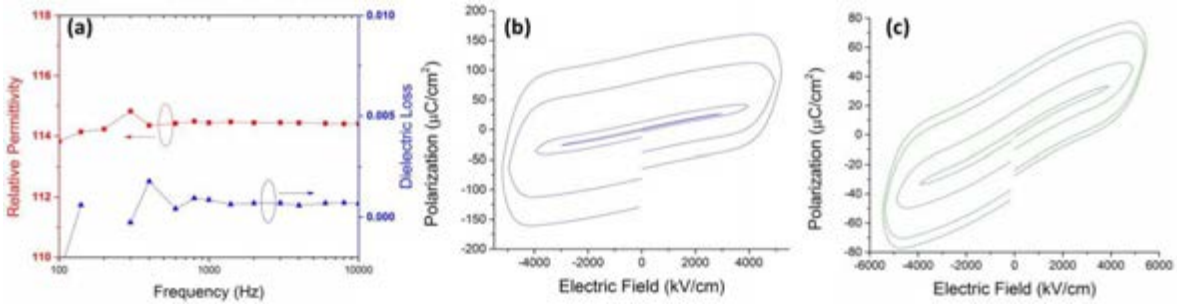

Figure 6-18. The (a) relative permittivity, (b) 1 kHz polarization-electric field behavior, and (c) 10 kHz polarization-electric field behavior for films of $Bi_{1.5}Zn_{0.9}Nb_{1.32}Si_{0.03}Ta_{0.15}O_{6.9}$.

6.4 Conclusions

Compositional tuning of bismuth zinc niobate with tantalum was pursued as a method to increase the band gap, and, consequently the breakdown strength, of this substitutional solid solution for energy storage applications. This family of materials exhibited moderate relative permittivities of between 55±2 and 145±5, for bismuth zinc tantalate and bismuth zinc niobate, respectively, and low loss tangents on the order of 0.0008. Increases in the tantalum concentration of the solid solution increased the dielectric breakdown strength. At an optimal tantalum concentration of ten mole percent, the maximum field sustained by the films at 10 kHz was 5.5 MV/cm, and the permittivity was 122. This improvement in the breakdown strength compensated for the reduction in the relative permittivity of material, which led to a high discharged energy storage density. At a measurement frequency of 10 kHz, the $Bi_{1.5}Zn_{0.9}Nb_{1.35}Ta_{0.15}O_{6.9}$ films exhibited a maximum recoverable energy storage density of 66.9 ± 2.4 J/cm^3, and at 1 kHz, the recoverable energy storage density was 54.1 ± 1.9 J/cm^3.

6.5 References

1] M. A. Subramanian, G. Aravamudan and G. V. Subba Rao, "Oxide pyrochlores- A review," *Progress in Solid State Chemistry,* vol. 15, no. 2, pp. 55-143, 1983.

2] A. Yoshikawa, H. Matsunami and Y. Nanishi, "Development and Applications of Wide Bandgap Semiconductors," in *Wide bandgap semiconductors: Fundamental properties and modern photonic and electronic devices*, Heidelberg, NY, Springer, 2007, pp. 1-23.

3] E. Franke, C. L. Trimble, M. J. DeVries, J. A. Woollam, M. Schubert and F. Frost, "Dielectric function of amorphous tantalum oxide from the far infrared to the deep ultraviolet spectral region measured by spectroscopic ellipsometry," *Journal of Applied Physics,* vol. 88, no. 9, pp. 5166-5174, 2000.

4] K. Yoshimura, T. Miki, S. Iwama and S. Tanemura, "Characterization of niobium oxide electrochromic thin films prepared by reactive d.c. magnetron sputtering," *Thin Solid Films,* vols. 281-282, pp. 235-238, 1996.

5] D. P. Cann, C. A. Randall and T. R. Shrout, "Investigation of the dielectric properties of bismuth pyrochlores," *Solid State Communications,* vol. 100, no. 7, pp. 529-534, 1996.

6] H.-J. Youn, C. Randall, A. Chen, T. Shrout and M. T. Lanagan, "Dielectric relaxation and microwave dielectric properties of Bi_2O_3–ZnO–Ta_2O_5 ceramics," *Journal of Materials Research,* vol. 17, no. 6, pp. 1502-1506, 2002.

7] H.-J. Youn, T. Sogabe, C. A. Randall, T. R. Shrout and M. T. Lanagan, "Phase relations and dielectric properties in the Bi_2O_3–ZnO–Ta_2O_5 system," *Journal of the American Ceramic Society,* vol. 84, no. 11, pp. 2557-2562, 2001.

8] W. D. Callister and D. G. Rethwisch, Materials Science and Engineering, Hoboken, NJ: John Wiley & Sons, Inc., 2011.

9] R. D. Shannon, "Revised effective ionic radii and systematic studies of interatomic distances in halides and chalcogenides," *Acta Crystallographica Section A,* vol. 32, no. 5, pp. 751-767, 1976.

10] L. Pauling, The Nature of the Chemical Bond, Ithaca, NY: Cornell University Press, 1960.

11] I. Levin, T. G. Amos, J. C. Nino, T. A. Vanderah, I. M. Reaney, C. A. Randall and M. T. Lanagan, "Crystal structure of the compound $Bi_2Zn_{2/3}Nb_{4/3}O_7$," *Journal of Materials Research,* vol. 17, no. 6, pp. 1406-1411, 2002.

12] C. C. Khaw, K. B. Tan, C. K. Lee and A. R. West, "Phase equilibria and electrical properties of pyrochlore and zirconolite phases in the Bi_2O_3–ZnO–Ta_2O_5 system," *Journal of the European Ceramic Society,* vol. 32, pp. 671-680, 2012.

13] I. Levin, T. G. Amos, J. C. Nino, T. A. Vanderah, C. A. Randall and M. T. Lanagan, "Structural study of an unusual cubic pyrochlore $Bi_{1.5}Zn_{0.92}Nb_{1.5}O_{6.92}$," *Journal of Solid State Chemistry,* vol. 168, no. 1, pp. 69-75, 2002.

14] J. Pankove, Optical Processes in Semiconductors, Mineola, NY: Courier Dover Publications, 1971.

15] S. M. Zanetti, S. A. da Silva and G. P. Thim, "A chemical route for the synthesis of cubic bismuth zinc niobate pyrochlore nanopowders," *Journal of Solid State Chemistry,* vol. 177, pp. 4546-4551, 2004.

16] G. Perenlei, P. C. Talbot and W. N. Martens, "Sol-gel synthesis and characterization of cubic bismuth zinc niobium oxide nanopowders," *Journal of Nanomaterials,* vol. 2014, p. 695973, 2014.

17] E. K. Michael and S. Trolier-McKinstry, "Cubic pyrochlore bismuth zinc niobate thin films for high-temperature dielectric energy storage," *Journal of the American Ceramic Society,* vol. 98, no. 4, p. 1223-1229, 2015.

18] S. Islam, "Polymer nano-dielectrics for high density energy storage," Ph.D. Thesis, University of South Carolina, 2014.

19] R. L. Thayer, C. A. Randall and S. Trolier-McKinstry, "Medium permittivity bismuth zinc niobate thin film capacitors," *Journal of Applied Physics,* vol. 94, no. 3, pp. 1941-1947, 2003.

20] H. Bartzsch, D. Gloβ, P. Frach, M. Gittner, E. Schultheiβ, W. Brode, and J. Hartung, "Electrical insulation properties of sputter-deposited SiO_2, Si_3N_4, and Al_2O_3 films at room temperature and 400°C," *Physica Status Solidi A,* vol. 206, no. 3, pp. 514-519, 2009.

21] R. E. Newnham, "Electroceramics," *Reports on Progress in Physics,* vol. 52, pp. 123-156, 1989.

22] T. K. Gupta, "Application of zinc oxide varistors," *Journal of the American Ceramic Society,* vol. 73, no. 7, pp. 1817-1840, 1990.

23] J. Liebault, J. Vallayer, D. Goeuriot, D. Treheux and F. Thevenot, "How the trapping of charges can explain the dielectric breakdown performance of alumina ceramics," *Journal of the European Ceramic Society,* vol. 21, no. 3, pp. 389-397, 2001.

24] E. Barsoukov and J. R. Macdonald, Impedance Spectroscopy: Theory, Experiment, and Applications, Hoboken, NJ: John Wiley & Sons, Inc., 2005.

25] J. T. Irvine, D. T. Sinclair and A. R. West, "Electroceramics: Characterization by impedance spectroscopy," *Advanced Materials,* vol. 2, no. 3, pp. 132-138, 1990.

26] A. J. Moulson and J. M. Herbert, Electroceramics: Materials, Properties, Applications, West Sussex, England: John Wiley & Sons, Ltd, 2003.

K. B. Tan, C. K. Lee, Z. Zainal, G. C. Miles and A. R. West, "Stoichiometry and doping
27] mechanism of the cubic pyrochlore phase in the system Bi_2O_3–ZnO–Nb_2O_5," *Journal of Materials Chemistry,* vol. 15, pp. 3501-3506, 2005.

X. Zhang, W. Ren, P. Shi, X. Wu, X. Chen and X. Yao, "Structures and dielectric properties
28] of pyrochlore bismuth zinc niobate thin films with zinc compensation," *Journal of Alloys and Compounds,* vol. 553, pp. 8-13, 2013.

J. Lu, Z. Chen, T. R. Taylor and S. Stemmer, "Composition control and dielectric properties
29] of bismuth zinc niobate thin films synthesized by radio-frequency magnetron sputtering," *Journal of Vacuum Science & Technology A,* vol. 21, no. 5, pp. 1745-1751, 2003.

K. M. Reddy, S. V. Manorama and A. R. Reddy, "Bandgap studies on anatase titanium
30] dioxide nanoparticles," *Materials Chemistry and Physics,* vol. 78, no. 1, p. 239–245, 2003.

S. E. LeBlanc and H. S. Fogler, "The role of conduction/valence bands and redox potential
31] in accelerated mineral dissolution," *American Institute of Chemical Engineers Journal,* vol. 32, no. 10, pp. 1702-1709, 1986.

S. S. Nekrashevich and V. A. Gritsenko, "Electronic structure of silicon dioxide (A review),"
32] *Physics of the Solid State,* vol. 56, no. 2, pp. 207-222, 2014.

Chapter 7

Nanocomposite Bismuth Zinc Niobate Tantalate for Flexible Energy Storage Applications

The dielectric energy storage characteristics of optimized crystalline bismuth zinc niobate tantalate films were described in Chapter 6. These films were processed at a maximum temperature of 600°C, limiting possible substrates to materials with high melting points. The second main objective of this work was to develop materials suitable for growth on polymeric substrates, such as polyimide, for flexible electronics applications. To avoid thermal degradation of the polyimide substrates, the maximum processing temperature for flexible films was limited to 350°C. This chapter describes the deposition of nanocomposite bismuth zinc niobate tantalate films on platinized polyimide substrates. In addition to discussing the phase identification, microstructure, and dielectric properties of these films, the results of flexible testing of released films will be presented.

7.1 The Fabrication of Nanocomposite Bismuth Zinc Niobate Tantalate Films

The deposition of dielectric thin films on polyimide substrates that were suitable for energy storage applications was achieved by limiting the maximum processing temperature to 350°C.

7.1.1 Thermal Instability of Polyimide Substrates at 400°C

Chapter 4 described the deposition of dense amorphous films of bismuth zinc niobate that were pyrolyzed using a maximum temperature of 400°C. Infrared spectroscopy, which has a routine detection limit of 0.1 wt% [1], indicated that the films were largely free of organic species. In order to densify and remove organic species from the as-deposited solution, films of bismuth zinc niobate tantalate, $Bi_{1.5}Zn_{0.9}Nb_{1.35}Ta_{0.15}O_{6.9}$, were prepared using the same methodology. The films were deposited on the platinized polyimide multilayer substrate stacks shown schematically in Figure 3-2. The substrates were preconditioned as described in section 3.1.1.2, and films were deposited from a 0.15 M solution with a 3:1 molar ratio of citric acid to organometallic precursor. The solution was spin coated at 4000 rpm for 40 seconds. The substrate was dried on a hotplate at 250°C for three minutes, pre-pyrolyzed on a second hotplate at 350°C for ten minutes, then pyrolyzed for ten minutes at 400°C.

Figure 7-1 shows the surface of a film deposited using these processing parameters. The micrograph indicates that the surface is not smooth, which is due to buckling of the polyimide substrate. Upon exposure to the 400°C hotplate, the surface of the film became less specularly reflective and developed a hazy appearance. Although polyimide has been documented to undergo thermal decomposition at temperatures of 620°C, the glass transition temperature of PI-2611 polyimide is 360°C [2]. Exposure to temperatures in excess of the polymer's glass transition temperature caused the polyimide to soften and wrinkle, rendering PI-2611 polyimide unsuitable for use as a substrate at temperatures above 400°C.

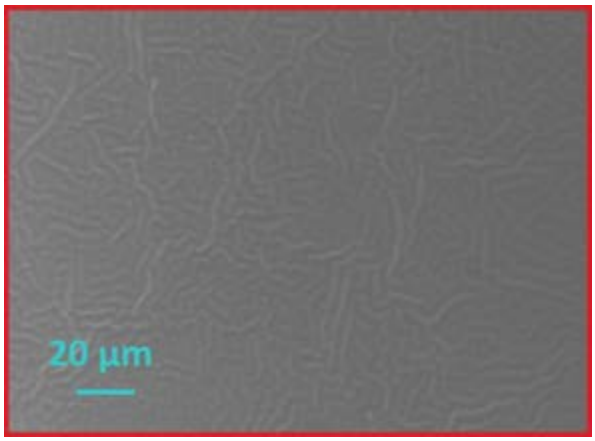

Figure 7-1. Scanning electron micrograph of the surface of a bismuth zinc niobate tantalate film on a polyimide substrate prepared using a maximum processing temperature of 400°C. The film exhibited wrinkling and was unsuitable for use in dielectric devices.

7.1.2 Reduction in the Maximum Processing Temperature of Films Deposited on Polyimide Substrates

To process films at temperatures below the glass transition temperature of PI-2611 polyimide, the solution chemistry developed in Chapter 4 was modified to facilitate pyrolysis and film densification at reduced processing temperatures. As discussed in Chapter 4, most Pechini chemistries involving a readily hydrolysable precursor, such as niobium and tantalum, use a citric acid to organometallic molar ratio of at least 3:1 to prevent selective hydrolysis of the moisture-sensitive cations [3, 4]. Solutions prepared for this work using this concentration of citric acid were stable towards hydrolysis and exhibited no precipitation for over a year. As seen in the thermal gravimetric analysis plot of Figure 7-2(a), for a 0.15 M $Bi_{1.5}Zn_{0.9}Nb_{1.5}O_{6.9}$ solution with a molar ratio of citric acid to organometallic precursor of 3:1, approximately half of the weight loss is complete when the solution reaches 250°C. When the solution reaches 400°C, approximately 11% weight loss remains. It has been reported that higher temperatures are necessary to combust

the polymer network of Pechini-based solutions relative to alcohol-based sol-gel solutions [4, 5, 6, 7]. This is due, in part, to the strong coordination exhibited by metal citrate complexes [8, 9, 10]. To decrease the temperature required to remove organic species, the amount of citric acid in the solution was reduced to a 1:1 molar ratio of citric acid to organometallic precursor. This reduction in the organic content of the precursor solution was intended to minimize the number of strong chelating bonds in the system. Figure 7-2(b) shows the thermal gravimetric analysis of a 0.15 M $Bi_{1.5}Zn_{0.9}Nb_{1.5}O_{6.9}$ solution with a molar ratio of citric acid to organometallic precursor of 1:1. It can be seen that approximately 75% of the weight loss occurred when the solution reached 175°C and that the weight loss occurring after 350°C was approximately six percent. Based upon the differences in the weight loss profiles of Figure 7-2, a 1:1 molar ratio was used to facilitate the removal of organic species at temperatures below the glass transition temperature of PI-2611 polyimide.

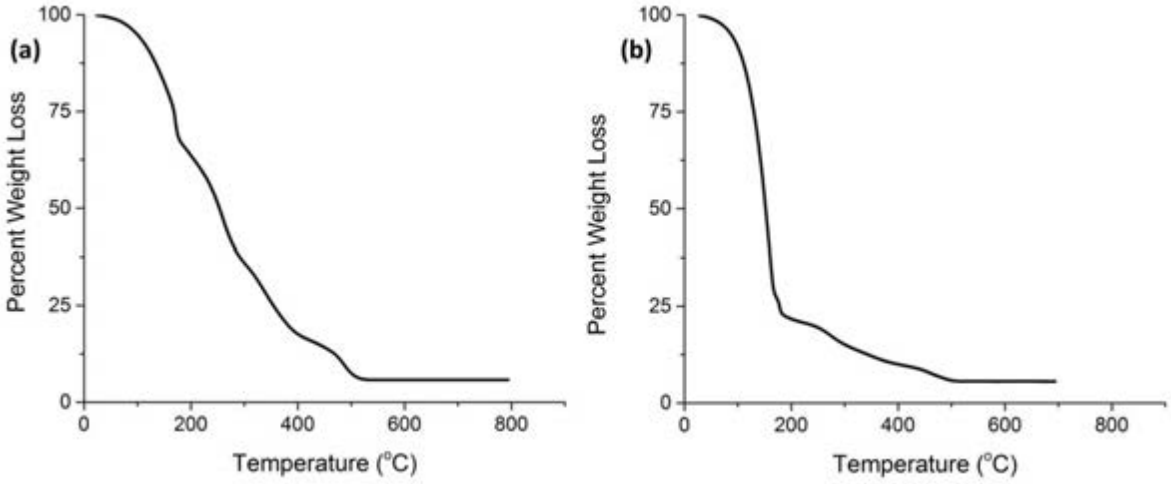

Figure 7-2. Thermal gravimetric analysis of a 0.15 M $Bi_{1.5}Zn_{0.9}Nb_{1.5}O_{6.9}$ solution with a (a) 3:1 and (b) 1:1 molar ratio of citric acid to organometallic precursor.

Films of $Bi_{1.5}Zn_{0.9}Nb_{1.35}Ta_{0.15}O_{6.9}$ were deposited on polyimide substrate stacks; this fabrication process employed a maximum processing temperature of 350°C. Following substrate preconditioning, films were deposited from a 0.15 M solution with equivalent molar ratios of citric acid and organometallic precursors. The solution was spin coated at 4000 rpm for 40 seconds. The substrate was dried on a hotplate at 250°C for three minutes and pyrolyzed on a second hotplate at 350°C for ten minutes. The infrared spectrum in Figure 7-3 indicates that the films were free of organic species within the 0.1 wt% detection limit of infrared spectroscopy. As discussed above, thermal gravimetric analysis indicated that weight loss was not complete when the liquid sample reached 350°C. This difference between the thermal gravimetric analysis and infrared spectroscopy results was likely due to kinetic differences. For thermal gravimetric analysis, a constant heating rate of 5°C/minute was employed, while the infrared spectrum in Figure 7-3 shows the results of a film subjected to rapid heating rates (the film was transferred from one preheated hotplate to another preheated hotplate) and lengthy hold times. The differences in the time that the sample was held at a given temperature, as well as the differences between static temperature holds and constant temperature increases, will change the kinetics of sample pyrolysis by affecting the reaction rates associated with the volatization of organics [11, 12, 13]. Therefore, thermal gravimetric analysis was used to probe the changes in pyrolysis temperature and weight loss due to the differing citric acid content in the solutions, while infrared spectroscopy confirmed the successful pyrolysis of the deposited thin films at reduced temperatures.

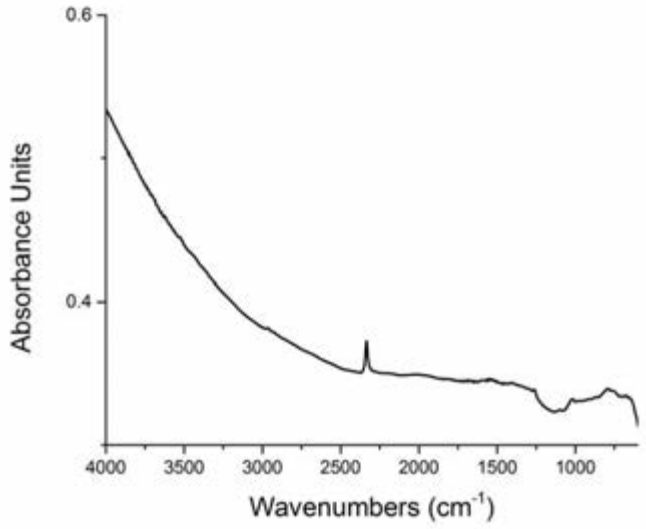

Figure 7-3. Infrared spectrum of a film of nanocomposite $Bi_{1.5}Zn_{0.9}Nb_{1.35}Ta_{0.15}O_{6.9}$ processed at a maximum temperature of 350°C. The lack of peaks corresponding to the vibrations of organic functional groups indicated that the film was free of organic species within the detection limits of infrared spectroscopy.

Figure 7-4 shows a cross-sectional scanning electron micrograph of a film deposited at 350°C. The film was dense, with a smooth interface between the dielectric and platinum bottom electrode. Furthermore, the surface of the film was smooth and free of wrinkles.

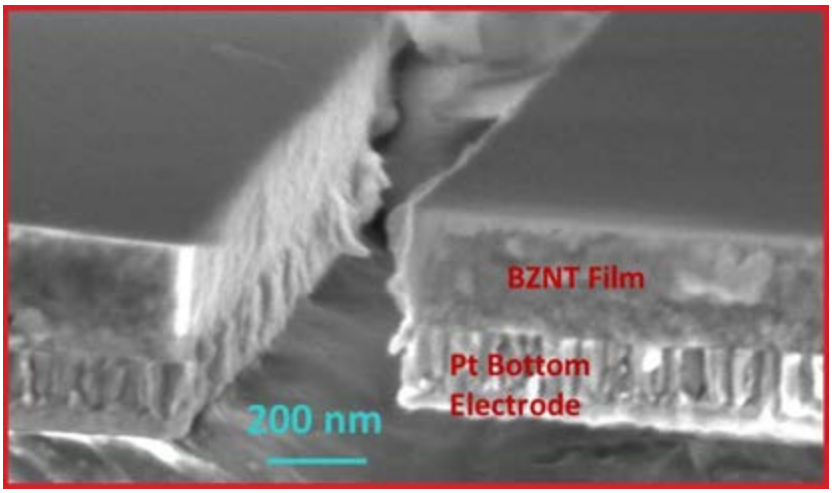

Figure 7-4. Cross-sectional scanning electron micrograph of a nanocomposite bismuth zinc niobate tantalate film processed at a maximum temperature of 350°C. These films were dense, and exhibited no wrinkling.

7.2 Phase Identification and Microstructure of the Nanocomposite

The phases present in nanocomposite bismuth zinc niobate tantalate and the microstructure of the films are discussed in this section. X-ray diffraction and transmission electron microscopy results were used for nanocomposite characterization.

7.2.1 Phase Identification of Nanocomposite Bismuth Zinc Niobate Tantalate

Films were deposited on platinized polyimide substrate stacks and analyzed using x-ray diffraction to determine if there was any evidence of crystallinity in the films. Figure 7-5 shows the XRD pattern for the nanocomposite films prior to release (black trace) and after release from the silicon carrier wafer (red trace). The pattern of the released film showed two peaks which were consistent with the diffraction peaks of δ-Bi_2O_3, which is related to the fluorite structure (PDF # 98-001-4679). As will be discussed in section 7.3.1, the crystalline phase detected by x-

ray diffraction is not pure Bi_2O_3, but likely a solid solution formed between δ-Bi_2O_3 and one or more of the transition metals in bismuth zinc niobate tantalate.

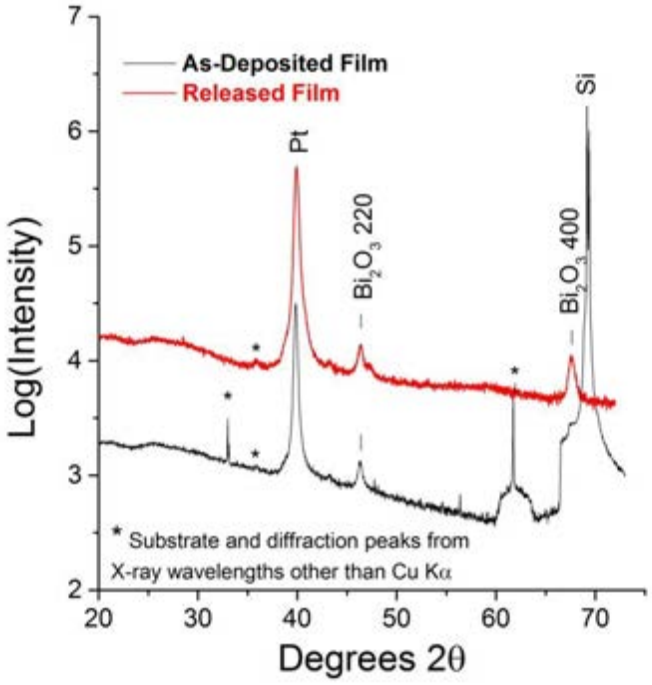

Figure 7-5. X-ray diffraction patterns of nanocomposite $Bi_{1.5}Zn_{0.9}Nb_{1.35}Ta_{0.15}O_{6.9}$ films on a platinized polyimide substrate prior to (black trace) and following (red trace) release from a rigid silicon carrier wafer.

7.2.2 Nanocomposite Bismuth Zinc Niobate Tantalate Microstructure

Transmission electron microscopy images of the film on a platinized silicon substrate confirmed the formation of a nanocomposite. The cross-sectional micrograph of Figure 7-6(a) depicts a dense film atop a crystalline platinum substrate. The film consists of high density particles randomly distributed throughout an amorphous network. These particles are likely nanocrystals of a fluorite related to delta-bismuth oxide, the crystalline phase identified in the x-ray diffraction pattern of Figure 7-5. The film-substrate interface is smooth, which should

minimize electric field amplification associated with electrode non-uniformities [14]. The high-magnification TEM micrograph of Figure 7-6(b) verified the formation of spherical, dense nanocrystals that are approximately 3 nm in diameter. Although some particles are isolated and others have formed aggregates consisting of two to three particles, each cluster is randomly dispersed throughout the film. The lack of percolation in these films should reduce the likelihood of the formation of a breakdown pathway.

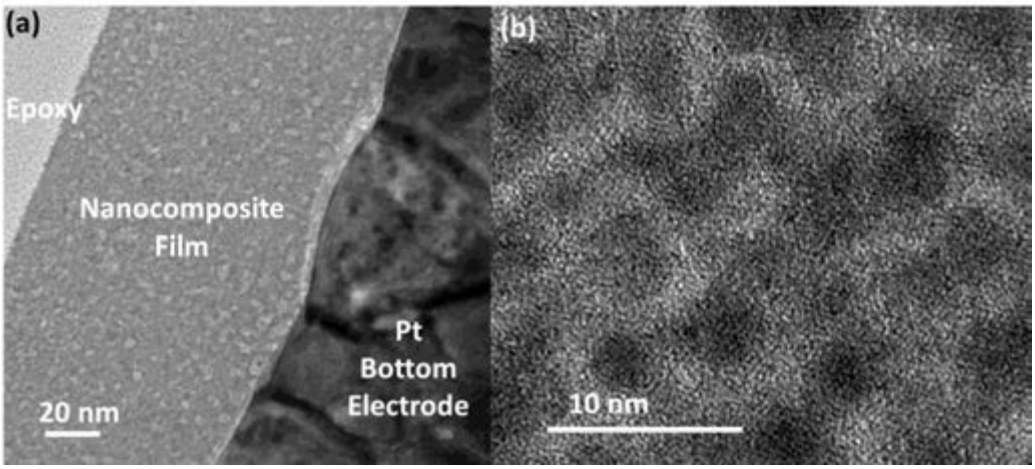

Figure 7-6. Transmission electron microscopy images of nanocomposite bismuth zinc niobate tantalate deposited on a platinized silicon substrate. In (a), a dense film consisting of an amorphous matrix with randomly dispersed nanoparticles is visible. In (b), high magnification TEM shows the formation of dense particles in an amorphous network.

It is unlikely that the nanocrystals in these films are caused by preferential segregation in the precursor solutions used for film deposition. It has been reported that multicomponent oxide materials prepared via a Pechini-based chemistry exhibit exceptional homogeneity relative to materials prepared using a sol-gel synthesis [9]. Alcohol-based syntheses can suffer from chemical and phase inhomogeneity due to differences in the hydrolysis and condensation reaction kinetics for each cation [15], while the Pechini process involves the formation of metal

complexes and dehydration reactions that drive esterification. Following esterification, the metal complexes are immobilized in a rigid polyester network, reducing the ability of the cations to segregate [15, 16]. Rather than attributing the nucleation of the nanocrystals to preferential cation segregation in solution, it is possible that the reduced citric acid content of the solution used for film deposition facilitated lower temperature formation of nanocrystals during pyrolysis that act as nucleating agents for the remainder of the film.

To investigate the formation of these nanoparticles, a $Bi_{1.5}Zn_{0.9}Nb_{1.5}O_{6.9}$ film was prepared with a 3:1 molar ratio of citric acid to organometallic precursor. This film was dried at 250°C for three minutes, pre-pyrolyzed at 350°C for ten minutes, and pyrolyzed at 400°C for ten minutes. This film was not crystallized, and, as can be seen in Figure 7-7(a), the film is amorphous according to x-ray diffraction. To determine if a small volume fraction of the film has segregated to form nanoparticles that may act as nucleating agents for the remainder of the film, transmission electron microscopy was used to investigate the microstructure of the pyrolyzed film. Figure 7-7(b) confirms the presence of segregation in this film. These dense segregated regions are isolated and randomly distributed throughout an amorphous matrix; the concentration of these particles in the amorphous matrix is significantly lower than the concentration of nanoparticles in the 1:1 nanocomposite films. The formation of these nanoparticles in the pyrolyzed films indicated that segregation may be an intermediate during the growth of fully crystalline, phase pure, pyrochlore films. This also opens the question as to whether the crystallites nucleate the pyrochlore phase in the crystalline films, helping to reduce the grain size.

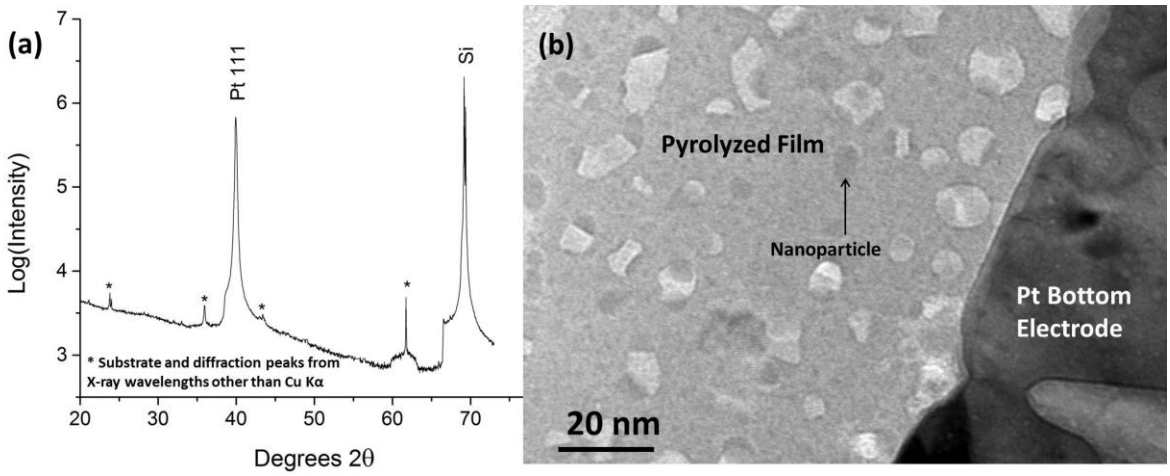

Figure 7-7. (a) X-ray diffraction pattern and (b) transmission electron microscopy image of a $Bi_{1.5}Zn_{0.9}Nb_{1.5}O_{6.9}$ film deposited from a solution containing a 3:1 molar ratio of citric acid to organometallic precursor prior to crystallization. The film is x-ray diffraction amorphous, and TEM confirms nanoparticle formation in the film.

7.3 Establishing a Baseline of Dielectric Properties

Prior to releasing the films for flexible testing, the dielectric properties of the nanocomposite were determined to create a baseline against which changes in film properties could be measured.

7.3.1 Low Field Dielectric Properties of Nanocomposite Bismuth Zinc Niobate Tantalate

Chapter 6 discussed the characterization of crystalline $Bi_{1.5}Zn_{0.9}Nb_{1.35}Ta_{0.15}O_{6.9}$ films with a relative permittivity of 122 ± 4 and a loss tangent of 0.0008 ± 0.0001. Nanocomposite bismuth zinc niobate tantalate (also with the composition $Bi_{1.5}Zn_{0.9}Nb_{1.35}Ta_{0.15}O_{6.9}$) is a novel material; thus, prior reports could not be found in the literature. Amorphous materials possess a lower permittivity than their crystalline counterparts [17, 18]; therefore, it was expected that the relative

permittivity of the nanocomposite would be lower than that of the crystalline films of Chapter 6. Figure 7-8 shows permittivity and loss tangent of the films as a function of frequency. The permittivity demonstrated a slight dependence on the frequency, which is likely due to small amounts of space charge present in the films. Bismuth oxide is known to be a conductive oxide [19, 20], which may result in the small amounts of space charge observed in this nanocomposite [21]. The films exhibited a relative permittivity of between 50 and 55, and low dielectric losses on the order of 0.03 ± 0.01. At lower frequencies, the loss tangent rises substantially.

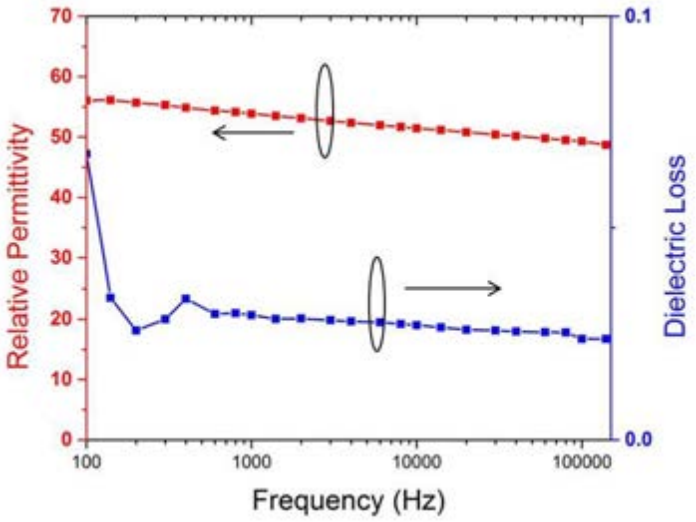

Figure 7-8. The relative permittivity and loss as a function of frequency for films of nanocomposite $Bi_{1.5}Zn_{0.9}Nb_{1.35}Ta_{0.15}O_{6.9}$.

The relative permittivity of the nanocomposite is higher than that of both amorphous $Bi_{1.5}Zn_{1.0}Nb_{1.5}O_{7.0}$ and crystalline Bi_2O_3. The relative permittivity of Bi_2O_3, calculated using the Clausius-Mossotti equation [21], is 30, while films of amorphous $Bi_{1.5}Zn_{1.0}Nb_{1.5}O_{7.0}$ have been demonstrated to possess a relative permittivity of approximately 40 and dielectric losses of 0.01 [22]. A nanocomposite with a permittivity value higher than those of the constituent materials violates dielectric mixing rules; thus, it is likely that the crystalline phase of the nanocomposite is

not pure bismuth oxide. δ-Bi_2O_3 has been shown to form solid solutions with several transition metals, including niobium and tantalum [23]. These solid solutions possess a fluorite crystal structure related to δ-Bi_2O_3, and exhibit large changes in their permittivity relative to Bi_2O_3. For example, a solid solution sample of δ-Bi_2O_3 with 14% niobium exhibited a permittivity of approximately 60 [23]. Thus, it is likely that the nanocrystalline particles in the nanocomposite films are not chemically pure bismuth oxide; the particles are likely a solid solution formed between δ-Bi_2O_3 and other transition metals in the film, such as zinc, niobium, or tantalum. To further confirm this, the lattice parameters of the crystalline phase were extracted from the XRD pattern in Figure 7-5. The calculated lattice parameter is 5.536 ± 0.001 Å (the fluorite crystal is cubic); bulk δ-Bi_2O_3 has a lattice parameter of 5.525 Å (PDF # 98-001-4679). It is unknown what increases the lattice parameter of the nanocomposite crystalline phase, but it may be due to the formation of oxygen vacancies [21]. It was concluded that the films were a nanocomposite consisting of a nanocrystalline fluorite related to delta-bismuth oxide in an amorphous matrix.

7.3.2 High Field DC Properties of Nanocomposite Bismuth Zinc Niobate Tantalate

Figure 7-9 shows the leakage current density as a function of DC electric field for nanocomposite bismuth zinc niobate tantalate thin films. The DC breakdown strength in these films was approximately 1.5 MV/cm; this is less than half of the DC breakdown strength of the crystalline films. The leakage current for this material is on the order of 10^{-9} A/cm^2, which is an order of magnitude higher than the leakage current exhibited by the crystalline films. These values are comparable with those reported for amorphous films of $Bi_{1.5}Zn_{1.0}Nb_{1.5}O_{7.0}$. Amorphous films of $Bi_{1.5}Zn_{1.0}Nb_{1.5}O_{7.0}$ were found to possess a DC breakdown strength of 1.25 MV/cm and a leakage current of 10^{-8} A/cm^2 [24]. Improvement in the DC breakdown field of the

nanocomposite films prepared here relative to amorphous bismuth zinc niobate was expected due to the incorporation of tantalum into the composition of the material, as discussed in Chapter 6.

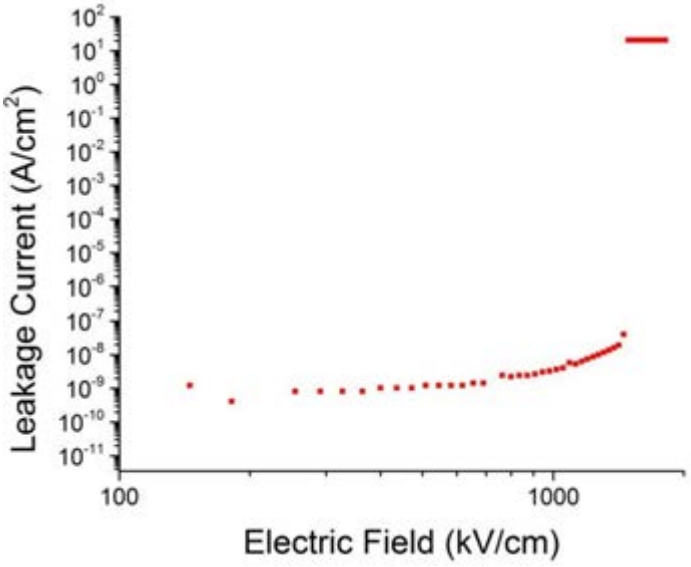

Figure 7-9. The leakage current as a function of DC bias for films of nanocomposite bismuth zinc niobate tantalate.

7.3.3 High Field AC Properties of Nanocomposite Bismuth Zinc Niobate Tantalate

Figure 7-10 shows the polarization versus electric field behavior prior to dielectric breakdown for nanocomposite bismuth zinc niobate tantalate films using two different measurement frequencies. The high-field hysteresis loops confirmed that the nanocomposite was a very weakly nonlinear, low loss dielectric. The 1 kHz and 10 kHz breakdown strength of these films was approximately 3.8 MV/cm. These breakdown fields are lower than those exhibited by the crystalline bismuth zinc niobate tantalate films of the same stoichiometry in Chapter 6. This disparity in the breakdown strengths exhibited by the nanocomposite and crystalline films is anomalous. The breakdown strengths of amorphous materials and amorphous-nanocrystalline composites typically exceeds those of crystalline materials, as the amorphous host eliminates the

possibility of a breakdown pathway forming along grain boundaries [17, 18]. As discussed in Chapter 6, the crystalline films in this thesis demonstrated highly resistive grain boundaries, resulting in high breakdown strengths. The lack of highly resistive lateral grain boundaries in the nanocomposite films resulted in breakdown strengths that were smaller than those of the fine-grained crystalline films.

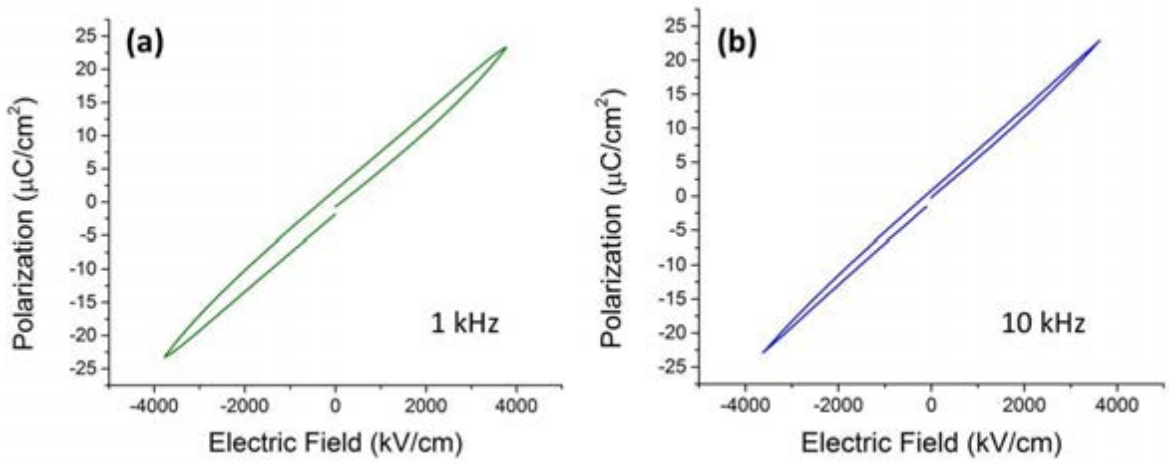

Figure 7-10. The polarization-electric field behavior for nanocomposite bismuth zinc niobate tantalate films prior to breakdown, measured at (a) 1 kHz and (b) 10 kHz.

7.3.4 Nanocomposite Bismuth Zinc Niobate Tantalate for Dielectric Energy Storage

Despite the lower breakdown strengths in these nanocomposite films relative to the crystalline films discussed earlier in this thesis, the low high field losses, minimal tunability, and reasonably high breakdown strengths contributed to a high energy storage density. Figure 7-11 shows the maximum energy storage density and discharge efficiency of the nanocomposite as a function of temperature and frequency. These films had a high room-temperature energy storage density of 40.2 ± 1.7 J/cm^3. The discharge efficiencies for these films were high as well,

mirroring the low high field loss of the material as the field and temperature were increased. The decrease in the energy storage density of these films with increasing temperature was due primarily to decreases in the achievable breakdown strength of the films at elevated temperatures. As an example, the 10 kHz breakdown field of the nanocomposite films at 200°C was 1.9 MV/cm. The 10 kHz polarization-electric field behavior at 200°C is shown in Figure 7-12. It can be seen that the high field losses in the material remain modest, and that the majority of the suppression in the energy storage density is attributable to a reduction in the breakdown strength.

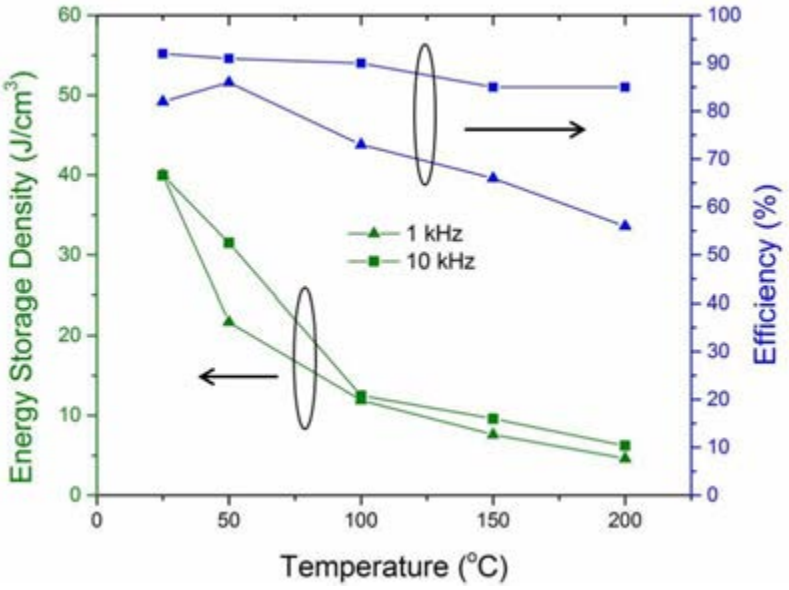

Figure 7-11. The energy storage density and discharge efficiency for thin films of nanocomposite bismuth zinc niobate tantalate as a function of temperature and frequency.

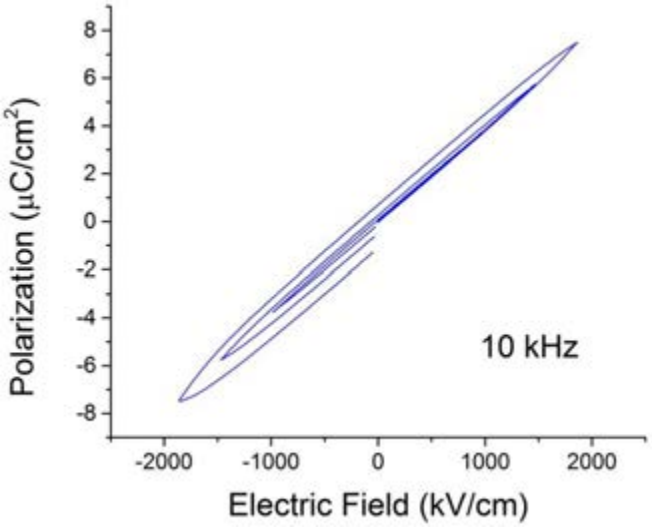

Figure 7-12. The 10 kHz polarization-electric field behavior for nanocomposite bismuth zinc niobate tantalate at 200°C.

The calculated power densities for the nanocomposite films at measurement frequencies of 1 kHz and 10 kHz are listed in Table 7-1 as a function of temperature.

Table 7-1. Power Storage Density of Nanocomposite Bismuth Zinc Niobate Tantalate Films

Temperature (°C)	1 kHz Power Density (MW/cm^3)	10 kHz Power Density (MW/cm^3)
25	3.7	87
50	2.7	76
100	1.0	33
150	0.59	15
200	0.25	15

7.4 Flexible Testing of Nanocomposite Bismuth Zinc Niobate Tantalate

Following preliminary dielectric testing, 250 nm films of the nanocomposite were released from their rigid silicon carrier wafers by chemically removing the gold sacrificial layer

from the substrate stack with a commercially available potassium iodide etchant (Gold Etchant, Standard, Sigma-Aldrich). Prior to flexible testing, the films were inspected using scanning electron microscopy to verify that they were free of cracks prior to bending. Scanning electron micrographs of the films showed a smooth surface without any obvious indication of crack formation. Following microstructural inspection, the films were mounted on the flexible testing apparatus depicted in Figure 3-3. To standardize the diameter of the bend and the resulting strain levels in the film, one sample was bent in compression while the other sample was simultaneously bent in tension. Nanocomposite bismuth zinc niobate tantalate was subjected to a maximum of 30,000 six-second mechanical bending cycles. The minimum bend diameter experienced by the nanocomposite was 7 mm, which correlates to a strain of approximately 0.10%, assuming no plastic deformation in the polyimide. The percent strain was calculated using the following equation [25]:

$$Strain = \frac{\delta}{r}$$

in which δ is the distance between the neutral plane and the top surface of the film and r is the bending radius of the film. The quantity δ was calculated as follows [25]:

$$\delta = \frac{\sum_{i=1}^{N} \bar{E}_i h_i (\sum_{j=1}^{i} h_j - \frac{h_i}{2})}{\sum_{i=1}^{N} \bar{E}_i h_i}$$

where N is the total number of layers in the multilayer film stack, h_i is the thickness of the ith layer (from the top surface of the stack), and $\bar{E}_i$ is the effective Young's modulus, which is defined as:

$$\bar{E}_i = \frac{E_i}{(1 - \vartheta_i)^2}$$

in which E_i is the Young's modulus of the ith layer and ϑ_i is Poisson's ratio of the ith layer. A 7 mm bend radius corresponded to a 0.1% film strain, under the assumption of purely elastic deformation.

At the conclusion of the bending cycles, the films were reexamined for evidence of cracking or other structural degradation using scanning electron microscopy. The films exhibited no cracking after flexing in either tension or compression, indicating that the nanocomposite bismuth zinc niobate tantalate films did not undergo catastrophic structural failure upon bending. The polarization-electric field behavior was measured for both samples, and the results of compressive bending tests are shown in Figure 7-13. The figure indicates that the relative permittivity, high field loss, breakdown strength, and energy storage densities of the films were unchanged after 30,000 bending cycles around a minimum bend diameter of 7 mm. The films that were flexed under the same conditions in tension also exhibited unchanged dielectric properties, indicating that films of nanocomposite bismuth zinc niobate tantalate may be suitable for incorporation into flexible dielectric energy storage applications.

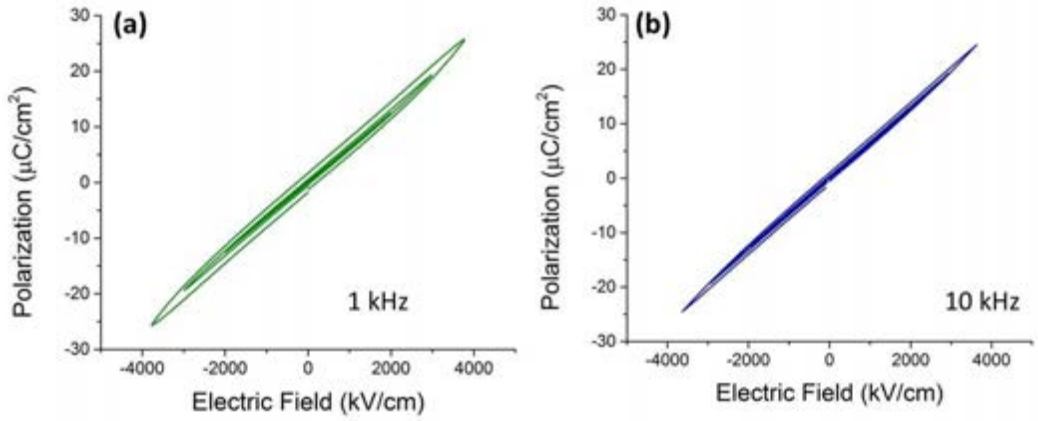

Figure 7-13. The (a) 1 kHz and (b) 10 kHz polarization-electric field behavior for released nanocomposite bismuth zinc niobate tantalate films after compressive bending for 30,000 cycles. The strain on these films was 0.10% and the bend diameter was 7 mm.

7.5 Conclusions

Nanocomposite films (with the average composition $Bi_{1.5}Zn_{0.9}Nb_{1.35}Ta_{0.15}O_{6.9}$) consisting of nanocrystalline fluorite related to delta-bismuth oxide in an amorphous matrix were deposited at 350°C on platinized polyimide substrate stacks. Low temperature film deposition was possible through a reduction in the citric acid concentration of the precursor solutions. The nanocomposite films exhibited a relative permittivity of approximately 50 and dielectric losses on the order of 0.03. The 1 kHz breakdown strength of the nanocomposite was 3.8 MV/cm, which resulted in a room-temperature energy storage density of approximately 40 J/cm^3. After establishing a baseline of dielectric properties, crack-free released films underwent compressive and tensile flexible testing. After bending the films around a minimum bend diameter of 7 mm (which corresponds to a maximum strain level of 0.10%) for 30,000 mechanical bending cycles, the dielectric properties and energy storage density of the films was unchanged, indicating that nanocomposite bismuth zinc niobate tantalate films may be suitable for flexible energy storage applications.

7.6 References

1] The Pennsylvania State University - Materials Research Institute, "Materials Research Institute Materials Characterization Lab," http://www.mri.psu.edu/facilities/mcl/capabilities/characterization-techniques/ft-ir.asp. [Accessed 25 February 2015].

2] HD MicroSystems, "HD MicroSystems," Available: http://hdmicrosystems.com.

3] A. Z. Simoes, A. Ries, C. S. Riccardi, A. H. Gonzalez, M. A. Zaghete, B. D. Stojanovic, M. Cilense and J. A. Varela, "Potassium niobate thin films prepared through polymeric precursor method," *Materials Letters,* vol. 58, pp. 2537-2540, 2004.

M. Galceran, M. C. Pujol, M. Aguilo and F. Diaz, "Sol-gel modified Pechini method for obtaining nanocrystalline $KRE(WO_4)_2$ (RE = Gd and Yb)," *Journal of Sol-Gel Science*

4] *and Technology,* vol. 42, pp. 79-88, 2007.

5] R. Sukumar, W. Sigmund and F. Aldinger, "Nanostructured yttria powders via gel combustion," *Journal of Materials Research,* vol. 14, no. 4, pp. 1524-1531, 1999.

6] D. A. Neumayer, P. R. Duncombe, R. B. Laibowitz and A. Grill, "Chemical solution deposition of $BaSrTiO_3$ films," *Integrated Ferroelectrics,* vol. 18, no. 1-4, pp. 297-309, 1997.

7] R. W. Schwartz and M. Narayanan, "Thermodynamics and Heating Processes," in *Chemical Solution Deposition of Functional Oxide Thin Films*, Wien, Springer, 2013, pp. 343-382.

8] P. D. Spagnol, J. A. Varela, M. A. Bertochi, B. D. Stojanovic and S. M. Tebcherani, "Effect of precursor solution on the formation of perovskite phase of $Pb(Mg_{1/3}Nb_{2/3})O_3$ thin films," *Thin Solid Films,* vol. 410, pp. 177-182, 2002.

9] K. Nishio and T. Tsuchiya, "Sol-gel processing of thin films with metal salts," in *Handbook of Sol-Gel Science and Technology*, Norwell, Massachusetts, Kluwer Academic Publishers, 2005, pp. 59-76.

10] M. Liu and D. Wang, "Preparation of $La_{1-z}Sr_zCo_{1-y}Fe_yO_{3-x}$ thin films, membranes, and coating on dense and porous substrates," *Journal of Materials Research,* vol. 10, pp. 3210-3221, 1995.

11] H. E. Kissinger, "Reaction kinetics in differential thermal analysis," *Analytical Chemistry,* vol. 29, no. 11, pp. 1702-1706, 1957.

12] C. D. Doyle, "Kinetic analysis of thermogravimetric data," *Journal of Applied Polymer Science,* vol. 5, no. 15, pp. 285-292, 1961.

13] D. A. Campbell, R. A. Pethrick and J. R. White, "Thermal Analysis," in *Polymer Characterization: Physical Techniques*, Cheltenham, UK, Stanley Thornes, 2000, pp. 362-407.

14] M. M. Samantaray, A. Gurav, E. C. Dickey and C. A. Randall, "Electrode defects in multilayer capacitors part I: Modeling the effect of electrode roughness and porosity on electric field enhancement and leakage current," *Journal of American Ceramic Society,* vol. 95, no. 1, pp. 257-263, 2012.

15] M. Kakihana and M. Yoshimura, "Synthesis and characteristics of complex multicomponent oxides prepared by polymer complex method," *Bulletin of the Chemical Society of Japan,* vol. 72, pp. 1427-1443, 1999.

16] N. G. Eror and H. U. Anderson, "Polymeric precursor synthesis of ceramic materials," *MRS Proceedings*, p. 571-577, 1986.

17] A. V. Wagner, G. W. Johnson and T. W. Barbee, "High energy density capacitors fabricated by thin film technology," *MRS Proceedings,* vol. 574, 1999.

[18] P. Barber, S. Balasubramanian, Y. Anguchamy, S. Gong, A. Wibowo, H. Gao, H. J. Ploehn and H.-C. zur Loye, "Polymer composite and nanocomposite dielectric materials for pulse power energy storage," *Materials,* vol. 2, pp. 1697-1733, 2009.

[19] T. Takahashi, H. Iwahara and Y. Nagai, "High oxide ion conduction in sintered Bi_2O_3 containing SrO, CaO or La_2O_3," *Journal of Applied Electrochemistry,* vol. 2, no. 2, pp. 97-104, 1972.

[20] L. Leontie and G. I. Rusu, "On the electronic transport properties of bismuth oxide thin films," *Journal of Non-Crystalline Solids,* vol. 352, no. 9-20, pp. 1475-1478, 2006.

[21] A. J. Moulson and J. M. Herbert, Electroceramics: Materials, Properties, Applications, West Sussex, England: John Wiley & Sons, Ltd, 2003.

[22] L. Friedman Edge, "Pulsed Laser Deposition of Bismuth Zinc Niobate Thin Films for Dielectric Applications," M.S. Thesis, The Pennylvania State University, 2002.

[23] M. Valant and D. Suvorov, "Dielectric characteristics of bismuth oxide solid solutions with a fluorite-like crystal structure," *Journal of the American Ceramic Society,* vol. 87, no. 6, pp. 1056-1061, 2004.

[24] W. Gang, L. Wei, L. Ping, L. Zuxiong, F. Xue and J. Jing, "A novel antifuse structure based on amorphous bismuth zinc niobate thin films," *Journal of Semiconductors,* vol. 33, no. 8, p. 084002, 2012.

[25] G.-T. Hwang, J. Yang, S. H. Yang, H.-Y. Lee, M. Lee, D. Y. Park, J. H. Han, S. J. Lee, C. K. Jeong, J. Kim, K.-I. Park and K. J. Lee, "A reconfigurable rectified flexible energy harvester via solid-state single crystal grown PMN–PZT," *Advanced Energy Materials,* DOI: 10.1002/aenm.201500051, 2015.

Chapter 8

Nanocomposite Lead Titanate for Dielectric Energy Storage

To explore the usefulness of a nanocomposite approach for low temperature processing of other complex oxide systems with a high energy storage density, nanocomposite lead titanate was investigated. A brief overview of composite materials is presented first. This is followed by a description of the solution chemistry used to deposit these films. Details regarding the characterization of film phase and microstructure are presented. Finally, the dielectric properties and energy storage characteristics of the nanocomposite are discussed.

8.1 Composite Materials and Lead Titanate as a Nanocomposite

The combination of two or more materials with desired properties, such as high relative permittivity and high breakdown strength, could enable a composite thin film material with an energy storage density superior to its constituents [1]. Reported examples usually consist of ceramic particles in a polymer matrix. The ceramic particles provide a component with a higher relative permittivity, while the polymer matrix is intended to provide high breakdown strength [2]. For example, at an optimized volume fraction of 22.5% barium titanate powder dispersed in a silicone elastomer (Sylgard184®, Dow Corning, Midland, MI), the permittivity of the composite approximately doubled, while the breakdown strength of the material remained approximately equal to that of the pure elastomer [1].

The ratio between the two materials must be carefully controlled; if an insufficient concentration of particles is used, the material will not have a large permittivity, and if the concentration of particles is too high, a pathway for current through the material may be introduced [1, 3]. The electrical resistivity of many composite materials can be described using percolation theory [4, 5, 6]. That is, as the volume fraction of a conducting filler in an insulating matrix increases, the filler particles will form a network at the percolation threshold, creating a conduction path through the composite. At the percolation limit, the connectivity of the composite transitions from having a 0-3 connectivity pattern to a 3-3 connectivity pattern [4]. Thus, the resistivity of an insulating composite will decrease by orders of magnitude at a critical volume fraction at which many conduction pathways form. The percolation threshold is affected by the shape, size, and dispersion of the conductive filler particles [4, 5, 7]. For example, the percolation threshold is typically larger for spherical particles than it is for randomly oriented ellipsoidal filler particles, because fewer contacts are required to achieve three dimensional connectivity for ellipsoids [6, 8]. When high aspect ratio filler particles are oriented, rather than randomly dispersed, the resulting anisotropy generates different percolation threshold values when the composite is examined in the in-plane or out-of-plane direction [6, 7]. In addition to the geometric features of the filler component, the percolation threshold can also be influenced by the properties of the matrix, particularly in polymeric systems [6]. For polymers, factors such as the degree of crystallization [9] and viscosity [10] may hinder the homogeneous distribution of filler particles, affecting percolation behavior.

Here, high energy density dielectrics for energy storage which could be processed at low temperatures were pursued by making nanocomposite thin films of a medium permittivity crystalline material in an amorphous matrix. This approach was used in Chapter 7 on a bismuth-based system, and the applicability of this approach to other complex oxide compositions was explored using $Pb_{1.1}TiO_{3.1}$. The intent was to use the amorphous host to increase the breakdown

strength by eliminating the possibility of a breakdown pathway forming along grain boundaries [3]. Furthermore, amorphous films are often smoother than polycrystalline films, minimizing electric field intensification at asperities [11]. The primary breakdown mechanisms for amorphous materials are typically residual ionic impurities from film processing or small, randomly distributed voids in the material that present a weak pathway or discharge channel [12]. Although the relative permittivity of amorphous and semicrystalline materials is lower than that of crystalline materials [12], a high energy storage density may be obtained if this reduction in permittivity is compensated by an enhancement in breakdown strength, as discussed in Chapter 6. As an additional example, Sethi et al. [13] achieved breakdown strengths as high as 4 MV/cm and an energy density of 14 J/cm^3 with amorphous tantalum pentoxide films (the relative permittivity was ~25).

The use of amorphous materials is advantageous because the high temperatures required to produce crystalline thin films limit possible substrates to materials with high melting points, preventing the use of polymeric substrates that may have uses in flexible electronics applications. In this work, nanocomposite lead titanate films were deposited via chemical solution deposition at temperatures of 400°C, without a vacuum system or stringent oxygen partial pressure control. Although crystalline lead titanate is well known, the properties of amorphous, undoped lead titanate have not been thoroughly investigated. Crystalline lead titanate has a polycrystalline permittivity of approximately 75 [14] and a leakage current of approximately 10^{-6} A/cm^2 [15]. Amorphous lead titanate has a relative permittivity between 20 and 30 [16].

8.2 Inverted Mixing Order Solution Preparation of $Pb_{1.1}TiO_{3.1}$

Nanocomposite, lead-rich lead titanate, $Pb_{1.1}TiO_{3.1}$, thin films were prepared on platinized silicon wafers via a chemical solution deposition method. Inclusion of excess lead in the

precursor solution was intended to promote the formation of lead oxide nanocrystallites in the amorphous lead titanate matrix of the final film. Ten percent excess lead acetate trihydrate (Sigma-Aldrich, St. Louis, MO) was used during solution preparation. Solutions were prepared using an inverted mixing order synthetic route [17, 18] to avoid the use of 2-methoxyethanol. In addition to the use of no teratogenic solvents, the inverted mixing order solution preparation, developed by Assink and Schwartz, offers synthetic simplicity and short preparation times, usually less than 30 minutes. The main disadvantage of this synthetic route is that there is no explicit control over solution hydrolysis because hydrated precursors, such as lead acetate trihydrate, are used directly, rather than after a dehydration step. This, in addition to ambient humidity, leads to poorly controlled water content in solution, which allows slow esterification and contributes to solution ageing [18]. If properly prepared, solutions should remain stable in storage for months or years [19].

To synthesize solutions suitable for the deposition of nanocomposite lead titanate thin films, the precursors used were lead acetate trihydrate and titanium isopropoxide (Sigma-Aldrich). The solvents used were acetic acid (≥99.7%, Sigma-Aldrich) and methanol (Sigma-Aldrich). Lead acetate trihydrate and titanium isoproxide were combined in acetic acid in a nitrogen atmosphere, and then stirred on an 85°C hotplate for approximately ten minutes to allow for chelation of the central metal atoms by acetyl ligands. Following this reaction step, the mixture was inert to atmospheric moisture, and the remainder of solution preparation was performed under ambient lab conditions. Methanol was added to control the viscosity and stability of the solution [20], along with another aliquot of acetic acid. The solution was stirred for an additional ten minutes. Methanol and acetic acid were added to reach a final molarity of 0.4 M, and the solution was stirred for ten minutes to homogenize. The final solution contained a 3:2 molar ratio of acetic acid to methanol. As described in Chapter 3, films were deposited using

spin-casting. As a summary, the processing route for film fabrication is shown schematically in Figure 8-1.

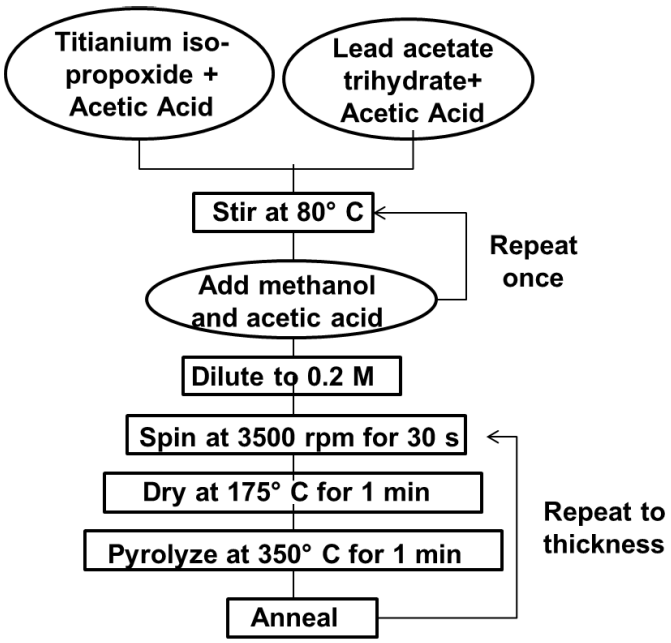

Figure 8-1. Flowchart for the processing of nanocomposite thin films of lead titanate. Solutions were prepared using an inverted mixing order solution preparation, spin cast onto a substrate, and thermally treated in three steps.

8.3 Phase Identification and Microstructure of $Pb_{1.1}TiO_{3.1}$

Phase identification and microstructure characterization of nanocomposite lead titanate are presented in this section. XRD and TEM results are described to define the phase formation window of the nanocomposite.

8.3.1 Nanocomposite Lead Titanate Phase Identification and Microstructure

A crystalline film was deposited using the method from Figure 8-1. To fully crystallize the material while minimizing the volatility of excess lead from the material, the film was annealed in a rapid thermal annealing system at 550°C for two minutes. The resulting XRD pattern is shown in Figure 8-2(a). The diffraction peaks are consistent with the perovskite structure of crystalline lead titanate (PDF# 00-006-0452, 1955) along with peaks from orthorhombic lead oxide (PDF# 00-035-1482, 1984) at 2θ values of 28.7° (111) and 59.5° (222). Figure 8-2(b) shows the XRD pattern of the lead titanate films that were annealed at 400°C for two minutes. These films are XRD amorphous; no diffraction peaks besides those attributable to the substrate are present. There is a hump between 2θ values of approximately 26° and 33°, the 2θ range within which the strongest lead oxide peak lies, corresponding to the 111 plane. The surface microstructures were smooth, without any noticeable topography.

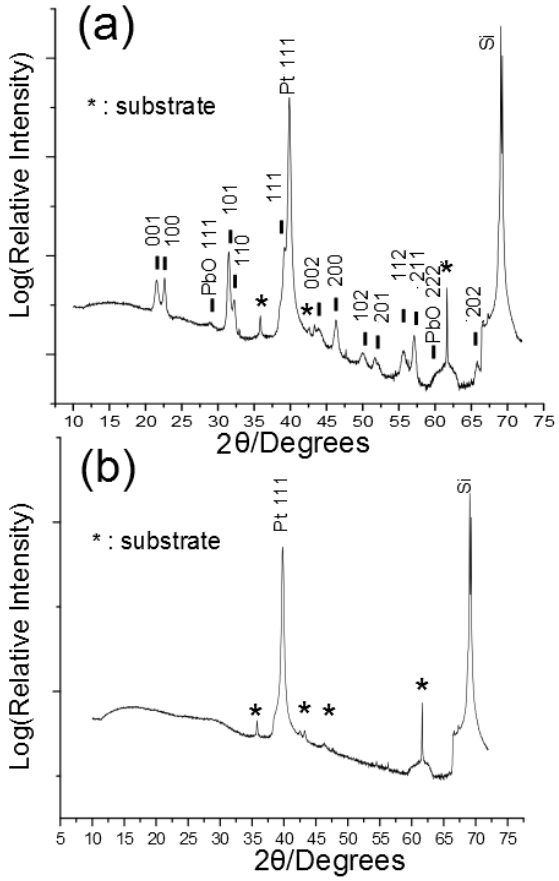

Figure 8-2. The x-ray diffraction pattern of (a) crystalline lead titanate film with 10% excess lead in the precursor solution and (b) nanocomposite lead titanate. In (a), the excess lead manifests itself as lead oxide, while in (b) the only diffraction peaks are those attributable to the substrate.

Figure 8-3 shows images obtained from transmission electron microscopy, which confirm the nanocomposite structure of the films. The cross-sectional transmission electron microscopy image of Figure 8-3(a) depicts a dense film atop a crystalline platinum substrate. The columnar grain structure of the underlying platinum can be seen, while the dielectric film consists of isolated nanocrystals randomly distributed throughout an amorphous matrix. The film-substrate interface is smooth, minimizing the electric field amplification associated with non-uniformities.

The high-magnification transmission electron microscopy image of Figure 8-3(b) shows the formation of small, dense nanocrystals in an amorphous matrix. This is verified in the inset image of Figure 8-3(b) by the presence of small diffraction spots within a diffuse ring. This ring was indexed to the 111 peak of orthorhombic lead oxide. The nucleation of isolated lead oxide nanocrystals was in agreement with the hump observed in the XRD pattern of Figure 8-2(b). These nanocrystals were isolated and randomly dispersed throughout the film; the lack of percolation should reduce the likelihood of the formation of a breakdown pathway.

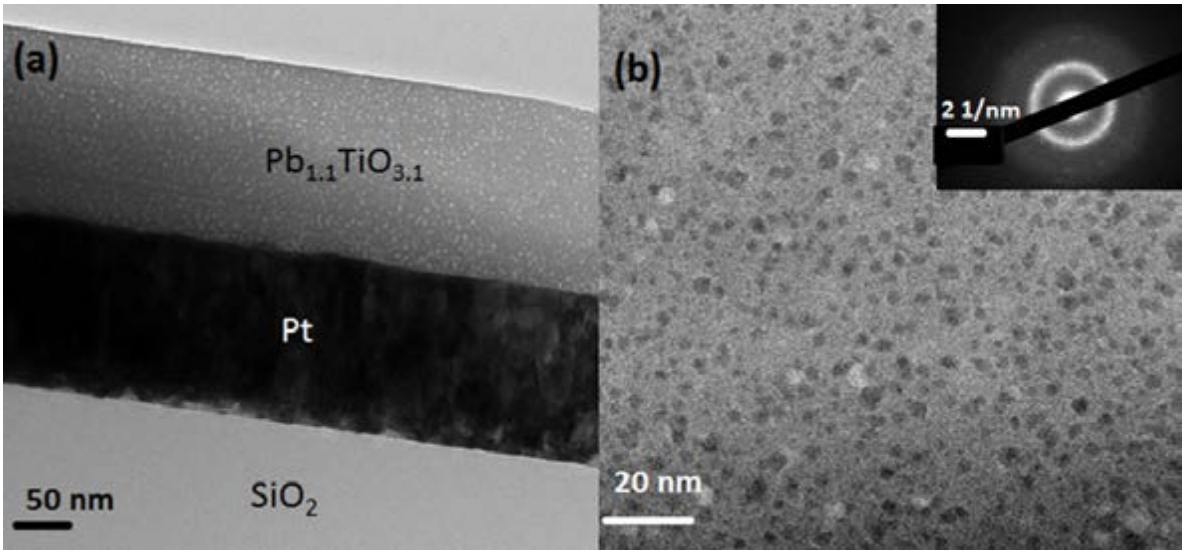

Figure 8-3. Transmission electron microscopy images of nanocomposite lead titanate deposited on a platinized silicon substrate. In (a), the columnar structure of the platinum layer is visible, contrasting with the dense lead titanate film. The amorphous matrix of the film is visible, as well as the random distribution of nanocrystals throughout the film. In (b), high magnification TEM shows the formation of dense, isolated nanocrystals in an amorphous network. This is further verified in the inset image of (b), which shows diffraction points within a diffuse ring.

8.3.2 Phase Formation of Nanocomposite Lead Titanate

The phase formation window for nanocomposite lead titanate exists for heat treatments between 350°C and 450°C. The TEM images of films annealed at 350°C are shown in Figure 8-4. The cross-sectional image of the amorphous lead titanate in Figure 8-4(a) shows a uniform contrast, with no evidence of nanoparticle formation. Furthermore, the selected area electron diffraction image in Figure 8-4(b) shows a diffuse circle, confirming that the film is amorphous, with no evidence of crystallinity.

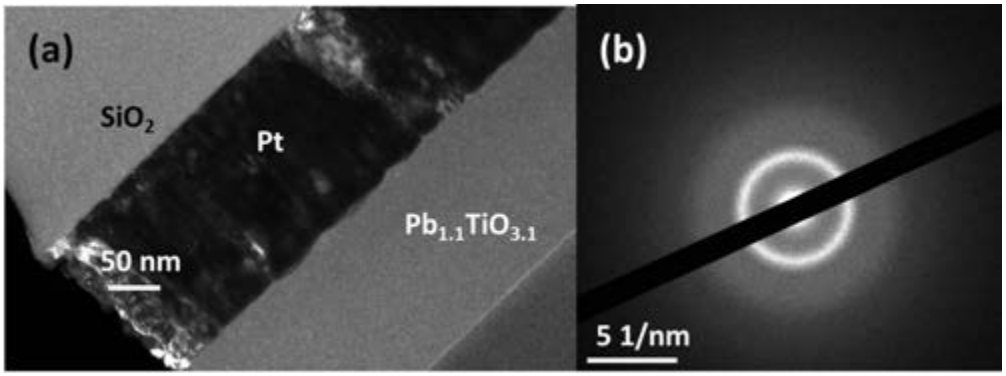

Figure 8-4. Transmission electron microscopy images of amorphous lead titanate deposited on a platinized silicon substrate. In (a), cross-sectional TEM confirms the amorphous structure of the film. This is further verified in (b), which shows only a diffuse ring.

8.4 Dielectric and Energy Storage Properties of $Pb_{1.1}TiO_{3.1}$

The dielectric and energy storage properties of nanocomposite lead titanate are presented in this section.

8.4.1 Dielectric Properties of Nanocomposite Lead Titanate

Figure 8-5 shows the 1 kHz polarization-electric field hysteresis loop for nanocomposite lead titanate swept to an electric field of 1 MV/cm. The loop shows nanocomposite lead titanate to be a linear, low loss dielectric. The relative permittivity was 33 ± 1, and the dielectric loss of the film was approximately 0.0008 ± 0.0001, indicating that there was little charge trapping and energy loss in the material at applied electric fields of 1 MV/cm. As the material was subjected to higher electric fields, the dielectric loss tangent of the film increased, as evidenced by the progressively wider hysteresis loops of Figure 8-6.

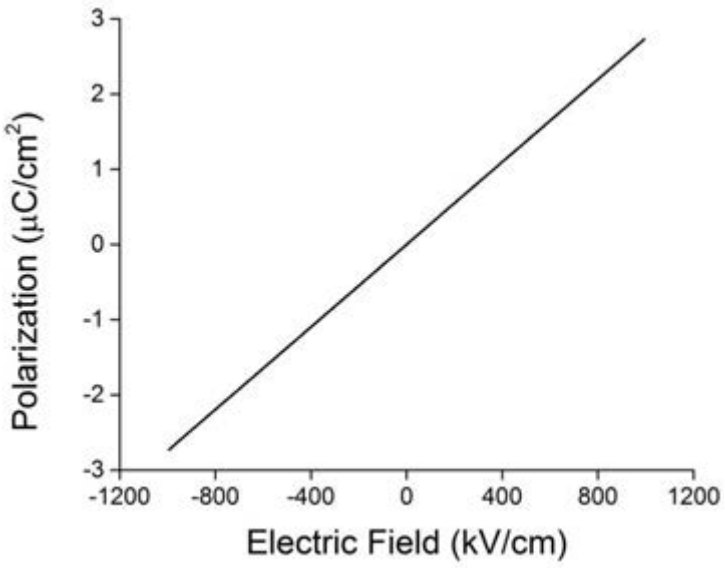

Figure 8-5. Polarization-electric field hysteresis loop for nanocomposite lead titanate. Note that data for both increasing and decreasing field are shown. Nanocomposite lead titanate is a linear, low loss dielectric.

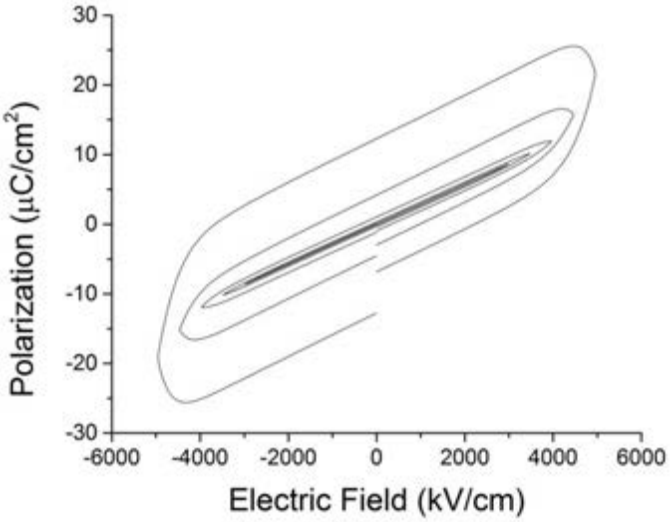

Figure 8-6. Polarization-electric field hysteresis loops for nanocomposite lead titanate swept to progressively higher electric fields. As the electric field approached the breakdown strength of 5 MV/cm, the dielectric loss of the film increased, widening the loops significantly.

8.4.2 Energy and Power Storage Characteristics of Nanocomposite Lead Titanate

Despite the large applied electric field, the high field loss reduced both the energy and power storage densities of the film. The energy and power storage densities for each loop in Figure 8-6, spanning an applied electric field range from 2.0 to 5.0 MV/cm, are given in Table 8-1. A plot of both energy and power density as a function of applied electric field are given in Figure 8-7. The maximum field sustained by the film was 5.0 MV/cm. The film recovered when the electric field was removed (the films did not reach catastrophic electrical breakdown), indicating that the increase in loss was due to an increase in conductivity, rather than a permanent damage mechanism.

Table 8-1. Energy Storage Density of Nanocomposite Lead Titanate

Maximum Electric Field MV/cm	Energy Storage Density ± Standard Deviation J/cm^3	Power Storage Density MW/cm^3
2.0	5.9 ± 0.5	21.1
2.5	8.8 ± 0.6	10.6
3.0	12.6 ± 0.9	5.0
3.5	16.8 ± 0.9	2.5
4.0	20.7 ± 1.0	1.2
4.5	24.9 ± 1.3	0.43
5.0	28.4 ± 1.2	0.19

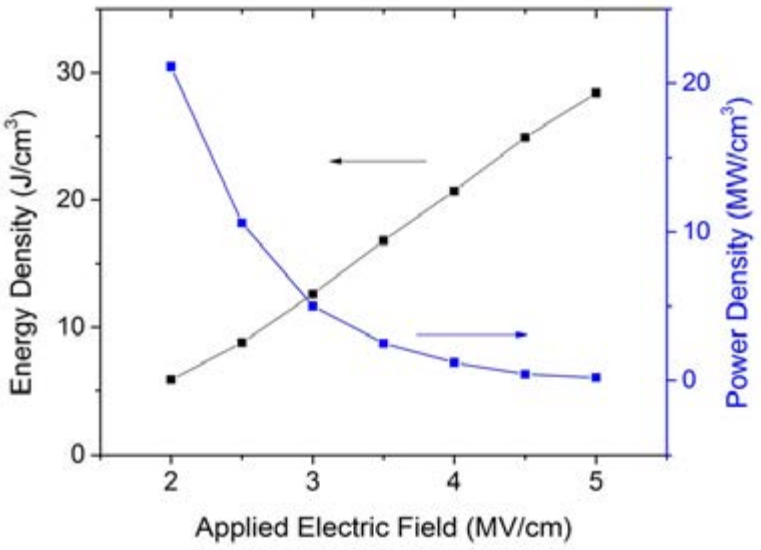

Figure 8-7. Energy and power storage density as a function of applied electric field. As the material was swept to higher electric fields, the dielectric loss in the film increased. Although the energy storage density of the film improved with applied electric field despite the increase in loss, the power storage density of the films decreased.

Figure 8-8 shows the polarization-electric field hysteresis loop for a film that was swept to a maximum applied electric field of 5.0 MV/cm, the electric field for which nanocomposite

lead titanate achieved its maximum energy storage density. The area that was calculated to determine the energy storage density is shaded. At this electric field, the energy storage density of the film was approximately 28 J/cm^3. The high breakdown strength of the material can likely be attributed to the amorphous lead titanate matrix of the film. The lack of structural periodicity of the amorphous matrix and the isolated, randomly distributed lead oxide nanocrystals do not present a conduction pathway through the film. The moderately high permittivity of the film was enhanced by the presence of lead oxide nanocrystals. Figure 8-9 shows the temperature dependence of the energy storage density. The decrease in the energy storage density at temperatures up to 150°C was attributable to a decrease in breakdown strength of the material at increased temperatures. As film temperature increased, the conductivity through the film also increased, promoting breakdown. At temperatures beyond 150°C, the energy storage density of the film drastically decreased.

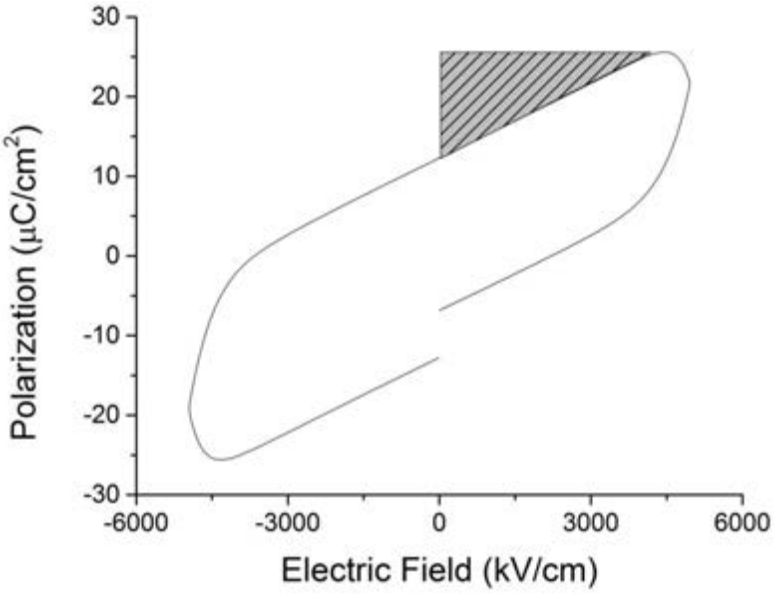

Figure 8-8. Polarization-electric field hysteresis loop for nanocomposite lead titanate at a maximum applied electric field of 5.0 MV/cm. At this electric field, the films attained their maximum energy storage density of ~28 J/cm^3 (calculated from the shaded area).

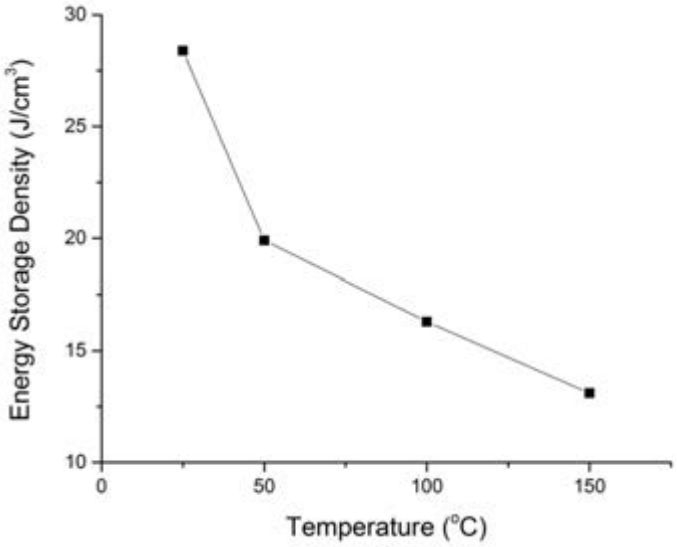

Figure 8-9. The energy storage density of nanocomposite lead titanate films as a function of temperature. The energy storage density exhibited a decrease as temperature was increased from room temperature to 150°C.

The high breakdown strength of these films, coupled with the moderate relative permittivity of the nanocomposite, resulted in a high energy storage density. It is possible that further improvements could be achieved using the nanocomposite lead titanate films via reduction of the dielectric loss at large applied electric fields. Among the avenues that should be explored are further densification of the film and the minimization of charge injection into the film. Finally, the dielectric properties of the material may be further improved by doping with niobium or lanthanum to lower the dielectric loss of lead titanate [21, 22, 23], potentially increasing the energy storage density of the films.

8.5 DC Properties of Nanocomposite Lead Titanate

The DC properties of nanocomposite lead titanate, such as the thin film leakage current and the high voltage I-V characteristics for relatively thicker films, are presented here.

8.5.1 Leakage Characteristics of Nanocomposite Lead Titanate

Figure 8-10 shows the leakage current density as a function of electric field for nanocomposite lead titanate films. The leakage current for this material is extremely low, on the order of 10^{-9} A/cm^2, which was attributed to the amorphous matrix of the film. As seen in Figure 8-10, the DC breakdown strength of the film was approximately 2.5 MV/cm. When the polarity of the electrodes was reversed, there was no change in either the magnitude of the leakage current or in the magnitude of the DC breakdown strength.

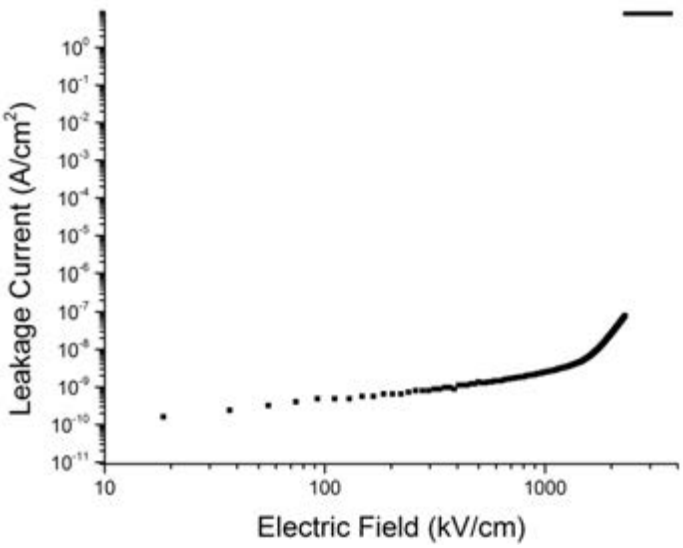

Figure 8-10. Leakage current density versus electric field for nanocomposite lead titanate. The nanocomposite lead titanate exhibited an extremely low leakage current density and DC breakdown strength of approximately 2.5 MV/cm.

8.5.2 High Voltage Behavior of Nanocomposite Lead Titanate

These films were processed at the relatively low annealing temperature of 400°C, so it may be possible to integrate these materials into displays or capacitors on glass substrates. Films with a thickness of 1.0 μm were deposited on platinized glass substrates (Eagle XG® Slim, Corning, Corning, NY) to determine the suitability of this substrate for nanocomposite lead titanate thin films. As expected, glass substrates were found to have an appropriate thermal budget for the deposition of nanocomposite lead titanate. These substrates have a room temperature thermal expansion coefficient of $35.5*10^{-7}$/°C [24]. At thicknesses greater than approximately 1.7 μm, cracks formed throughout the film. High voltage testing on a crack-free film revealed that a 1.0 μm film would reliably withstand 350 V, which corresponds to an applied electric field of 3.5 MV/cm, as seen in Figure 8-11. This was the highest voltage sustained by the material, as films with a thickness of 1.7 μm were only able to sustain 300V before the occurrence of breakdown. This is likely due to the increased probability of encountering a large critical flaw resulting from the deposition of films with many layers. These defects will reduce the maximum electric field that can be placed across the material before it undergoes catastrophic electrical breakdown.

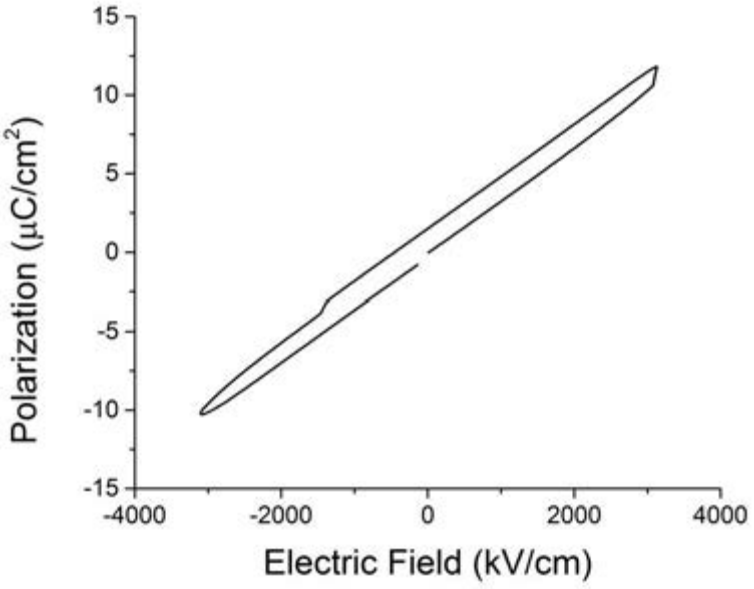

Figure 8-11. The polarization-electric field behavior for a 1.0 μm thick film of nanocomposite lead titanate prior to reaching breakdown.

8.6 Conclusions

Nanocomposite, lead-rich lead titanate ($Pb_{1.1}TiO_{3.1}$) thin films were investigated for their potential use in energy storage applications. The films were fabricated via chemical solution deposition using a precursor solution that was synthesized with an inverted mixing order process. The films were smooth and dense. Transmission electron microscopy showed the nucleation of isolated nanocrystals of lead oxide in an amorphous lead titanate matrix. The nanocomposite had a permittivity of 33 and a low loss tangent of 0.0008. The DC breakdown strength of the material was approximately 2.5 MV/cm, while the 1 kHz AC breakdown strength of the material exceeded 5 MV/cm. The material exhibited low leakage currents (on the order of 10^{-9} A/cm^2), and a 1 kHz energy storage density of ~28 J/cm^3. The maximum energy storage density occurred when the

material was subjected to an electric field of 5.0 MV/cm, and was limited by dielectric loss in the film.

8.7 References

1] V. Tomer, C. A. Randall, G. Polizos, J. Kostelnick and E. Manias, "High- and low-field dielectric characteristics of dielectrophoretically aligned ceramic/polymer nanocomposites," *Journal of Applied Physics,* vol. 103, p. 034115, 2008.

2] P. Barber, S. Balasubramanian, Y. Anguchamy, S. Gong, A. Wibowo, H. Gao, H. J. Ploehn and H.-C. zur Loye, "Polymer composite and nanocomposite dielectric materials for pulse power energy storage," *Materials,* vol. 2, pp. 1697-1733, 2009.

3] A. V. Wagner, G. W. Johnson and T. J. W. Barbee, "High energy density capacitors fabricated by thin film technology," *Materials Research Society Symposium Proceedings,* vol. 574, pp. 219-224, 1999.

4] D. S. McLachlan, M. Blaszkiewicz and R. E. Newnham, "Electrical resistivity of composites," *Journal of the American Ceramic Society,* vol. 73, no. 8, pp. 2187-2203, 1990.

5] D. S. McLachlan and G. Sauti, "The AC and DC conductivity of nanocomposites," *Journal of Nanomaterials,* pp. 1-9, 2007.

6] C. W. Nan, Y. Shen and J. Ma, "Physical properties of composites near percolation," *Annual Review of Materials Research,* vol. 40, pp. 131-151, 2010.

7] C. A. Randall, S. Miyazaki, K. L. More, A. S. Bhalla and R. R. Newnham, "Structural-property relationships in dielectrophoretically assembled $BaTiO_3$ nanocomposites," *Materials Letters,* vol. 15, no. 1, pp. 26-30, 1992.

8] W.-Z. Cai, S.-T. Tu and J.-M. Gong, "A physically based percolation model of the effective electrical conductivity of particle filled composites," *Journal of Composite Materials,* vol. 40, no. 23, pp. 2131-2142, 2006.

9] M. Narkis and A. Vaxman, "Resistivity behavior of filled electrically conductive crosslinked polyethylene," *Journal of Applied Polymer Science,* vol. 29, pp. 1639-1652, 1984.

10] K. P. Sau, T. K. Chaki and D. Khastgir, "Conductive rubber composites from different blends of ethylene-propylene-diene rubber and nitrile rubber," *Journal of Materials Science,* vol. 32, pp. 5717-5724, 1997.

A. J. Moulson and J. M. Herbert, Electroceramics: Materials, Properties, Applications, West

11] Sussex, England: John Wiley & Sons, Ltd, 2003.

12] P. J. Phillips, "Morphology-electrical property relations in polymers," *IEEE Transactions on Electrical Insulation,* vols. EI-13, no. 2, pp. 69-81, 1978.

13] G. Sethi, M. Olszta, J. Li, J. Sloppy, M. W. Horn, E. C. Dickey and M. T. Lanagan, "Structure and dielectric properties of amorphous tantalum pentoxide thin film capacitors," *2007 Annual Report Conference on Electrical Insulation and Dielectric Phenomena,* pp. 815-818, 2007.

14] M. J. Haun, "Thermodynamic theory of the lead zirconate-titanate solid solution system," Ph.D. Thesis, The Pennsylvania State University, 1988.

15] A.-C. Dippel, T. Schneller and R. Waser, "Thin films of undoped lead titanate: Morphology and electrical properties," *Integrated Ferroelectrics,* vol. 98, no. 1, pp. 3-10, 2008.

16] T. Nakamura, M. Takashige, H. Terauchi, Y.-i. Miura and W. N. Lawless, "The structural, dielectric, Raman-spectral and low-temperature properties of amorphous $PbTiO_3$," *Japanese Journal of Applied Physics,* vol. 23, no. 10, pp. 1265-1273, 1984.

17] R. A. Assink and R. Schwartz, "^{1}H and ^{13}C NMR investigations of $Pb(Zr,Ti)O_3$ thin-film precursor solutions," *Chemistry of Materials,* vol. 5, pp. 511-517, 1993.

18] R. Schwartz, "Chemical solution deposition of perovskite thin films," *Chemistry of Materials,* vol. 9, pp. 2325-2340, 1997.

19] G. L. Brennecka, J. F. Ihlefeld, J.-P. Maria, B. A. Tuttle and P. G. Clem, "Processing technologies for high-permittivity thin films in capacitor applications," *Journal of the American Chemical Society,* vol. 93, no. 12, pp. 3935-3954, 2010.

20] C. J. Brinker and G. W. Scherer, Sol-gel Science: the Physics and Chemistry of Sol-gel Processing, Boston: Academic Press, 1990.

21] K. Furuta and K. Uchino, "Electric-field-induced strain in $(Pb,La)(Zr,Ti)O_3$ ceramics," *Advanced Ceramic Materials,* vol. 1, pp. 61-63, 1986.

22] I. Stolichnov, A. Tagantsev, N. Setter, S. Okhonin, P. Fazan, J. S. Cross and M. Tsukada, "Dielectric breakdown in $(Pb,La)(Zr,Ti)O_3$ ferroelectric thin films with Pt and oxide electrodes," *Journal of Applied Physics,* vol. 87, pp. 1925-1931, 2000.

23] J. S. Cross, M. Fujiki, M. Tsukada, Y. Kotaka and Y. Goto, "Microstructure and electrical properties of chemical solution deposition $(Pb,La)(Zr,Ti)O_3$ thin films on Pt electrodes," *Journal of Materials Research,* vol. 14, no. 11, p. 4366–4371, 1999.

24] Corning, "Corning Eagle XG Slim Glass," August 2013. http://www.corning.com/WorkArea/showcontent.aspx?id=64215.

Chapter 9

Conclusions and Recommendations for Future Work

This chapter briefly summarizes the findings of the work documented in this thesis. In addition, several suggestions for related future work are provided.

9.1 Conclusions

The development of dielectric thin films for energy storage applications was intended to accomplish two broadly defined objectives. The first part of this thesis described the deposition, compositional tuning, microstructure, and dielectric properties of crystalline bismuth pyrochlore films for energy storage applications. The second portion of this thesis discussed the deposition and characterization of nanocomposite films processed at temperatures compatible with polymeric or glass substrates.

9.1.1 Crystalline Bismuth Pyrochlores for Dielectric Energy Storage Applications

Dielectric thin films with high energy and high power storage densities are required for power electronics. The bismuth pyrochlores are a compositionally tunable family of materials that possess high breakdown strengths and medium permittivities in addition to exhibiting low loss tangents, making them candidates for dielectric energy storage. Thin films of cubic pyrochlore bismuth zinc niobate, bismuth zinc tantalate, and bismuth zinc niobate tantalate, were

fabricated using a solution chemistry based upon the Pechini method. As described in Chapter 4, this novel solution chemistry is advantageous because it avoids the use of teratogenic solvents. Reasonably dense films were prepared using a set of optimized processing parameters that were described in Chapter 4 and Appendix A. Based on pyrolysis studies, it was concluded that a pre-pyrolysis heat treatment was needed to deposit dense films; when this step was omitted, the films exhibited extensive porosity. The films fabricated using this solution chemistry had small grains that were approximately 27 nm in lateral size and 35 nm through the thickness of the film. Chapter 6 linked the fine-grained microstructure of these films to the dielectric properties of the material. The grain boundaries were found to be highly resistive relative to the interior of the grain, and it was concluded that the presence of many resistive grain boundaries impeded conduction through the films, resulting in high breakdown strengths.

Chapter 5 described the characterization of thin films of cubic pyrochlore bismuth zinc niobate ($Bi_{1.5}Zn_{0.9}Nb_{1.5}O_{6.9}$), a weakly nonlinear dielectric, for use in energy storage applications. The films demonstrated a medium relative permittivity of 145 and low loss tangents. At frequencies of 1 kHz, the films exhibited a loss tangent of 0.00065, and sustained a maximum field of approximately 4.7 MV/cm. At 100 Hz and 10 kHz, the maximum field sustained by the films increased to 5.0 MV/cm and 5.1 MV/cm. At a measurement frequency of 10 kHz, the maximum energy storage density achieved was 60.8 J/cm^3 while at a measurement frequency of 100 Hz, the maximum energy density was 46.7 J/cm^3. The films maintained a high energy storage density across a range of frequencies and temperatures. As the temperature was increased to 200°C, the maximum energy storage density remained high; as an example, the 10 kHz maximum energy density was 27.3 J/cm^3. Cubic pyrochlore bismuth zinc niobate was also demonstrated to have a DC breakdown strength between 3 and 4 MV/cm and a low field leakage current of approximately 10^{-10} A/cm^2.

Chapter 6 discussed the modification of bismuth zinc niobate with tantalum as a method to increase the band gap, and, consequently the breakdown strength, of this substitutional solid solution. As the tantalum concentration of the solid solution increased, the dielectric breakdown strength of the material improved. Films of bismuth zinc tantalate ($Bi_{1.5}Zn_{0.9}Ta_{1.5}O_{6.9}$), an end member of the solid solution, were demonstrated to possess a relative permittivity of 55, loss tangents of 0.0004, and a 10 kHz breakdown strength of 6.1 MV/cm. The maximum discharged energy storage density for the bismuth zinc tantalate films was 60.7 J/cm^3 at 10 kHz, which is comparable with the maximum discharged energy storage density of the bismuth zinc niobate films in Chapter 5. In this case, any improvement in the energy storage density of the tantalate composition due to an enhancement in breakdown strength, reduced tunability, and lower high field loss was offset by the reduction in relative permittivity of the bismuth zinc tantalate. Intermediate bismuth zinc niobate tantalate compositions were also explored to enhance the energy storage density. At an optimal tantalum concentration of ten mole percent, the maximum field sustained by the bismuth zinc niobate tantalate films at 10 kHz was 5.5 MV/cm, and the permittivity was 122. This improvement in the breakdown strength compensated for the reduction in the relative permittivity of material, which led to a high discharged energy storage density. At a measurement frequency of 10 kHz, the $Bi_{1.5}Zn_{0.9}Nb_{1.35}Ta_{0.15}O_{6.9}$ films exhibited a maximum recoverable energy storage density of 66.9 J/cm^3, and at 1 kHz, the recoverable energy storage density was 54.1 J/cm^3. As can be seen in Figure 9-1 and discussed in section 9.1.3, this is the highest reproducible energy storage density reported in the literature.

9.1.2 Nanocomposite Dielectrics for Flexible Energy Storage Applications

Nanocomposite films consisting of a nanocrystalline fluorite related to delta-bismuth oxide in an amorphous bismuth zinc niobate tantalate matrix were fabricated in Chapter 7. These

films were prepared by reducing the citric acid concentration of the precursor solution, relative to the crystalline films, allowing the removal of organic species at a maximum processing temperature of 350°C. The nanocomposite had a relative permittivity of 50 and dielectric losses on the order of 0.03. For measurement frequencies of 1 kHz and 10 kHz, the nanocomposite demonstrated a breakdown strength of 3.8 MV/cm, and a room-temperature energy storage density of approximately 40 J/cm^3, which is the highest reported energy storage density for a material processed at a maximum temperature of 350°C, as seen in Figure 9-1 and discussed in section 9.1.3. Nanocomposite films that were deposited on platinum-coated polyimide substrates underwent compressive and tensile flexible testing and were subjected to a maximum strain of 0.10%. After bending the films around a minimum bend diameter of 7 mm 30,000 times, the energy storage density of the films was unchanged, indicating that nanocomposite bismuth zinc niobate tantalate films may be suitable for flexible energy storage applications.

Chapter 8 described the preparation and characterization of thin films of nanocomposite lead titanate, to demonstrate the broader applicability of the nanocomposite approach to developing energy storage dielectrics at low processing temperatures. The films were deposited using an inverted mixing order solution preparation, and annealed at a maximum temperature of 400°C. X-ray diffraction indicated the presence of nanocrystalline ordering, and transmission electron microscopy confirmed the nucleation of isolated nanocrystals of lead oxide in an amorphous lead titanate network. The lead titanate nanocomposite demonstrated a relative permittivity of 33 and a low loss tangent of 0.0008. The AC breakdown strength of the material exceeded 5.0 MV/cm, resulting in an energy storage density of ~28 J/cm^3.

9.1.3 Improvements in Dielectric Energy Storage: Impacting the Energy Storage Landscape

As discussed in section 2.1.2, a comparison of the maximum discharged energy densities reported in the literature can be difficult due to differences between measurements. To contextualize the energy storage density results of this thesis and to facilitate some assessment of the usefulness of these materials, Figure 9-1 shows the maximum reported energy storage density of several state of the art energy storage dielectrics as a function of their maximum processing temperature [1, 2, 3, 4, 5, 6, 7, 8, 9, 10, 11, 12, 13, 14]. Because many of the data points were measured under different conditions, the figure should be regarded as a guideline only. The materials investigated in this thesis are highlighted in bold, blue text. As can be seen from the figure, the dielectrics developed in this work possess some of the highest energy storage densities reported in the literature, confirming the usefulness of the $Bi_{1.5}Zn_{0.9}Nb_{(1.5-x)}Ta_xO_{6.9}$ solid solution, nancomposite bismuth zinc niobate tantalate, and nanocomposite lead titanate for dielectric energy storage applications.

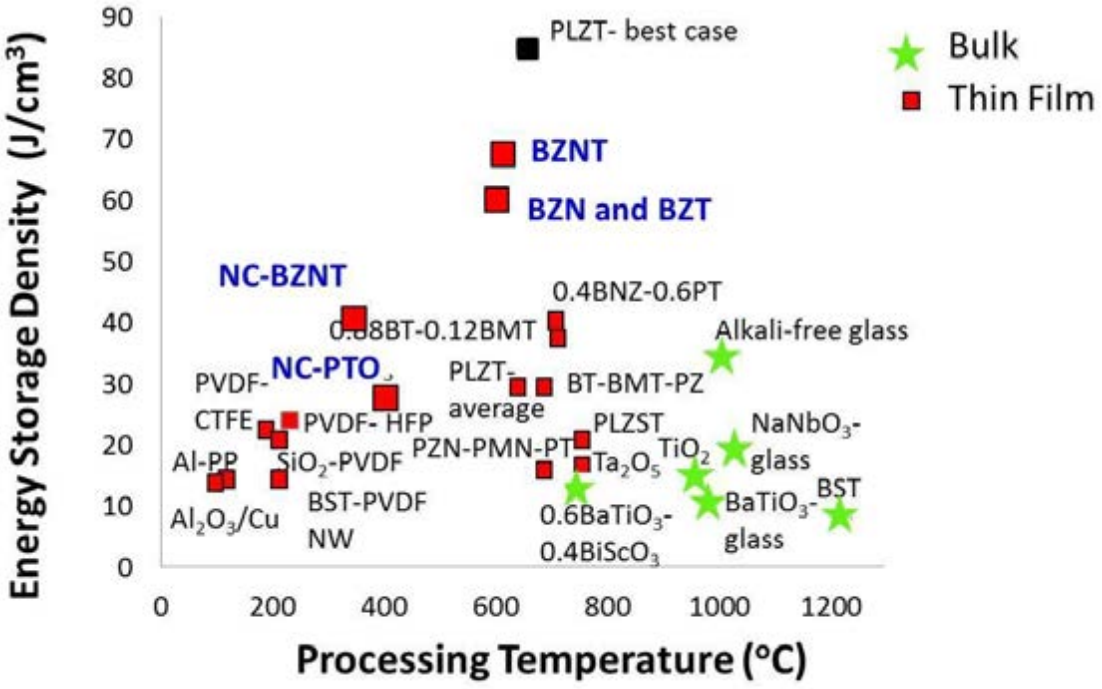

Figure 9-1. Energy storage density as a function of maximum processing temperature for several state of the art dielectrics [1, 2, 3, 4, 5, 6, 7, 8, 9, 10, 11, 12, 13, 14]. The abbreviations are: PLZT, lead lanthanum zirconate titanate; PLZST, lanthanum-doped lead zirconate stannate titanate; PVDF, polyvinylidene fluoride; HFP, hexafluoropropene; CTFE, chlorotrifluoroethylene; PP, polypropylene; BST, barium strontium titanate; Al-PP, aluminum polypropylene nanocomposite. The results of this thesis are shown in the blue, bold text where BZN stands for bismuth zinc niobate, BZT for bismuth zinc tantalate, BZNT for bismuth zinc niobate tantalate, NC-BZNT for nanocomposite bismuth zinc niobate tantalate, and NC-PTO for nanocomposite lead titanate.

As a summary of the materials investigated in this work, Table 9-1 lists the maximum processing temperature, relative permittivity, maximum sustained electric field or breakdown

strength at 10 kHz, and the room-temperature 10 kHz energy storage density for each of the compositions examined.

Table 9-1. Summary of the Maximum Processing Temperatures and Dielectric Properties of Investigated Compositions

	Maximum Processing Temperature (°C)	Relative Permittivity	10 kHz Breakdown Strength (MV/cm)	10 kHz Energy Storage Density (J/cm^3)
$Bi_{1.5}Zn_{0.9}Nb_{1.5}O_{6.9}$	600	145 ± 5	5.1	60.8 ± 2.0
$Bi_{1.5}Zn_{0.9}Ta_{0.075}Nb_{1.425}O_{6.9}$	600	130 ± 5	5.4	61.7 ± 2.2
$Bi_{1.5}Zn_{0.9}Ta_{0.15}Nb_{1.35}O_{6.9}$	600	122 ± 4	5.5	66.9 ± 2.4
$Bi_{1.5}Zn_{0.9}Ta_{0.225}Nb_{1.275}O_{6.9}$	600	108 ± 4	5.7	65.0 ± 2.3
$Bi_{1.5}Zn_{0.9}Ta_{1.5}O_{6.9}$	600	55 ± 2	6.1	60.7 ± 2.0
$Bi_{1.5}Zn_{0.9}Ta_{0.15}Nb_{1.335}Mn_{0.015}O_{6.9}$	600	134 ± 4	3.0	33.1 ± 1.6
$Bi_{1.5}Zn_{0.882}Ti_{0.018}Ta_{0.15}Nb_{1.5}O_{6.9}$	600	117 ± 4	4.5	51.6 ± 2.4
$Bi_{1.5}Zn_{0.9}Ta_{0.15}Nb_{1.32}Si_{0.03}O_{6.9}$	600	114 ± 4	5.6	67.9 ± 3.5
$Bi_2Zn_{2/3}Nb_{4/3}O_7$	600	71 ± 2	4.3	45.3 ± 1.9
Nanocomposite $Bi_{1.5}Zn_{0.9}Ta_{0.15}Nb_{1.35}O_{6.9}$	350	50 ± 2	3.7	40.2 ± 1.7
Nanocomposite $Pb_{1.1}TiO_{3.1}$	400	33 ± 1	5.0	28.4 ± 1.2

To facilitate a comparison between the materials investigated in this thesis with several of the metrics required for commercial pulsed power applications, Table 9-2 lists the energy storage densities, power delivery requirements (where available), and approximate frequency ranges for the dielectrics currently used in these devices. The energy storage densities of the materials investigated in this work exceed those of the dielectrics currently used in these commercial applications. The future work discussed in the next section of this thesis, particularly the reliability and lifetime testing described in section 9.2.2, should determine the viability of the bismuth-based pyrochlores as a replacement for commercially available energy storage dielectrics.

Table 9-2. Comparison of the Energy Storage Density Requirements for Commercial Pulsed Power Applications

	Current Capacitor Material	Frequency Requirements	Energy Storage Density (J/cm^3)	Power Metrics
Commercial Capacitors [15]	Polypropylene	1 Hz – 10 kHz	~2.0	---
Implantable Heart Defibrillator [16]	Aluminum or tantalum electrolytic	1 kHz	5.0	1000 W
Navy Defense Applications [17]	Polypropylene	1-10 kHz	2.68	---
Future Power Electronics [18]	---	>1 kHz	10.0	---

9.2 Recommendations for Future Work

This section provides several suggestions for possible future work stemming from observations made during the course of this study.

9.2.1 Determining the Conduction Mechanism for Bismuth Zinc Niobate Tantalate Thin Films

A determination of the conduction mechanism for these bismuth zinc niobate tantalate films could lead to improvements in both the AC and DC breakdown strengths of the films. The conduction mechanism of films is often extracted by measuring the temperature-dependent leakage current, plotting the data according to the conductivity equations in Table 9-3 [19], and fitting the linear portion of the data. Using the slope and y-intercept of the linear fit, a value for the refractive index and the activation energy for conduction can be extracted; if these extracted

quantities are reasonable, it is likely that the equation used corresponds with the dominant conduction mechanism.

Table 9-3. Possible Thin Film Conduction Mechanisms [19]

Conduction Mechanism	I-V Characteristic Equation	Axes for Conduction Plot
Schottky Emission	$J_S = AT^2 \exp\left[-\frac{q\varphi_B}{kT}\right] \exp\left[\frac{q\sqrt{qE/4\pi\epsilon_0\epsilon_\infty}}{kT}\right]$	$Ln(J/T^2)$ versus $E^{1/2}$
Tunneling	$J_T = \frac{q^2E^2}{8\pi h\varphi_B} \exp -\left[\frac{8\pi(2m)^{\frac{1}{2}}}{3hqE} * (q\varphi_B)^{\frac{3}{2}}\right]$	$Ln(J/E^2)$ versus 1/E
Space Charge	$J_{SCL} = \frac{9\mu\epsilon_0\epsilon_\infty}{8}\frac{E^2}{d}$	Ln(J) versus Ln(E)
Ionic Conduction	$J_{ion} = \frac{aE}{kT} \exp\left[-\frac{E}{kT}\right]$	Ln(J/E) versus 1/T
Intrinsic Conduction	$J_{Int} = bT^{3/2} \exp\left[-\frac{E_G}{2kT}\right] E$	$Ln(J/T^{3/2})$ versus E
Poole-Frenkel Emission	$J_{PF} = cE \exp\left[-\frac{q\varphi_i}{kT}\right] \exp\left[\frac{q\sqrt{qE/\pi\varepsilon_0\epsilon_\infty}}{kT}\right]$	Ln(J/E) versus $E^{1/2}$

The following abbreviations have been made for the variables in Table 9-3: *J*, current density; *A*, Richardson constant; *T*, temperature; *q*, charge of an electron; Φ_B, Schottky barrier; *k*, Boltzmann constant; *E*, electric field; ε_o, permittivity in a vacuum; ε_∞, high frequency relative permittivity; *h*, Planck's constant; *m*, mass of an electron; μ, mobility; *d*, distance over which current flow occurs; *a*, *b*, and *c,* constants; E_G, band gap; Φ_i, trap energy level.

Rather than fitting data to all six possible conduction mechanisms in Table 9-3, several assumptions and observations were made prior to fitting, allowing the number of possible conduction mechanisms to be reduced. For example, as seen in Figure 9-2, the current-voltage characteristics and the breakdown strength of $Bi_{1.5}Zn_{0.9}Nb_{1.35}Ta_{0.15}O_{6.9}$ films show a clear dependence on temperature. Thus, tunneling cannot be the conduction mechanism in these films,

as tunneling is temperature independent. Ultimately, Schottky and Poole-Frenkel conduction mechanisms were investigated in detail.

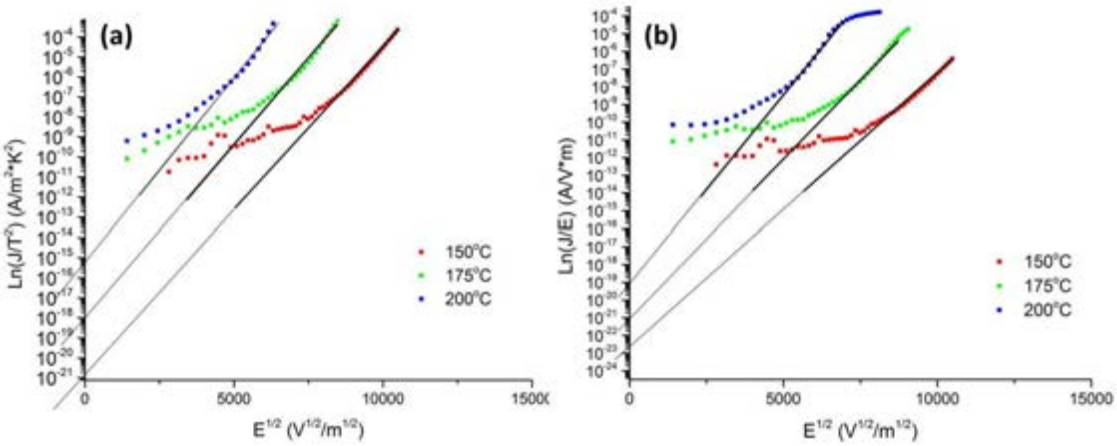

Figure 9-2. The current-voltage characteristics as a function of temperature for (a) Schottky and (b) Poole-Frenkel conduction through $Bi_{1.5}Zn_{0.9}Nb_{1.35}Ta_{0.15}O_{6.9}$ films. There is clearly a transition in conduction mechanism with increasing field. Quasi-linear fits could be drawn for both cases.

The leakage current of $Bi_{1.5}Zn_{0.9}Nb_{1.35}Ta_{0.15}O_{6.9}$ films at 150°C, 175°C, and 200°C were measured, and the data were fit to both Schottky and Poole-Frenkel conduction equations. As seen in Figure 9-2, the data do not exhibit a clear linear region. As a result, linear fits could be drawn with a great deal of subjectivity. The linear fit of the I-V characteristics in Figure 9-2 shows one of the possible fits. Due to the nonlinearity of the data, it was concluded that a mixed conduction mechanism was likely responsible for charge transport through these films. Although further investigation is necessary to fully characterize conduction in these films, it is likely that Schottky barriers are a critical factor to conduction, as shown in Figure 9-3. When the bottom electrode was changed from platinum to lanthanum nickel oxide, the magnitude of the leakage current increased by several orders of magnitude and the DC breakdown strength of the films decreased. This indicates that the Schottky barrier created at the interface of the dielectric and the

bottom electrode is important to the conduction behavior of the material. A better knowledge of the conduction mechanism should be pursued in the future to enable further increases in energy storage in this family of materials.

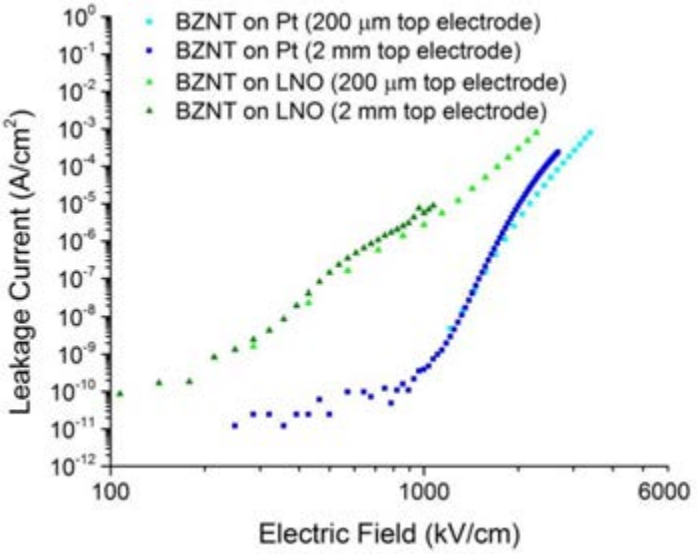

Figure 9-3. The current-voltage characteristics for $Bi_{1.5}Zn_{0.9}Nb_{1.35}Ta_{0.15}O_{6.9}$ films deposited on a platinum bottom electrode (blue squares) and a lanthanum nickel oxide (LNO) bottom electrode (green triangles). The magnitude of the leakage current and the breakdown strength is affected by the composition of the bottom electrode. The electrode size refers to the electrode diameter.

9.2.2 Examining the Reliability of Bismuth Zinc Niobate Tantalate Thin Films

As the use of personal electronics increases, the lifetime and reliability of the materials within the device becomes increasingly important. To determine the usefulness of these films for commercial applications, reliability and mean time to failure measurements should be performed. Highly accelerated lifetime testing (HALT) may be used to determine degradation mechanisms and the lifetime of these films. During HALT measurements, constant voltages are applied to a

sample at several temperatures. The time to failure is measured for a set of capacitors, and the expected lifetimes under different conditions can be predicted using the Eyring equation:

$$\frac{t_1}{t_2} = \frac{V_1}{V_2}^{-N} \exp[\frac{E_a}{k_B}\left(\frac{1}{T_1} - \frac{1}{T_2}\right)]$$

where t is the mean time to failure, V is the applied voltage, N is the voltage acceleration factor, E_a is the activation energy, k_B is Boltzmann's constant, and T is the measurement temperature [20]. Preliminary HALT measurements on thin film samples of pulsed laser deposited amorphous bismuth zinc niobate demonstrated an activation energy of 0.66 ± 0.49 eV [21]; the large error bars for this value were likely due to differences between samples that could be associated with processing, as each sample yielded only one or two electrodes that were used for data collection. Although this activation energy is lower than that typically exhibited by $BaTiO_3$ multilayer ceramics (1.1 eV [22]) in which the migration of oxygen vacancies under electric field is known to be the dominant degradation mechanism [23], this activation energy is comparable with values reported for some bulk pyrochlore oxides. For example, the reported activation energies for oxygen vacancy migration in samples of bulk $Nd_2Zr_2O_7$ and $Sm_2Zr_2O_7$ ceramics were 0.76-0.84 eV and 0.69 eV, respectively [24]. However, the samples of bismuth zinc niobate tantalate in this work exhibited resistivity values for the grain boundaries which were two orders of magnitude higher than the resistivity values for the grain interior. The increased resistivity of the grain boundary may be due to oxidation, which suppresses the formation of oxygen vacancies [25, 26, 27]. Therefore, it is possible that these films exhibit a different degradation mechanism than other oxide pyrochlores.

In addition to HALT measurements to investigate the reliability and degradation characteristics of these bismuth zinc niobate tantalate films, charge to breakdown measurements should be pursued. This approach measures the total charge injected into a dielectric layer prior to breakdown [28]. This model is useful in assessing the quality of some gate oxides, as SiO_2, for

example, has been reported to undergo breakdown when a critical injected charge (or, a critical density of traps) has been reached [29, 30, 31]. Although several methods can be used to measure the charge to breakdown of a dielectric, one of the most straight-forward techniques applies a constant current to the sample while the voltage is monitored as a function of time [29]. After the devices fails, the charge to breakdown can be calculated as the product of the applied current and the time to failure. This method probes the existence of trap states in the material. As current is initially applied to the sample, charge is trapped in pre-existing trap states, as indicated by a change in the measured voltage [28]. Under constant current, traps will be generated in the sample due to damage sustained by the material; by inducing sufficient damage, the oxide will experience breakdown [31]. Deep-level transient spectroscopy (DLTS) could also be used in the future to probe and characterize the existence of trap states in these films.

9.2.3 Improving the Processing of Bismuth Pyrochlore Thin Films

The importance of processing on the microstructure and dielectric properties of these bismuth pyrochlore thin films was discussed in Chapter 4. Improvements in the relative permittivity, breakdown strength, and the resulting dielectric energy storage density were enabled by the deposition of dense films. It may be possible to further enhance the performance of these films through improvements in processing, specifically by optimizing the grain size and controlling the residual carbon content in the films prior to crystallization.

9.2.3.1 Confirming the Relationship between Grain Size and Breakdown Strength

The link between the fine grained microstructure and the high breakdown strengths observed in these films was examined in section 6.2.2.4. Here, impedance spectroscopy was used to quantify the contributions of both the grain interior and the grain boundaries on the overall resistivity of the films; it was found that highly resistive grain boundaries exist in the material, which impede conduction through the film and enhance the breakdown strength. Further experiments should be done to confirm the relationship between the film microstructure and dielectric properties, which may contribute to the optimization of the energy storage density. To conclusively relate the breakdown strength to the microstructure, the grain size of the films could be modulated and the density of grain boundaries through the film thickness correlated to changes in the breakdown strength. If the resistivity of the grain boundaries enhances the breakdown strength of these films, the formation of smaller grains should improve the breakdown strength due to an increase in the number of grain boundaries. One potential route to achieve this would be to vary nucleation conditions for the crystalline phase to maximize the nucleation density. Additionally, the composition of these grain boundaries should be probed using high resolution transmission electron microscopy to confirm whether the high resistivity was due to oxidation of the grain boundaries.

9.2.3.2 Investigating the Residual Carbon Content of Pyrolyzed Thin Films

The ability to detect and characterize residual carbon in these films may enable additional improvement in the film properties. Chapter 7 discussed the deposition of nanocomposite bismuth zinc niobate tantalate films. Infrared spectroscopy, shown in Figure 7-3, for example, was used to detect organic species remaining in the nanocomposite film after deposition. The

lack of peaks corresponding to the vibrations of organic functional groups indicated the absence of organic species from the films exceeding the 0.1 wt% level [32]. Thus, it is possible that residual organic species remain in the film after the 350°C pyrolysis treatment. Residual carbon has been reported to affect the crystallization behavior of materials and to increase leakage current through the film [33, 34, 35]. As there have been relatively few studies focused on the possible influence of residual carbon content (<0.5 – 1%) on crystallization temperature [35], it is possible that there may be ramifications on the crystallization temperature of the nanocomposite films. Secondary ion mass spectrometry, which has a routine detection limit on the order of ppm, which corresponds to 0.0001 wt% [36], could be used to detect residual carbon content in films.

9.2.4 Further Development of Bismuth Pyrochlore Nanocomposites

As illustrated in Chapters 7 and 8, one approach to maximizing the dielectric energy storage density of materials processed at low temperatures is through the fabrication of nanocomposites. The nanocomposite thin films developed in this work were composed of a medium permittivity crystalline material in an amorphous matrix. As discussed in Chapters 7 and 8, the amorphous host was intended to increase the breakdown strength, while the crystalline ceramic was intended to increase the permittivity of the material [9, 37]. Although the relative permittivity of amorphous materials is lower than that of crystalline materials, a high energy storage density may be obtained if this reduction in permittivity is compensated by an enhancement in breakdown strength. The compromise between relative permittivity and breakdown strength in the bismuth zinc niobate tantalate nanocomposites should be explored by systematically varying the volume fraction of the crystalline phase in the system. To quantify the contributions of the crystalline and amorphous phases to the nanocomposite resistivity, this investigation should be coupled to impedance spectroscopy.

In addition to the crystalline-amorphous nanocomposite materials examined here, it may be advantageous to fabricate crystalline-polymer nanocomposites using bismuth pyrochlore nanoparticles embedded in a polymeric matrix. In addition to potentially achieving higher breakdown strengths and energy storage densities than the crystalline-amorphous nanocomposite films, the use of a polymer matrix may allow processing of nanocomposites with a high energy storage density at temperatures that cannot be achieved with the nanocomposite approach in Chapters 7 and 8.

9.2.5 Low Temperature Deposition of Crystalline Bismuth-Based Pyrochlore Thin Films

The energy storage density of crystalline $Bi_{1.5}Zn_{0.9}Nb_{1.35}Ta_{0.15}O_{6.9}$ was found to exceed that of the nanocomposite films of the same composition prepared in this thesis. It may be possible to improve the energy storage density of films processed on flexible polyimide substrates via low-temperature crystallization. It was suggested that the formation of nanoparticles during pyrolysis act as nucleating agents for the remainder of the film, resulting in the fine-grained microstructure observed here. If the grain structure and highly resistive grain boundaries are retained during low-temperature crystallization, it may be possible to fabricate crystalline thin films of $Bi_{1.5}Zn_{0.9}Nb_{1.35}Ta_{0.15}O_{6.9}$ on polyimide substrates with improved energy densities. Several approaches to low temperature crystallization could be pursued, such as pulsed laser annealing or aerosol deposition with a post-deposition recrystallization.

9.2.5.1 Pulsed Laser Annealing of Nanocomposite Bismuth Zinc Niobate Tantalate

Pulsed laser annealing could be used to crystallize sol-gel deposited nanocomposite films at reduced substrate temperatures. Although there are relatively limited reports on the use of

pulsed laser annealing for the crystallization of ceramic thin films, pulsed laser annealing has been used to successfully crystallize $Ba_{0.7}Sr_{0.3}TiO_3$ [38], $SrFe_yCo_{1-y}O_{2.5+x}$ [39], $Bi_{1.5}Zn_{0.5}Nb_{1.5}O_{6.5}$ [40], and various lead zirconate titanate (PZT) compositions [41] using reduced substrate temperatures. Cheng et al. demonstrated [40] that cubic pyrochlore bismuth zinc niobate could be crystallized at substrate temperatures of 400°C using pulsed laser annealing. Although pulsed laser annealing initiated crystallinity within the film, a second annealing step in oxygen for two hours completed crystallization. It was hypothesized that the laser annealing process generated nuclei within the film, while the oxygen anneal completed crystallization from the laser generated nuclei. These films exhibited similar permittivity values, loss tangents, breakdown strengths, and optical properties to crystalline bismuth zinc niobate thin films in the literature [42, 43, 44]. The nanocomposite films discussed in this thesis consisted of a nanocrystalline nucleating agents dispersed throughout an amorphous matrix; thus, it may be possible to use these particles to lower the temperature required for crystallization to at least 350°C using pulsed laser annealing.

9.2.5.2 Aerosol Deposition of Crystalline Bismuth Zinc Niobate Tantalate

Aerosol deposition could be pursued as a method to deposit crystalline films at room temperature [45, 46]. In the aerosol deposition technique, submicron sized particles are accelerated by gas flow at a substrate. Although the actual deposition mechanism underlying this technique has reached no consensus in the literature, it is likely that as the particles collide and interact with the substrate, the kinetic energy of the accelerated particles is converted into bonding energy between both the substrate and the particles and the particles with one another [45, 47, 48]. This technique has been used to grow phase pure films of crystalline Al_2O_3 [46], PZT [46], AlN [47], and $MgBr_2$ [47] at room temperature. The resulting films, which grow at a rate of one to fifty microns per minute [45, 47], have been shown to possess densities in excess of

95% of the theoretical density [45, 46]. Recent results by Balachandran et al. [49] demonstrated the room-temperature aerosol deposition of eight micron thick films of crystalline lanthanum-doped PZT on aluminum foil substrates. These films possessed a zero-field relative permittivity of 80, low dielectric losses of 0.02, and breakdown fields of approximately 1 MV/cm [49, 50]. These films had an energy storage density of approximately 6 J/cm^3 [50]. Three micron thick films of lanthanum-doped PZT on aluminum foil substrates were bent around a minimum bend radius of 1.04 mm [49]; no changes in the dielectric properties were observed after bending [50]. It would be interesting to deposit films of crystalline bismuth zinc niobate tantalate on polymeric substrates at room temperature using this technique.

9.2.5.3 UV-Assisted Processing of Bismuth-Based Thin Films

The growth of crystalline complex oxide thin films, such as $PbTiO_3$ and $BiFeO_3$, has been accomplished at maximum processing temperatures of 400°C via UV-assisted processing [51]. These films were fabricated using chemical solution deposition with solutions that were prepared using an aqueous citrate method [52]. Following spin casting, the films were dried at 100°C and 200°C for ten minutes. The films were then pyrolyzed under a UV lamp (wavelength = 222 nm) for ten minutes at 270°C and 350°C. Finally, the films were annealed at 400°C for one hour. It was demonstrated [51] that many of the species that formed during the decomposition of citric acid during pyrolysis are UV-active. As described in section 4.3.2.2 many of these species are also evolved during the drying and pyrolysis steps that were used to deposit films throughout this work. To verify that these dried and partially pyrolyzed films are UV-active, UV-Vis spectroscopy was performed. Figure 9-4 shows the UV-Vis spectra of films of $Bi_{1.5}Zn_{0.9}Nb_{1.35}Ta_{0.15}O_{6.9}$ with a 3:1 molar ratio of citric acid to organometallic precursor following a three minute drying step at 250°C (blue trace) and a ten minute pyrolysis step at

350°C (black trace). Both spectra show a strong absorption peak at approximately 250 nm, indicating that the dried and partially pyrolyzed films are active in the ultraviolet portion of the electromagnetic spectrum. UV-assisted processing could be pursued for both low temperature thin film deposition and also as a means to remove any residual carbon content in the films prior to crystallization (discussed in section 9.2.3.2).

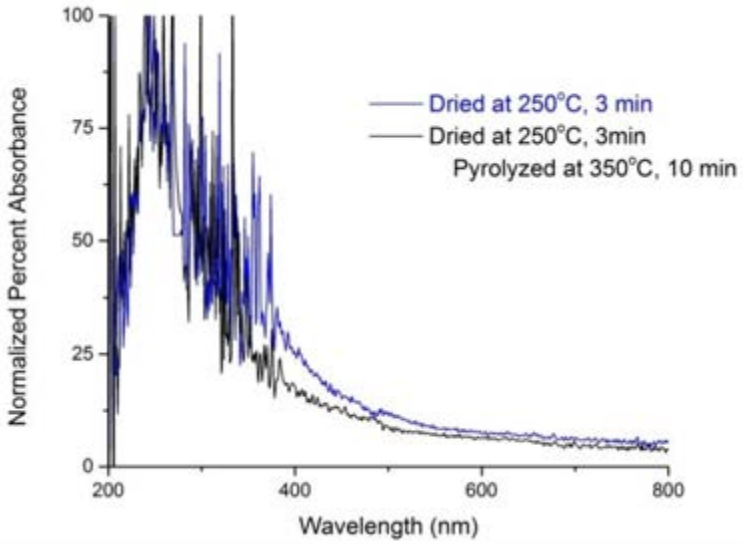

Figure 9-4. UV-Vis spectra of films of $Bi_{1.5}Zn_{0.9}Nb_{1.35}Ta_{0.15}O_{6.9}$ following a three minute drying step at 250°C (blue trace) and a ten minute pyrolysis step at 350°C (black trace).

9.3 References

1] E. K. Michael and S. Trolier-McKinstry, "Amorphous-nanocrystalline lead titanate thin films for dielectric energy storage," *Journal of the Ceramic Society of Japan,* vol. 122, no. 4, p. 250-255, 2014.

2] N. H. Fletcher, A. D. Hilton and B. W. Ricketts, "Optimization of energy storage density in ceramic capacitors," *Journal of Physics D: Applied Physics,* vol. 29, p. 253–258, 1996.

3] N. J. Smith, B. Rangarajan, M. T. Lanagan and C. G. Pantano, "Alkali-free glass as a high energy density dielectric material," *Materials Letters,* vol. 63, pp. 1245-1248, 2009.

U. Balachandran, M. Narayanan, S. Liu and B. Ma, "Development of film-on-foil ceramic

4] dielectrics for embedded capacitors for power inverters in electric drive vehicles," *Japanese Journal of Applied Physics,* vol. 52, p. 05DA10, 2013.

5] G. Sethi, M. Olszta, J. Li, J. Sloppy, M. W. Horn, E. C. Dickey and M. T. Lanagan, "Structure and dielectric properties of amorphous tantalum pentoxide thin film capacitors," *2007 Annual Report Conference on Electrical Insulation and Dielectric Phenomena,* pp. 815-818, 2007.

6] X. Zhou, X. Zhao, Z. Suo, C. Zou, J. Runt, S. Liu, S. Zhang and Q. M. Zhang, "Electrical breakdown and ultrahigh electrical energy density in poly(vinylidene fluoride-hexafluoropropylene) copolymer," *Applied Physics Letters,* vol. 94, p. 162901, 2009.

7] M. S. Mirshekarloo, K. Yao and T. Sritharan, "Large strain and high energy storage density in orthorhombic perovskite $(Pb_{0.97}La_{0.02})(Zr_{1-x-y}Sn_xTi_y)O_3$ antiferroelectric thin films," *Applied Physics Letters,* vol. 97, p. 142902, 2010.

8] H. Ogihara, C. A. Randall and S. Trolier-McKinstry, "High-energy density capacitors utilizing $0.7BaTiO_3$–$0.3BiScO_3$ ceramics," *Journal of the American Ceramic Society,* vol. 92, no. 8, pp. 1719-1724, 2009.

9] A. V. Wagner, G. W. Johnson and T. W. Barbee, "High energy density capacitors fabricated by thin film technology," *MRS Proceedings,* vol. 574, p. 219, 1999.

10] P. Khanchaitit, K. Han, M. R. Gadinski and Q. Wang, "Ferroelectric polymer networks with high energy density and improved discharged efficiency for dielectric energy storage," *Nature Communications,* vol. 4, p. 2845, 2013.

11] L. A. Fredin, Z. Li, M. T. Lanagan, M. A. Ratner and T. J. Marks, "Substantial recoverable energy storage in percolative metallic aluminum-polypropylene nanocomposites," *Advanced Functional Materials,* vol. 23, no. 28, pp. 3560-3569, 2012.

12] S. Chao and F. Dogan, "Processing and dielectric properties of TiO_2 thick films for high-energy density capacitor applications," *International Journal of Applied Ceramic Technology ,* vol. 8, no. 6, pp. 1363-1373, 2011.

13] J. W. Claude, "Ferroelectric polymers for electrical energy storage," Ph.D Thesis, The Pennsylvania State University, 2008.

14] E. K. Michael and S. Trolier-McKinstry, "Cubic pyrochlore bismuth zinc niobate thin films for high-temperature dielectric energy storage," *Journal of the American Ceramic Society,* vol. 98, no. 4, pp. 1223-1229, 2015.

15] F. C. Beach and I. R. McNab, "Present and Future Naval Applications for Pulsed Power," *Proceedings of the IEEE Pulsed Power Conference,* pp. 1-7, 2005.

16] D. F. Untereker, A. M. Crespi, A. Rorvick, C. L. Schmidt and P. M. Skarstad, "Power Systems for Implantable Pacemakers, Cardioverters, and Defibrillators," in *Clinical Cardiac Pacing, Defibrillation and Resynchronization Therapy*, Philadelphia, PA,

Elsevier, 2011, pp. 175-190.

17] F. W. MacDougall, J. B. Ennis, R. A. Cooper, J. Bates and K. Seal, "High energy density pulsed power capacitors," in *Proceedings of the 14th IEEE International Pulsed Power Conference*, p. 513-517, 2003.

18] T. W. Barbee and G. W. Johnson, "High energy density capacitors for power electronic applications using nano-structure multilayer technology," Lawrence Livermore National Laboratory, Livermore, CA, 1995. http://www.osti.gov/scitech/servlets/purl/258017

19] M. Ohring, Materials Science of Thin Films, Hoboken, NJ: Academic Press, 1992.

20] R. Munikoti and P. Dhar, "Highly accelerated life testing (HALT) for multilayer ceramic capacitor qualification," *IEEE Transactions on Components, Hybrids, and Manufacturing Technology,* vol. 11, no. 4, pp. 342-345, 1988.

21] L. Friedman Edge, "Pulsed Laser Deposition of Bismuth Zinc Niobate Thin Films for Dielectric Applications," M.S. Thesis, The Pennylvania State University, 2002.

22] G. H. Maher, "Highly accelerated life testing (HALT) of K-4500 low fired X7R," *The 9th US-Japan Seminar on Dielectric and Piezoelectric Ceramic,* pp. 357-359, 1999.

23] R. Waser, T. Baiatu and K.-H. Härdtl, "dc Electrical Degradation of Perovskite-Type Titanates: I, Ceramics," *Journal of the American Ceramic Society,* vol. 73, no. 6, p. 1645–1653, 1990.

24] M. Pirzada, R. W. Grimes, L. Minervini, J. F. Macguire and K. E. Sickafus, "Oxygen migration in $A_2B_2O_7$ pyrochlores," *Solid State Ionics,* vol. 140, no. 3-4, pp. 201-208, 2001.

25] R. E. Newnham, "Electroceramics," *Reports on Progress in Physics,* vol. 52, pp. 123-156, 1989.

26] T. K. Gupta, "Application of zinc oxide varistors," *Journal of the American Ceramic Society,* vol. 73, no. 7, pp. 1817-1840, 1990.

27] J. Liebault, J. Vallayer, D. Goeuriot, D. Treheux and F. Thevenot, "How the trapping of charges can explain the dielectric breakdown performance of alumina ceramics," *Journal of the European Ceramic Society,* vol. 21, no. 3, pp. 389-397, 2001.

28] M. Lampert and P. Mark, Charge Injection in Solids, Waltham, MA: Academic Press, 1970.

29] J. F. Verweij and J. H. Klootwijk, "Dielectric breakdown I: A review of oxide breakdown," *Microelectronics Journal,* vol. 27, pp. 611-622, 1996.

E. Rosenbaum, J. C. King and C. Hu, "Accelerated testing of SiO_2 reliability," *IEEE*

30] *Transactions on Electron Devices,* vol. 43, no. 1, pp. 70-80, 1996.

Y.-C. Yeo, Q. Lu and C. Hu, "MOSFET gate oxide reliability: Anode hole injection model
31] and its applications," *International Journal of High Speed Electronics and Systems,* vol. 11, no. 3, pp. 849-886, 2001.

The Pennsylvania State University - Materials Research Institute, "Materials Research
32] Institute Materials Characterization Lab," http://www.mri.psu.edu/facilities/mcl/capabilities/characterization-techniques/ft-ir.asp.

R. W. Schwartz, T. Schneller and R. Waser, "Chemical solution deposition of electronic
33] oxide films," *Comptes Rendus Chimie,* vol. 7, no. 5, pp. 433-461, 2004.

R. W. Schwartz and M. Narayanan, "Chemical Solution Deposition — Basic Principles," in
34] *Solution Processing of Inorganic Materials*, Hoboken, NJ, John Wiley & Sons, Inc, 2009, pp. 33-76.

R. W. Schwartz and M. Narayanan, "Thermodynamics and Heating Processes," in *Chemical*
35] *Solution Deposition of Functional Oxide Thin Films*, Wien, Springer, 2013, pp. 343-382.

The University of Edinburgh School of Geosciences, "Ion Microprobe Facility," 13 October
36] 2012. http://www.geos.ed.ac.uk/facilities/ionprobe/SIMS4.pdf.

P. Barber, S. Balasubramanian, Y. Anguchamy, S. Gong, A. Wibowo, H. Gao, H. J. Ploehn
37] and H.-C. zur Loye, "Polymer composite and nanocomposite dielectric materials for pulse power energy storage," *Materials,* vol. 2, pp. 1697-1733, 2009.

O. Baldus and R. Waser, "Laser crystallization studies of barium strontium titanate thin
38] films," *Journal of the European Ceramic Society,* vol. 24, no. 10-11, pp. 3013-3020, 2004.

X. Du, J. J. Dubowski, M. Post, D. Wang and J. Tunney, "Excimer laser annealing of p-type
39] perovskite thin films," *Journal of Vacuum Science & Technology A,* vol. 22, p. 870, 2004.

J.-G. Cheng, J. Wang, T. Dechakupt and S. Trolier-McKinstry, "Low-temperature
40] crystallized pyrochlore bismuth zinc niobate thin films by excimer laser annealing," *Applied Physics Letters,* vol. 87, p. 232905, 2005.

S. S. Bharadwaja, J. Kulik, R. Akarapu, H. Beratan and S. Trolier-McKinstry, *IEEE*
41] *Transactions on Ultrasonics, Ferroelectrics, and Frequency Control,* vol. 57, no. 10, p. 2182, 2010.

J. Lu and S. Stemmer, "Low-loss, tunable bismuth zinc niobate films deposited by rf
42] magnetron sputtering," *Applied Physics Letters,* vol. 83, no. 12, pp. 2411-2413, 2003.

R. L. Thayer, C. A. Randall and S. Trolier-McKinstry, "Medium permittivity bismuth zinc
43] niobate thin film capacitors," *Journal of Applied Physics,* vol. 94, no. 3, pp. 1941-1947,

2003.

44] M. Biegalski, R. Thayer, J. Nino and S. Trolier-McKinstry, "Dielectric Properties of Capacitor Materials in the Optical Frequency Range," in *Proceedings of the 13th IEEE International Symposium on Applications of Ferroelectrics*, p. 7-10, 2002.

45] J. Akedo, "Aerosol deposition method for fabrication of nanocrystal ceramic layer," *Materials Science Forum,* Vols. 449-452, pp. 43-48, 2004.

46] J. Akedo, "Aerosol deposition of ceramic thick films at room temperature: Densification mechanism of ceramic layers," *Journal of the American Ceramic Society,* vol. 89, no. 6, p. 1834–1839, 2006.

47] J. Akedo, M. Lebedev, A. Iwata, H. Ogiso and S. Nakano, "Aerosol deposition method (ADM) for nano-crystal ceramics coating without firing," *MRS Proceedings,* vol. 779, p. W7.10.1/U8.10.1, 2003.

48] Y. Imanaka and J. Akedo, "Embedded Ceramic Passive on FR-4 using Aerosol Deposition," in *Advances in Dielectric Materials and Electronic Devices*, Danvers, MA, Copyright Clearance Center, 2006, pp. 27-38.

49] U. B. Balachandran, B. Ma, T. H. Lee, J. E. Emerson and S. E. Dorris, "Cost-Effective Fabrication of High-Temperature Ceramic Capacitors for Power Inverters," 2014. http://energy.gov/sites/prod/files/2014/07/f17/ape061_balachandran_2014_o.pdf.

50] U. B. Balachandran, B. Ma, T. H. Lee and S. E. Dorris, Writers, *Development of PLZT-based Ceramic Capacitors for Power Electronics in Electric Drive Vehicles.* Presented at 2015 TMS Annual Meeting & Exhibition, March 17, 2015.

51] C. De Dobbelaere, M. Calzada, R. Jimenez, J. Ricote, I. Bretos, J. Mullens, A. Hardy, and M. Van Bael, "Aqueous solutions for low-temperature photoannealing of functional oxide films: Reaching the 400°C Si-technology integration barrier," *Journal of the American Chemical Society,* vol. 133, p. 12922–12925, 2011.

52] C. De Dobbelaere, A. Hardy, J. D'Haen, H. Van den Rul, M. Van Bael, and J. Mullens, "Morphology of water-based chemical solution deposition (CSD) lead titanate films on different substrates: Towards island formation," *Journal of the European Ceramic Society,* vol. 29, p. 1703–1711, 2009.

Appendix A

Thin Film Pyrolysis Conditions

The development of processing parameters for depositing dense films of bismuth zinc niobate was investigated, and the optimized processing parameters are detailed in Chapter 4. Here, a partial table of other investigated deposition parameters is given, along with qualitative comments about the process. In general, thin film densification was pursued by depositing thinner layers of material, altering the drying and pyrolysis temperatures, and increasing the length of the pyrolysis steps. With two exceptions that are noted in the table, all of these conditions resulted in porous films. To facilitate a side-by-side comparison between samples, a solution of bismuth zinc niobate ($Bi_{1.5}Zn_{0.9}Nb_{1.5}O_{6.9}$) with a 3:1 molar ratio of citric acid to organometallic precursor was used for optimization experiments. The initial molarity for all solutions was 0.15 M.

Table A-1. Processing Parameters for the Optimization of Thin Films Prepared via a Pechini-Based Solution Chemistry

Spin Conditions	Drying Conditions	Pyrolysis Conditions	Comments
5,000 rpm (30 s)	150°C (5 min), 200°C (5 min)	400°C (5 min)	---
5,000 rpm (30 s)	150°C (5 min), 250°C (5 min)	400°C (20 min)	---
5,000 rpm (30 s)	150°C (5 min), 250°C (5 min)	400°C (20 min)	The solution was diluted to 0.075 M with acetic acid to slow condensation rates in the drying film and to deposit thinner layers. It was found that acetic acid esterified with ethylene glycol, producing non-uniformities in the film.
5,000 rpm (30 s)	150°C (5 min), 250°C (5 min)	400°C (20 min)	The solution was diluted to 0.075 M with water to reduce layer thickness.
6,000 rpm (45 s)	150°C (5 min), 250°C (5 min)	400°C (20 min)	This approach utilized both a 0.15 M solution and a 0.075 M solution that was diluted with water.
6,000 rpm (45 s)	250°C (3 min)	350°C (7 min), 400°C (7 min)	---
6,000 rpm (45 s)	250°C (3 min)	350°C (7 min), 400°C (10 min)	---
6,000 rpm (45 s)	250°C (3 min)	350°C (10 min), 400°C (7 min)	---
6,000 rpm (45 s)	250°C (3 min)	Ramp at 1°C/min to 400°C; hold at 400°C (1 hr)	Pyrolysis in a furnace yielded dense films
6,000 rpm (45 s)	150°C (5 min), 250°C (5 min)	Ramp at 1°C/min to 400°C; hold at 400°C (1 hr)	Pyrolysis in a furnace yielded dense films

Appendix B

Dielectric Properties of Zirconolite $Bi_2Zn_{2/3}Nb_{4/3}O_7$

In addition to the cubic pyrochlore crystal structure of bismuth zinc niobate that was extensively investigated in this thesis, there is a closely related zirconolite structure adopted by materials with the composition $Bi_2Zn_{2/3}Nb_{4/3}O_7$. This composition has a lower relative permittivity around 80, and dielectric losses of approximately 0.005 [1, 2]. The room temperature permittivity of $Bi_2Zn_{2/3}Nb_{4/3}O_7$ is nearly field independent through applied fields of 1 MV/cm [2], while at 77 K and applied fields of 4.0 MV/cm, the materials has a tunability of approximately 20% [1]. Although zirconolite bismuth zinc niobate exhibits a lower tunability relative to the cubic pyrochlore phase, it was anticipated that the lower polarizability of the material would not lead to energy storage densities of a magnitude comparable to those of the cubic pyrochlore. To verify this hypothesis, thin films of $Bi_2Zn_{2/3}Nb_{4/3}O_7$ were briefly pursued, and the results are summarized here.

To prepare thin films with the composition $Bi_2Zn_{2/3}Nb_{4/3}O_7$, solutions were prepared using the synthesis and film deposition procedures described in Chapters 3 and 4. These films were crystallized at 750°C to form the monoclinic zirconolite phase [1, 2]. The films were analyzed using x-ray diffraction to verify the phase content. The XRD pattern obtained for these films is shown in Figure B-1. The diffraction peaks are consistent with the zirconolite structure of bismuth zinc niobate [3]. There are no peaks that correspond to the formation of a secondary phase or to reaction intermediates, such as ZnO, Bi_2O_3, or Nb_2O_5. This is consistent with the findings of Thayer et al. [1] that $Bi_2Zn_{2/3}Nb_{4/3}O_7$ is the stable phase at film firing temperatures of

750°C. It was reported that when films were fired at and below 650°C, a cubic phase formed, and that at crystallization temperatures of 700°C, a mixture of the zirconolite and cubic phases formed [1, 2, 3].

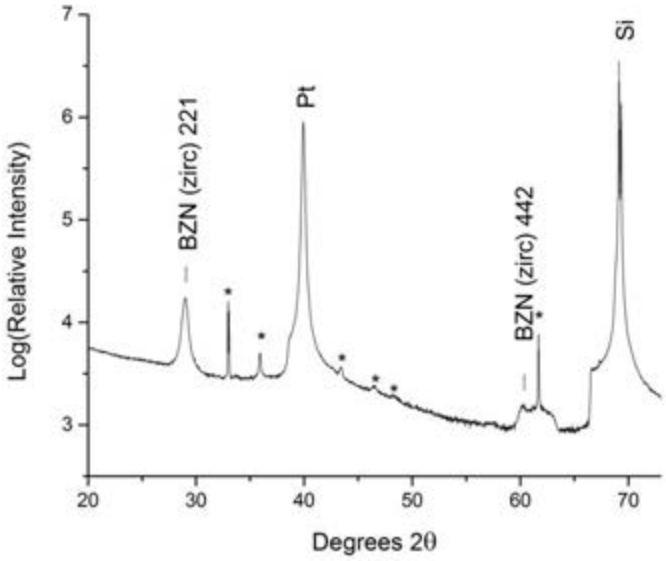

Figure B-1. The x-ray diffraction pattern of zirconolite $Bi_2Zn_{2/3}Nb_{4/3}O_7$ on a platinized silicon substrate. Peaks marked with an asterisk (*) are due to the substrate or are diffraction from X-ray wavelengths other than Cu Kα.

Figure B-2 shows the polarization versus electric field behavior for zirconolite bismuth zinc niobate measured using an AC electric field of 3.0 MV/cm at a measurement frequency of 1 kHz. The hysteresis loop shows $Bi_2Zn_{2/3}Nb_{4/3}O_7$ to be a slightly nonlinear, low loss dielectric. The plot also confirms the relative permittivity value of 71 ± 2 measured using an LCR meter. The dielectric loss for these films was 0.0009. The relative permittivity and loss tangent for the films were slightly lower than other reports in the literature, which may be due to modest amounts of porosity present between the layers of the final film [1]. The room temperature

tunability for these films was calculated to be approximately 7% at applied electric fields of 1.5 MV/cm, which is comparable with reported room temperature tunability values [2].

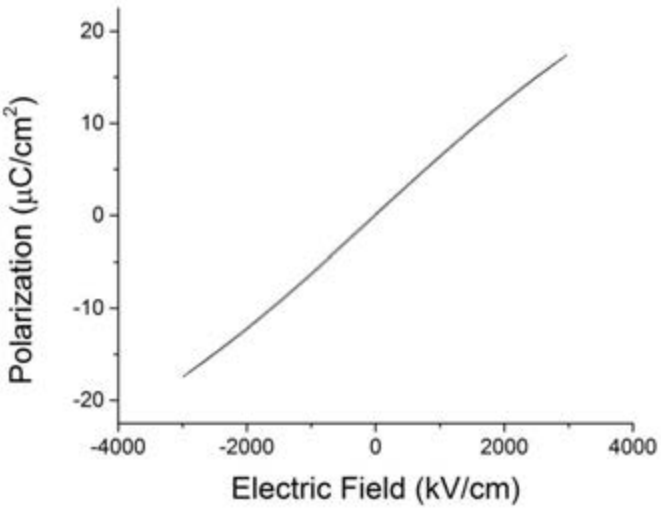

Figure B-2. Polarization-electric field behavior for zirconolite $Bi_2Zn_{2/3}Nb_{4/3}O_7$, a slightly nonlinear, low loss dielectric.

Figure B-3 shows the high-field polarization-electric field hysteresis loops at (a) 1 kHz and (b) 10 kHz for the zirconolite bismuth zinc niobate films. The 1 kHz breakdown strength for the zirconolite films was 3.7 MV/cm, and the 10 kHz breakdown strength for the films was 4.3 MV/cm. Despite the reduced tunability exhibited by the zirconolite composition relative to the cubic pyrochlore films, the relatively lower breakdown strengths resulted in lower energy storage densities for the zirconolite films. At 1 kHz, the maximum energy storage density was 35.1 ± 1.3 J/cm^3, and at 10 kHz, the maximum energy storage density was 45.3 ± 1.9 J/cm^3.

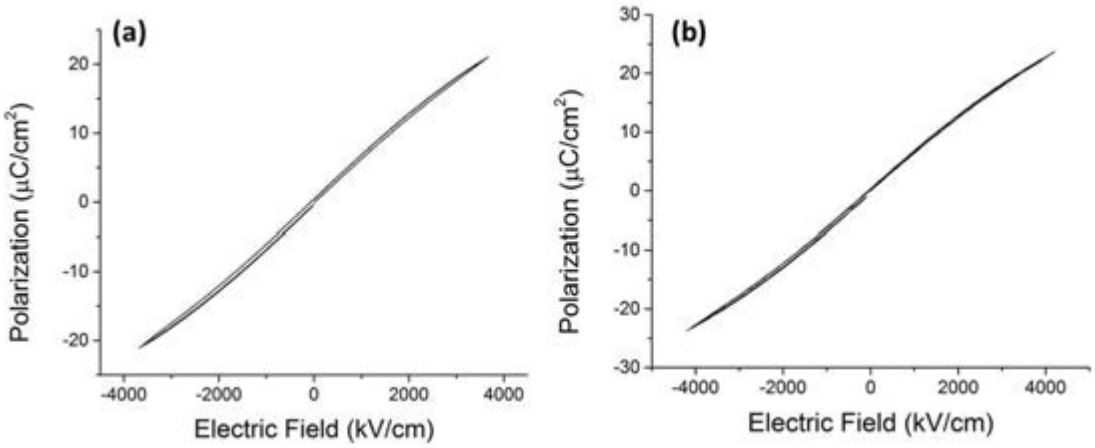

Figure B-3. The polarization-electric field behavior for films of zirconolite bismuth zinc niobate, $Bi_2Zn_{2/3}Nb_{4/3}O_7$, at (a) 1 kHz and (b) 10 kHz.

1] R. L. Thayer, C. A. Randall and S. Trolier-McKinstry, "Medium permittivity bismuth zinc niobate thin film capacitors," *Journal of Applied Physics,* vol. 94, no. 3, pp. 1941-1947, 2003.

2] W. Ren, S. Trolier-McKinstry, C. Randall and T. R. Shrout, "Bismuth zinc niobate pyrochlore dielectric thin films for capacitive applications," *Journal of Applied Physics,* vol. 89, no. 1, pp. 767-774, 2000.

3] K. B. Tan, C. K. Lee, Z. Zainal, C. C. Khaw, Y. P. Tan and H. Shaari, "Reaction Study and Phase Formation in Bi_2O_3-ZnO-Nb_2O_5 Ternary System," *The Pacific Journal of Science and Technology,* vol. 9, no. 2, pp. 468-479, 2008.

VITA

Elizabeth (Lizz) Michael was born in Columbia, Maryland on January 25, 1989. She travelled the world throughout her childhood and young adult life, living in six countries and attending ten schools before arriving at Grove City College to study chemistry and mathematics. Lizz graduated Magna Cum Laude with High Honors in Chemistry from Grove City in 2010. She graduated in May 2012 from Penn State with her M.S. in Materials Science and Engineering, and joined the Trolier-McKinstry group for her Ph.D. work. Under the guidance of Dr. Trolier-McKinstry, Dr. Michael graduated with her Ph.D. in Materials Science and Engineering in August 2015. She is joining the Electronic Materials, Exploratory R&D team with the Dow Chemical Company in the fall.